ADVANCED FINITE-ELEMENT TECHNIQUES FOR SIMULATION OF COMPOSITE MATERIALS AND LARGE-SCALE SCATTERING PROBLEMS

BY

KEDI ZHANG

DISSERTATION

Submitted in partial fulfillment of the requirements
for the degree of Doctor of Philosophy in Electrical and Computer Engineering
in the Graduate College of the
University of Illinois at Urbana-Champaign, 2018

Urbana, Illinois

Doctoral Committee:

Professor Jianming Jin, Chair
Professor Philippe H. Geubelle
Professor Lynford L. Goddard
Assistant Professor Songbin Gong
Professor José E. Schutt-Ainé

Abstract

This dissertation aims at developing sophisticated finite-element based numerical algorithms for efficient electromagnetic modeling and design of composite materials, fast frequency-domain scattering analysis of electrically large problems on massive parallelized computers, and efficient broadband analysis of resonant waveguide structures. To these ends, first, an interface-enriched generalized finite-element method (IGFEM) is introduced for electromagnetic analysis of heterogeneous materials. To avoid using conformal meshes, the method assigns generalized degrees of freedom at material interfaces to capture the discontinuities of the field and its derivatives, and maintains the same level of solution accuracy and computational complexity as the standard FEM based on conformal meshes. The fixed mesh nature combined with an analytical sensitivity analysis significantly reduces the computational cost in gradient-based shape optimization. Second, an efficient parallelization strategy is proposed for the domain decomposition based dual-primal finite-element tearing and interconnecting (FETI-DP) algorithm. Load balancing, global, neighboring, inter-processor communication minimization, and preconditioning techniques are adopted to improve the computational and parallel efficiency. An inhomogeneous truncation boundary condition is presented to enable the FETI-DP simulation of a stratified medium. The parallel FETI-DP algorithm is also combined with a fast near- to far-field transformation and a linear interpolation technique for efficient vectorial field imaging of electrically large objects. Finally, a hybrid technique that consists of the time- and frequency-domain computations and model-order reduction strategy is developed for the efficient simulations of resonant waveguide structures. Numerous results are presented to demonstrate the accuracy, efficiency, and capability of the proposed methods.

To my parents, for their unconditional love and support.

Acknowledgments

The accomplishments in this dissertation would not have been possible without the aid and support of many people. First of all, my cordial gratitude goes to my advisor, Professor Jian-Ming Jin, for his support, guidance, and encouragement throughout these years. Often, he helped me to get through hard times. To me, he is more than an excellent advisor. His kindness, persistence, attitudes, and principles always remind me what kind of person I should be.

My sincere gratitude goes to Professor Philippe H. Geubelle and Professor Lynford L. Goddard for their support, guidance, and encouragement in my research and for being so considerate. The working experiences with them are wonderful. I am also very grateful to Professor José E. Schutt-Ainé and Professor Songbin Gong for serving as members of my doctoral committee and for their valuable time and important suggestions. I would like to thank the professors and my colleagues at the University of Illinois for their friendship and their helpful discussions and suggestions. Especially, I would like to express my thanks to Dr. Jian Guan for introducing me to Professor Jin's Group and for more than ten years' friendship. My thanks extend to Dr. Mingfeng Xue, Dr. Su Yan, Dr. Tianjian Lu, Dr. Ahmad R. Najafi, and Dr. Jinlong Zhu for their tutoring and discussions.

My special thanks go to my wife, Yue Cai, who has made many sacrifices for our family. I would also like to thank my lovely daughter, Danielle, for the joys she brings to me everyday. Finally, I am extremely thankful and indebted to my parents, for their unconditional love and kindness and for being a constant source of encouragement and inspiration for me. This dissertation is dedicated to you!

Table of Contents

List of Tables

List of Figures

Chapter 1

Introduction

Because of its strong adaptability to complex structures, highly inhomogeneous materials, and ability to achieve higher-order numerical accuracy, the finite-element method (FEM) for electromagnetic analysis has experienced tremendous progress in the past few decades [1–3]. While early developments were mainly focused on higher-order vector basis functions (VBFs) [4–6], truncation boundary conditions [7–10], hybrid simulation techniques [11–14], and transient analysis to accurately model various electromagnetic problems [10, 15–17], current developments of the FEM place more emphasis on extending its capability to simulate and optimize advanced materials with complicated internal structures [18–21], utilizing computer clusters to model electrically large and complex targets [22–30], and performing multiphysics and multiscale simulation of real-life engineering applications [31–35]. In this dissertation, we present our progress on the first two topics and on the development of new hybrid methods for broadband analysis of resonant waveguide structures.

1.1 Modeling of Composite Materials

The continued evolution of lighter, stronger, and more efficient systems in civil, industrial, and military applications has fostered a long-standing drive to develop novel sophisticated composite materials [36–38]. To analyze the structural, thermal, and electromagnetic properties of these heterogeneous materials, the FEM is usually adopted for its strong adaptability to complex geometries and high numerical accuracy [3, 39–49]. At the material interfaces where the field normally exhibits C^0-continuity, the FEM has to resort to meshes that are conformal with the interfaces to yield an accurate representation of the solution. However, it is generally acknowledged that creating a conformal mesh inside a complex object with high quality elements is nontrivial, especially in three-dimensional (3-D) problems [50]. There are also other occasions, such as crack growth simulations [44,51], shape/topology optimizations [45,46,52,53], and transient field analysis [47,54], where the generation of multiple conformal meshes needed to capture the geometric changes is cumbersome, expensive and sometimes impractical. The repeated creation of conformal meshes from scratch can even undermine the robustness of the standard FEM in certain mechanical applications because of the violation of local energy conservation [51], and might compromise the overall numerical solution accuracy in multi-physics analysis or co-simulations [31–33].

One possible method that can address the preceding issue of creating (multiple) conformal meshes is the generalized FEM (GFEM), which is based on point clouds/partition of unity instead of tessellation [42, 48, 49, 55]. As it is intensively studied in structural and thermal problems and has been introduced in computational electromagnetics for solving scattering/reflection from perfect electrically conducting (PEC) objects [42, 55], it is a promising approach for alleviating the problem of mesh generation. However, such an approach is not appropriate for electromagnetic analysis of highly inhomogeneous media, as is often the case in the composite material analysis. Another approach that can eliminate creating conformal meshes and re-meshing geometries repeatedly is the fully overlapping domain decomposition method (DDM) [46]. By separating the discretization of the fine geometrical detail region from the uniform background region, one can employ the detail region solution as an equivalent source for the background region and the background region solution as a boundary condition for the detail region, and solve these two problems iteratively until a desired accuracy is achieved. Although the conditioning issues associated with the high aspect ratios of the elements in the two different regions have been tackled and an acceptable accuracy has been achieved, the detail region problem, the background region problem, and the coupling between the two regions must be solved many times to yield a converged solution, which makes this method time-consuming. The third approach, which we refer to as the subdivision FEM, is to explicitly intersect material interfaces with a background mesh and subdivide those non-conformal elements at the material interfaces into several conformal sub-elements, where non-conformal means that the mesh does not conform to material interfaces. Although it is quite straightforward and free of problems like those that appear in the aforementioned two approaches, this approach introduces some extra unknowns and often generates highly irregular elements, thus giving rise to a significantly deteriorated FEM system matrix. Another simple approach is to employ basis functions defined only on the original background mesh and to consider the effect of different materials inside a non-conformal element by performing integration over sub-regions defined by material properties. However, the failure to represent the C^0-continuous field along material interfaces results in a low accuracy.

Recently, an interface-enriched generalized FEM (IGFEM) has been developed to alleviate the aforementioned issues of generating conformal meshes inside highly inhomogeneous domains and repetitively creating meshes with morphing geometries [40, 43, 56]. By enriching the solution space with basis functions associated with generalized degrees of freedom (DoFs) at the intersections of material interfaces and finite elements, this method uses meshes that do not conform to the material interfaces while achieving a level of accuracy comparable to that of the standard FEM with conformal meshes. Although the method has been initially introduced to solve structural and thermal problems with nodal basis functions, it can be extended to analyze electromagnetic problems where VBFs are prevalent, and this extension is one of the main objectives of this dissertation.

The advantages of the IGFEM over the standard FEM are more pronounced in shape/topology optimizations. Combined with a gradient-based shape optimizer and an analytical evaluation of sensitivities of the objective functions and constraints, the IGFEM can significantly speed up the optimization process due to its fixed mesh nature, where the so-called *design velocity field* only needs to be calculated at material interfaces [21]. The application of IGFEM in the gradient-based shape optimization of electromagnetic problems is another objective of this dissertation.

1.2 Modeling of Electrically Large and Complex Targets

The FEM has been demonstrated for decades to be a versatile approach to modeling complicated materials/systems with high numerical accuracy [1,3]. Unfortunately, due to the requirement of a volumetric discretization, the

FEM often yields a linear system with millions or even billions of unknowns for modern engineering applications such as for phased-antenna array analysis, radar signature prediction of electrically large objects, and full-wave synthesis of on-board circuit design. The domain decomposition-based FEMs have been therefore developed to enable large-scale electromagnetic simulations [22–24, 57, 58], among which the dual-primal finite-element tearing and interconnecting (FETI-DP) algorithm for electromagnetic analysis has been shown to be highly powerful because of its numerical stability and potential scalability [22, 23].

The FETI-DP algorithm divides an entire computational domain into many nonoverlapping subdomains and enforces transmission conditions at the subdomain interfaces to form an equivalent order-reduced interface problem. Once the interface problem is solved, the original problem is converted into fully decoupled subdomain problems which can be solved with a high scalability. The interface problem is usually solved by a Krylov subspace method in order to analyze very large problems and exploit the power of high-performance computer clusters. To accelerate the iterative convergence of the interface problem, a global coarse system, which relates only primal unknowns at the corner edges of the subdomain interfaces and functions as a multigrid coarse correction, is constructed and solved using a direct solver [22, 23, 59, 60]. Due to the global communication overhead of explicitly forming the coarse system and the relatively poor parallel performance of direct solvers on distributed computing systems, the achieved parallel efficiency with an increasing number of computation nodes for the previous parallel FETI-DP implementation is limited, especially when simulating large-scale complex problems involving a large number of corner unknowns. Hence, to address the bottleneck in the parallel solution of the global coarse corner system is another major objective of this dissertation.

The application of the parallel FETI-DP algorithm to simulate various challenging and electrically large objects is also a topic of this dissertation. One of the most challenging yet important problems in computational electromagnetics is the scattering analysis of objects above, straddling, and/or embedded in a stratified medium. Such problems are typically found in patch antenna design, interconnect and monolithic microwave integrated circuit simulations, biomedical imaging, nondestructive testing, target identification, geophysical exploration, and remote sensing [61–63]. Integral-equation

(IE) based methods with a multilayer Green's function are usually adopted to simulate these problems [2,62,64]. Although these methods are very accurate, the numerical evaluation of the multilayer Green's function is very difficult and prone to have convergence issues. Moreover, the IE based methods are not efficient for analyzing highly inhomogeneous structures. Therefore, this dissertation also aims at developing a truncation boundary condition for the parallel FETI-DP algorithm to enable large-scale scattering analysis with the presence of a stratified medium.

Another challenging problem is the numerical modeling of coherent optical microscopes, which are widely used in scientific research and industrial applications, such as medical imaging [65, 66], optical lithography [67], semiconductor inspection [68] and metrology [69]. Because of the expensive computational costs, from the near-field modeling of the scatterers, to the far-field transformation, and finally to the calculation of images, past simulations were limited to electrically small objects [70]. However, at optical frequencies, many samples are at least tens of wavelengths or even more than hundreds of wavelengths in size. Hence, to develop an efficient and systematic numerical modeling of optical microscopes for the imaging of electrically large objects is one of the research topics of this dissertation as well.

1.3 Modeling of Resonant Waveguide Structures

Efficient broadband modeling of resonant waveguide devices, such as filters, multiplexers, and power dividers, can significantly reduce the design periods, and therefore has been an important research topic for decades [3, 10, 71–81]. Early developments were mainly focusing on the equivalent circuit theory and mode matching (MM) method, which typically have a low solution accuracy or convergence problems [71–75]. In the past few years, hybrid algorithms that combine the efficiency of the MM method and flexibility of the full-wave simulation techniques were proposed [79, 80]. Although these high-fidelity algorithms can handle rather complicated structures, the broadband analysis is usually inefficient since the calculations are normally performed in the frequency domain. As an alternative to the frequency-domain methods, a time-domain algorithm can be used to analyze the broadband responses. However, the number of time marching steps is often prohibitively large for highly resonant devices. To alleviate the aforementioned issues, an accurate and efficient hybrid algorithm that combines the rigorous full-wave finite-element time-domain (FETD) [3, 81] method with the generalized scattering matrix (GSM) technique is investigated in this dissertation.

Unlike the broadband simulation of resonant waveguide microwave devices, the broadband monostatic simulation of electromagnetic scattering from a large and deep open cavity [82–100] is even more challenging due to the large electrical size of the geometry and wide angle sweep. Despite the significant progress in computational electromagnetics over the years, the efficient broadband monostatic analysis of large and deep cavities with high fidelity is still rare in the literature. The well-known finite element-boundary integral (FEBI) method [95–98] is efficient for fast monostatic radar cross-section (RCS) calculation. Unfortunately, its efficiency deteriorates quickly with a larger cavity aperture and is ineffective for a broadband RCS analysis. The DDMs [90, 91, 93, 94] are also popular for the scattering analysis of a large and deep cavity. These methods can harness the power of parallel computing; because they are frequency-domain methods, the iterative solution in the DDMs is not efficient for the monostatic RCS calculation or for a broadband sweep. Therefore, the final goal of this dissertation is to develop a hybrid time- and frequency-domain computation technique and the model-order reduction strategy to efficiently compute the broadband monostatic RCS of a large and deep open cavity.

1.4 Organization

The remainder of this dissertation is organized as follows. Chapters 2 and 3 present the IGFEM formulations for two- and three-dimensional problems. Numerical examples are then provided to study the method's accuracy, h-refinement convergence, computational complexity, and system matrix conditioning. Engineering applications are simulated to demonstrate the capability of the proposed method. Chapter 4 applies the IGFEM to the gradient-based shape optimization problems. The formulations for the analytical sensitivity analysis are derived, followed by several numerical examples to demonstrate the efficiency of the proposed optimizer. Chapter 5 introduces an efficient parallelization of the FETI-DP algorithm for large-scale electromagnetic simulations. Specifically, load balancing among various parallelization stages, a tailored communication-avoiding iterative solver for the global coarse corner system, preconditioning for the iterative solver, and nonblocking communications are discussed in detail. Several large numerical examples are simulated to demonstrate the accuracy, scalability, and capability of the parallel scheme. Chapter 6 applies the parallel FETI-DP algorithm to model the scattering from a stratified medium. The truncation boundary condition and fast far-field calculation equations for a stratified medium are derived and numerical examples are presented to verify the solution accuracy. Chapter 7 applies the parallel FETI-DP algorithm to the modeling of coherent optical microscopes. The formulations for imaging using far-field results are presented, followed by several verification examples and electrically large examples to demonstrate the efficiency and capability of the systematic imaging scheme. Chapter 8 introduces a hybrid FETD-GSM technique for accurate and efficient broadband analysis of highly resonant microwave devices. The formulations for the FETD method, time-domain waveguide port boundary condition (WPBC), and cascading of GSM are presented. Several waveguide filters are given to demonstrate the accuracy and efficiency of this hybrid technique. Chapter 9 presents a broadband monostatic RCS and inverse synthetic aperture radar (ISAR) calculation of large and deep open cavities. The FETD method with the complex-frequency shifted perfectly matched layers (CFS-PML) for waveguide port truncation, inhomogeneous eigen-solver, and ISAR imagery is discussed. Different open cavity structures are presented to demonstrate the accuracy and efficiency of the proposed algorithm. Finally, the conclusion of this dissertation is drawn in Chapter 10, together with the discussion of future work.

Chapter 2

Interface-Enriched Generalized FEM for 2-D Problems

2.1 Introduction

Composite materials are made by combining two or more significantly different materials to explore certain properties that are not available in each individual material, such as higher strength- and/or stiffness-to-weight ratio, reduced fatigue, increased or reduced thermal insulation, or even possession of multifunctionality [101, 102]. In recent years, composite materials have experienced rapid evolution and found enormous applications in almost every aspect of human life (automotive, aerospace, wind energy, body armor, furniture, sporting goods, marine, electronics, and communication). In fact, taking aerospace applications for example, the proportion of composite on structural weight has increased 20-fold in the past four decades and 2-fold in the past ten years, as illustrated in Fig. 2.1. Unfortunately, due to the complexity of the internal structures, the standard FEM, which is based on conformal meshes, is not efficient for electromagnetic modeling of such composite materials.

In this chapter, we introduce the IGFEM, which was initially developed for solving thermal and structural problems using nodal basis functions, to solve the curl-curl wave equation using VBFs. In Section 2.2, we present the basic formulation for the electromagnetic problem of interest and a brief introduction of the VBFs. We then discuss the proposed enriched VBFs and illustrate their implementation in Section 2.3. In Section 2.4, we study the accuracy, h-refinement convergence, computational complexity, and condition number of the resultant system matrix by analyzing the scattering of a dielectric slab in free space and a circular inclusion in free space. Finally, two application examples involving four sinusoidal micro-channels and fifty-six circular inclusions, respectively, are simulated in Section 2.5 to demonstrate the capability of the proposed method.

2.2 Problem Description

Given an inhomogeneous and source-free medium shown schematically in Fig. 2.2 with material properties specified by permittivity ϵ and permeability μ, the frequency-domain Maxwell's equations are

$$\nabla \times \mathbf{E} = -\mathrm{j}\omega\mu\mathbf{H}, \tag{2.1}$$

$$\nabla \times \mathbf{H} = \mathrm{j}\omega\epsilon\mathbf{E}, \tag{2.2}$$

where $\mathbf{E}$ is the total electric field, $\mathbf{H}$ is the total magnetic field, and ω is the angular frequency. The time dependence $e^{\mathrm{j}\omega t}$ has been assumed and is suppressed throughout this dissertation [39].

From (2.1) and (2.2), we can derive a partial differential equation to be solved by the FEM:

$$\nabla \times \left(\frac{1}{\mu_\mathrm{r}}\nabla \times \mathbf{E}\right) - k_0^2\epsilon_\mathrm{r}\mathbf{E} = 0, \tag{2.3}$$

where $\mu_\mathrm{r} = \mu/\mu_0$, $\epsilon_\mathrm{r} = \epsilon/\epsilon_0$, $k_0 = \omega\sqrt{\mu_0\epsilon_0}$, and ϵ_0 and μ_0 are two physical constants defined as the permittivity and permeability of free space. To make the solution unique in the desired computational domain, proper boundary conditions must be applied. The Dirichlet, Neumann, and Robin boundary conditions are respectively represented by

$$\hat{n} \times \mathbf{E} = \mathbf{P} \quad \text{on} \quad \partial\Omega_D, \tag{2.4}$$

$$\hat{n} \times \left(\frac{1}{\mu_\mathrm{r}}\nabla \times \mathbf{E}\right) = \mathbf{Q} \quad \text{on} \quad \partial\Omega_N, \tag{2.5}$$

$$\hat{n} \times \left(\frac{1}{\mu_\mathrm{r}}\nabla \times \mathbf{E}\right) + \mathrm{j}\frac{k_0}{\eta_\mathrm{r}}\hat{n} \times (\hat{n} \times \mathbf{E}) = \mathbf{U} \quad \text{on} \quad \partial\Omega_R, \tag{2.6}$$

where $\mathbf{P}$, $\mathbf{Q}$, and $\mathbf{U}$ are known quantities, and $\eta_\mathrm{r} = \sqrt{\mu_\mathrm{r}/\epsilon_\mathrm{r}}$. For PEC and perfect magnetic conductor (PMC) boundaries, both $\mathbf{P}$ and $\mathbf{Q}$ vanish. To simulate wave propagation in an infinite homogeneous space, either an absorbing boundary condition (ABC) or a perfectly matched layer (PML) is required to truncate the computational domain [3, 7, 8, 39]. Although ABC has a larger numerical reflection than does PML, especially at a large oblique incident angle, its simplicity and ease of implementation have won it wide popularity. In this chapter, we choose ABC to truncate the computational domain. For the first-order ABC, the quantity **U** in the Robin boundary condition becomes

$$\mathbf{U} \approx \hat{n} \times \left(\frac{1}{\mu_\mathrm{r}} \nabla \times \mathbf{E}^\mathrm{inc} \right) + \mathrm{j} \frac{k_0}{\eta_\mathrm{r}} \hat{n} \times \left(\hat{n} \times \mathbf{E}^\mathrm{inc} \right). \tag{2.7}$$

In the standard FEM procedure, the unknown electric field intensity **E** is expanded as

$$\mathbf{E} = \sum_{i=1}^{N} \alpha_i \mathbf{N}_i, \tag{2.8}$$

where $\mathbf{N}_i$ are the vector basis functions associated with each element edge, α_i are the corresponding unknown coefficients, and N is the number of vector basis functions defined over the entire computational domain. By employing Galerkin's method, a linear system is formed:

$$[K]\{\alpha\} = \{b\}, \tag{2.9}$$

where

$$\begin{aligned} K_{ij} = &\int_\Omega \left[\frac{1}{\mu_\mathrm{r}} (\nabla \times \mathbf{N}_i) \cdot (\nabla \times \mathbf{N}_j) - k_0^2 \epsilon_\mathrm{r} \mathbf{N}_i \cdot \mathbf{N}_j \right] d\Omega \\ &+ \mathrm{j} \frac{k_0}{\eta_\mathrm{r}} \int_{\partial\Omega_R} (\hat{n} \times \mathbf{N}_i) \cdot (\hat{n} \times \mathbf{N}_j)\, d\Gamma, \end{aligned} \tag{2.10}$$

$$b_i = \int_{\partial\Omega_R} (\hat{n} \times \mathbf{N}_i) \cdot \left(\frac{1}{\mu_\mathrm{r}} \nabla \times \mathbf{E}^\mathrm{inc} + \mathrm{j} \frac{k_0}{\eta_\mathrm{r}} \hat{n} \times \mathbf{E}^\mathrm{inc} \right) d\Gamma. \tag{2.11}$$

The resulting sparse linear system can be conveniently solved by either an iterative or a direct solver [103–105]. After the unknown coefficients are determined, other desired physical quantities, for instance power reflection coefficient, can be readily evaluated. A challenging problem, as is well known, is that standard FEM solutions only guarantee the field with C^0-continuity. When a non-conformal mesh, such as that illustrated in Fig. 2.2, is adopted for the FEM solution, the standard FEM fails to capture the discontinuities of the normal derivative of the field's tangential component. These discontinuities, which are caused by the difference in the adjacent material properties, result in a poor numerical accuracy. This issue has been alleviated recently with a new interface-enriched generalized FEM (IGFEM) [40,43], where extra basis functions are introduced at the material interfaces to enrich the solution space and retrieve the "missing" field information. This kind of scheme has been shown to be effective and efficient in various thermal and structural applications [40, 43]. However, using this method to solve electromagnetic problems creates a challenge to extend the enrichment ideas from the nodal to the VBFs. There are mainly three difficulties: 1) where we should define the enriched VBFs; 2) what the expressions of the enriched VBFs are; and 3) how many enriched VBFs are required. These issues are addressed in the next section.

2.3 Vector Basis Functions and Their Enrichment

To better illustrate the basic idea of IGFEM, let us first review triangular and quadrilateral elements that are commonly adopted in the standard two-dimensional FEM. For a triangle with three vertices $(x_1, y_1), (x_2, y_2), (x_3, y_3)$ in the xy-coordinate system and $(0, 0), (1, 0), (0, 1)$ in the $\xi\eta$-coordinate system, the linear form that maps the triangle from the $\xi\eta$-system to the xy-system is given by

$$\begin{bmatrix} x \\ y \end{bmatrix} = \begin{bmatrix} x_1 & x_2 & x_3 \\ y_1 & y_2 & y_3 \end{bmatrix} \cdot \begin{bmatrix} 1-\xi-\eta \\ \xi \\ \eta \end{bmatrix}. \tag{2.12}$$

The first-order curl-conforming VBFs defined on each edge of the triangle are expressed as [3]

$$\begin{bmatrix} \mathbf{N}_1 \\ \mathbf{N}_2 \\ \mathbf{N}_3 \end{bmatrix} = \begin{bmatrix} (1-\eta)\nabla\xi + \xi\nabla\eta \\ -\eta\nabla\xi + \xi\nabla\eta \\ -\eta\nabla\xi - (1-\xi)\nabla\eta \end{bmatrix} \circ \begin{bmatrix} l_{12} \\ l_{23} \\ l_{31} \end{bmatrix}, \tag{2.13}$$

where $l_{ij} = \sqrt{(x_i - x_j)^2 + (y_i - y_j)^2}$ and $\circ$ denotes the Hadamard product.

Similarly, for a quadrilateral with four vertices (x_1, y_1), (x_2, y_2), (x_3, y_3), (x_4, y_4) in the xy-coordinate system and $(-1, -1)$, $(1, -1)$, $(1, 1)$, $(-1, 1)$ in the $\xi\eta$-coordinate system, the bilinear form that maps the quadrilateral from the $\xi\eta$-system to the xy-system is given by

$$\begin{bmatrix} x \\ y \end{bmatrix} = \begin{bmatrix} x_1 & x_2 & x_3 & x_4 \\ y_1 & y_2 & y_3 & x_4 \end{bmatrix} \cdot \begin{bmatrix} (1-\xi)(1-\eta)/4 \\ (1+\xi)(1-\eta)/4 \\ (1+\xi)(1+\eta)/4 \\ (1-\xi)(1+\eta)/4 \end{bmatrix}. \tag{2.14}$$

The first-order curl-conforming VBFs defined on each edge of the quadrilateral are given by [3]

$$\begin{bmatrix} \mathbf{N}_1 \\ \mathbf{N}_2 \\ \mathbf{N}_3 \\ \mathbf{N}_4 \end{bmatrix} = \begin{bmatrix} (1-\eta)\nabla\xi/4 \\ (1+\xi)\nabla\eta/4 \\ -(1+\eta)\nabla\xi/4 \\ -(1-\xi)\nabla\eta/4 \end{bmatrix} \circ \begin{bmatrix} l_{12} \\ l_{23} \\ l_{34} \\ l_{41} \end{bmatrix}. \tag{2.15}$$

It is worth mentioning that each of these VBFs has a constant tangential component along the associated edge and a linear normal component along other edges. In electromagnetics, the field inside a region can be uniquely determined as long as the tangential component of the field is uniquely defined [39]. Although the divergence-free property would be satisfied by the VBFs for a triangular element, it turns out that for an arbitrary quadrilateral the divergence is not necessarily zero [3]. Fortunately, numerical results indicate that the non-zero divergence of the quadrilateral basis functions does not significantly affect the solution accuracy, as will also be observed in the numerical examples provided in Sections 2.4 and 2.5.

At material interfaces, one expects a gradient discontinuity of the tangential component of the electric field. It is obvious that an enriched VBF, defined along the intersection of an element coincident with the material interface, with a constant tangential component along the intersection and no tangential component along other edges, would capture the normal derivative discontinuity of the tangential field while at the same time preserving tangential field continuity along other edges. With the enriched VBF described above, the electric field inside an arbitrary element can be uniformly expressed as

$$\mathbf{E} = \sum_{i=1}^{N} \alpha_i \mathbf{N}_i + \sum_{i=1}^{N_{en}} \beta_i \mathbf{N}_i^{en}, \tag{2.16}$$

where β_i and N_{en} are the unknown coefficients and total number of the enriched VBF $\mathbf{N}_i^{en}$. In a triangular element, $\mathbf{N}_i^{en}$ is given by

$$\mathbf{N}^{en} = \mathbf{N}^{C1} + \mathbf{N}^{C2}, \tag{2.17}$$

where $\mathbf{N}^{C1}$ and $\mathbf{N}^{C2}$ are VBFs defined along the intersection within the first and second children elements, respectively. Two different scenarios of the enriched VBF are demonstrated in Fig. 2.3. It is observed that the enriched VBF has a constant tangential component along the material interface and no tangential component along other edges. Besides that, the proposed enriched VBF enjoys several advantages on the implementation aspects: 1) Since the enrichment only occurs at the intersection of an element and a material interface, it adds a minimal number of extra unknowns to the original linear system in order to retrieve the missing field information caused by material mismatch. 2) Due to the fact that an enriched basis function never coincides with the geometry boundary, the proposed method avoids potential difficulties in assigning the prescribed values of the tangential field along Dirichlet boundaries.

2.4 Accuracy and Convergence Study

To investigate the accuracy and convergence of the proposed IGFEM, the L_2-norm of the solution error, expressed as

$$\left\|\mathbf{E} - \mathbf{E}^h\right\|_{L_2(\Omega)} = \sqrt{\int_\Omega \left\|\mathbf{E} - \mathbf{E}^h\right\|^2 d\Omega}, \tag{2.18}$$

is calculated and compared with those obtained from the standard FEM with conformal meshes. In the above equation, $\mathbf{E}$ is the exact solution obtained by the analytical solution and $\mathbf{E}^h$ is the numerical solution calculated by either IGFEM or the standard FEM with respect to the mesh size h.

In many real applications, the power reflection coefficient R_P, defined as

$$R_P = R_E^2 = \frac{\left\|\mathbf{E}^{\text{sca}}\right\|^2}{\left\|\mathbf{E}^{\text{inc}}\right\|^2}, \tag{2.19}$$

is usually the only measurable or accessible quantity, where R_E stands for the field reflection coefficient, $\mathbf{E}^{\text{sca}}$ and $\mathbf{E}^{\text{inc}}$ are the scattered and incident fields, respectively. Hence, in the following examples, we calculate the power reflection coefficient and compare it with the analytical solution whenever possible.

The method proposed in this chapter, which is similar to the subdivision FEM in the sense that both of these two methods divide the background triangular mesh into sub-triangular and quadrilateral meshes with the material interface, may introduce certain sub-elements with extremely small sizes and/or poor aspect ratios. It is therefore important to investigate how severely the final system matrix will be deteriorated by those sub-elements. A good factor to characterize a system matrix $[K]$ is its condition number, which can be defined as

$$\kappa\left([K]\right) = \frac{\sigma_{max}\left([K]\right)}{\sigma_{min}\left([K]\right)}, \tag{2.20}$$

where $\sigma_{max}\left([K]\right)$ and $\sigma_{min}\left([K]\right)$ are maximal and minimal singular values of $[K]$ respectively. To systematically study the condition of the system matrix generated by IGFEM and demonstrate its superiority in handling sub-elements with very small sizes and/or highly irregular shapes, in the following two verification examples, we calculate the condition numbers of system matrices generated from both the IGFEM and the subdivision FEM, and compare them with those from the standard FEM system matrices.

For all the numerical examples, the uniform incident plane wave is illuminated from the left of the object and propagates towards the right. The polarization of the incident electric field resides in the xy-plane. The FEM resultant linear system is usually rather ill-conditioned, which is challenging to solve using iterative methods without constructing an effective preconditioner [3, 106]. In this chapter, the linear systems are solved by the highly efficient direct solver PARDISO [105]. The computations are carried out in double float precision on a laptop with 8-GB memory and one Intel Core i7-3720QM CPU.

2.4.1 Dielectric Slab in Free Space

The first example considered here is an infinitely large dielectric slab placed in free space and illuminated by a plane wave, as shown in Fig. 2.4. To simulate the infinite region, the top and bottom boundaries are enforced as PEC. The first-order ABC is adopted to truncate the computational domain at the left and right boundaries. The dielectric slab is $2/15\lambda_0 \times \lambda_0$ with respect to the frequency at 1 GHz. The total computational domain is $2\lambda_0 \times \lambda_0$. The material properties of the dielectric slab are $\mu_1 = \mu_0$ and $\epsilon_1 = (3 - \mathrm{j}4)\epsilon_0$, respectively. Fig. 2.5a shows the IGFEM solution of the total electric field under a 1-GHz incident plane wave with a mesh size of $\lambda_0/15$. For comparison, the total electric field obtained using the standard FEM with the same mesh size is depicted in Fig. 2.5b. As can be seen from Fig. 2.5, even with a non-conformal mesh, the IGFEM captures the normal derivative discontinuity at the material interface.

For an infinitely large dielectric slab with thickness d, the electric field reflection coefficient for a normal incident plane wave is

$$R_E = R_{01} \frac{1 - e^{-\mathrm{j}2k_1 d}}{1 - R_{01}^2 e^{-\mathrm{j}2k_1 d}}, \tag{2.21}$$

where

$$R_{01} = \frac{\epsilon_1 k_0 - \epsilon_0 k_1}{\epsilon_1 k_0 + \epsilon_0 k_1}, \quad k_1 = \omega\sqrt{\mu_1 \epsilon_1}, \quad d = \frac{2}{15}\lambda_0. \tag{2.22}$$

Figure 2.6a shows the comparisons of the power reflection coefficients calculated from IGFEM, the standard FEM, and the analytical solution with the frequencies ranging from 0.01 to 1 GHz. An excellent agreement is observed between the analytical and numerical solutions. The convergence rate of the L_2-norm of the field solution error with respect to the mesh size h is given in Fig. 2.6b. As shown there, the IGFEM yields a convergence rate similar to that of the standard FEM, with a slightly better precision for larger mesh sizes.

Besides achieving a comparable solution accuracy, the IGFEM, without requiring a mesh conforming to the material interfaces, also maintains the same level of computational complexity as the standard FEM. As depicted in Fig. 2.7a, the memory consumption and total computational time for both the IGFEM and the standard FEM are nearly the same. The condition numbers of system matrices generated by the standard FEM, IGFEM, and subdivision FEM are systematically studied in Fig. 2.7b. For this verification problem, structured background meshes are adopted so that sub-elements with poor aspect ratios will never be created even when their sizes are extremely small. Since the IGFEM evaluates the integrations involved in the stiffness and mass matrices calculations over the background mesh, and the vector basis functions are normalized to have a unitary tangential component, the IGFEM generated system matrices should have condition numbers approximately equal to those of the standard FEM generated system matrices, as is apparent in Fig. 2.7b. The subdivision FEM, however, performing the integrations over each sub-elements, has much higher condition numbers when very small sub-elements are created.

2.4.2 Dielectric Cylinder in Free Space

The second example is the scattering of an infinitely long dielectric cylinder in free space. The radius of the cylinder is $\lambda_0/3$ and the total computational domain is $5\lambda_0 \times 5\lambda_0$, both with respect to the free-space wavelength at 10 GHz, as shown in Fig. 2.8a. The material properties of the dielectric cylinder are given as $\mu_1 = \mu_0$ and $\epsilon_1 = 4\epsilon_0$. To truncate the simulation domain, all four boundaries are enforced as ABC. The analytical solution for this problem is [39]: (i) For the field outside the dielectric cylinder:

$$E_\rho = \frac{1}{k_0\rho}\sum_{n=0}^{\infty}(-\mathrm{j})^{n-1} n \sin(n\phi)\delta_n \left[J_n(k_0\rho) - a_n H_n^{(1)}(k_0\rho)\right], \tag{2.23}$$

$$E_\phi = \sum_{n=0}^{\infty}(-\mathrm{j})^{n-1}\cos(n\phi)\delta_n \left[J_n'(k_0\rho) - a_n H_n^{(1)'}(k_0\rho)\right]. \tag{2.24}$$

(ii) For the field inside the dielectric cylinder:

$$E_\rho = \frac{1}{k_1\rho\sqrt{\epsilon_r}}\sum_{n=0}^{\infty}(-\mathrm{j})^{n} n \sin(n\phi) b_n \delta_n J_n(k_1\rho), \tag{2.25}$$

$$E_\phi = \eta_\mathrm{r}\sum_{n=0}^{\infty}(-\mathrm{j})^{n}\cos(n\phi) b_n \delta_n J_n'(k_1\rho). \tag{2.26}$$

where $\epsilon_{\mathrm{r}} = \epsilon_1/\epsilon_0$, $\eta_{\mathrm{r}} = 1/\sqrt{\epsilon_{\mathrm{r}}}$, and ρ is the radius of the cylinder. The coefficients a_n, b_n and δ_n are given by

$$a_n = \frac{J_n'(k_0a)J_n(k_1a) - \eta_{\mathrm{r}} J_n(k_0a)J_n'(k_1a)}{H_n^{(1)'}(k_0a)J_n(k_1a) - \eta_{\mathrm{r}} H_n^{(1)}(k_0a)J_n'(k_1a)}, \tag{2.27}$$

$$b_n = \frac{2}{\pi k_0 a}\frac{1}{H_n^{(1)'}(k_0a)J_n(k_1a) - \eta_{\mathrm{r}} H_n^{(1)}(k_0a)J_n'(k_1a)}, \tag{2.28}$$

$$\delta_n = 1 \text{ for } n = 0 \text{ and } \delta_n = 2 \text{ for } n \neq 0. \tag{2.29}$$

In the above expressions, $J_n(x)$ stand for the Bessel functions of the first kind of order n, $H_n^{(1)}(x)$ stand for the Hankel functions of the first kind of order n, $J_n'(x)$ and $H_n^{(1)'}$ are the first derivative of $J_n(x)$ and $H_n^{(1)}(x)$, respectively.

The convergence rate of the L_2-norm of the field solution error with respect to the mesh size h is shown in Fig. 2.8b. Since the first-order ABC introduces a certain error at an oblique incident angle which increases with an increasing incident angle [3], the error caused by ABC becomes dominant when the mesh is refined. Therefore, the L_2-norm of the field solution error does not scale as the theoretical expectation for very fine meshes. Nevertheless, the IGFEM still yields a precision comparable to that of the standard FEM, especially when the mesh size is large.

Figure 2.9a shows the IGFEM solution of the total electric field under a 10-GHz incident plane wave with a mesh size of $\lambda_0/15$. For comparison, Fig. 2.9b shows the electric field at the same frequency and with the same mesh size obtained with the standard FEM. As is apparent there, a good agreement is achieved between IGFEM and FEM solutions.

The peak memory usage and total solution time for both the standard FEM and the IGFEM are plotted in Fig. 2.10a, indicating that the IGFEM does not increase computational complexity much to achieve the same solution accuracy as the standard FEM. The condition numbers of the FEM system matrices are investigated in Fig. 2.10b. For this verification problem, unstructured background meshes are used to make sure that sub-elements with poor aspect ratios and very small sizes will be created. Although sub-elements with irregular shapes inevitably deteriorate the system matrices, the IGFEM manages to increase the condition numbers only a little bit while the subdivision FEM increases the condition numbers dramatically, both compared with those from the standard FEM.

2.5 Applications

In this section, we present two more complex examples to demonstrate the capability of the IGFEM in analyzing electromagnetic problems in heterogeneous materials. Emphasis is placed on capturing the total electric field distribution and the power reflection coefficient.

2.5.1 Heterogeneous Material with Multiple Microvascular Channels

The first example is inspired by the recently developed multi-functional microvascular composites [37, 38]. By circulating various fluids inside the microvascular channels, this new class of material has many potential aerospace applications in active cooling, self-healing, health monitoring, and electromagnetic stealth.

The specific problem considered here, as shown in Fig. 2.11, is a PEC-backed polynaphthalene material with four sinusoidal microvascular channels inside. The top and bottom boundaries are enforced as PEC to mimic the spatial periodicity of the material distribution. The left boundary is set as ABC to truncate the infinite computational domain. The free-space region (ϵ_0) and background material region ($\epsilon_1 = 2.2\epsilon_0$) both have a dimension of $5\lambda_0 \times 5\lambda_0$, making the total computational domain $10\lambda_0 \times 5\lambda_0$, where λ_0 is the free-space wavelength of the incident plane wave at 1.5 GHz frequency. The incident field is polarized in the **E** direction and propagates in the **k** direction, which are shown in Fig. 2.11. The geometry configuration and material properties of the sinusoidal microvascular channels are listed in Table 2.1.

The computed field solution using IGFEM with a mesh size of $\lambda_0/40$ is given in Fig. 2.12. As is apparent there, the normal derivative discontinuity of the tangential field at material interfaces is well captured by IGFEM. It is worth mentioning that, with about 280,000 degrees of freedom, the total computational time is less than 5.9 seconds. The power reflection coefficient, evaluated with frequencies ranging from 0.01 to 1.5 GHz, is depicted in Fig. 2.13. Since the background material is lossless and the attenuation caused by the sinusoidal microchannels is very small in the low-frequency regime due to their small diameters and low-loss properties, most of the incident power is reflected back by the PEC. The strong oscillations in the mid-frequency regime are caused by the multi-reflections between material interfaces.

2.5.2 Heterogeneous Material with Multiple Circular Inclusions

The second example is motivated by the development of a particulate composite, composed of a glass matrix with ellipsoid alumina inclusion for high-temperature applications [107]. Since these materials are usually coated on objects for thermal insulation or heat dissipation, it is important to analyze their influences on the electromagnetic scattering properties of the original objects, especially for the military objects which have a severe restriction on the reflection of radar waves.

The problem considered here, illustrated in Fig. 2.14, is a PEC-backed composite material containing 56 circular inclusions that have various diameters and material properties. An ABC is adopted along the left boundary to truncate the infinite computational domain. A PEC is enforced for the top and bottom boundaries to mimic the spatial periodicity of the material distribution. The free-space region (ϵ_0) and background material region ($\epsilon_1/\epsilon_0 = 3 - \mathrm{j}0.1$) both have a dimension of $10\lambda_0 \times 15\lambda_0$, making the total computational domain $20\lambda_0 \times 15\lambda_0$, where λ_0 is the free-space wavelength of a 3-GHz incident plane wave. The incident field is polarized in the $\mathbf{E}$ direction and propagates in the $\mathbf{k}$ direction, as shown in Fig. 2.14. The geometrical configurations and material properties of the circular inclusions are listed in Table 2.2.

With the smallest circular inclusions having a radius of only $\lambda_0/5$, the total computational domain is uniformly discretized by planar triangular patches with size of $\lambda_0/20$. Figure 2.15 shows the computed total electric field distribution using IGFEM under an incident plane wave at 3 GHz. As observed from the figure, IGFEM successfully captures the normal derivative discontinuity of the tangential field caused by material mismatch. Although the number of the degrees of freedom is more than 400,000, the total solution time is less than 9 seconds. The power reflection coefficient, evaluated with frequencies ranging from 0.01 to 3 GHz, is depicted in Fig. 2.16. Since the background material and the inclusions are much more lossy than those in the previous example, the power reflection coefficient decreases rapidly when the frequency increases. The strong oscillation in the low-frequency regime is caused by the multi-reflections between material interfaces. In the high-frequency regime, most of the insignificant reflections are absorbed by the lossy materials leaving only several leading reflections. Hence, the power reflection coefficient curve is much flatter and tends to be a constant.

2.6 Summary

In this chapter, we presented an IGFEM for solving electromagnetic scattering problems from targets with highly inhomogeneous materials. To avoid creating conformal meshes within a complex computational domain and preparing multiple meshes during optimization, we introduced enrichment VBFs that are defined over the discretized elements intersected by a material interface to capture the normal derivative discontinuity of the tangential field component. We analyzed the properties of the enrichment functions and constructed them directly from a linear combination of the VBFs of the sub-elements. Then we presented several numerical examples to verify the algorithm with analytical solutions and demonstrate its h-refinement convergence rate. We showed that the proposed IGFEM is able to achieve the same level of accuracy as the standard FEM without the need for conformal meshes. Finally, we analyzed two more complex examples, with multiple microvascular channels and circular inclusions of different radii, to illustrate the capability of the introduced approach in handling heterogeneous media with complex-shape material interfaces.

2.7 Figures and Tables

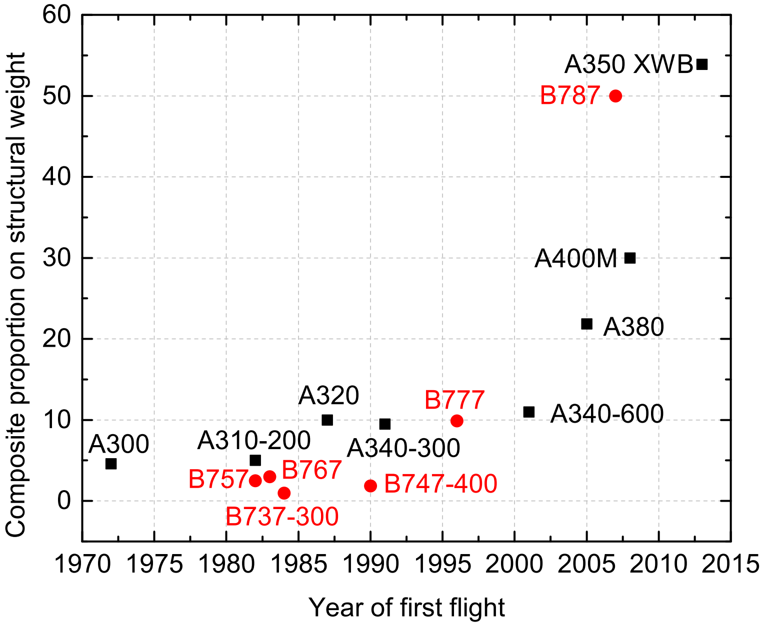

Figure 2.1: Composite proportion on structural weight of aerospace systems.

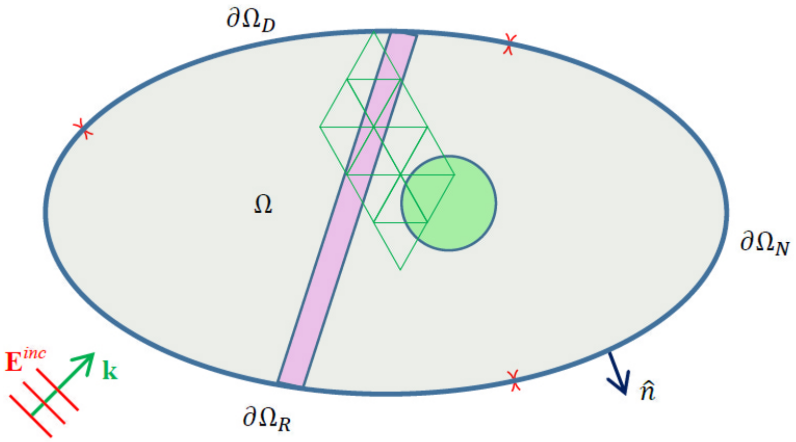

Figure 2.2: An inhomogeneous region illuminated by a uniform incident plane wave. The plane wave is polarized in the $\mathbf{E}^{\text{inc}}$ direction and propagates along the $\mathbf{k}$ direction, where $\mathbf{E}^{\text{inc}}$ stands for the incident electric field. The object Ω consists of several heterogeneous materials. Dirichlet, Neumann, and Robin boundary conditions are applied along $\partial\Omega_D$, $\partial\Omega_N$, and $\partial\Omega_R$, respectively. The outward unit normal direction of the boundary $\partial\Omega$ is denoted as $\hat{n}$. Non-conformal elements, which cross the material interfaces, are also depicted.

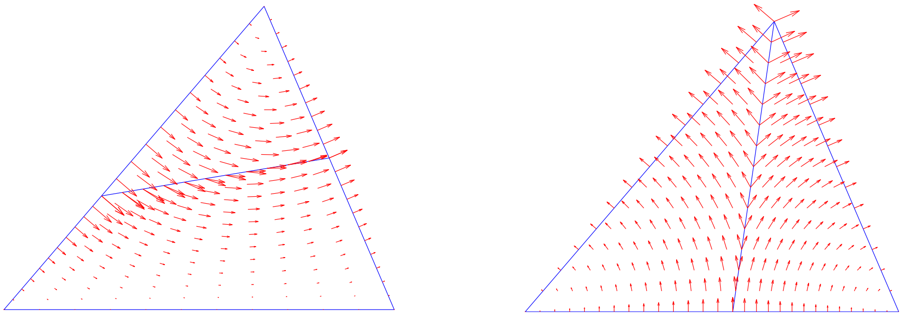

(a)

(b)

Figure 2.3: Field distribution of the enriched basis function for two different scenarios. For both cases, the enriched VBF has a constant tangential component along the material interface and no tangential component along other edges. (a) A triangular element is divided into a sub-triangle and a sub-quadrilateral. (b) A triangular element is divided into two sub-triangles.

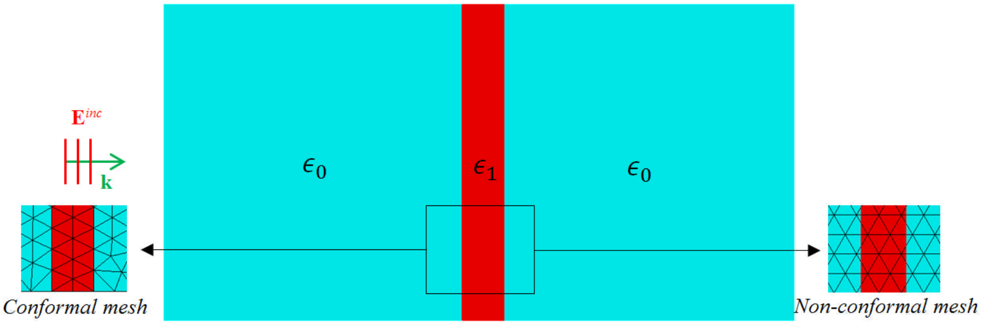

Figure 2.4: A plane wave illuminates a lossy slab placed in free space. The dielectric slab is $2/15\lambda_0$ thick and $\epsilon_1 = (3 - \mathrm{j}4)\epsilon_0$. The slab is $1/75\lambda_0$ right offset of the middle of the computational domain. The total computational domain is $2\lambda_0 \times \lambda_0$. The top and bottom boundaries are enforced as PEC while the left and right boundaries are set as ABC. The left and right insets show a part of the conformal and non-conformal meshes, both of which have a mesh size of $\lambda_0/15$.

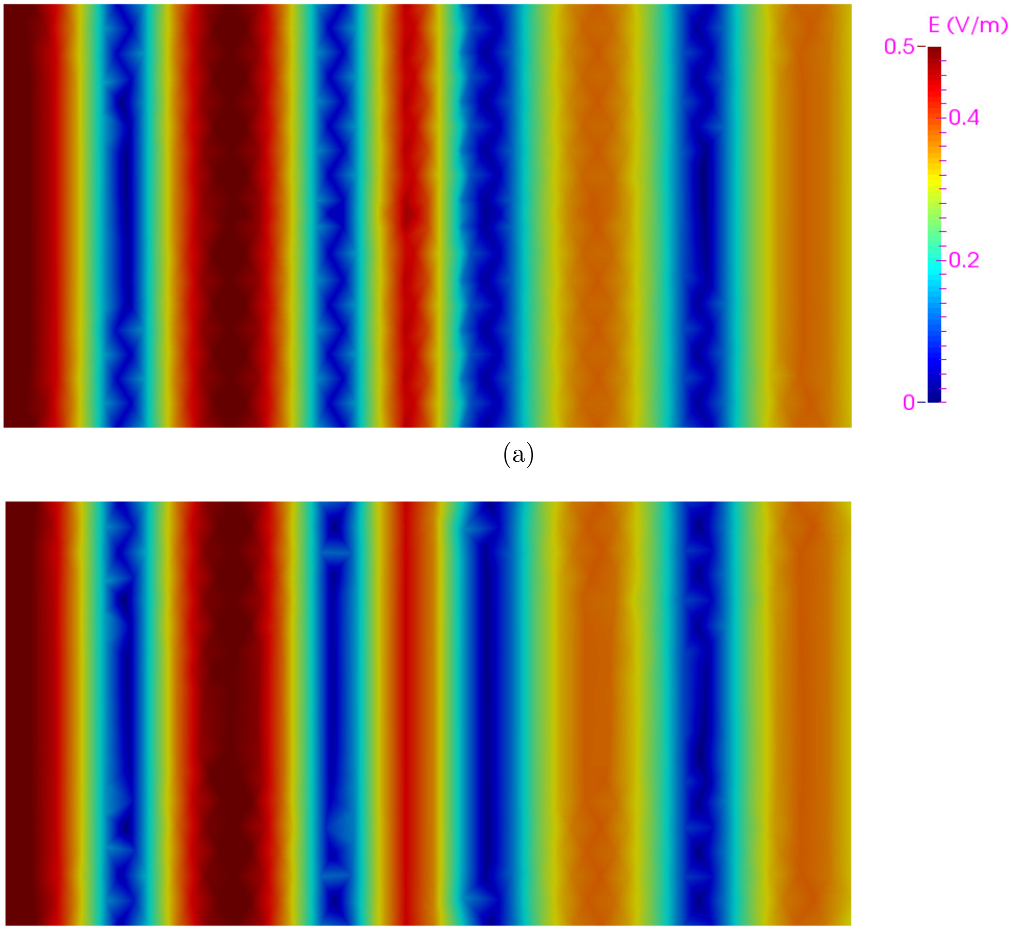

(a)

(b)

Figure 2.5: Total electric field distribution for the test problem shown in Fig. 2.4. The 1-GHz incident plane wave comes from the left boundary and propagates towards the right boundary. Both of the fields are calculated with a mesh size of $\lambda_0/15$. (a) IGFEM solution. (b) Standard FEM solution.

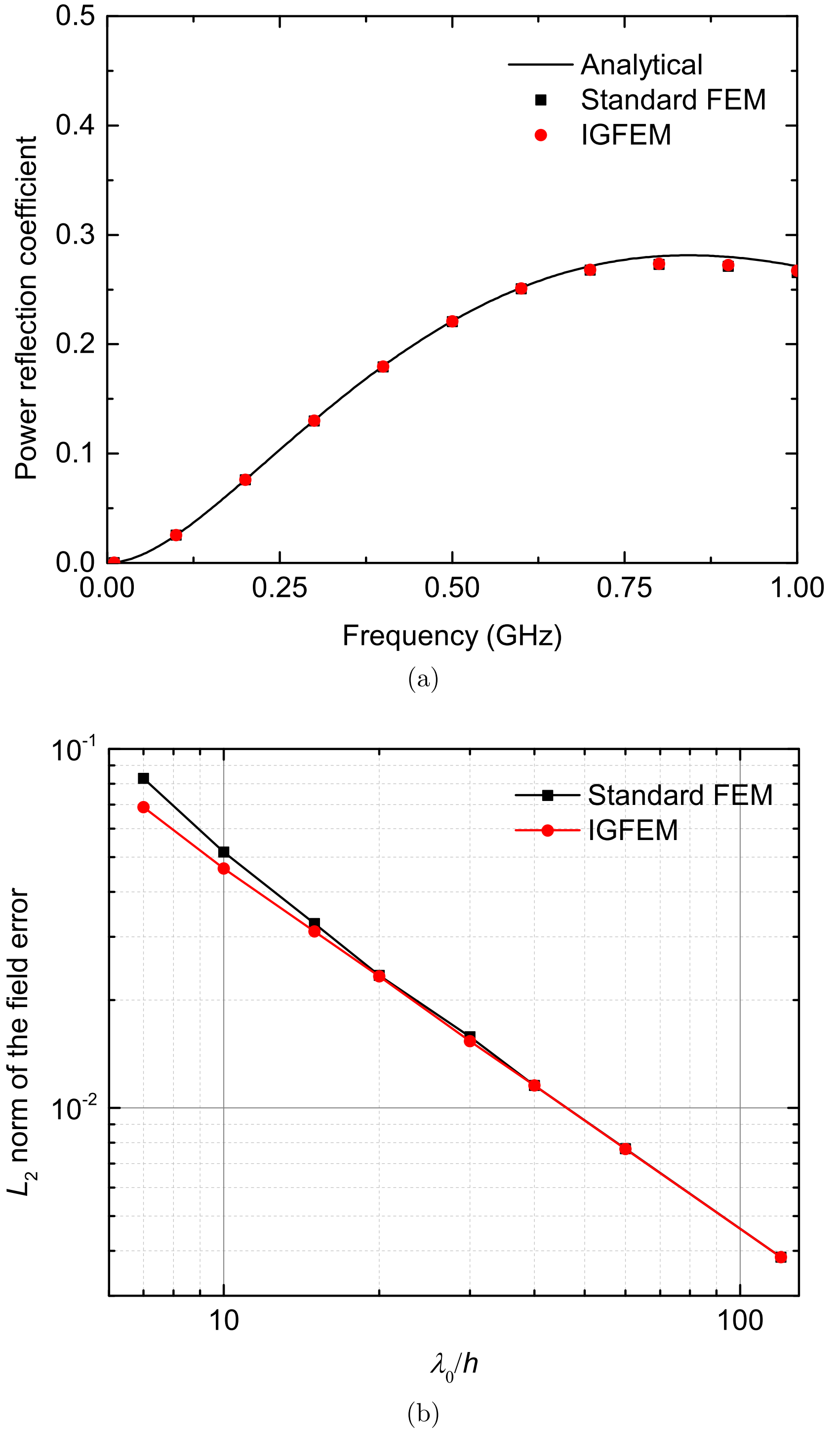

Figure 2.6: Power reflection coefficient and L_2-norm of the field solution error of an infinitely large lossy slab for the test problem shown in Fig. 2.4. (a) Power reflection coefficient with respect to the frequency. (b) L_2-norm of the field solution error with respect to the mesh size h.

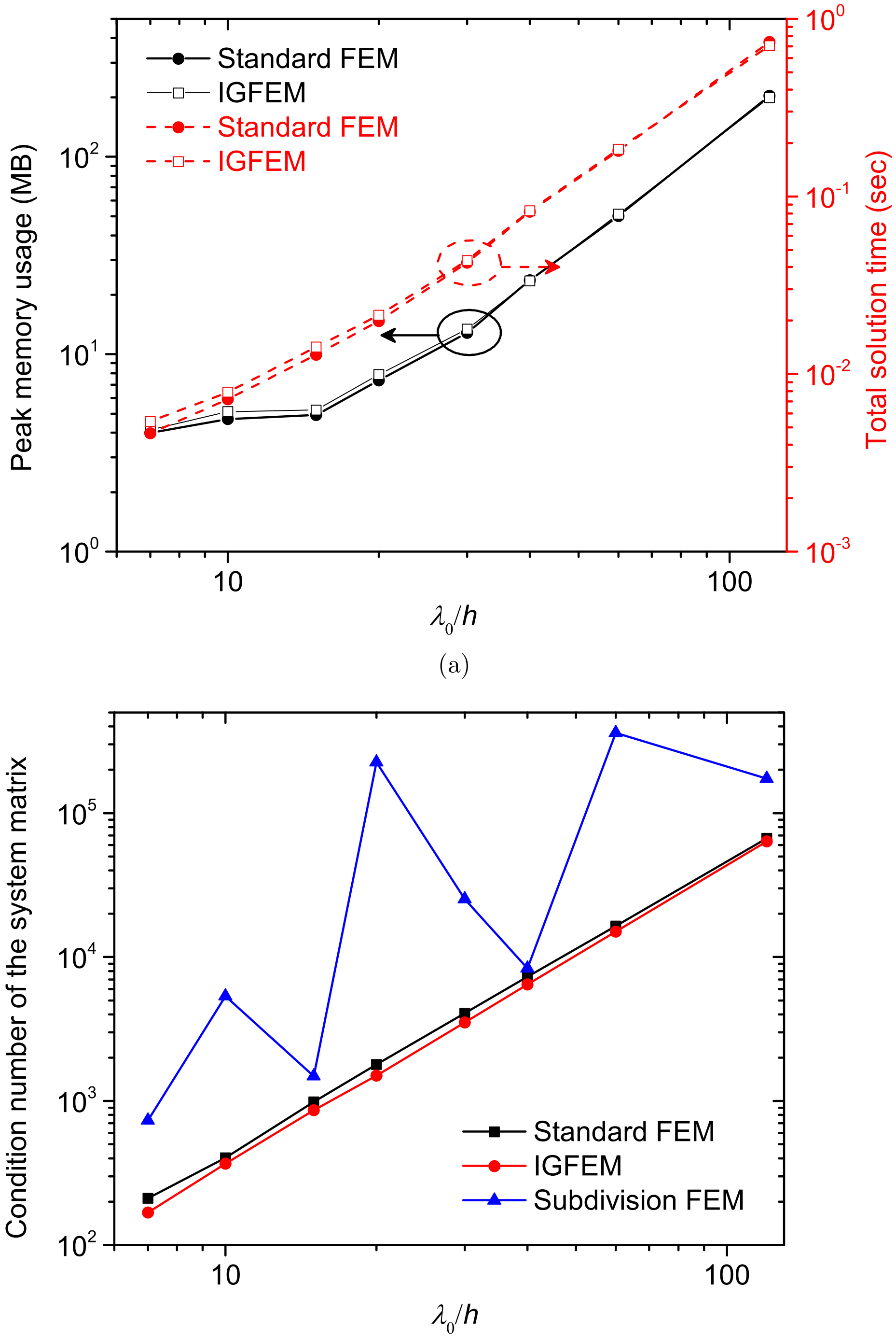

(a)

(b)

Figure 2.7: Computational complexity and condition number of the system matrix of an infinitely large lossy slab for the test problem shown in Fig. 2.4. (a) Peak memory usage and total solution time with respect to the mesh size h. (b) Condition number of the system matrix with respect to the mesh size h.

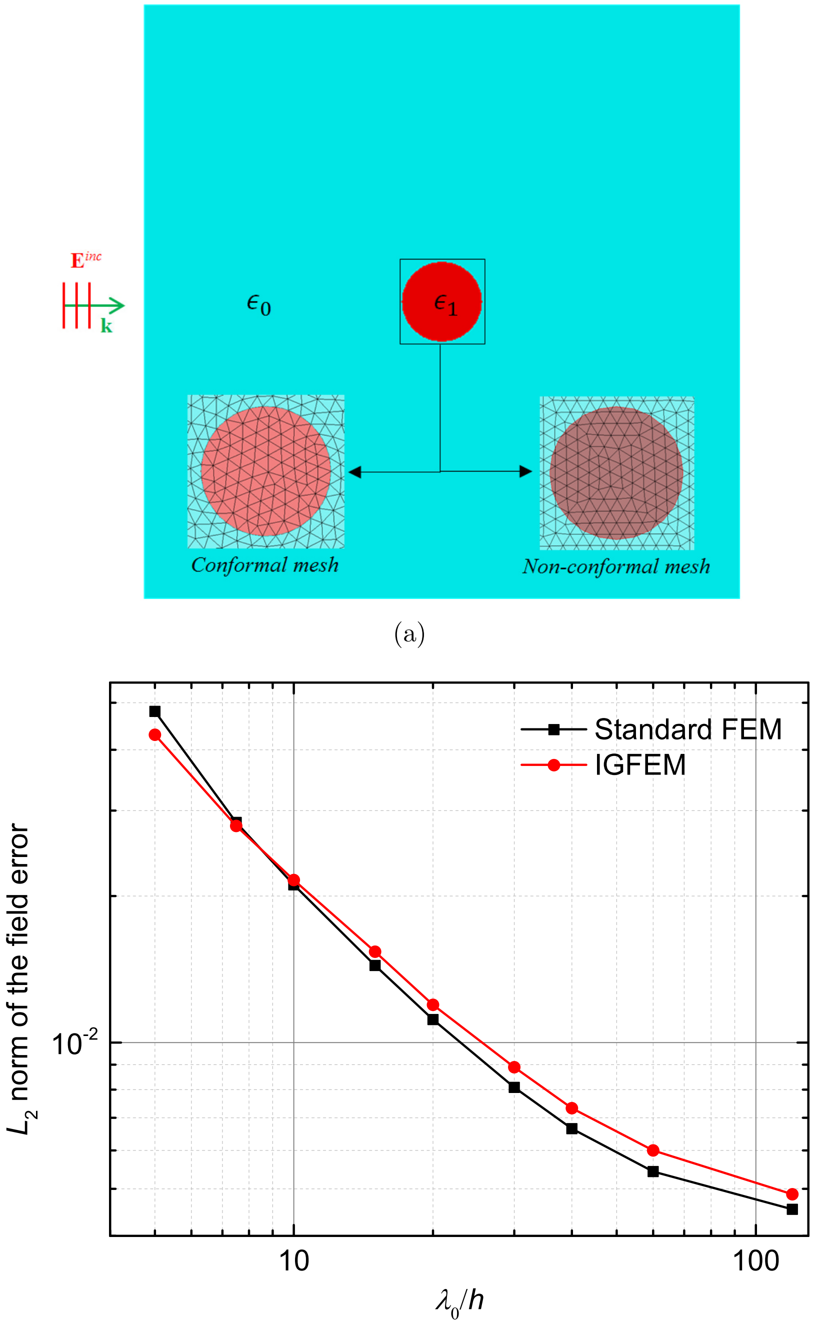

(a)

(b)

Figure 2.8: A plane wave illuminates an infinitely long dielectric cylinder placed in free space. The radius of the dielectric cylinder is $\lambda_0/3$ and $\epsilon_1 = 4\epsilon_0$. The total computational domain is $5\lambda_0 \times 5\lambda_0$. All the boundaries are enforced as ABC. (a) Geometrical configuration. The conformal and non-conformal meshes, both with a mesh size of $\lambda_0/15$, are depicted in the left and right insets, respectively. (b) L_2-norm of the field solution error with respect to the mesh size h.

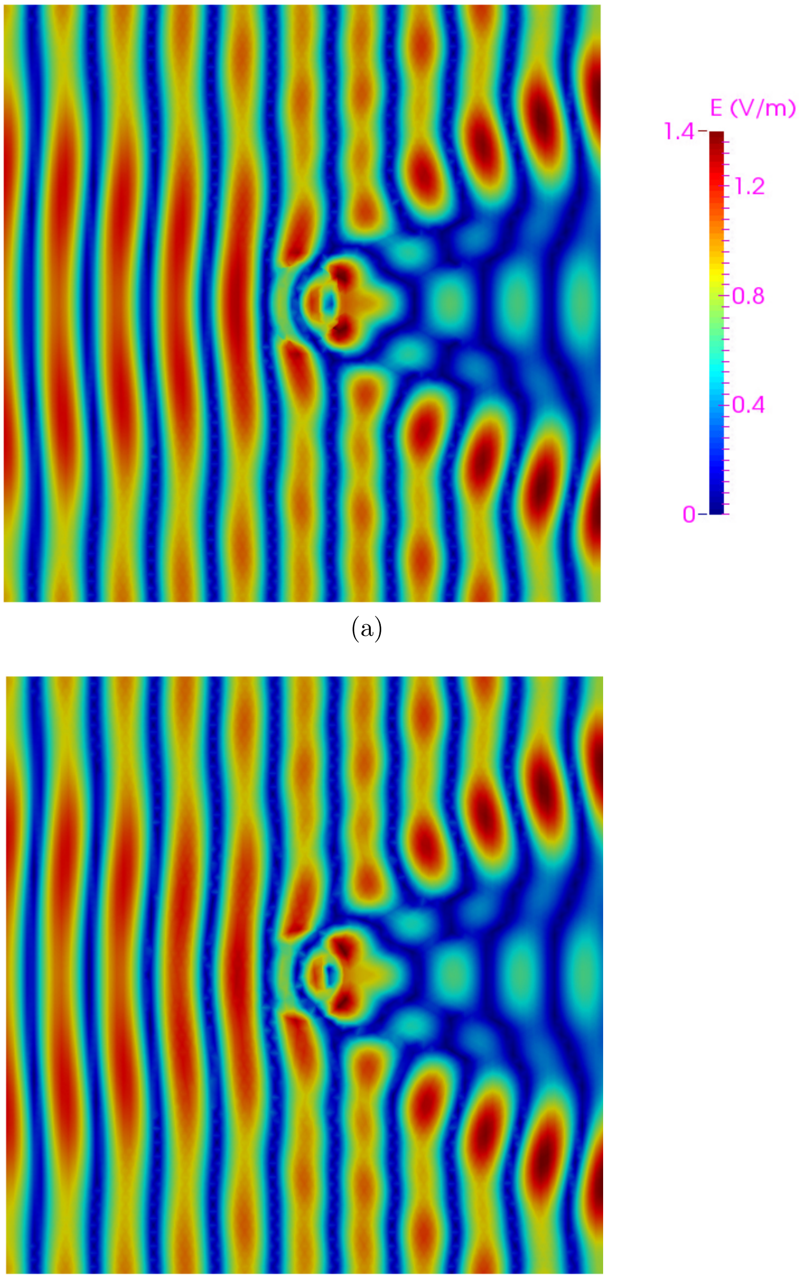

Figure 2.9: Total electric field distribution for the test problem shown in Fig. 2.8a. The 10-GHz incident plane wave comes from the left boundary and propagates towards the right boundary. Both of the fields are calculated with a mesh size of $\lambda_0/15$. (a) IGFEM solution. (b) Standard FEM solution.

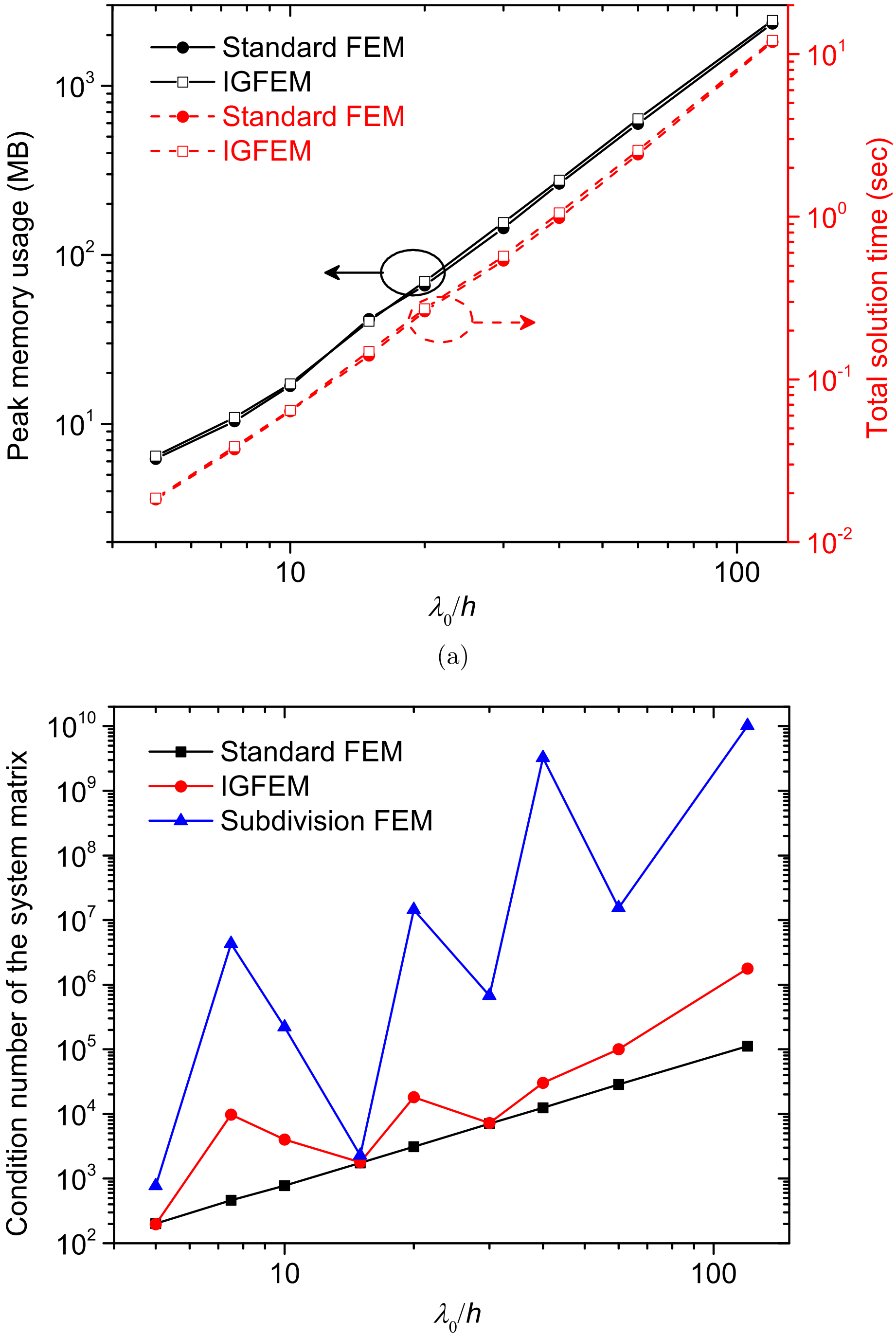

(a)

(b)

Figure 2.10: Computational complexity and condition number of the system matrix of an infinitely long dielectric cylinder for the test problem shown in Fig. 2.8a. (a) Peak memory usage and total solution time with respect to the mesh size h. (b) Condition number of the system matrix with respect to the mesh size h.

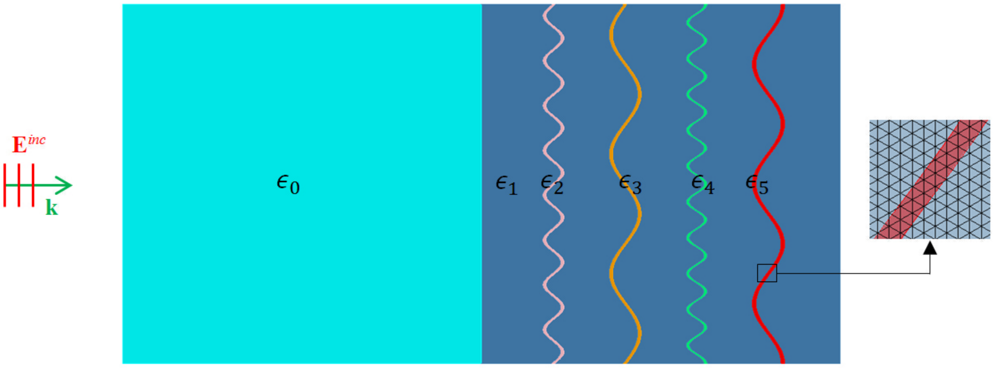

Figure 2.11: Geometrical configurations of the heterogeneous material with four sinusoidal microchannels of different wavelengths. The diameter of the microvascular channels is $0.05\lambda_0$, where λ_0 is the free-space wavelength with respect to the 1.5-GHz plane wave. The dimension of the total computational domain is $10\lambda_0 \times 5\lambda_0$. The left boundary is set as ABC while the others are all enforced as PEC. The detailed configurations and material properties of the sinusoidal channels are presented in Table 2.1. The inset shows a part of the non-conformal mesh used in the IGFEM simulation.

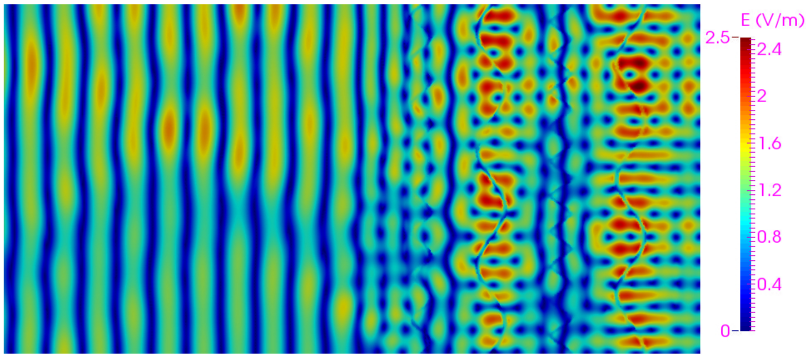

Figure 2.12: Magnitude of the total electric field for the test problem shown in Fig. 2.11. The incident plane wave propagates from left to right. The field is calculated using the IGFEM with a uniform, nonconforming mesh size of $\lambda_0/40$.

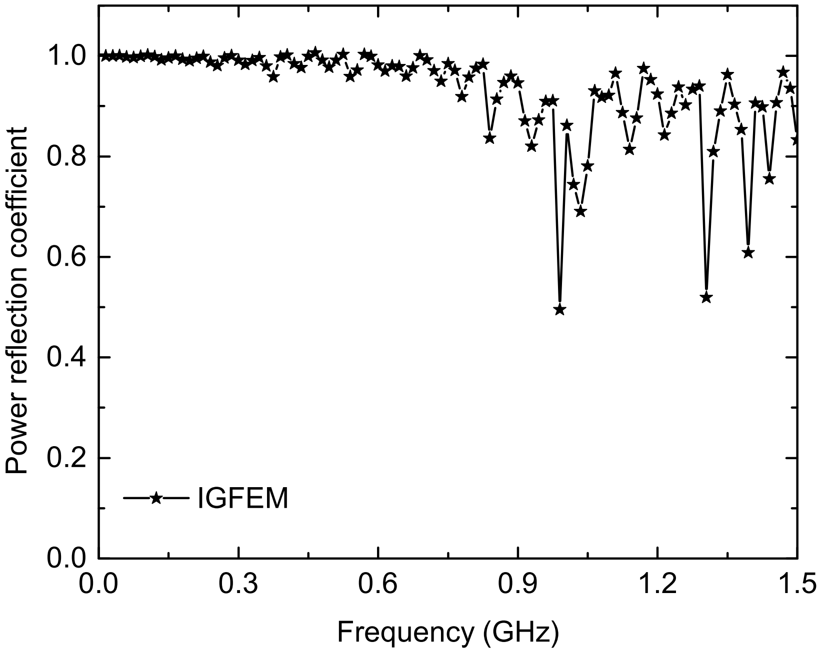

Figure 2.13: Power reflection coefficient with respect to frequency for the test problem shown in Fig. 2.11.

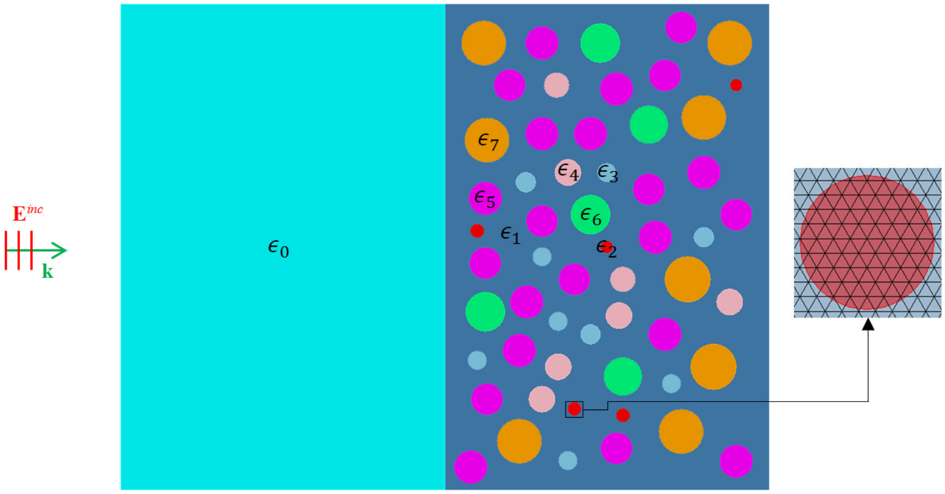

Figure 2.14: Geometrical configurations of the heterogeneous material with 56 circular inclusions. The radii of the inclusions range from $0.2\lambda_0$ to $0.7\lambda_0$, where λ_0 is the free-space wavelength with respect to the 3-GHz incident plane wave. The dimension of the total computational domain is $20\lambda_0 \times 15\lambda_0$. The left boundary is enforced as ABC while the others are all set as PEC. The detailed configurations and material properties of the circular inclusions are provided in Table 2.2. The inset shows a part of the non-conformal mesh used in the IGFEM simulation.

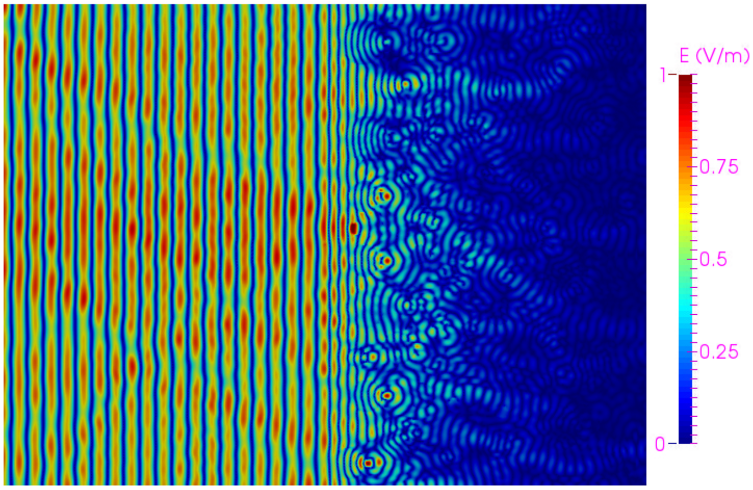

Figure 2.15: Total electric field magnitude for the test problem shown in Fig. 2.14 for a 3-GHz right-traveling incident plane wave. The field is calculated using IGFEM with a mesh size of $\lambda_0/20$.

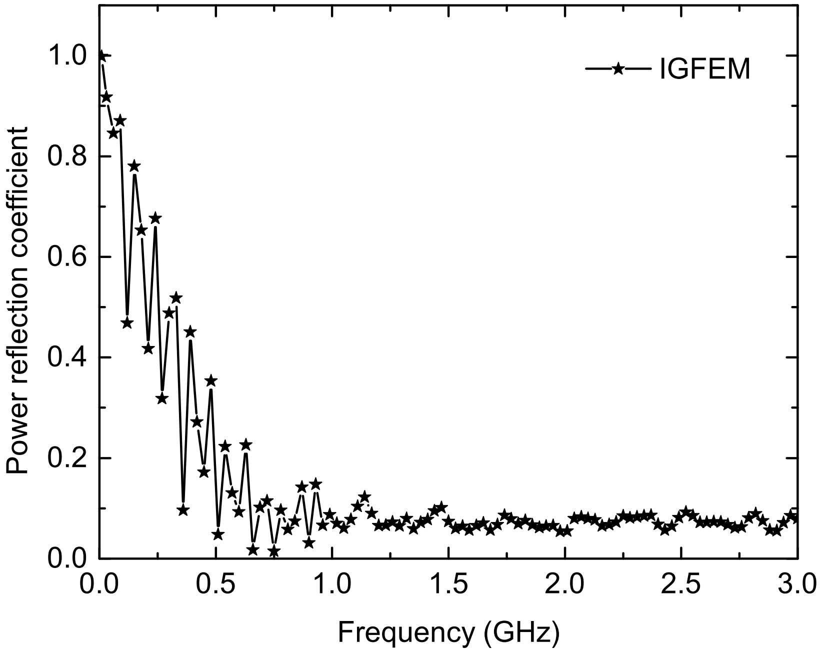

Figure 2.16: Power reflection coefficient with respect to frequency for the test problem shown in Fig. 2.14.

Table 2.1: Geometry configurations and material properties of the sinusoidal microvascular channels.

Channel ID	1	2	3	4
Wavelength / λ_0	8/5	3/5	2	3/5
Diameter / λ_0	0.05	0.05	0.05	0.05
Amplitude / λ_0	0.125	0.2	0.125	0.2
Permittivity / ϵ_0	5.8-j0.01	6.4-j0.03	7-j0.02	4.8-j0.05

Table 2.2: Geometry configurations and material properties of the circular inclusions (inclusion ID ranges from 2 to 7).

Inclusion ID	2	3	4	5	6	7
Radius / λ_0	0.02	0.03	0.04	0.05	0.06	0.07
Permittivity / ϵ_0	1	7-j0.1	5-j0.2	6.2-j0.1	4-j0.4	6.8-j0.5

Chapter 3

Interface-Enriched Generalized FEM for 3-D Problems

3.1 Introduction

The IGFEM alleviates the geometrical complexity of discretizing the complex features by using a virtual model based on finite elements that do not need to conform with material interfaces, yet provide the same level of accuracy as the standard FEM using conformal meshes. Encouraged by the success of extending the IGFEM from structural and thermal analysis with nodal basis functions to electromagnetic analysis with VBFs for 2-D problems in Chapter 2 [18, 40, 43], we further extend the IGFEM to 3-D full-wave analysis. Since the formulation of the IGFEM for 2-D problems, together with a convergence/accuracy study and a conditioning comparison of this method with the subdivision FEM, has been reported previously in Chapter 2, we place more emphasis in this chapter on the application of this method for modeling composite materials with randomly distributed inclusions and/or intricate internal geometries.

The rest of this chapter is organized as follows. In the next section, we present the basic formulation describing the periodic radiation condition (PRC) used to simulate composite periodic materials. In Section 3.3, we present the extension of the enrichment ideas from the 2-D IGFEM based on triangular elements to the 3-D IGFEM based on tetrahedral elements. A short discussion about the advantages of the IGFEM over the subdivision FEM, together with the comparison of the condition numbers of their elemental matrices, is also provided. We then study in Section 3.4 the h-refinement convergence, computational complexity, and condition numbers of the resultant system matrices by analyzing two reference problems: reflection of a dielectric slab backed by a PEC boundary and scattering by a dielectric sphere in free space. In Section 3.5, we first present the simulation results of scattering from a monolayer dielectric sphere array to verify the implementation of the PRC, the specular reflection coefficient calculation, and the accuracy of the IGFEM. We then present the results for three engineering problems to demonstrate the capability of the proposed method to handle electromagnetic analysis of periodic composite materials with complex micro-structures.

3.2 Problem Description and FEM Formulation

To simulate objects with periodicity in the xy-plane with periodic length vector $\mathbf{T} = (\hat{x}T_x + \hat{y}T_y + \hat{z}0)$, as shown schematically in Fig. 3.1, a periodic boundary condition (PBC) has to be implemented together with an accurate PRC in the nonperiodic direction [3]:

$$\mathbf{E}(\mathbf{r}+\mathbf{T})e^{\mathrm{j}\mathbf{k}_0^{\mathrm{inc}}\cdot\mathbf{T}} = \mathbf{E}(\mathbf{r}), \quad \mathbf{r} \in \partial\Omega_{\mathrm{PBC}}, \tag{3.1}$$

$$\hat{n} \times \nabla \times \mathbf{E}(\mathbf{r}) - S(\mathbf{E}) = \mathbf{Q}(\mathbf{r}), \quad \mathbf{r} \in \partial\Omega_{\mathrm{PRC}}, \tag{3.2}$$

where the wave vector $\mathbf{k}_0^{\mathrm{inc}} = \hat{k}^{\mathrm{inc}}k_0 = \hat{x}k_{x0}^{\mathrm{inc}} + \hat{y}k_{y0}^{\mathrm{inc}} + \hat{z}k_{z0}^{\mathrm{inc}}$. In this implementation, the PBC on $\partial\Omega_{\mathrm{PBC}}$ given in (3.1) is applied on the four side surfaces of a periodic unit cell to enforce the field dependence stated by Floquet's theorem [108], and the PRC on $\partial\Omega_{\mathrm{PRC}}$ defined in (3.2) is employed on the top and bottom surfaces of the unit cell for truncation, with the boundary excitation $\mathbf{Q}$ related to the incident field by

$$\mathbf{Q} = \begin{cases} -2\mathrm{j}k_0\eta_0\hat{n} \times \mathbf{H}^{\mathrm{inc}}, & \text{top surface,} \\ 0, & \text{bottom surface.} \end{cases} \tag{3.3}$$

The surface integral $S(\mathbf{E})$, which represents the magnetic field generated by the equivalent magnetic sources on the PRC, can be expressed as

$$S(\mathbf{E}) = 2k_0^2\hat{n} \times \sum_{p,q=-\infty}^{\infty} \tilde{\bar{\mathbf{G}}}_{pq} \cdot (\hat{n} \times \tilde{\mathbf{E}}_{pq})e^{-\mathrm{j}(k_{xp}x + k_{yq}y)}, \tag{3.4}$$

where $\tilde{\bar{\bar{\mathbf{G}}}}_{pq}$ represents the periodic dyadic Green's function in the spectral domain, expressed as

$$\tilde{\bar{\bar{\mathbf{G}}}}_{pq} = -\frac{\mathrm{j}}{2k_0^2\sqrt{k_0^2 - k_{xp}^2 - k_{yq}^2}} \begin{bmatrix} k_0^2 - k_{xp}^2 & -k_{xp}k_{yq} \\ -k_{xp}k_{yq} & k_0^2 - k_{yq}^2 \end{bmatrix}. \tag{3.5}$$

In (3.4) and (3.5), k_{xp} and k_{yq} are the Floquet harmonics of order p and q, which can be systematically written as

$$k_{ij} = k_{i0} - \frac{2\pi j}{T_i}, \quad i = \{x, y\} \text{ and } j = \{p, q\}. \tag{3.6}$$

The term $\tilde{\mathbf{E}}_{pq}$ required by the surface integral $S(\mathbf{E})$ is the Fourier expansion of the electrical field in the spectral domain and is given by

$$\tilde{\mathbf{E}}_{pq} = \frac{1}{T_xT_y}\int_{\partial\Omega_{\mathrm{PRC}}} \mathbf{E}e^{\mathrm{j}(k_{xp}x + k_{yq}y)}d\mathbf{r}. \tag{3.7}$$

To approximate the solution of the boundary value problem (BVP) defined by (2.3)-(2.6), (3.1) and (3.2), a weak-form representation is derived by multiplying (2.3) by a testing function $\mathbf{E}$ and integrating over Ω:

$$\begin{aligned} &\int_\Omega \left[\mu_{\mathrm{r}}^{-1}(\nabla \times \mathbf{E}) \cdot (\nabla \times \mathbf{E}) - k_0^2\epsilon_{\mathrm{r}}\mathbf{E}\cdot\mathbf{E}\right] d\mathbf{r} \\ &\qquad = -\oint_{\partial\Omega} \mathbf{E}\cdot(\hat{n} \times \nabla \times \mathbf{E})d\mathbf{r}. \end{aligned} \tag{3.8}$$

By following the standard FEM procedure, the unknown electric field $\mathbf{E}$ is expanded in terms of a set of VBFs $\{\mathbf{N}_i\}$ [3]

$$\mathbf{E} = \sum_{i=1}^{N} E_i\mathbf{N}_i, \tag{3.9}$$

where $\{E_i\}$ are the corresponding unknown coefficients and N denotes the total number of DoFs. By substituting (3.9) into (3.8) and applying pertinent boundary conditions, a linear system is formed:

$$[K]\{E\} = \{f\}, \tag{3.10}$$

where $\{f\}$ is the known vector associated with the incident field. The resulting matrix $[K]$ for problems without boundary conditions (3.1) and (3.2) is highly sparse and symmetric. However, when periodic structures are considered, the matrix $[K]$ is partially sparse and partially full if higher-order Floquet modes are included in (3.2), and it also loses symmetry for oblique incidences because of (3.1) [109]. Nevertheless, the resulting linear system can still be solved conveniently by an efficient direct solver for either scenario [104, 105]. For the standard FEM, the field solution obtained with the aforementioned procedure is accurate provided that a mesh conformal to the internal geometries is used. For a non-conformal mesh, where tetrahedra are crossed by material interfaces, the standard FEM produces the field solution with a poor numerical accuracy since it cannot represent the discontinuities of the field and its derivatives along the material interfaces. The IGFEM has been, therefore, proposed to alleviate this drawback [18, 40, 43, 56]. By introducing additional basis functions associated with material interfaces to enrich the FEM solution space, the IGFEM can correctly resolve the discontinuities of the field and its derivatives even without a conformal mesh. The extension of the IGFEM from thermal and structural problems with nodal basis functions to 2D electromagnetic analysis with VBFs was discussed in [18]. In the next section, we extend the enrichment idea to the more challenging 3D case.

3.3 Vector Basis Functions and Enrichment

For the sake of clarity and without losing generality, let us assume that the computational domain is discretized into tetrahedra which are not necessarily conforming to the internal geometries. We further assume that the internal structures are smooth and non-overlapping so that, when the dimensions of the tetrahedra are small enough, each element is at most intersected by one material interface. Under these three assumptions, four distinct scenarios are possible for a tetrahedron interacting with a material interface, as schematically displayed in Fig. 3.2.

The tangential component of the field exhibits a gradient discontinuity along a material interface. To interpolate the field without resorting to conformal meshes, one possible approach is to enrich the solution space S by employing the IGFEM [18] as

$$S = span\{\mathbf{N}_i\} + span\{\mathbf{N}_i^{\mathrm{en}}\}, \tag{3.11}$$

where $span\{\mathbf{N}_i\}$ is the standard FEM solution space and $span\{\mathbf{N}_i^{\mathrm{en}}\}$ is the enriching solution space that is associated with material interfaces. The enriching solution space should satisfy the following three criteria: (1) it can capture the gradient discontinuity of the tangential field component at material interfaces; (2) it can represent the discontinuity of the normal field component caused by material mismatch; and (3) it should not introduce any tangential field component along other edges so that the tangential field continuity condition will not be violated. It is obvious that an enriching solution space spanned by H(curl) conforming basis functions is adequate to retrieve the "missing" field information. In this thesis, we construct the enriching solution space

$$span\{\mathbf{N}_i^{\mathrm{en}}\} = span\{\mathbf{N}_i^{\mathrm{S}_1}\} + span\{\mathbf{N}_i^{\mathrm{S}_2}\} \tag{3.12}$$

to satisfy these three criteria, where $\mathbf{N}_i^{\mathrm{S}_1}$ and $\mathbf{N}_i^{\mathrm{S}_2}$ are respectively VBFs associated with the first and the second sub-elements that share a common edge, as illustrated in Fig. 3.2. The sub-elements can be tetrahedral, prismatic, and pyramidal, and the construction of the VBFs for such elements can be found in [4,110,111]. To make this chapter self-contained so that readers are able to implement the proposed algorithm conveniently, we list the formulae of the VBFs for the three elements here. For each element, we construct its VBFs $\{\mathbf{W}_i\}$ in the $\xi\eta\zeta$-coordinate system (the simplex coordinate system). Once $\{\mathbf{W}_i\}$ in the simplex coordinate system are available, it is fairly easy to obtain the VBFs $\{\mathbf{N}_i\}$ and curl of the VBFs $\{\nabla \times \mathbf{N}_i\}$ in the xyz-coordinate system (the physical coordinate system) via the following expressions [110]:

$$\begin{aligned} \mathbf{N}_i &= \mathbf{J}^{-1}\mathbf{W}_i, \\ \nabla \times \mathbf{N}_i &= \frac{\mathbf{J}^{\mathrm{T}}}{\det(\mathbf{J})}\nabla \times \mathbf{W}_i, \end{aligned} \tag{3.13}$$

where $\mathbf{J}$ is the Jacobian matrix that connects the simplex and physical coordinate systems, and can be calculated from

$$\mathbf{J} = \frac{\partial(x,y,z)}{\partial(\xi,\eta,\zeta)} = \begin{bmatrix} \frac{\partial x}{\partial \xi} & \frac{\partial y}{\partial \xi} & \frac{\partial z}{\partial \xi} \\ \frac{\partial x}{\partial \eta} & \frac{\partial y}{\partial \eta} & \frac{\partial z}{\partial \eta} \\ \frac{\partial x}{\partial \zeta} & \frac{\partial y}{\partial \zeta} & \frac{\partial z}{\partial \zeta} \end{bmatrix}. \tag{3.14}$$

It is worth noting that the gradient operator is *w.r.t.* the physical coordinates in $\nabla \times \mathbf{N}_i$ but *w.r.t.* the simplex coordinates in $\nabla \times \mathbf{W}_i$.

3.3.1 Vector Basis Functions for a Tetrahedron

The isoparametric transformation that maps a tetrahedral element from the simplex coordinate system to the physical coordinate system can be written as

$$\mathbf{r} = \sum_{i=1}^{4} \lambda_i \mathbf{r}_i \tag{3.15}$$

for the case shown in Fig. 3.3, where $\mathbf{r}_i$ is a row vector specified by the location of vertex i in the physical coordinate system and $\boldsymbol{\lambda}$ is a vector with each of its entries associating with a surface in the simplex coordinate system:

$$\boldsymbol{\lambda} = [1-\xi-\eta-\zeta, \xi, \eta, \zeta]. \tag{3.16}$$

Letting $\nabla\lambda_i$ be a column vector, the Jacobian matrix $\mathbf{J}$ is given by

$$\mathbf{J} = \sum_{i=1}^{4} \nabla\lambda_i \cdot \mathbf{r}_i^{\mathrm{T}}. \tag{3.17}$$

The VBF associated with an arbitrary edge e can be formulated as [4]

$$\lambda_{e_1}\nabla\lambda_{e_2} - \lambda_{e_2}\nabla\lambda_{e_1}, \tag{3.18}$$

where e_1 and e_2 are the two vertexes of the edge e.

3.3.2 Vector Basis Functions for a Prism

For a prismatic element, as illustrated in Fig. 3.4, the transformation that maps a point (ξ,η,ζ) in the simplex coordinate system to the point $\mathbf{r} =$

(x, y, z) in the physical coordinate system can be expressed as

$$\mathbf{r} = \beta_1 \sum_{i=1}^{3} \lambda_i \mathbf{r}_i + \beta_2 \sum_{i=4}^{6} \lambda_i \mathbf{r}_i, \tag{3.19}$$

where λ_i and β_i, which are associated with a vertical and a horizontal surface, respectively, are given by

$$\begin{aligned} \lambda_1 &= \lambda_4 = 1 - \xi - \eta, \\ \lambda_2 &= \lambda_5 = \xi, \\ \lambda_3 &= \lambda_6 = \eta, \\ \beta_1 &= 1 - \zeta, \\ \beta_2 &= \zeta. \end{aligned} \tag{3.20}$$

Following the definition in (3.14), the Jacobian matrix $\mathbf{J}$ for a prismatic element is readily derived as

$$\mathbf{J} = \sum_{i=1}^{3} (\lambda_i \nabla \beta_1 + \beta_1 \nabla \lambda_i) \cdot \mathbf{r}_i^{\mathrm{T}} + \sum_{i=4}^{6} (\lambda_i \nabla \beta_2 + \beta_2 \nabla \lambda_i) \cdot \mathbf{r}_i^{\mathrm{T}}. \tag{3.21}$$

The VBF for a horizontal edge e, with e_1 and e_2 denoting its two vertices and e_f representing the horizontal opposite face, can be formulated as [111]

$$(\lambda_{e_1} \nabla \lambda_{e_2} - \lambda_{e_2} \nabla \lambda_{e_1}) \beta_{e_f}. \tag{3.22}$$

For a vertical edge e, the VBF is [111]

$$\lambda_{e_f} \nabla \beta_2, \tag{3.23}$$

where e_f describes the face that does not contain any vertex of the edge e.

3.3.3 Vector Basis Functions for a Pyramid

The transformation for a pyramidal element shown in Fig. 3.5 can be expressed as

$$\mathbf{r} = \sum_{i=1}^{5} \lambda_i \mathbf{r}_i, \tag{3.24}$$

where λ_i are the nodal basis functions and are given by [110]

$$\boldsymbol{\lambda} = \left[\frac{\beta_1\beta_2}{1-\zeta}, \frac{\beta_2\beta_3}{1-\zeta}, \frac{\beta_3\beta_4}{1-\zeta}, \frac{\beta_4\beta_1}{1-\zeta}, \zeta\right], \tag{3.25}$$

and β_i are parameters associated with triangular faces and are given by

$$\boldsymbol{\beta} = \frac{1}{2}\left[1-\xi-\zeta, 1-\eta-\zeta, 1+\xi-\zeta, 1+\eta-\zeta\right]. \tag{3.26}$$

With the mapping function defined in (3.24), it is trivial to obtain the Jacobian matrix $\mathbf{J}$ for a pyramidal element:

$$\mathbf{J} = \sum_{i=1}^{5} \nabla\lambda_i \cdot \mathbf{r}_i^{\mathrm{T}}. \tag{3.27}$$

The VBF associated with a horizontal edge e can be expressed as [110]

$$\lambda_{e_1}\nabla(\lambda_{e_2} + \lambda_{e_3}) - \lambda_{e_2}\nabla(\lambda_{e_1} + \lambda_{e_4}), \tag{3.28}$$

where e_1 and e_2 are the two vertices of the edge e, and e_3 and e_4 are respectively the adjacent vertices of e_2 and e_1 that reside on the horizontal edges other than the edge e. For a non-horizontal edge e, the VBF can be written as [110]

$$\lambda_{e_1}\nabla\lambda_5 - \lambda_5\nabla\lambda_{e_1}, \tag{3.29}$$

where e_1 is one of the vertices of e that belongs to the horizontal plane.

In our implementation, all the VBFs are normalized to have a unit tangential component for better conditioning of the resultant system matrix. It is worth noting that, because of the weak or strong discontinuities exhibited in the enriched elements, the conventional quadrature rule that directly applies to a tetrahedron is no longer accurate enough for evaluating the stiffness and mass matrices. A common practice is to perform integration over each sub-element and add up the contributions from the sub-elements to form an accurate final quadrature [56]. The quadrature rules for various elements have been systematically studied and can be found in [112].

The unique feature that distinguishes the IGFEM from the subdivision FEM and makes it a better choice is the definition of the VBFs on the non-conformal elements. Unlike the subdivision FEM that defines the VBFs on sub-elements, the IGFEM defines the VBFs on the original tetrahedral elements. Consequently, when sub-elements with an extremely small size are created, entries in certain rows and columns of the subdivision FEM system matrix are trivial because of the small volumes associated with the supporting sub-elements, which inevitably lead to a significantly poorly conditioned system. In contrast, the conditioning of the IGFEM generated system matrix is barely affected since the integration domains are the original tetrahedra. Even if sub-elements with a poor aspect ratio are encountered, where some VBFs tend to be prone to produce a rank-deficient system, the IGFEM still outperforms the subdivision FEM because it has fewer DoFs related to the ill-shaped sub-elements. The above analysis can be easily verified through evaluating the condition number of the system matrix obtained by an enriched element, as shown in Fig. 3.6, and also by the numerical examples described in Section 3.5.

Figure 3.6 shows the condition number for the two most common scenarios when an interface passes through a tetrahedron. The functional under consideration is

$$\mathcal{L} = \int_{\Omega} \left[(\nabla \times \mathbf{E}) \cdot (\nabla \times \mathbf{E}) - k_0^2 \mathbf{E} \cdot \mathbf{E} \right] d\mathbf{r}, \tag{3.30}$$

which is discretized respectively by the standard FEM, the IGFEM, and the subdivision FEM. The dimension of the tetrahedron, normalized with the free-space wavelength λ_0, is also displayed. The intersection points, which are represented by black dots, are controlled by the variable $t \in [\delta, 1-\delta]\, \lambda_0$, where $\delta = 10^{-10}$. As observed from the figures, the IGFEM produces much better conditioned system matrices than the subdivision FEM in both of these scenarios.

3.4 Convergence and Conditioning Study

The IGFEM proposed in this chapter aims at facilitating the electromagnetic analysis of 3-D problems with a high geometric complexity. Without resorting to meshes that conform to internal geometries, the IGFEM introduces enrichment VBFs at the material interfaces to represent the discontinuities of the field and its derivatives caused by adjacent material mismatch. Since sub-elements with very small sizes and/or poor aspect ratios are occasionally created, it is necessary to investigate the accuracy, h-refinement convergence, and conditioning of the proposed IGFEM.

The conditioning of the system matrix $[K]$ generated by the three different FEM schemes is characterized by its condition number, which is defined as [113]

$$\kappa\left([K]\right) = \left\|[K]\right\|_1 \left\|[K]^{-1}\right\|_1 . \tag{3.31}$$

Note that the matrix 1-norm is adopted for the evaluation of the condition number since it is less computationally intensive than the spectral norm [113].

For all of the following numerical examples, the standard FEM is based on meshes that conform to the internal geometries, whereas the subdivision FEM and IGFEM are based on background meshes which are created without considering the internal structures and hence do not necessarily conform to the material interfaces. The resulting linear systems are solved by the highly efficient direct solver PARDISO [105]. The computations are carried out in single float precision on a Cisco computer cluster with each computing node configured with 256-GB memory and two Intel Xeon E5-2680 v2 CPUs.

3.4.1 Dielectric Slab Backed by a PEC Boundary

The first example considered here is an infinitely large dielectric slab backed by a PEC boundary and illuminated by a uniform plane wave, as shown in Fig. 3.7. The incident wave is polarized in the x direction and propagates in the z direction. To mimic the infinite region, the top and bottom surfaces are enforced as PEC boundary, and the front and back surfaces are enforced as PMC boundary. The first-order ABC is employed to truncate the computational domain at the left boundary. The dimensions of the dielectric slab and the total computational domain are $\lambda_0 \times \lambda_0 \times \lambda_0$ and $\lambda_0 \times \lambda_0 \times 2\lambda_0$, respectively. The nonmagnetic material property of the dielectric slab is specified by $\epsilon_1 = (3 - \mathrm{j})\epsilon_0$, where ϵ_0 is the free-space permittivity. For the IGFEM and subdivision FEM simulations, the entire computational domain is meshed into tetrahedra without any specification of the dielectric-air interface. For the standard FEM simulations, the interface is specified before the mesh generation so that the mesh is conformal with the interface.

The convergence rate of the L_2-norm of the field solution error with respect to the number of DoFs is depicted in Fig. 3.8a. The reference solution of the electric field in the computational domain is derived from the power reflection coefficient, which is given by a closed-form expression in [3]. As the number of DoFs increases from 4,800 to 7.3 million, and the mesh size h accordingly decreases from $\lambda_0/6$ to $\lambda_0/100$, the IGFEM shows a convergence rate comparable to that of the standard FEM and a higher numerical accuracy than the subdivision FEM, especially when sub-elements with very small sizes and/or poor aspect ratios are encountered. Despite the fact that the IGFEM needs to determine intersections between the tetrahedra and the material interface and introduces extra DoFs at material interfaces to retrieve "missing" field information, Fig. 3.8a indicates that such an additional cost is trivial and the computational complexity is essentially the same as that of the standard FEM. The condition numbers of the system matrices generated by different FEM schemes are shown in Fig. 3.8b. Obviously, the proposed IGFEM is less sensitive to the quality of the sub-elements and outperforms the subdivision FEM in maintaining a well-conditioned system matrix.

3.4.2 Dielectric Sphere in Free Space

The second example involves the scattering of a dielectric sphere in free space. As shown in Fig. 3.9, the sphere has a diameter of $1.0\lambda_0$ and is placed at the center of a cubic box, whose edge length is set as $3.3\lambda_0$. The material properties of the nonmagnetic sphere and the cubic box are taken to be $\epsilon_1 = 2.56\epsilon_0$ and ϵ_0, respectively. The ABC is applied at the six surfaces of the cube to truncate the computational domain. The incident plane wave travels in the z direction and is polarized in the x direction. Similar to the first example, the entire computational domain is discretized into tetrahedral elements without considering the spherical interface for the IGFEM and subdivision FEM simulations. For the standard FEM simulation, however, the internal geometry is specified before the mesh generation so that the created tetrahedra conform to the spherical interface.

The convergence rate of the L_2-norm of the field solution error, the total solution time, and the condition number of the system matrix, all with respect to the number of DoFs, are displayed in Fig. 3.10. The reference closed-form solution can be found in [39]. For this test problem, the mesh size h ranges from $\lambda_0/6$ to $\lambda_0/50$, and the corresponding number of DoFs ranges from 5,600 to 11.7 million. As in the first test problem, the IGFEM using non-conformal meshes yields a solution accuracy similar to that of the standard FEM using conformal meshes. The IGFEM also maintains the same computational complexity even though it has to identify intersections at material interfaces. The comparison of the condition numbers of the system matrices generated by the three different FEM schemes (Fig. 3.10b) shows that the IGFEM produces system matrices with much smaller condition numbers than those associated with the subdivision FEM.

3.5 Application to Periodic Structures

In the preceding section, the proposed IGFEM using non-conformal meshes has been shown to have the same level of solution accuracy as the standard FEM that uses conformal meshes. In this section, we apply the IGFEM to simulate periodic structures which arise from a variety of composite materials. For electromagnetic modeling of the composite materials, the specular reflection coefficient is usually preferred to characterize the macroscopic, i.e., homogenized, material properties. The specular reflection coefficient R, evaluated at the top surface of the periodic structure, can be obtained by taking the ratio of the scattered magnetic field $\mathbf{H}_{00}^{\mathrm{sca}}$ in the fundamental mode to the incident magnetic field, where $\mathbf{H}_{00}^{\mathrm{sca}}$ can be calculated as

$$\mathbf{H}_{00}^{\mathrm{sca}} = \mathbf{H}^{\mathrm{inc}} - 2\mathrm{j}\frac{k_0}{\eta_0}\tilde{\bar{\bar{\mathbf{G}}}}_{00} \cdot (\mathbf{E} \times \hat{n}). \tag{3.32}$$

3.5.1 Monolayer of Dielectric Sphere Array

The verification example considered here is the reflection from a monolayer periodic array consisting of dielectric spheres with radius r that are positioned in a cubic lattice with periodic length d. The dielectric constant of the spheres is taken to be $\epsilon_{\mathrm{r}} = 3$, and the radius of the spheres is specified by $r/d = 0.4$. The PRC is placed at the top and bottom surfaces for truncation. Practically, the infinite summation in (3.4) is always truncated with a finite number of Floquet modes. A sufficient number of modes has to be included to effectively absorb the propagating and evanescent waves that impinge on the PRC. Fortunately, numerical tests indicate that the magnitude of the Floquet harmonics decreases rapidly with increasing p and q and an inclusion of modes up to the fourth order ($|p| \leq 4$ and $|q| \leq 4$) in this case is typically enough to produce convergent results.

Figure 3.11 depicts the power reflection coefficient as a function of the free-space wavelength λ_0. The plane wave is obliquely incident on the sphere array at an angle of $\theta^{\text{inc}} = 20^\circ$ and $\phi^{\text{inc}} = 0^\circ$. To resolve the field variation in the dielectric spheres, the computational domain is discretized by tetrahedra with a mesh size of $\lambda_0/30$. The reflection coefficients calculated under transverse-magnetic (TM) and transverse-electric (TE) polarizations are respectively displayed in Figs. 3.11a and 3.11b together with the reference theoretical results extracted from Fig. 2 in [114]. It is worth mentioning that the cut-off frequency for the first high-order mode at the given incident angle corresponds to $d/\lambda_0 = 0.745$, and we intentionally increase d/λ_0 to 0.8 to make sure that higher-order Floquet modes are excited so that the effectiveness of the PRC can be fully demonstrated. The good agreement between the IGFEM and analytical results in Fig. 3.11 not only confirms that the formulas for the PRC and the specular reflection coefficient calculation are implemented correctly, but also demonstrates the accuracy of the proposed IGFEM.

3.5.2 Composite Material with Spherical Particles

Motivated by the desire to develop materials with given properties, composite materials with inclusions of various types and shapes have been the focus of multiple studies [107]. The problem considered here is a particular composite, which consists of a polyethylene matrix ($\epsilon_{\text{r}} = 2.25 - \text{j}0.00225$) and 65 spherical inclusions with three different radii, as displayed in Fig. 3.12a. Among all these particles, 24 of them are made of silicon nitrate ($\epsilon_{\text{r}} = 7$) with a radius of $0.04\lambda_0$, 27 of them are FR4 epoxy particles ($\epsilon_{\text{r}} = 4.4 - \text{j}0.088$) with a radius of $0.06\lambda_0$, and the rest are made of alumina ($\epsilon_{\text{r}} = 9.2 - \text{j}0.0736$) with a radius of $0.08\lambda_0$. The composite material is periodic in the x and y directions. The PBC is applied on the four sides of the unit cell and the PRC is applied on both the top and bottom surfaces. The unit cell has dimensions of $\lambda_0 \times \lambda_0 \times 0.5\lambda_0$ and is discretized into non-conforming tetrahedra of size

$\lambda_0/50$.

The computed field distribution using the IGFEM for the normally incident TM polarized plane wave is displayed in Fig. 3.12b. As can be seen, the IGFEM captures the discontinuities of the field and its derivatives at material interfaces. Figure 3.13a presents the specular field reflection coefficient as a function of the incident angles, showing a good agreement between the IGFEM and standard FEM results. The small discrepancies are believed to be caused by the geometrical discretization error. In fact, the conformal mesh for the standard FEM contains 544,376 tetrahedral elements while the background mesh for the IGFEM has only 368,097 tetrahedral elements despite that the same mesh size is adopted for generating the two meshes. Since the IGFEM and the standard FEM use two completely different sets of meshes, and multi-reflections and higher-order Floquet modes co-exist in the computational domain, a sufficiently fine mesh together with enough truncation terms in (3.4) is necessary to produce a better agreement. The mesh generation times for the conformal mesh and the background mesh are 20.5 and 11.2 seconds, respectively. Because the IGFEM uses a background mesh that has a smaller number of elements, the total solution time for the IGFEM is 8.7 hours as opposed to 11.2 hours for the standard FEM using a conformal mesh.

Because the IGFEM produces accurate results without resorting to conformal meshes, the proposed approach is particularly attractive when dealing with problems with constantly changing internal structures, such as those encountered in the electromagnetic analysis of a random medium. To take into account the randomness of the spatial distribution of the inclusions, many unit cells have to be considered for the computation of the statistics of homogenized properties. In Fig. 3.13b, 33 different spatial arrangements of the 65 spherical inclusions are studied to investigate the effect of the randomness on the field reflection. All the IGFEM simulations are performed with a single non-conforming background mesh, thereby greatly simplifying this statistical analysis. Each set of specular reflection coefficient curves consists of 91 incident angles and takes less than 9 hours to sweep all these angles. As can be observed from the figure, the variations of the reflection coefficients generally increase with decreasing incident angles. Large variations are also exhibited at certain incident angles where resonance modes are believed to be excited.

3.5.3 Composite Material with Ellipsoidal Inclusions

The second example involves a particulate composite composed of a glass matrix with ellipsoidal alumina inclusions for high-temperature applications [107]. Since this kind of material is commonly coated on targets for thermal insulation, and because the targets are normally exposed to an electromagnetic environment, it is necessary to study their reflection of electromagnetic waves. The test problem, illustrated in Fig. 3.14, is based on a unit cell of the glass/alumina composite material, where the material properties of the alumina particles and the glass matrix are respectively specified by $\epsilon_\mathrm{r} = 9.2 - \mathrm{j}0.0736$ and $\epsilon_\mathrm{r} = 5.5$. The unit cell, with 45 ellipsoids embedded, has a dimension of $\lambda_0 \times \lambda_0 \times \frac{2}{3}\lambda_0$ and is uniformly discretized into tetrahedral elements with the mesh size $h = \lambda_0/50$. The PBC is enforced at the four sides and the PRC is applied on the top and bottom surfaces as truncation. All of the ellipsoidal particles are randomly distributed in the unit cell with their axes arbitrarily oriented and their shape described by

$$\frac{\tilde{x}^2 + \tilde{y}^2}{3 + 0.8e^{-\tilde{z}^2}} + \frac{\tilde{z}^2}{3^2} = 1, \tag{3.33}$$

where the particle coordinates $(\tilde{x}, \tilde{y}, \tilde{z})$ are normalized with the free-space wavelength λ_0.

The IGFEM evaluated electric field distribution under a normally incident TM polarized plane wave, and the field reflection coefficients for 15 configurations with incident angle θ^{inc} sweeping from $0°$ to $90°$, are displayed in Figs. 3.15a and 3.15b, respectively. Because of the irregular shapes of the ellipsoids, the commercial software CUBIT [115] fails to generate a conformal mesh for this problem. In contrast, the IGFEM, which does not rely on a conformal mesh, takes less than 1 second to determine the intersections on the material interfaces even though the background mesh contains 453,059 tetrahedra. For each configuration, the IGFEM needs approximately 9.5 hours to produce the reflection coefficient curves for 91 incident angles. The reflection curves shown in Fig. 3.15b are generally smoother than those depicted in Fig. 3.13b, especially for large oblique incidences. This phenomenon might be due to the smaller dielectric contrast in the glass/alumina composite material. It is interesting to note that the glass/alumina composite material exhibits a large angle range (from $50°$ to $75°$) of low reflectivity for TM polarization.

3.5.4 Microvascular Composite Material

The last problem is driven by the recent development of multi-functional microvascular composite materials [38]. By circulating different fluids along the micro-channels, this composite material can be effectively used for heat dissipation, energy storage, self-healing, or even to dynamically modulate material property. The application problem, shown in Fig. 3.16a, consists of a plexiglass matrix ($\epsilon_\mathrm{r} = 3.4 - \mathrm{j}0.0034$) with eight embedded sinusoidal channels filled with ethylene glycol ($\epsilon_\mathrm{r} = 7 - \mathrm{j}5.46$). The wavy channels, with a cross section radius of $0.06\lambda_0$ and a geometrical periodicity of λ_0, are infinitely long in the x direction and are periodically stacked in the y direction with a center-to-center distance of $0.18\lambda_0$. The unit cell is taken to have a size of $1.5\lambda_0 \times 0.72\lambda_0 \times 0.6\lambda_0$ and is uniformly discretized into tetrahedral elements with the mesh size specified as $\lambda_0/50$ without any consideration of the micro-channels. The PRC is applied on the top and bottom surfaces to truncate the computational domain from the free space. The sides of the unit cell are set as PBC to emulate the infinite array in the xy plane.

The IGFEM calculated field reflection coefficients for the TM and TE polarizations are depicted in Fig. 3.16b. Since the internal structures are well ordered and free of random small inclusions that could potentially induce strong multi-reflections, the reflection coefficient curves are very smooth. The standard FEM solutions are not provided because of the difficulty of creating a conformal mesh for such a complex geometry, especially of assigning the PBC at surfaces that are perpendicular to the x axis. It is worth mentioning that even with such complex material interfaces, the IGFEM takes less than 3 seconds to find all the intersections, which is trivial compared to the 12 hours of the total solution time for sweeping 91 incident angles from 0° to 90°. The electric field distributions for the TM and TE polarizations are shown in Figs. 3.17a and 3.17b, respectively. Again, as expected, the IGFEM successfully captured the discontinuities of the field and its derivatives.

3.6 Summary

In this chapter, we presented a 3-D IGFEM for accurate and efficient electromagnetic analysis of composite materials. To eliminate the requirement of generating conformal meshes for geometrically complex domains, we enriched the FEM solution space at material interfaces to capture the discontinuities of the field and its derivatives. We then discussed the construction of the enriching solution space and analyzed its advantages over the subdivision-based FEM. Several verification examples were then presented to investigate the conditioning, accuracy, and h-refinement convergence rate of the proposed IGFEM. The investigation showed that the IGFEM is not sensitive to the quality of the sub-elements and it maintains the same level of solution accuracy and computational complexity as the standard FEM based on conformal meshes. Finally, we presented three application problems with complex internal structures to demonstrate the ability of the proposed method to efficiently analyze highly inhomogeneous composite materials, without needing to create multiple meshes for problems with randomly distributed inclusions.

3.7 Figures

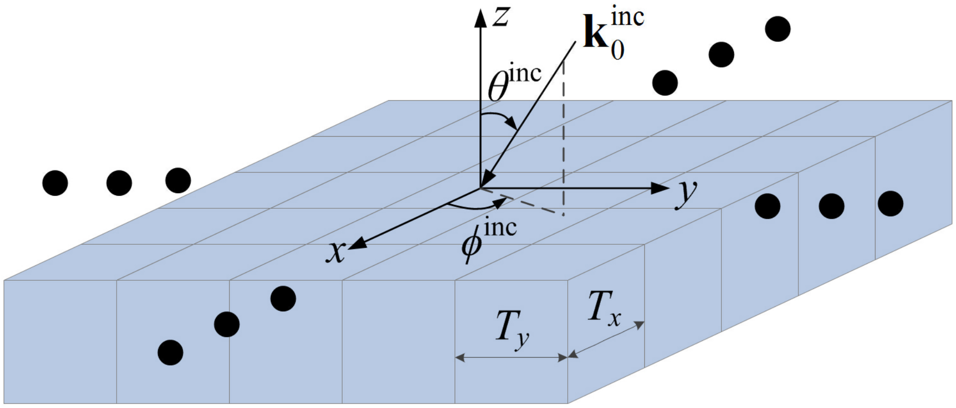

Figure 3.1: A monolayer periodic array illuminated by a uniform plane wave. The plane wave has an incident angle of $(\theta^{\text{inc}}, \phi^{\text{inc}})$ and propagates with a wave vector of $\mathbf{k}_0^{\text{inc}}$. The periodic lengths of the primitive cell are T_x and T_y in the x and y directions, respectively.

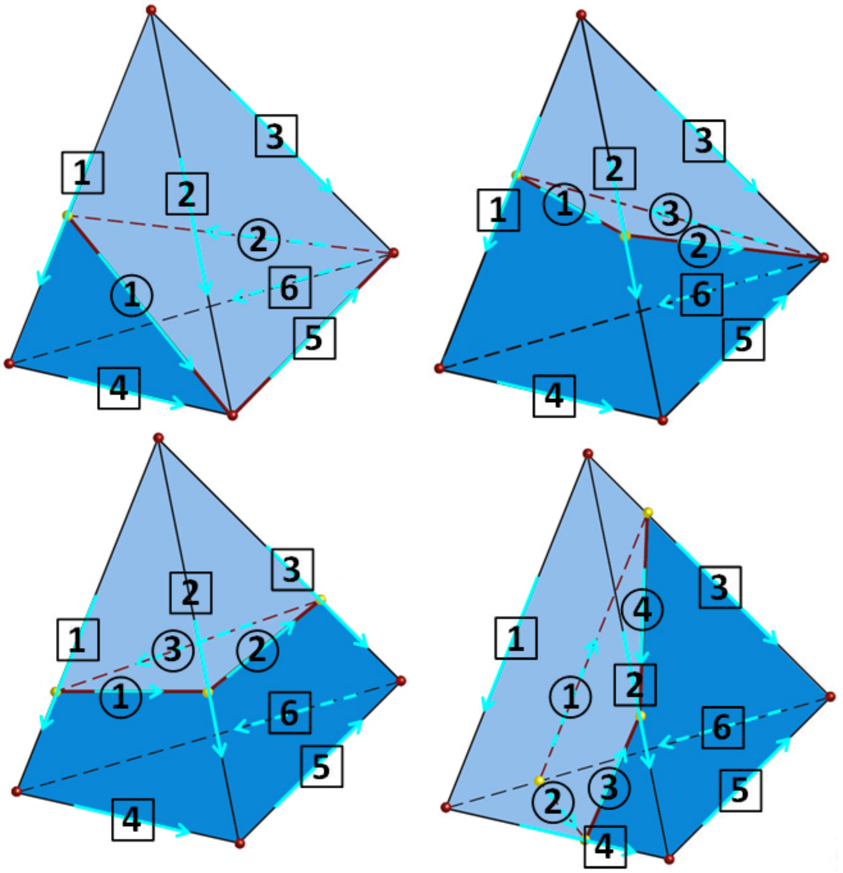

Figure 3.2: Four scenarios for the intersection of a material interface with a tetrahedron. The VBFs, defined on the edges of the original tetrahedron, are numbered in boxes. The enriched VBFs, defined on the edges of the material interface, are numbered in circles.

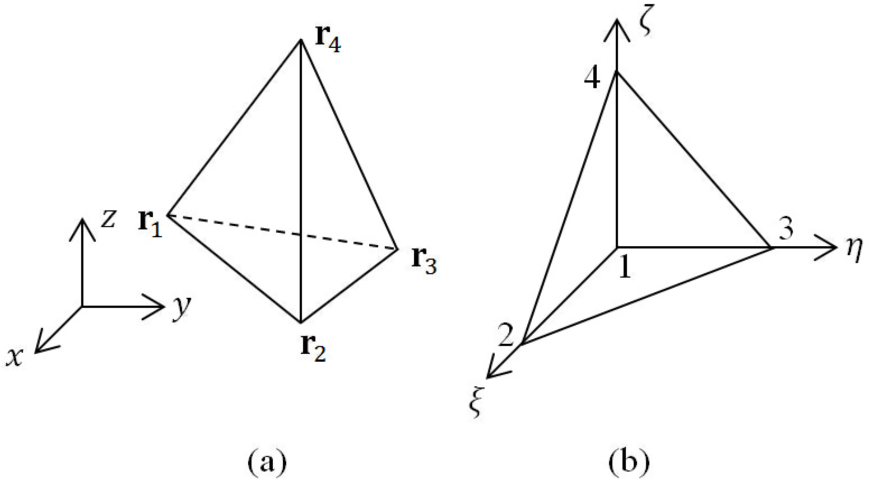

Figure 3.3: (a) Tetrahedral element in the physical coordinate system. (b) Tetrahedral element in the simplex coordinate system.

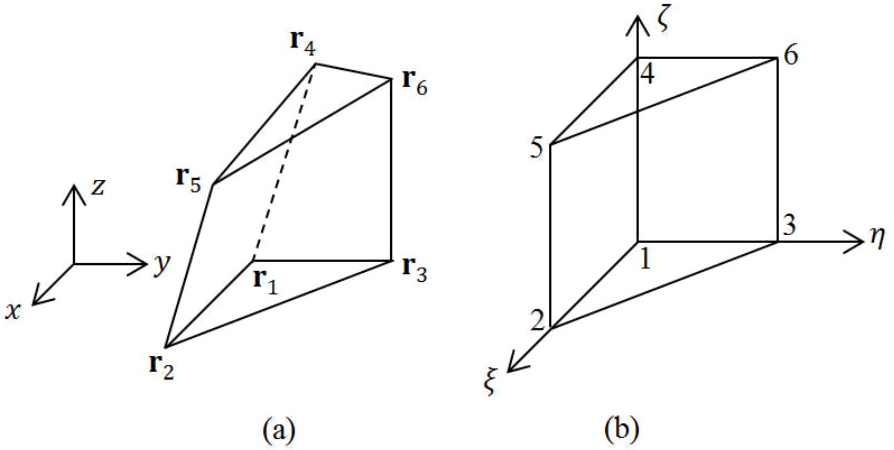

Figure 3.4: (a) Prismatic element in the physical coordinate system. (b) Prismatic element in the simplex coordinate system.

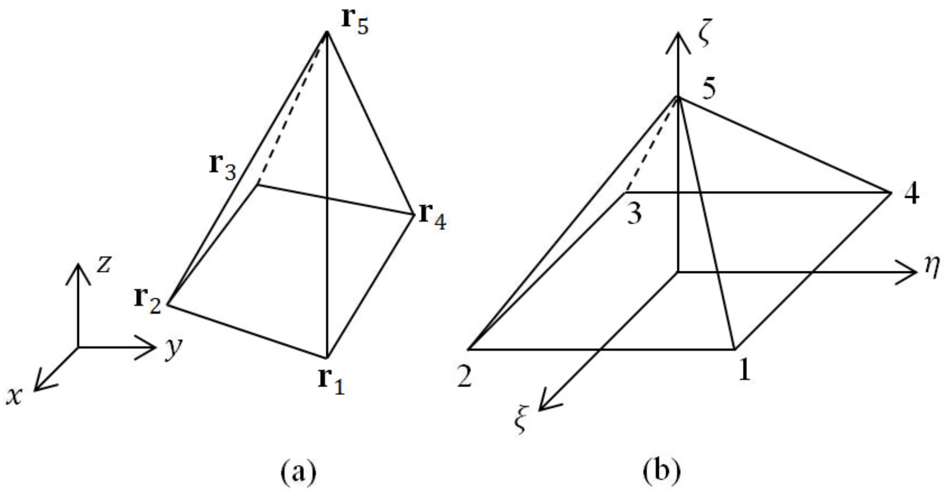

Figure 3.5: (a) Pyramidal element in the physical coordinate system. (b) Pyramidal element in the simplex coordinate system.

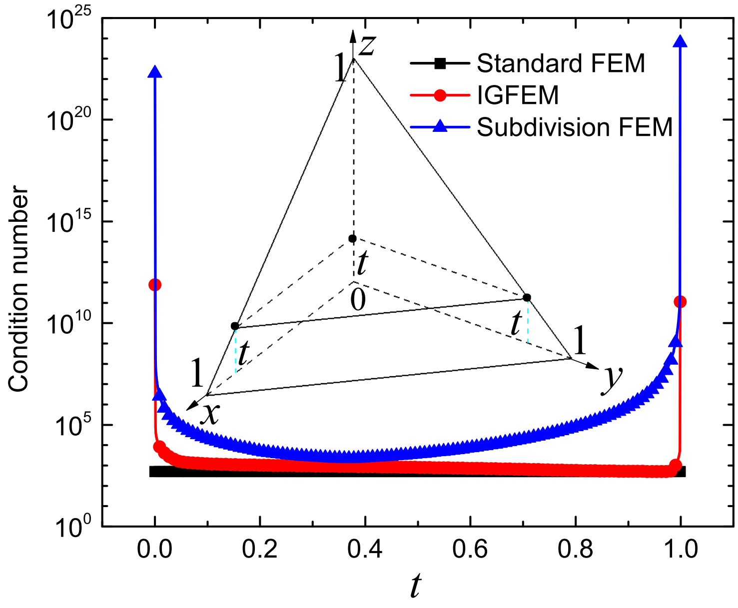

(a)

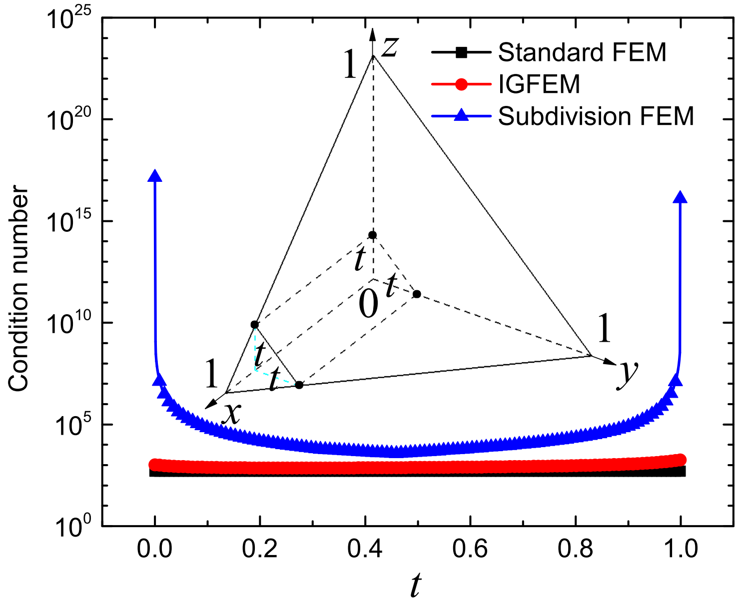

(b)

Figure 3.6: Condition number of an enriched tetrahedral element using different FEM schemes. The coordinates of the four vertices of the tetrahedron, normalized with the free-space wavelength λ_0, are specified by the *standard 3-simplex*. The condition number of the matrix $[\mathcal{L}]$ is evaluated as a function of intersection position, which is controlled by t. (a) A tetrahedron is divided into a sub-tetrahedron and a sub-prism. (b) A tetrahedron is divided into two sub-prisms.

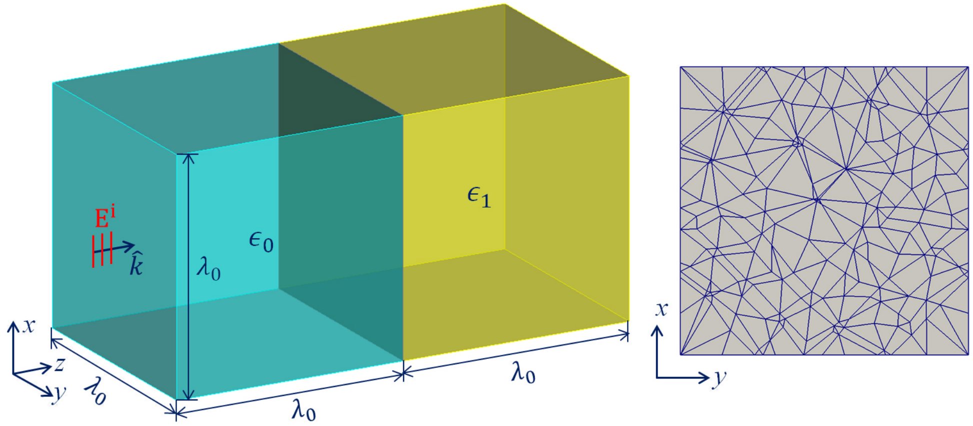

Figure 3.7: A plane wave propagates normally into a PEC-backed lossy dielectric slab with electric field polarized in the x direction. The PEC and PMC boundaries are respectively enforced at the surfaces perpendicular to the x and y axes to emulate the infinite dielectric slab. The left surface is truncated by an ABC. The right figure illustrates the intersected meshes at the planar material interface in the subdivision FEM and IGFEM simulations with the background mesh size $h = \lambda_0/6$.

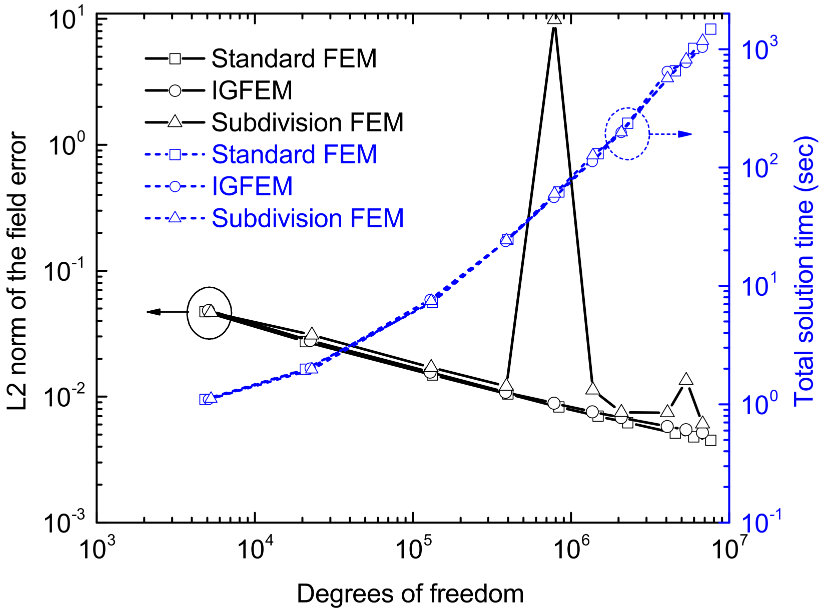

(a)

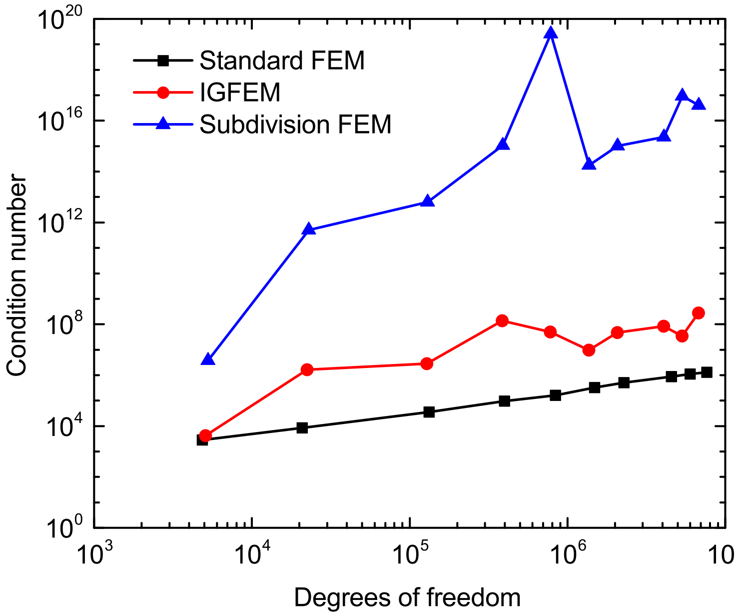

(b)

Figure 3.8: L_2-norm of the field solution error, total solution time, and condition number of the system matrix for the test problem shown in Fig. 3.7. (a) L_2-norm of the field solution error and total solution time with respect to the number of DoFs. Note that the total solution time includes time for estimating the condition number and calculating L_2-norm of the field solution error. The meshing time for these three FEM schemes is not included in the total solution time. (b) Condition number of the system matrix with respect to the number of DoFs.

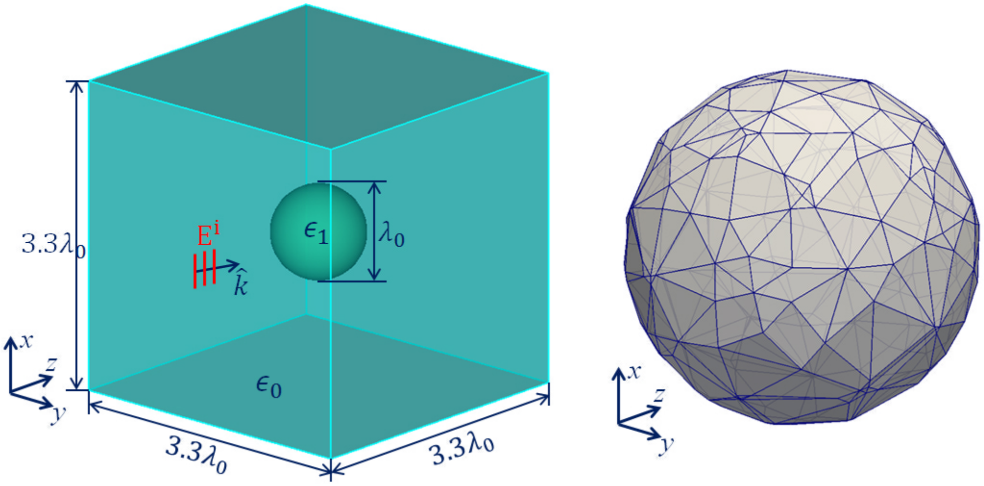

Figure 3.9: A plane wave illuminates a dielectric sphere in free space. The computational domain is truncated by an ABC. The right figure shows nonconforming tetrahedral elements with a size of $\lambda_0/10$, used in the subdivision FEM and IGFEM simulations, as they intersect the spherical interface.

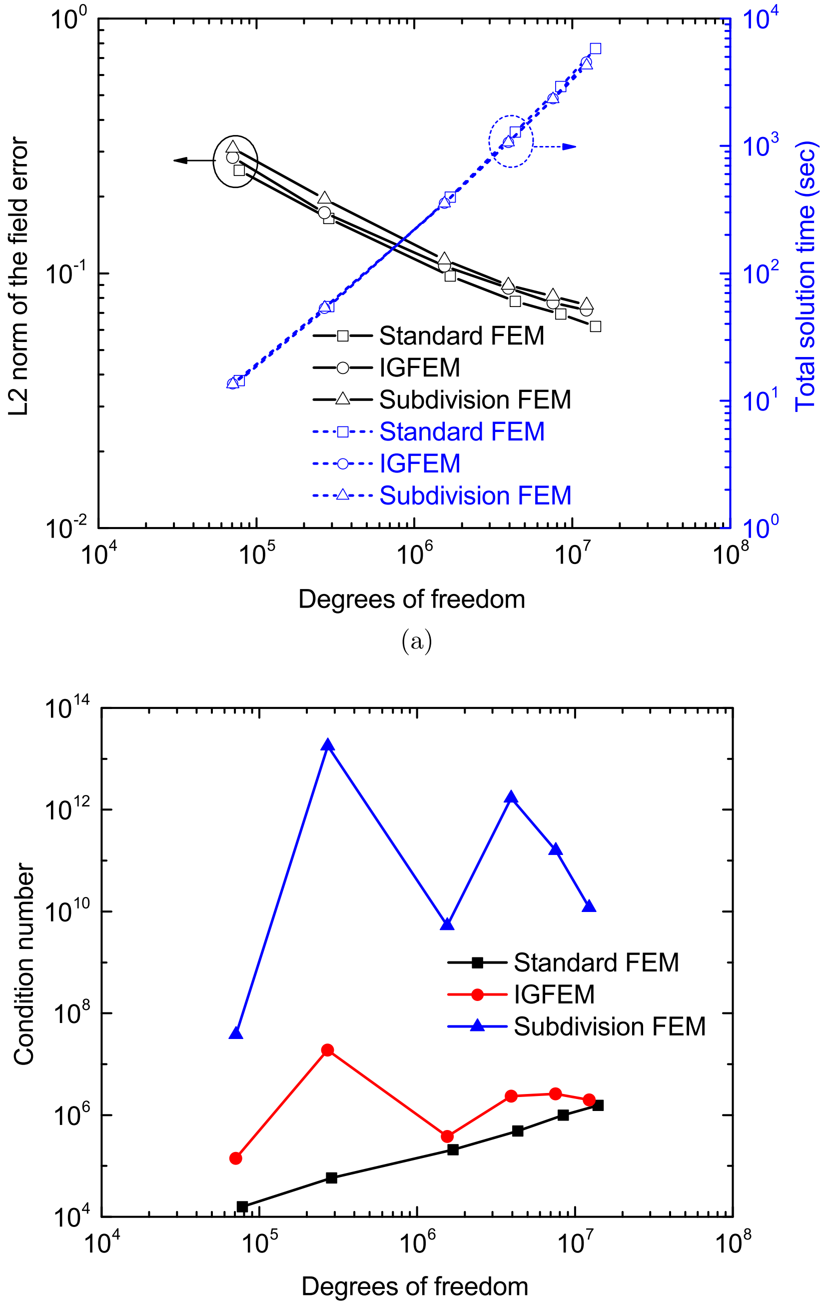

(a)

(b)

Figure 3.10: L_2-norm of the field solution error, total solution time, and condition number of the system matrix for the test problem shown in Fig. 3.9. (a) L_2-norm of the field solution error and total solution time with respect to the number of DoFs. Note that the total solution time includes time for estimating the condition number and calculating L_2-norm of the field solution error. The meshing time for these three FEM schemes is not included in the total solution time. (b) Condition number of the system matrix with respect to the number of DoFs.

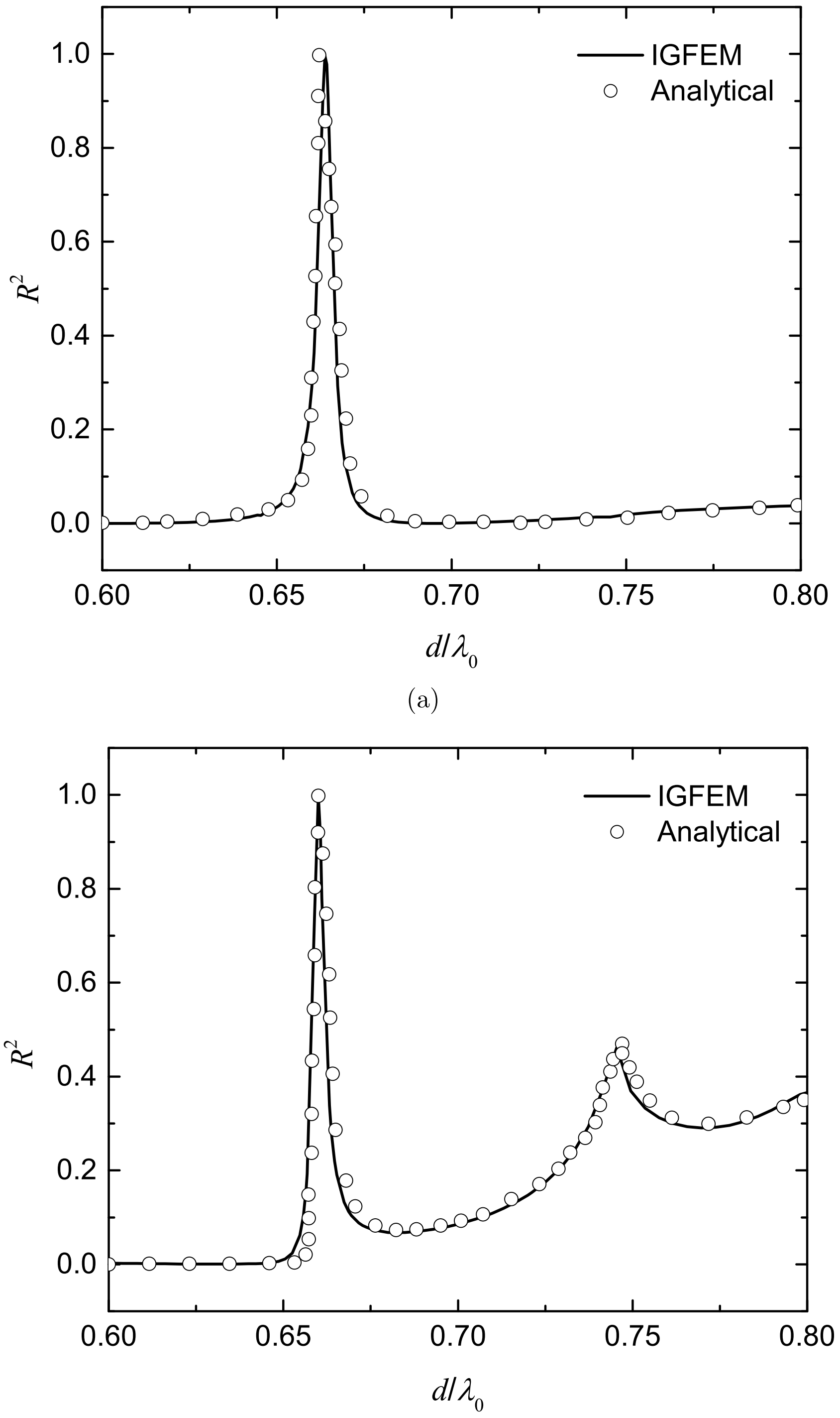

(a)

(b)

Figure 3.11: Power reflection coefficient versus the free-space wavelength λ_0 of a monolayer array of dielectric spheres with $\epsilon_\mathrm{r} = 3$ and $r/d = 0.4$. The incident angle of the plane wave is $\theta^\mathrm{inc} = 20°$ and $\phi^\mathrm{inc} = 0°$. (a) TM polarization. (b) TE polarization.

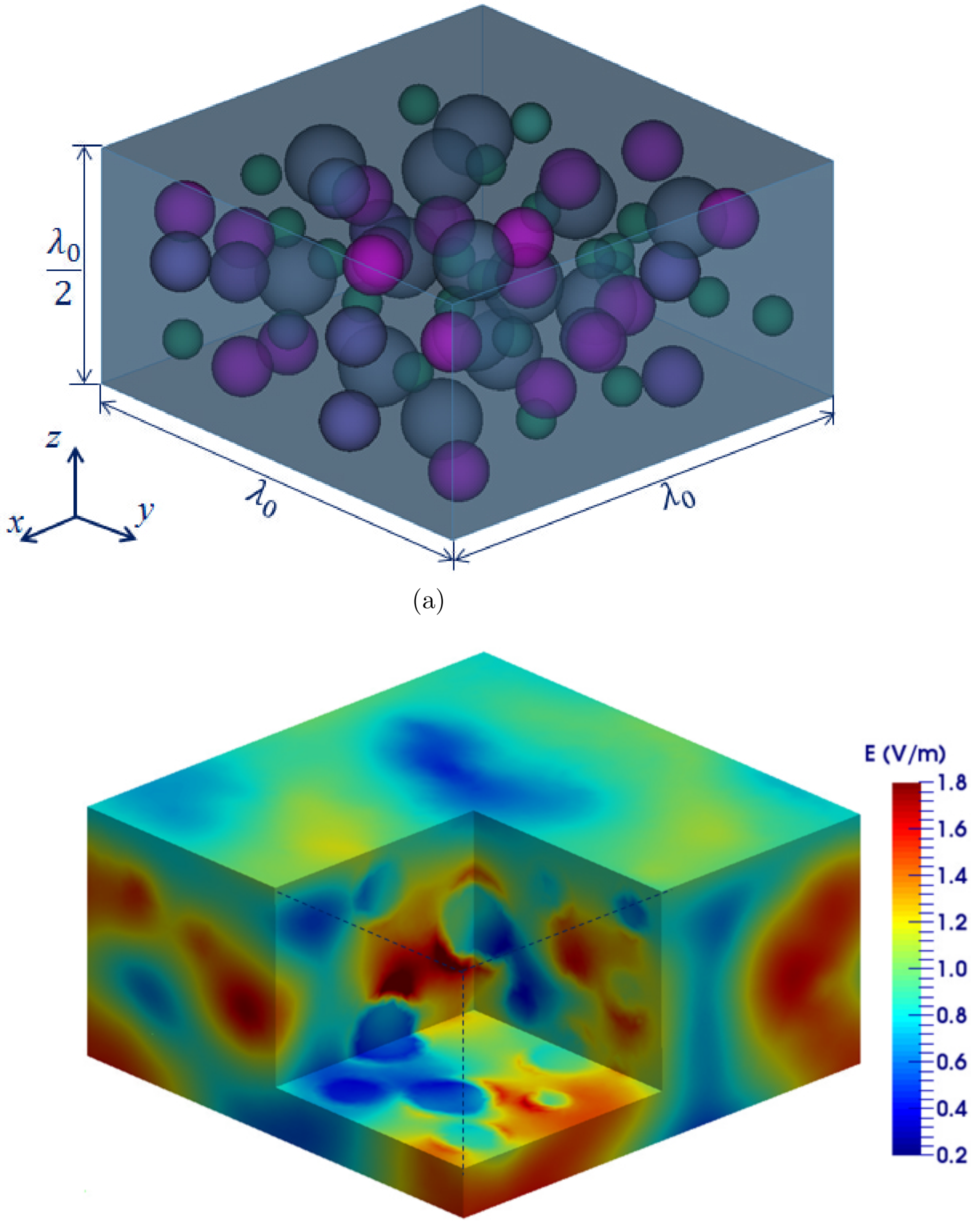

(a)

(b)

Figure 3.12: Geometrical configuration and electric field distribution of a composite material unit cell with 65 spherical particles. The particles, with different radii and material properties, are randomly distributed in the unit cell. (a) Spatial arrangements of the inclusions in the unit cell. (b) Magnitude of the electrical field for a normally incident TM polarized plane wave.

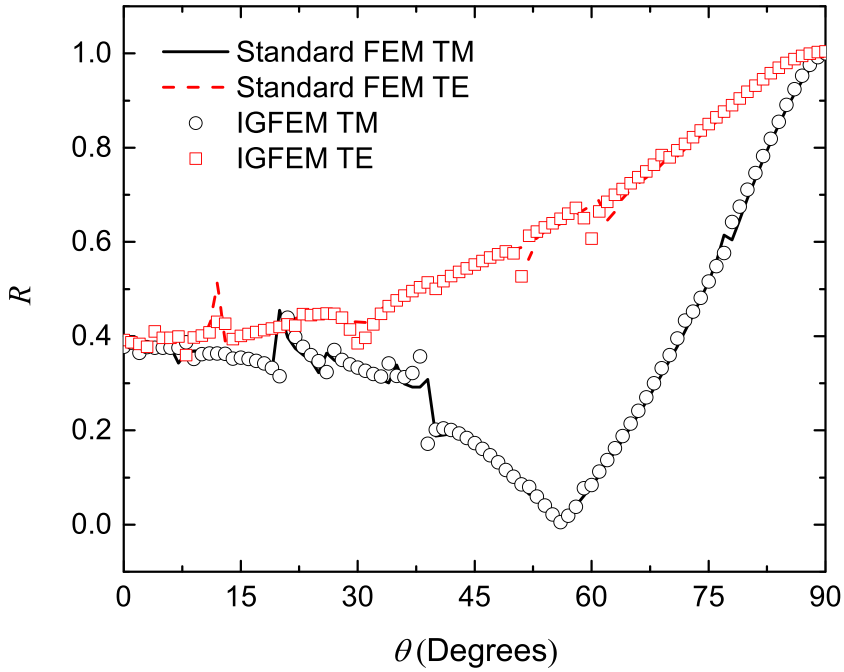

(a)

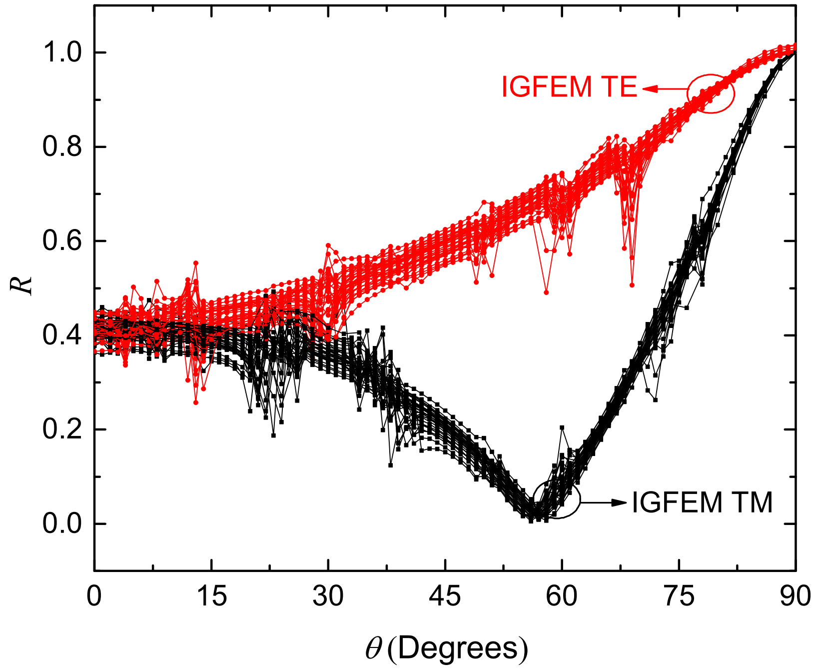

(b)

Figure 3.13: Field reflection coefficient for the problem shown in Fig. 3.12a. (a) Comparison between the IGFEM and the standard FEM results. (b) Field reflection coefficients for 33 different spatial arrangements of the spherical particles.

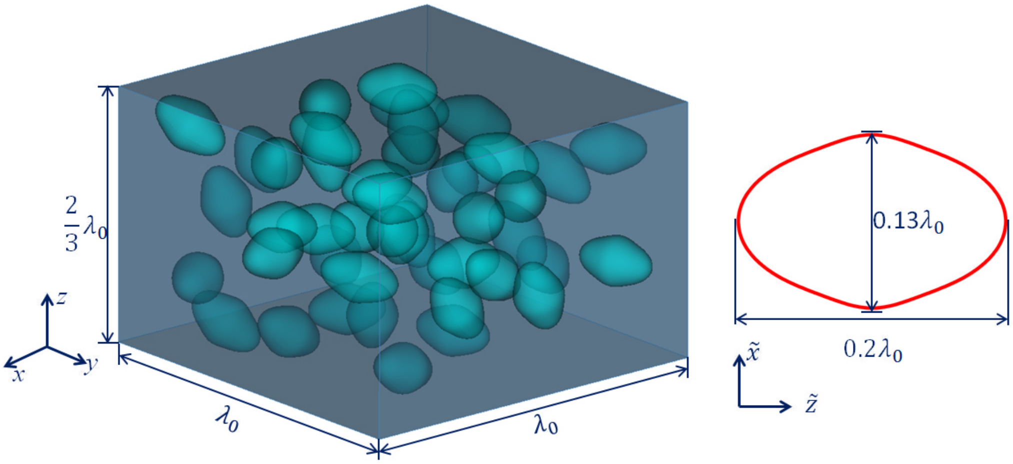

Figure 3.14: Geometrical configuration of a glass/alumina composite material unit cell with 45 ellipsoidal inclusions. The ellipsoids are randomly arranged and their principal axes are arbitrarily oriented. The right figure displays the profile of the ellipsoid with its major- and minor-axes specified by $0.2\lambda_0$ and $0.13\lambda_0$, respectively.

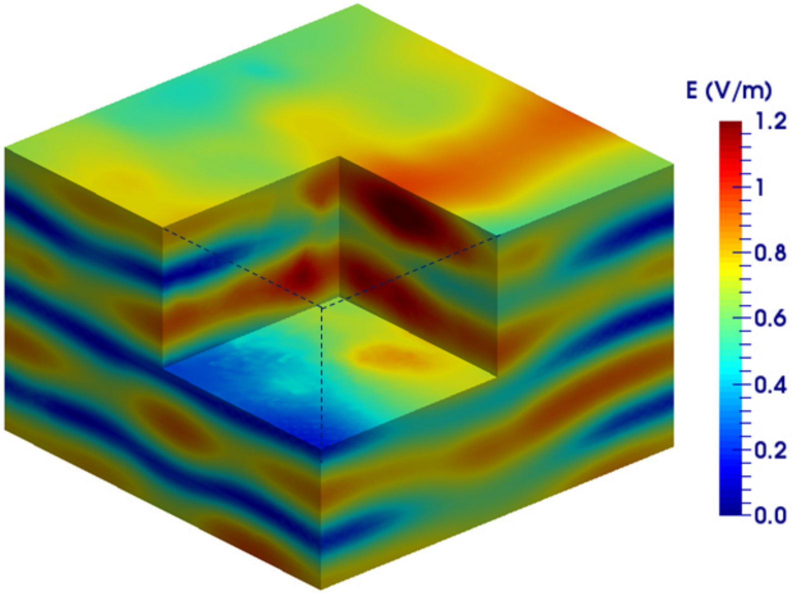

(a)

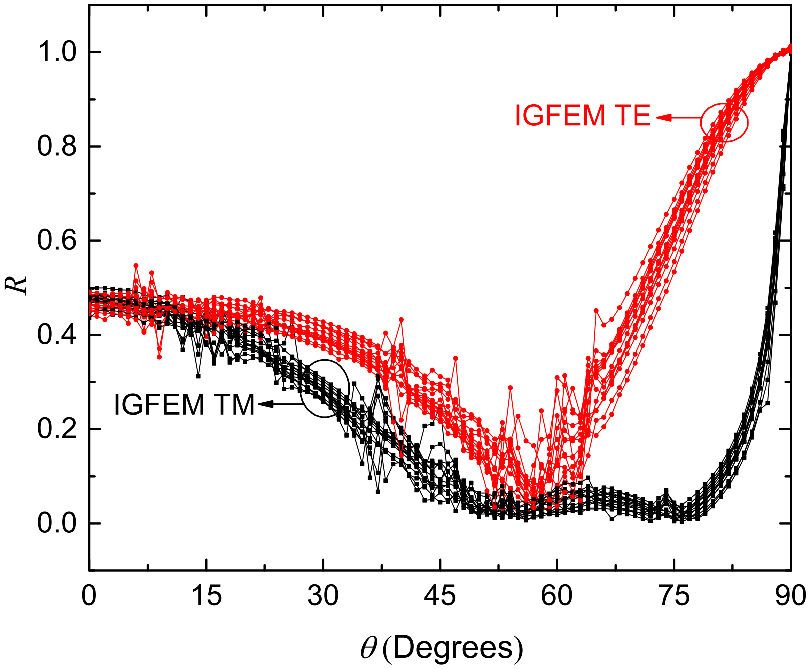

(b)

Figure 3.15: Field distribution and reflection coefficient for the problem shown in Fig. 3.14. (a) Magnitude of the electric field for a normally incident TM polarized plane wave. (b) Field reflection coefficients for 15 configurations of the periodic unit cell of the composite.

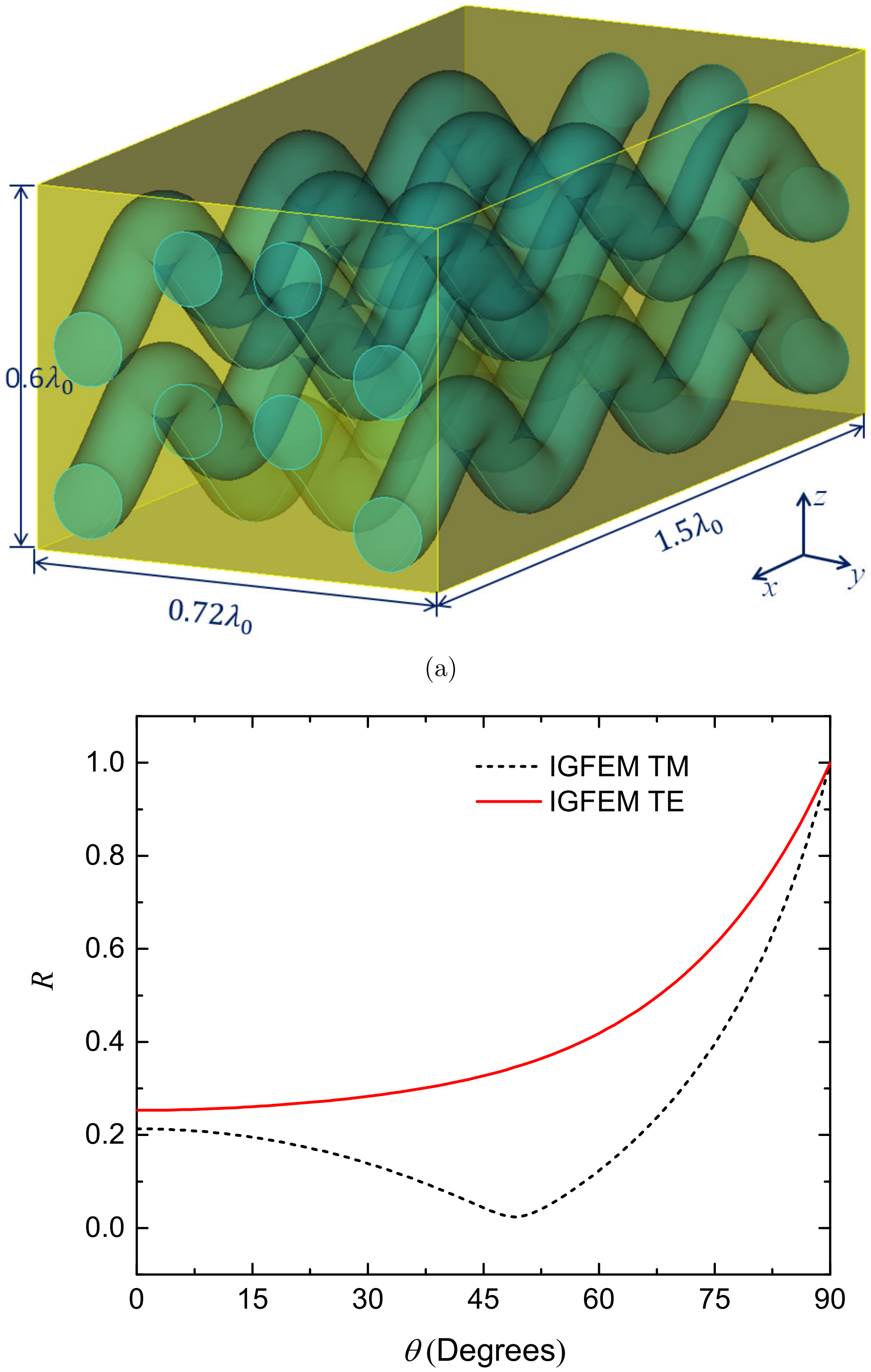

(a)

(b)

Figure 3.16: Geometrical configuration of a composite material unit cell with eight sinusoidal channels and field reflection coefficient of the infinite periodic array. The channels, filled with ethylene glycol, are embedded in a plexiglass matrix. (a) Spatial arrangements of the eight wavy channels. (b) Field reflection coefficient as a function of incident angles.

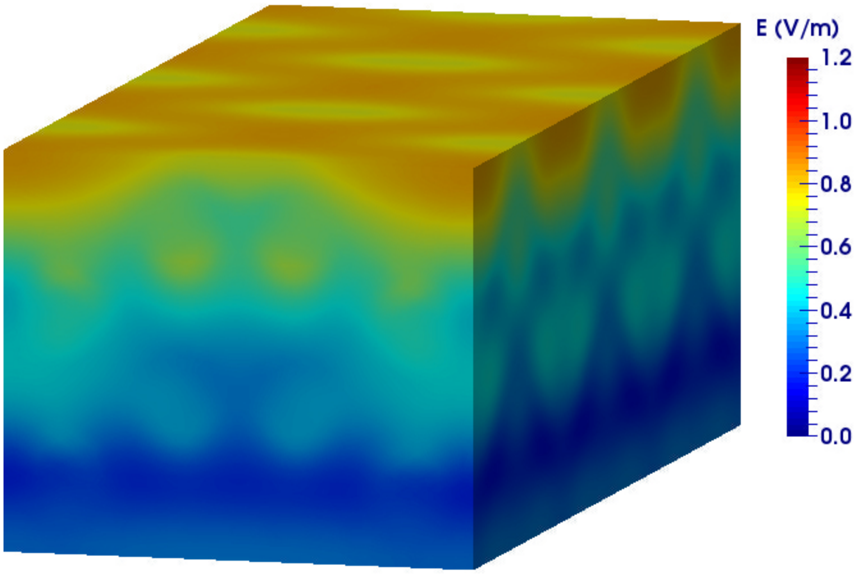

(a)

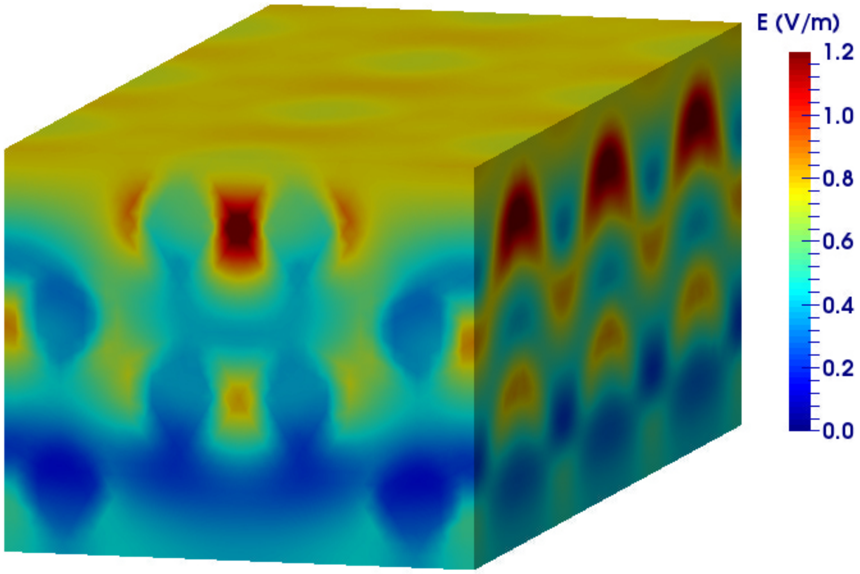

(b)

Figure 3.17: Magnitude of the electrical field for a normally incident plane wave illuminating the application problem shown in Fig. 3.16a. (a) TM polarization. (b) TE polarization.

Chapter 4

IGFEM for Gradient-Based Shape Optimization

4.1 Introduction

Optimization of electromagnetic problems has been discussed in the literature for a while and a wide variety of methods have been proposed [20,116]. These approaches can be grouped into two main categories: evolutionary algorithms and gradient-based methods. Based on the natural principles of mutation and selection, evolutionary algorithms such as genetic algorithms (GAs) have been adopted for electromagnetic device optimization [116]. While GAs offer the potential to search for global optima even in the presence of many design variables, they are often prohibitively expensive. While not necessarily guaranteeing a convergence to a global optimum, gradient-based optimization techniques based on the analytical evaluation of the sensitivity of the objective functions and constraints with respect to the design variables are often considered as the approach of choice due to their high efficiency, when the initial design is close to the optimal [20].

To model complex materials/systems with a high numerical accuracy, a gradient-based shape optimization using the FEM is preferred. However, the standard FEM relies on a conformal mesh to achieve a high solution accuracy. Even if the structure shapes have small variations, a new conformal mesh has to be recreated from scratch, which is cumbersome and expensive. In addition, the remeshing process also compromises the efficiency of the optimizer since the so-called *design velocity field* term has to be evaluated over all the nodes in the computational domain instead of only those residing on the modified interfaces.

In this chapter, we adopt a gradient-based shape optimization scheme, which was recently developed for structural/thermal problems [21], using the IGFEM to remove the remeshing issue and accelerate the evaluation of the *design velocity field* term. The BVPs for radar signature prediction, reflection and transmission from a periodic composite material and S-parameters evaluation in waveguide devices are discussed. The derivatives of the enriched bases and their gradients with respect to the design variables, which are required in the IGFEM-based analytical sensitivity analysis, are derived. Three numerical examples are presented to demonstrate the efficiency of this optimizer.

4.2 Formulation

For the sake of simplicity, let us consider 2D electromagnetic problems for the gradient-based shape optimization. The governing equation, with $\phi = E_z$, can be written as

$$\nabla \cdot \left(\frac{1}{\mu_{\mathrm{r}}} \nabla \phi \right) + k_0^2 \epsilon_{\mathrm{r}} \phi = 0, \tag{4.1}$$

together with the Dirichlet, Neumann, and Robin boundary conditions

$$\phi = \phi_D \quad \text{on } \partial\Omega_D, \tag{4.2}$$

$$\hat{n} \cdot \left(\frac{1}{\mu_{\mathrm{r}}} \nabla \phi \right) = \phi_N \quad \text{on } \partial\Omega_N, \tag{4.3}$$

$$\hat{n} \cdot \left(\frac{1}{\mu_{\mathrm{r}}} \nabla \phi \right) + \gamma(\phi) = q \qquad \text{on } \partial\Omega_R, \tag{4.4}$$

where ϕ_D and ϕ_N are the prescribed values, q is the known excitation, and $\gamma(\phi)$ is a function of ϕ and its forms depend on specific problems.

4.2.1 Radar Signature Prediction

For scattering analysis with the first-order ABC enforced on the boundaries for truncation, as illustrated in Fig. 2.2, q and $\gamma(\phi)$ are given by

$$q = \hat{n} \cdot \nabla \phi^{\mathrm{inc}} + \mathrm{j} k_0 \phi^{\mathrm{inc}}, \tag{4.5}$$

$$\gamma(\phi) = \mathrm{j} k_0 \phi, \tag{4.6}$$

where ϕ^{inc} is the incident plane wave. Once the field inside the computational domain is determined, the radar signature (or echo width) can be evaluated through the near-field to far-field transformation. For a unit-power plane wave incidence, the echo width can be written as [3]

$$\sigma_{2\mathrm{D}} = \lim_{\rho\to\infty} \frac{k_0}{4} \left| \oint_{\partial\Omega} \left[\hat{n}' \cdot \hat{\rho}\phi(\boldsymbol{\rho}') - \frac{1}{\mathrm{j}k_0} \hat{n}' \cdot \nabla'\phi(\boldsymbol{\rho}') \right] \mathrm{e}^{\mathrm{j}k_0\hat{\rho}\cdot\boldsymbol{\rho}'} \mathrm{d}\boldsymbol{\rho}' \right|^2 . \tag{4.7}$$

4.2.2 Reflection and Transmission from Periodic Structures

Consider a structure that is periodic in the x-direction illuminated by an incident plane wave polarized in the z-direction, as demonstrated in Fig. 4.1. According to Floquet's theorem [108], the field satisfies the PBC

$$\phi(x + T_x, y) = \phi(x, y)\mathrm{e}^{-\mathrm{j}k_x^{\mathrm{inc}}T_x} \tag{4.8}$$

between adjacent unit cells, where T_x is the periodic length. In the non-periodic direction, the field satisfies the Robin boundary condition with

$$q = -\mathrm{j}2k_y^{\mathrm{inc}}\phi^{\mathrm{inc}}, \tag{4.9}$$

$$\gamma(\phi) = \frac{1}{T_x} \sum_{m=-\infty}^{\infty} \mathrm{j}k_{ym}\mathrm{e}^{-\mathrm{j}k_{xm}x} \int_{T_x} \phi\mathrm{e}^{\mathrm{j}k_{xm}x}\mathrm{d}x \tag{4.10}$$

at the upper boundary, where

$$k_{xm} = k_x^{\mathrm{inc}} - \frac{2\pi m}{T_x} \text{ and } k_{ym} = \sqrt{k_0^2 - k_{xm}^2}. \tag{4.11}$$

At the bottom boundary, $\gamma(\phi)$ remains the same except that the source term q vanishes. The reflection coefficient in the specular direction and the transmission coefficient in the forward direction are respectively given by

$$R = \frac{1}{T_x} \int_{T_x} (\phi - \phi^{\mathrm{inc}})\mathrm{d}x \text{ and } T = \frac{1}{T_x} \int_{T_x} \phi\mathrm{d}x. \tag{4.12}$$

4.2.3 S-Parameters Calculation in Filter Analysis

Most of the waveguide filters work at the fundamental mode. To simulate such structures, the waveguide port boundary condition (WPBC) is usually adopted for truncation since it can absorb all the waveguide modes [3,10,117]. When the WPBC is placed far enough away from geometrical discontinuities, as the one shown in Fig. 4.2, the field at waveguide ports can be simply expressed as the summation of the incident and reflected fundamental mode. At an active port, the WPBC satisfies the Robin boundary condition with

$$q = 2\mathrm{j}k_x\phi^{\mathrm{inc}}, \tag{4.13}$$

$$\gamma(\phi) = \mathrm{j}k_x\phi, \tag{4.14}$$

where ϕ^{inc} is the fundamental modal incidence, $k_x = \sqrt{k_0^2 - k_y^2}$, $k_y = \pi/a$, and a is the dimension of the port. For a passive port, q vanishes because no incident field is applied. Once the field in the computational domain is obtained, the reflection and transmission coefficients can be respectively calculated through

$$R = \frac{\phi - \phi^{\mathrm{inc}}}{\phi^{\mathrm{inc}}} \text{ and } T = \frac{\phi}{\phi^{\mathrm{inc}}}. \tag{4.15}$$

4.3 Analytical Sensitivity Analysis

For most electromagnetic problems, the objective function is not a direct function of design parameters. Hence, a general shape optimization problem can be written as [21]

$$\begin{aligned} \min_{\mathbf{d}} \quad & g\left(\mathbf{U}(\mathbf{X}(\mathbf{d}))\right), \\ \text{such that: } & h_i\left(\mathbf{d}\right) \leq 0 \text{ for } i \in [1, l], \\ & d_{i,\min} \leq d_i \leq d_{i,\max} \text{ for } i \in [1, m], \\ \text{and } & \mathbf{K}(\mathbf{X}(\mathbf{d}))\mathbf{U}(\mathbf{X}(\mathbf{d})) = \mathbf{F}(\mathbf{X}(\mathbf{d})), \end{aligned} \tag{4.16}$$

where g is the objective function to minimize, h_i denotes the constraint function, $\mathbf{X}$ is the nodal coordinate vector at quadrature points, $\mathbf{d}$ is the design variable vector, and $\mathbf{K}$, $\mathbf{U}$, and $\mathbf{F}$ are respectively the IGFEM system matrix, unknown vector, and excitation vector. In our analysis, g, h_i, $\mathbf{X}$, and $\mathbf{d}$ are all real-valued, and $\mathbf{K}$, $\mathbf{U}$, and $\mathbf{F}$ are complex-valued.

The sensitivity analysis of the objective and constraint functions is conducted by an analytical discrete derivative approach. Taking the objective function, for instance, the analytical sensitivity can be derived as

$$\begin{aligned}\frac{\mathrm{d}g}{\mathrm{d}d_i} &= \left(\frac{\partial g}{\partial \Re\{\mathbf{U}\}}\right)^{\mathrm{T}} \frac{\partial \Re\{\mathbf{U}\}}{\partial d_i} + \left(\frac{\partial g}{\partial \Im\{\mathbf{U}\}}\right)^{\mathrm{T}} \frac{\partial \Im\{\mathbf{U}\}}{\partial d_i} \\ &= \left(\frac{\partial g}{\partial \Re\{\mathbf{U}\}}\right)^{\mathrm{T}} \Re\left\{\frac{\partial \mathbf{U}}{\partial d_i}\right\} + \left(\frac{\partial g}{\partial \Im\{\mathbf{U}\}}\right)^{\mathrm{T}} \Re\left\{-\mathrm{j}\frac{\partial \mathbf{U}}{\partial d_i}\right\} \\ &= \Re\left\{\left(\frac{\partial g}{\partial \Re\{\mathbf{U}\}}\right)^{\mathrm{T}} \frac{\partial \mathbf{U}}{\partial d_i}\right\} + \Re\left\{-\mathrm{j}\left(\frac{\partial g}{\partial \Im\{\mathbf{U}\}}\right)^{\mathrm{T}} \frac{\partial \mathbf{U}}{\partial d_i}\right\} \\ &= \Re\left\{\left(\frac{\partial g}{\partial \Re\{\mathbf{U}\}} + \mathrm{j}\frac{\partial g}{\partial \Im\{\mathbf{U}\}}\right)^{\mathrm{H}} \frac{\partial \mathbf{U}}{\partial d_i}\right\},\end{aligned} \tag{4.17}$$

where $\partial g/\partial \Re\{\mathbf{U}\}$ and $\partial g/\partial \Im\{\mathbf{U}\}$ are explicitly evaluated. To evaluate $\partial \mathbf{U}/\partial d_i$, we start from differentiating the finite-element system with respect to each of the design variables d_i, resulting in a series of pseudo problems

$$\frac{\partial \mathbf{K}}{\partial d_i}\mathbf{U} + \mathbf{K}\frac{\partial \mathbf{U}}{\partial d_i} = \frac{\partial \mathbf{F}}{\partial d_i}. \tag{4.18}$$

Note that the right-hand side is vanishing because the boundary of the computational domain does not change with design parameters during the optimization process. Hence, the sensitivity can be simplified as

$$\frac{\mathrm{d}g}{\mathrm{d}d_i} = -\left(\frac{\partial g}{\partial \mathbf{U}}\right)^{\mathrm{T}} \mathbf{K}^{-1}\frac{\partial \mathbf{K}}{\partial d_i}\mathbf{U}. \tag{4.19}$$

To evaluate $\partial \mathbf{K}/\partial d_i$, we need to determine the system matrix first. In FEM, the elemental system matrix is expressed as

$$\mathbf{K}_e = \int_{\Omega_e} \frac{1}{\mu_{\mathrm{r}}}\mathbf{B}^{\mathrm{T}}\mathbf{B}\mathrm{d}\mathbf{r} - k_0^2 \int_{\Omega_e} \epsilon_{\mathrm{r}}\mathbf{N}^{\mathrm{T}}\mathbf{N}\mathrm{d}\mathbf{r} + \int_{\partial\Omega_e} \zeta(\mathbf{N})\mathrm{d}\mathbf{r}, \tag{4.20}$$

where $\zeta(\mathbf{N})$ is the line integrand introduced by the Robin boundary condition, and $\mathbf{N}$ and $\mathbf{B}$ are respectively the basis functions and their gradients, which are given by

$$\mathbf{N} = [\mathbf{N}_{\mathrm{p}} \quad \mathbf{N}_{\mathrm{c}}] \text{ and } \mathbf{B} = \frac{\partial \mathbf{N}}{\partial \mathbf{X}}, \tag{4.21}$$

with $\mathbf{N}_{\mathrm{p}}$ representing the original basis functions defined on the background finite elements and $\mathbf{N}_{\mathrm{c}}$ denoting the enriched basis functions defined on the material interfaces. The evaluation of $\partial \mathbf{K}_e/\partial d_i$ is given by

$$\begin{aligned}\frac{\partial \mathbf{K}_e}{\partial d_i} &= \int_{\Omega_e} \frac{1}{\mu_\mathrm{r}} \left(\frac{\partial \mathbf{B}^\mathrm{T}\mathbf{B}}{\partial d_i} + \mathbf{B}^\mathrm{T}\mathbf{B}\nabla \cdot \mathbf{V}_i \right) \mathrm{d}\mathbf{r} \\ &\quad - k_0^2 \int_{\Omega_e} \epsilon_\mathrm{r} \left(\frac{\partial \mathbf{N}^\mathrm{T}\mathbf{N}}{\partial d_i} + \mathbf{N}^\mathrm{T}\mathbf{N}\nabla \cdot \mathbf{V}_i \right) \mathrm{d}\mathbf{r} \\ &= \int_{\Omega_e} \frac{1}{\mu_\mathrm{r}} \left(\mathbf{B}^\mathrm{T}\frac{\partial \mathbf{B}}{\partial d_i} + \frac{\partial \mathbf{B}^\mathrm{T}}{\partial d_i}\mathbf{B} + \mathbf{B}^\mathrm{T}\mathbf{B}\nabla \cdot \mathbf{V}_i \right) \mathrm{d}\mathbf{r} \\ &\quad - k_0^2 \int_{\Omega_e} \epsilon_\mathrm{r} \left(\mathbf{N}^\mathrm{T}\frac{\partial \mathbf{N}}{\partial d_i} + \frac{\partial \mathbf{N}^\mathrm{T}}{\partial d_i}\mathbf{N} + \mathbf{N}^\mathrm{T}\mathbf{N}\nabla \cdot \mathbf{V}_i \right) \mathrm{d}\mathbf{r},\end{aligned} \tag{4.22}$$

with the *design velocity field* $\mathbf{V}_i$ defined as

$$\mathbf{V}_i = \frac{\partial \mathbf{X}}{\partial d_i} = \mathbf{N}_\mathrm{c}\frac{\partial \mathbf{X}_\mathrm{c}}{\partial d_i}. \tag{4.23}$$

In (4.23), $\mathbf{X}_\mathrm{c}$ is the vertex coordinate vector of a child element, as illustrated in Fig. 4.3, which shows the isoparametric mappings for evaluating the basis functions over the the second child element. It is worth mentioning that the line integral term in $\mathbf{K}_e$ does not contribute in the derivation of (4.22) since the outmost boundary of the computational domain is fixed. Moreover, we utilize

$$\frac{\partial \mu_\mathrm{r}^{-1}}{\partial d_i} = 0 \text{ and } \frac{\partial \epsilon_\mathrm{r}}{\partial d_i} = 0 \tag{4.24}$$

to further simplify (4.22) since material properties do not change with d_i at integration points. For an enriched element, the derivatives of basis functions with respect to the design parameters are expressed as

$$\frac{\partial \mathbf{N}}{\partial d_i} = \begin{bmatrix} \frac{\partial \mathbf{N}_\mathrm{p}}{\partial d_i} & \frac{\partial \mathbf{N}_\mathrm{c}}{\partial d_i} \end{bmatrix}, \tag{4.25}$$

where

$$\begin{aligned}\frac{\partial \mathbf{N}_\mathrm{p}}{\partial d_i} &= \frac{\partial \mathbf{r}_\mathrm{p}}{\partial d_i}\frac{\partial \mathbf{N}_\mathrm{p}}{\partial \mathbf{r}_\mathrm{p}} \\ &= \frac{\partial \mathbf{X}}{\partial d_i}\frac{\partial \mathbf{r}_\mathrm{p}}{\partial \mathbf{X}}\frac{\partial \mathbf{N}_\mathrm{p}}{\partial \mathbf{r}_\mathrm{p}} \\ &= \mathbf{V}_i\mathbf{J}_\mathrm{p}^{-1}\frac{\partial \mathbf{N}_\mathrm{p}}{\partial \mathbf{r}_\mathrm{p}} \\ &= \mathbf{V}_i\mathbf{B}_\mathrm{p}\end{aligned} \tag{4.26}$$

and

$$\frac{\partial \mathbf{N}_\mathrm{c}}{\partial d_i} = 0. \tag{4.27}$$

In the derivation of (4.26), $\mathbf{r}_\mathrm{p}$ is the coordinate vector in the master parent element and $\mathbf{J}_\mathrm{p}$ is the Jacobian matrix of the parent element. Since the basis function vector $\mathbf{N}_\mathrm{c}$ is evaluated on the quadrature points of the child master element, which does not change with the design parameters, (4.27) is zero. Similarly, the derivatives of the gradient of basis functions with respect to the design parameters are expressed as

$$\frac{\partial \mathbf{B}}{\partial d_i} = \begin{bmatrix} \frac{\partial \mathbf{B}_\mathrm{p}}{\partial d_i} & \frac{\partial \mathbf{B}_\mathrm{c}}{\partial d_i} \end{bmatrix}, \tag{4.28}$$

where

$$\frac{\partial \mathbf{B}_\mathrm{p}}{\partial d_i} = 0 \tag{4.29}$$

and

$$\begin{aligned} \frac{\partial \mathbf{B}_\mathrm{c}}{\partial d_i} &= \frac{\partial \mathbf{J}_\mathrm{c}^{-1}}{\partial d_i}\frac{\partial \mathbf{N}_\mathrm{c}}{\partial \mathbf{r}_\mathrm{c}} \\ &= -\mathbf{J}_\mathrm{c}^{-1}\frac{\partial \mathbf{J}_\mathrm{c}}{\partial d_i}\mathbf{J}_\mathrm{c}^{-1}\frac{\partial \mathbf{N}_\mathrm{c}}{\partial \mathbf{r}_\mathrm{c}} \\ &= -\mathbf{J}_\mathrm{c}^{-1}\frac{\partial \mathbf{N}_\mathrm{c}}{\partial \mathbf{r}_\mathrm{c}}\frac{\partial \mathbf{X}_\mathrm{c}}{\partial d_i}\mathbf{J}_\mathrm{c}^{-1}\frac{\partial \mathbf{N}_\mathrm{c}}{\partial \mathbf{r}_\mathrm{c}} \\ &= -\mathbf{B}_\mathrm{c}\frac{\partial \mathbf{X}_\mathrm{c}}{\partial d_i}\mathbf{B}_\mathrm{c}. \end{aligned} \tag{4.30}$$

Because $\mathbf{B}_\mathrm{p}$ is a constant for a linear triangle element, (4.29) vanishes. In the derivation of (4.30), $\mathbf{r}_\mathrm{c}$ is the coordinate vector of quadrature points in the master child element and $\mathbf{J}_\mathrm{c}$ is the Jacobian matrix of the child element.

Now it remains to calculate the velocity of the enriched nodes ($\partial \mathbf{X}_\mathrm{c}/\partial d_i$) in order to perform an analytical sensitivity analysis. Assume a material interface, described by

$$y_0 = S(x_0, \mathbf{d}), \tag{4.31}$$

intersects an finite-element edge, described by

$$y_0 = a x_0 + b, \tag{4.32}$$

at $\mathbf{X}_0 = (x_0, y_0)$. The velocity of the enriched node is expressed as

$$\frac{\partial \mathbf{X}_\mathrm{c}}{\partial d_i} = \frac{\partial S/\partial d_i}{a - \partial S/\partial x} \begin{bmatrix} 1 & a \end{bmatrix}^\mathrm{T}. \tag{4.33}$$

Once the sensitivity of the objective and constraint functions are evaluated, the design variables can be updated through an optimizer, for instance, MATLAB's *fmincon* function, which provides increments opposite the gradient directions.

4.4 Numerical Results

In this section, we present three numerical examples to verify and demonstrate the efficiency of the gradient-based shape optimization using IGFEM.

4.4.1 Echo Width of a Dielectric Cylinder

To verify the proposed scheme, we consider a simple problem, which is to optimize the radius of a dielectric cylinder to achieve the desired echo width (σ_2D). As shown in Fig. 4.4, the cylinder, with a radius a and $\epsilon_\mathrm{r} = 4$, is placed at the center of a computational domain of $4\lambda_0 \times 4\lambda_0$ and illuminated by a uniform plane wave, where λ_0 is the free-space wave length. The computational domain is discretized into 58,896 triangles without considering the geometry of the cylinder. The IGFEM-calculated σ_2D is compared with the analytical solution in Fig. 4.5, showing a good agreement. The objective function defined as

$$g = -\sigma_\mathrm{2D}/\lambda_0, \tag{4.34}$$

is adopted to optimize a with a bound $a \in [0.65, 0.8]\lambda_0$. Figure 4.6 depicts the convergence history of the proposed method with a starting from $0.65\lambda_0$. Apparently, the proposed method converges in less than 10 iterations with the optimal $a = 0.738\lambda_0$, which gives the minimum of the objective function, i.e., the largest σ_2D of $5.98\lambda_0$.

4.4.2 Transmission from a Composite with Elliptical Inclusions

In this example, the objective is to minimize the transmission coefficient of a composite material that is periodic in the x-direction. The unit cell, as illustrated in Fig. 4.7, has a square region of $6.5\lambda_0 \times 6.5\lambda_0$, with four embedded elliptical inclusions whose major and minor axes are respectively $0.6\lambda_0$ and $0.3\lambda_0$. The entire computational domain is discretized into 160,714 triangular elements, without considering the presence of the four elliptical inclusions. The relative permittivities for the background matrix and inclusions are $2.0 - \mathrm{j}0.001$ and $3.4 - \mathrm{j}1.0$, respectively. The incident plane wave propagates in the negative y-direction from the top of the composite material. The design parameters for the ith inclusion are its orientation θ_i and center coordinates (x_i, y_i). The bounds for the design parameters are

$$0 \leq \theta_i \leq \pi, \; 0.5\lambda_0 \leq x_i \leq 5.6\lambda_0, \text{ and } 0.5\lambda_0 \leq y_i \leq 5.6\lambda_0. \tag{4.35}$$

To avoid inclusions overlapping with each other, six constraints are applied to the center coordinates of the inclusions

$$d_{ij} = \sqrt{(x_i - x_j)^2 + (y_i - y_j)^2} \geq 1.3\lambda_0 \text{ for } i \neq j. \tag{4.36}$$

The initial design, with the four elliptical inclusions intentionally positioned horizontally at the bottom of the unit cell to produce a very large transmission, is shown in Fig. 4.8a. During the optimization process, the inclusions gradually rotate themselves to the vertical direction and spread vertically to enhance the absorption of electromagnetic waves, as depicted in Figs. 4.8a–f. It is also obvious that the optimizer is eventually stuck into a local minimum since the bottom two inclusions did not split apart in the vertical direction. The convergence history of the objective function with respect to iteration for the first trial is given in Fig. 4.9, which shows a fast convergence rate for the first 13 iterations followed by trapping into a local minimum.

Since the gradient-based shape optimization does not guarantee convergence to the global optimum, it is necessary to try several initial guesses. Figure 4.10 shows the convergence history with nine different initial guesses. As expected, different initial guesses converge to their own local minimum.

Figure 4.11 plots three different initial guesses and their corresponding final designs to demonstrate shape changes in the optimization process.

4.4.3 S-Parameter of a Waveguide Filter with Dielectric Posts

The last example in this chapter is motivated by the broad applications of dielectric materials in the microwave communication systems. Because of their low-loss, temperature-stable, and high-permittivity characteristics, dielectric materials are critical to the miniaturization of satellite and broadcasting equipment, and to many other wireless systems [118–121]. Figure 4.2 shows an H-plane evanescent mode filter with circular dielectric resonators ($\epsilon_\mathrm{r} = 24$) designed to have a pass-band centered at 11 GHz with 300 MHz bandwidth and return losses greater than 23 dB [121]. To achieve these specifications, one of the possible designs was given by [121], with $a = 19.05$ mm, $W = 8$ mm, $R_1 = 0.777$ mm, $R_2 = 2.169$ mm, $L_1 = 2.4179$ mm, $L_2 = 10.182$ mm, and $L_3 = 10.9919$ mm. In this example, we offset the locations and radii of the posts in the reference design by certain values to test if the proposed method can still converge to the original design. Because of the symmetry in the x- and y-directions, only four design parameters need to be considered, i.e., the y coordinates (y_1, y_2) and radii (R_1, R_2) of the first two dielectric posts. Letting

$$\mathbf{V}^* = [y_1^*, y_2^*, R_1^*, R_2^*] \tag{4.37}$$

be the reference design variable vector, we choose

$$\mathbf{V}_0 = \mathbf{V}^* - [0.05, 0.05, 0.05, 0.05] \tag{4.38}$$

as the initial guess and

$$[-0.1, -0.1, -0.1, -0.1] \leq \mathbf{V}_0 - \mathbf{V}^* \leq [0.1, 0.1, 0.1, 0.1] \tag{4.39}$$

as the bounds for the design variables. The objective is to minimize the root-mean-square error (RSME) between the calculated S_{11} and reference S_{11}^*, where the RSME is given by

$$\mathrm{RSME} = \sqrt{\frac{1}{N}\sum_{n=1}^{N}\left(S_{11} - S_{11}^*\right)^2} \tag{4.40}$$

with N representing the number of frequency sampling points.

The entire computational domain, without considering the four dielectric posts, is discretized into 451,192 triangles. The convergence histories of the objective function and design parameters are plotted in Fig. 4.12, which only need 16 iterations to converge to the reference design. The detailed evolution of S_{11} during the optimization process is depicted in Fig. 4.13, showing more information about how the calculated S_{11} approaches the reference S_{11}^{*}.

To further demonstrate the effectiveness of the proposed optimizer, we choose another initial guess

$$\mathbf{V}_0 = \mathbf{V}^{*} + [0.05, 0.05, 0.05, 0.05], \tag{4.41}$$

with the rest of the settings unchanged. The convergence histories and evolution of S_{11} for the new initial guess are plotted in Figs. 4.14 and 4.15, respectively. As expected, the design parameters quickly converge to the reference values.

It is worth mentioning that, like all the other gradient-based shape optimization methods, the proposed method also requires the initial guess to be close enough to the optima to converge to the desired values. For problems with multiple local minima and large searching ranges, it is more practical to adopt evolutionary algorithms to roughly estimate several initial guesses and then utilize the proposed method to accelerate the convergence to the global minimum. Alternatively, one can subdivide the large searching range and apply the proposed optimizer to the smaller ranges to increase the possibility of finding the optimal design parameters.

4.5 Summary

A gradient-based shape optimization scheme combined with the IGFEM is proposed to efficiently optimize electromagnetic problems. To avoid mesh distortion and the expensive process of repeatedly creating a conformal mesh for each design configuration, the problem geometry is projected onto a fixed background mesh that is not necessarily conformal to the geometry. The IGFEM, with an enriched solution space in nonconformal elements, is adopted for an accurate electromagnetic simulation. An analytical sensitivity analysis is presented to compute the derivatives of the objective and constraint functions. Because of the fixed background mesh, the *design velocity field* term in the sensitivity analysis is evaluated only at the geometry interfaces, and the efficiency of this method is significantly enhanced. Three numerical examples are presented to verify the proposed method and to demonstrate its efficiency.

4.6 Figures

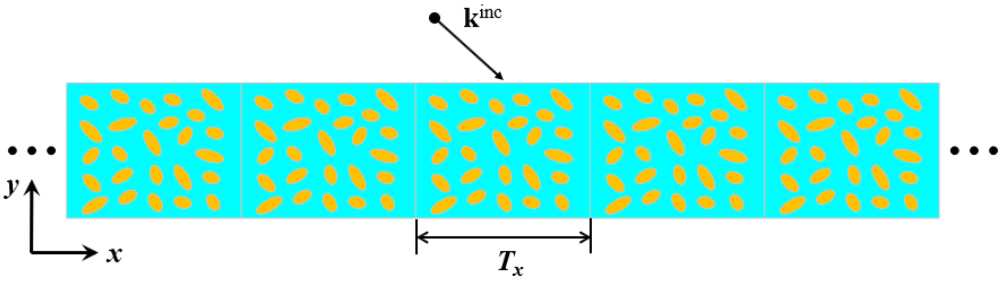

Figure 4.1: One-dimensional periodic structure.

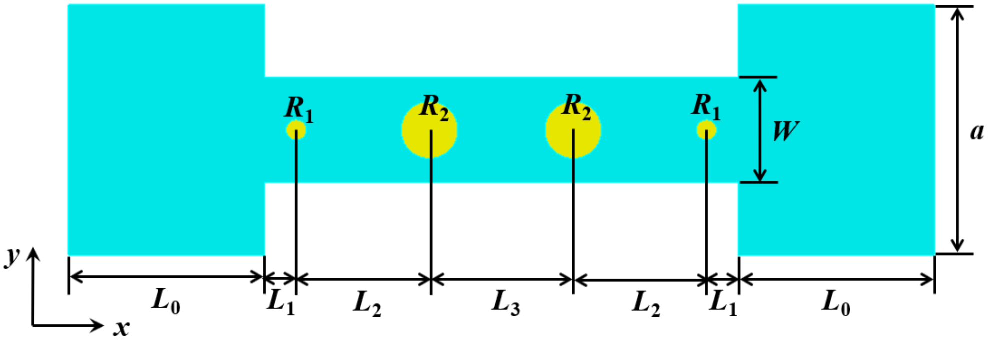

Figure 4.2: A waveguide filter with dielectric posts.

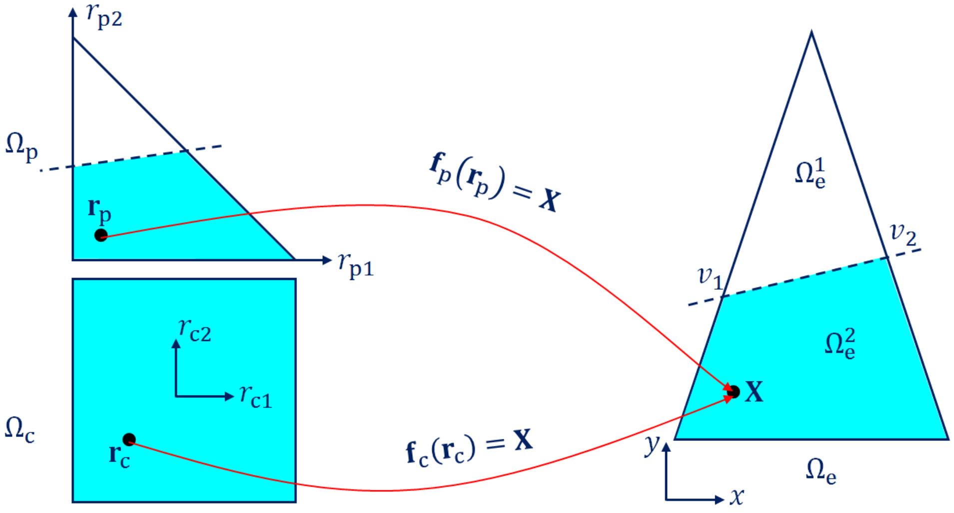

Figure 4.3: Mappings used to evaluate the bases at an integration point $\mathbf{X}$. $\mathbf{f}_{\text{c}}(\mathbf{r}_{\text{c}})$ maps the master element Ω_{c} to the integration element Ω_{e}^2, and $\mathbf{f}_{\text{p}}(\mathbf{r}_{\text{p}})$ maps the master element Ω_{p} to the physical element Ω_{e}.

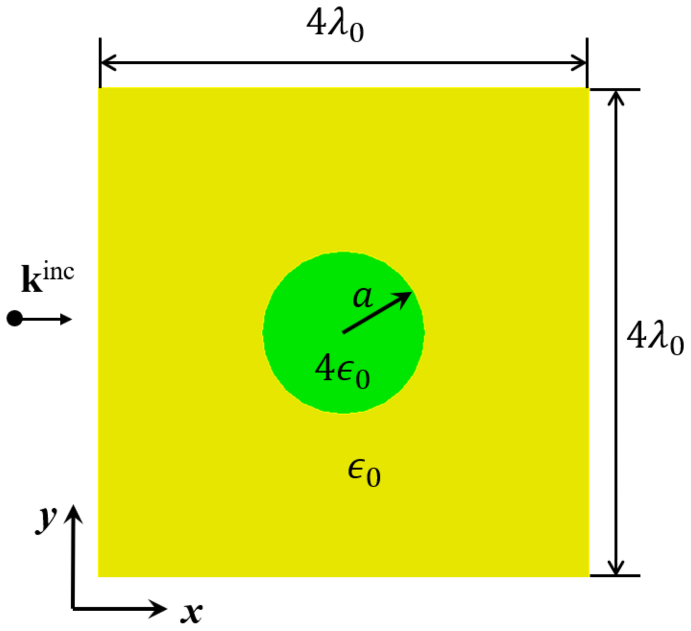

Figure 4.4: Scattering analysis of a dielectric cylinder in the free space.

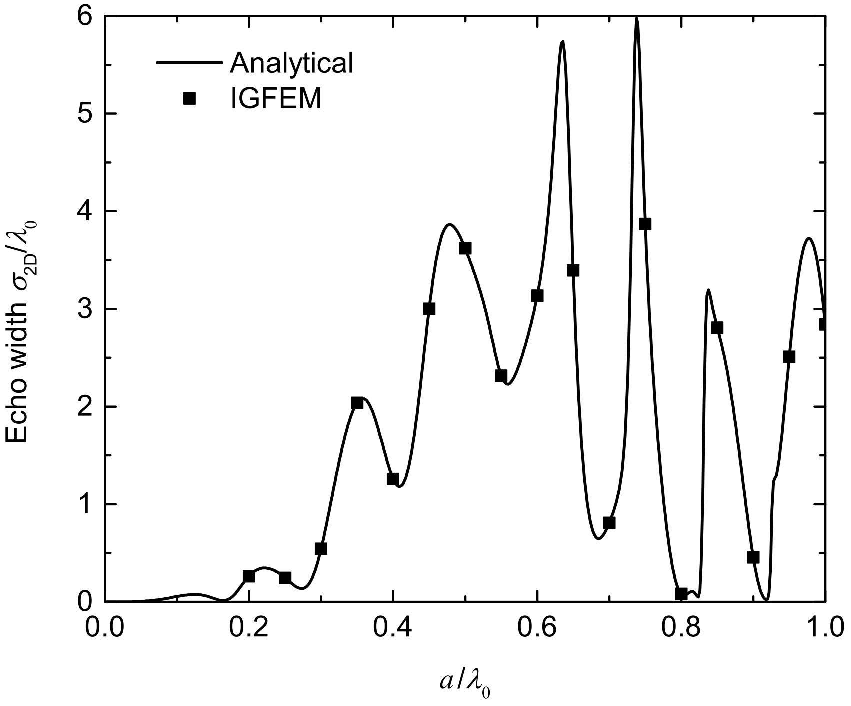

Figure 4.5: Echo width of a dielectric cylinder versus its normalized radius.

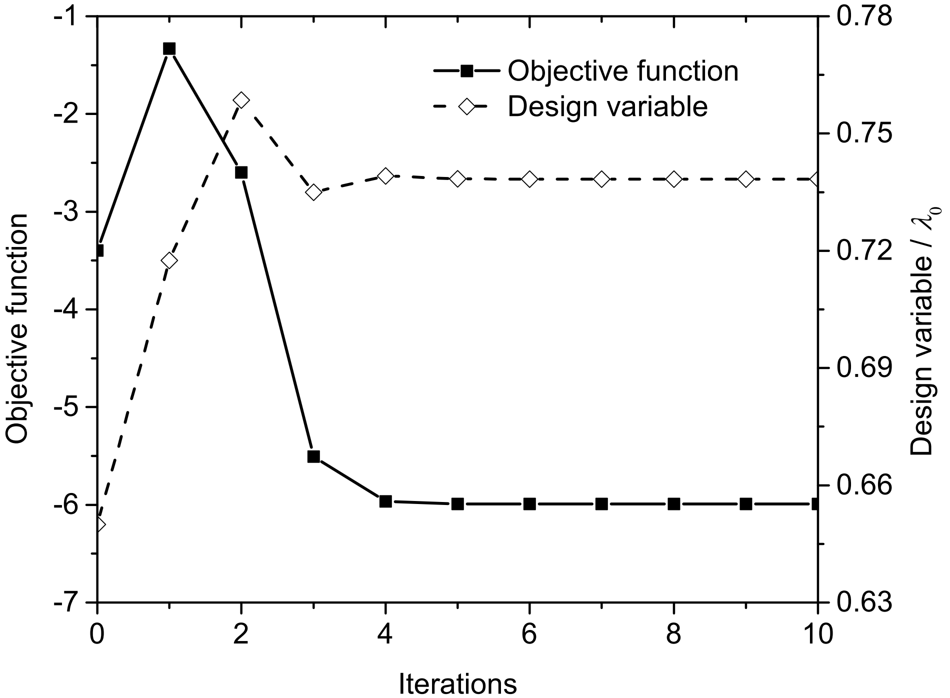

Figure 4.6: Convergence history of the objective function and design variable for the dielectric cylinder optimization problem.

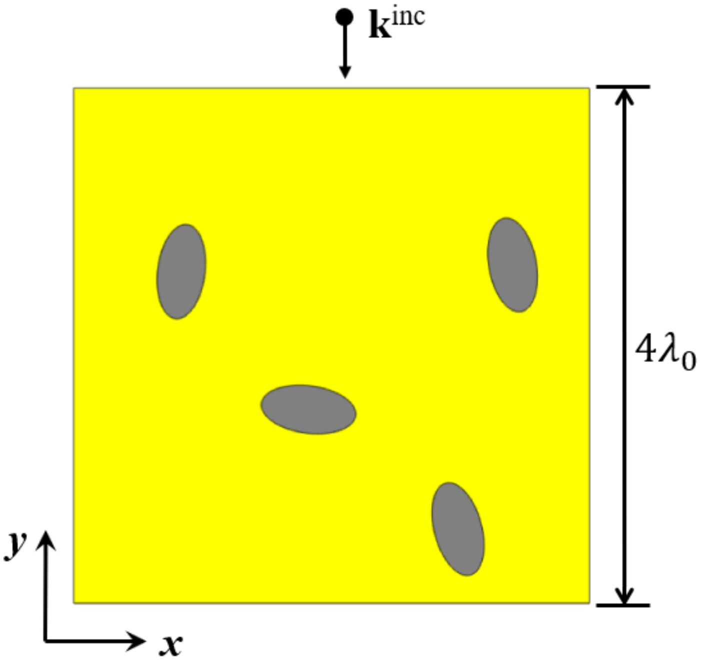

Figure 4.7: A composite unit cell with four elliptical inclusions illuminated by a uniform plane wave from the top.

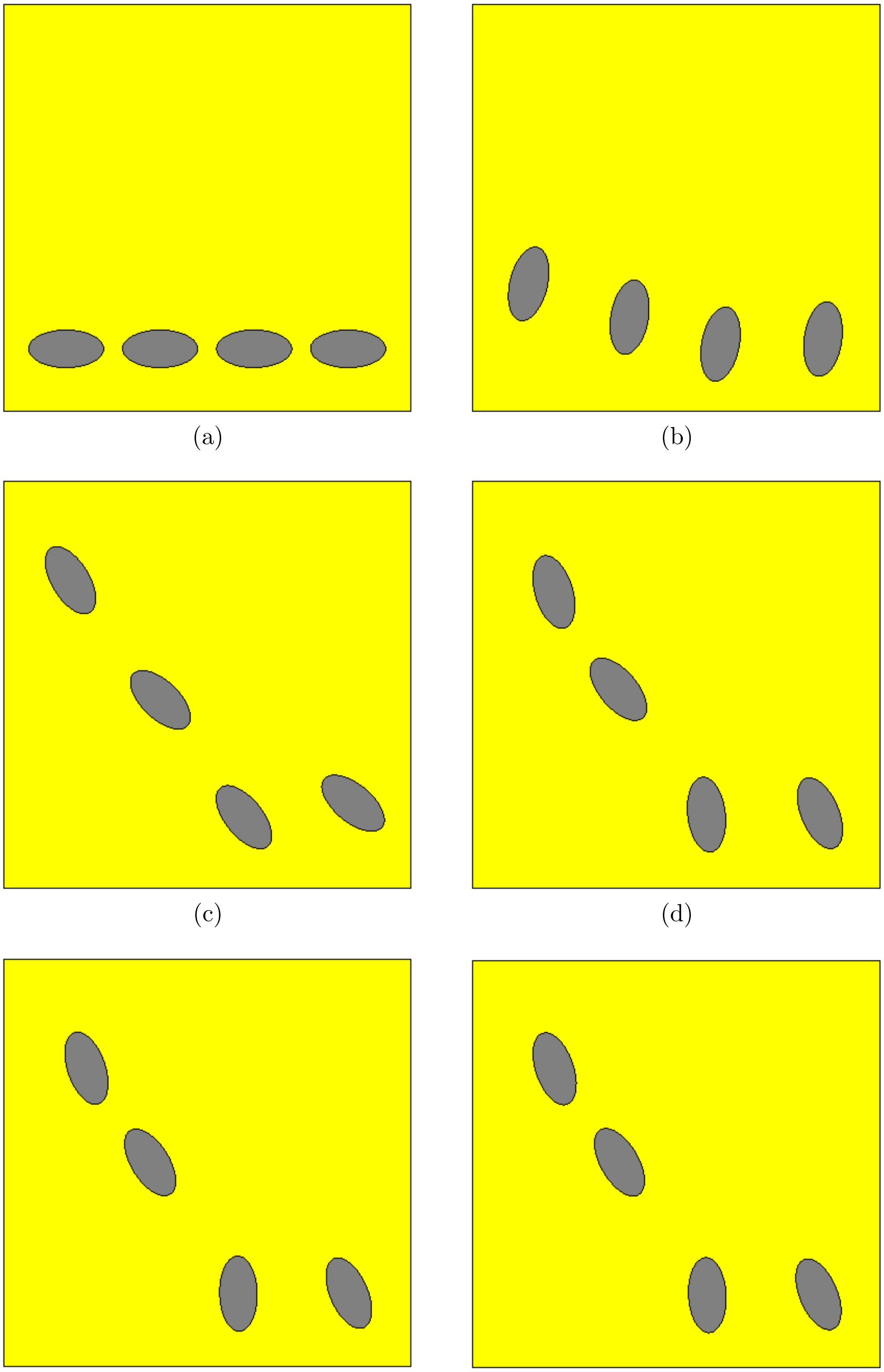
(a) (b) (c) (d) (e) (f)

Figure 4.8: Geometry changes with iterations for the first trial. (a) Iteration 0. (b) Iteration 5. (c) Iteration 10. (d) Iteration 25. (e) Iteration 40. (f) Iteration 53.

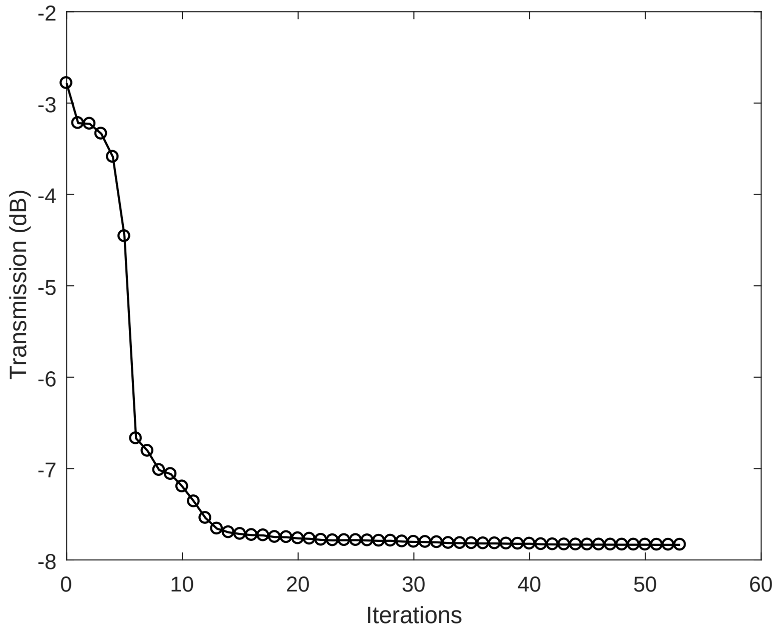

Figure 4.9: Convergence history for the composite unit cell during the first try.

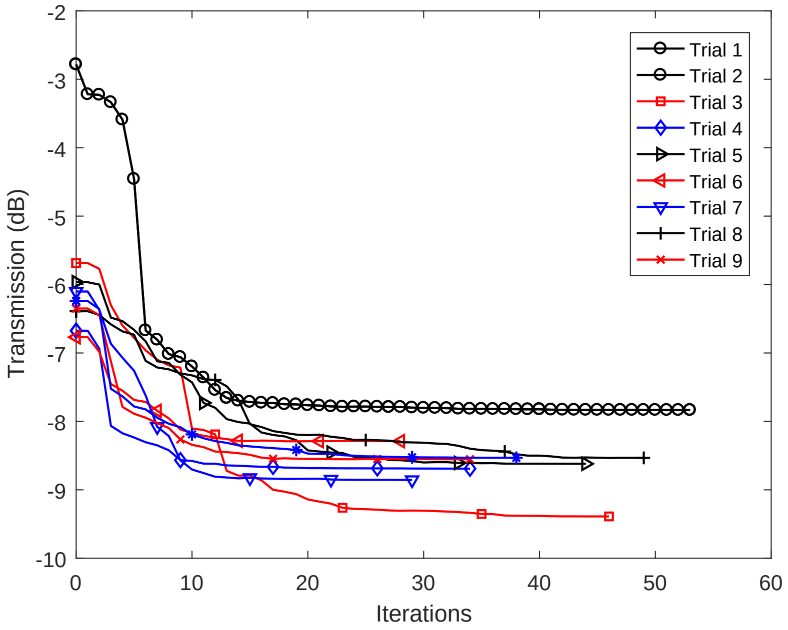

Figure 4.10: Convergence histories for the composite unit cell with nine tries.

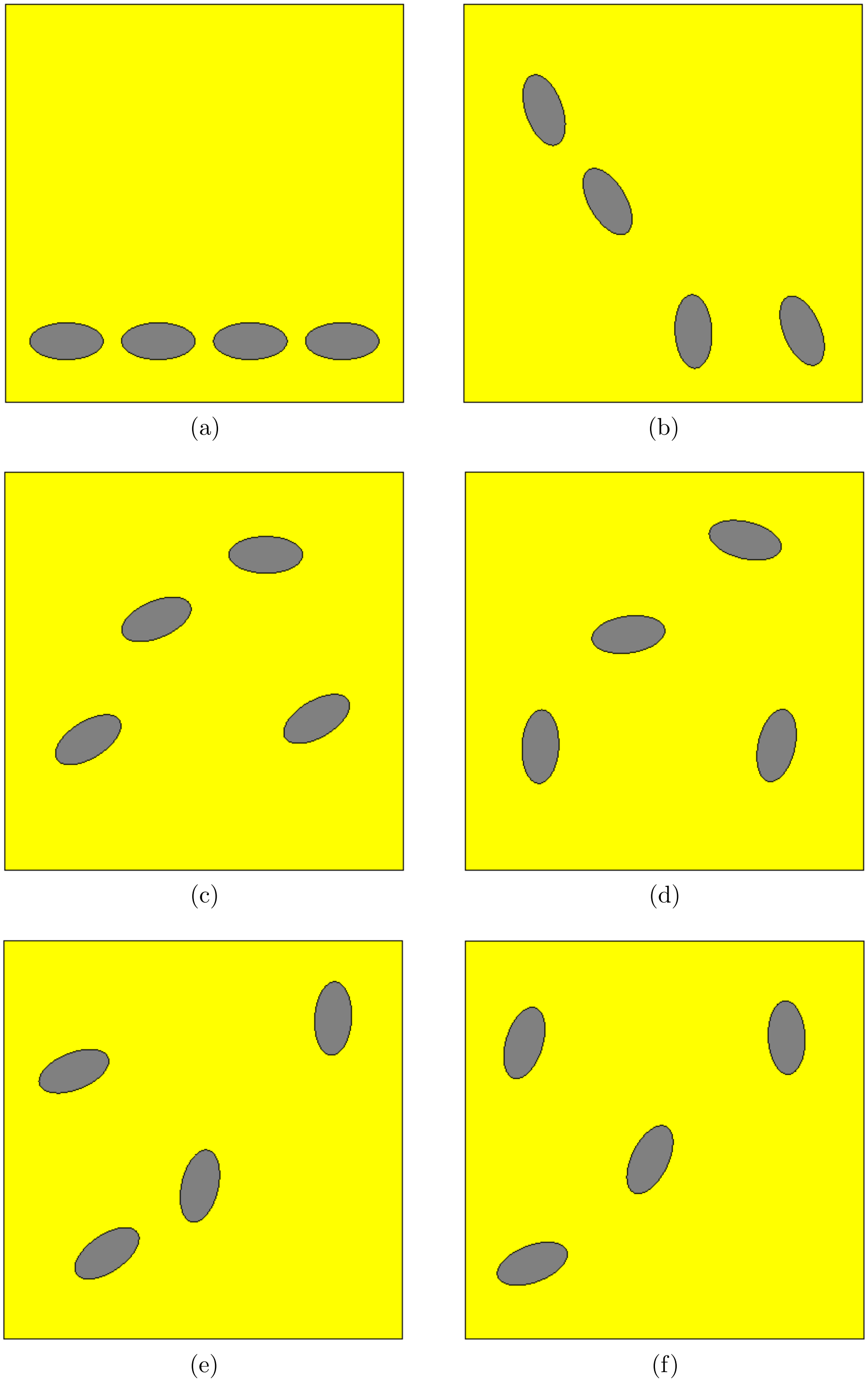
(a) (b) (c) (d) (e) (f)

Figure 4.11: Initial guesses and final designs for different trials. (a) Trial 1 initial guess. (b) Trial 1 final design. (c) Trial 5 initial guess. (d) Trial 5 final design. (e) Trial 9 initial guess. (f) Trial 9 final design.

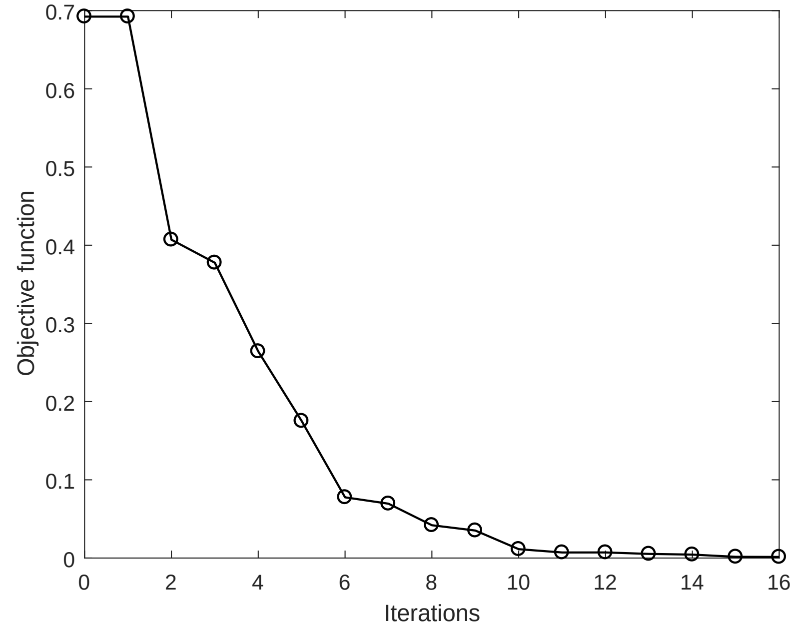

(a)

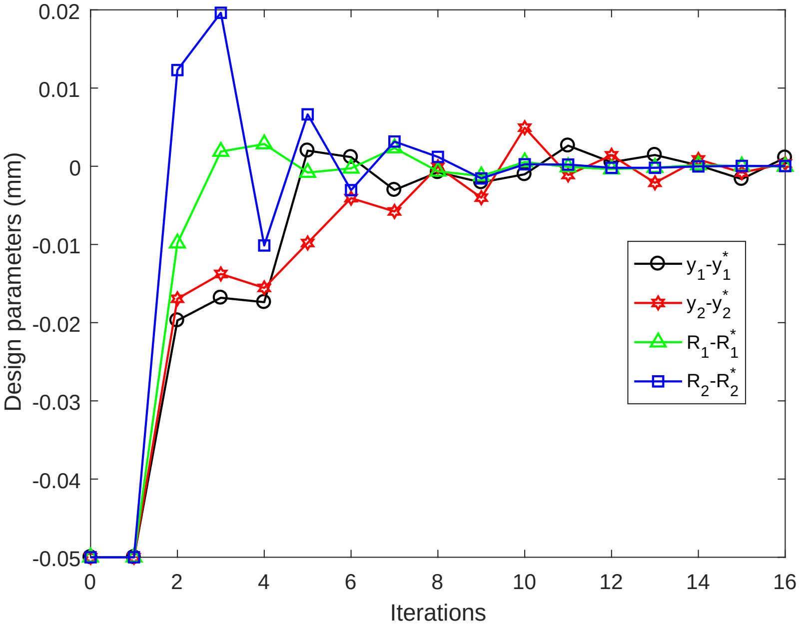

(b)

Figure 4.12: Convergence histories for the optimization of the waveguide filter with four dielectric posts using $\mathbf{V}_0 = \mathbf{V}^* - [0.05, 0.05, 0.05, 0.05]$ as the initial guess. (a) Objective function. (b) Design parameters.

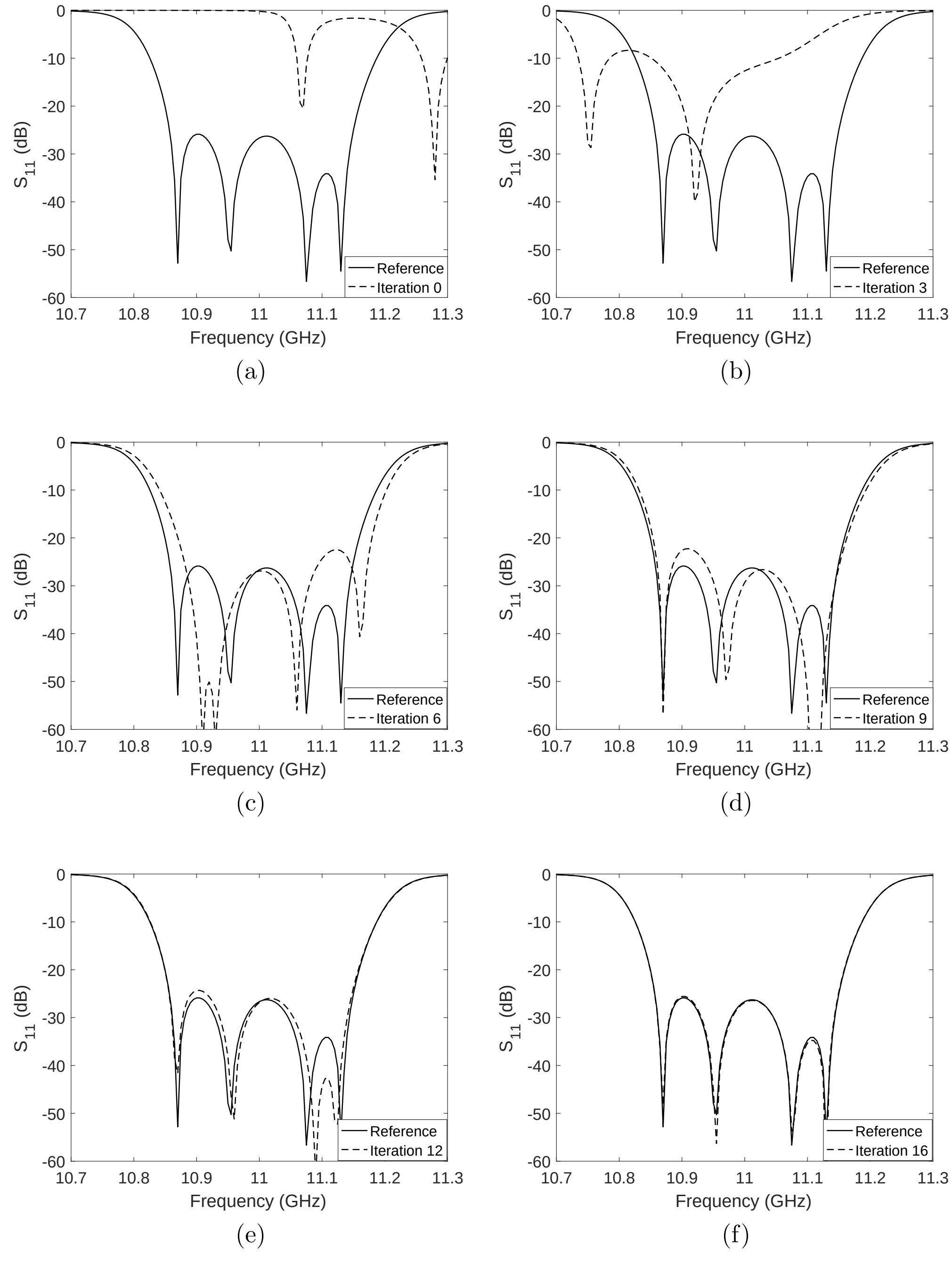

Figure 4.13: Evolution of S_{11} for the waveguide filter with four dielectric posts using $\mathbf{V}_0 = \mathbf{V}^* - [0.05, 0.05, 0.05, 0.05]$ as the initial guess. (a) Iteration 0. (b) Iteration 3. (c) Iteration 6. (d) Iteration 9. (e) Iteration 12. (f) Iteration 16.

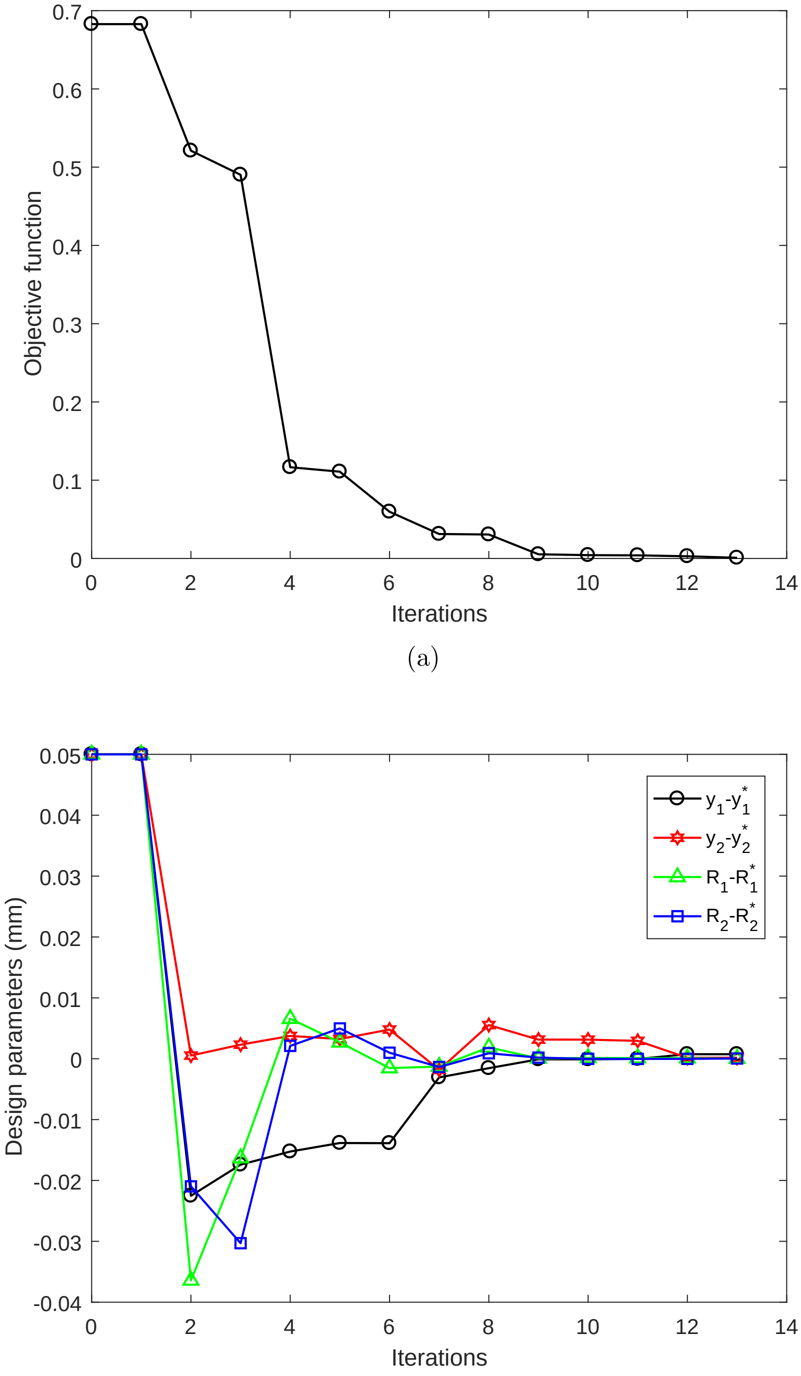

(a)

(b)

Figure 4.14: Convergence histories for the optimization of the waveguide filter with four dielectric posts using $\mathbf{V}_0 = \mathbf{V}^* + [0.05, 0.05, 0.05, 0.05]$ as the initial guess. (a) Objective function. (b) Design parameters.

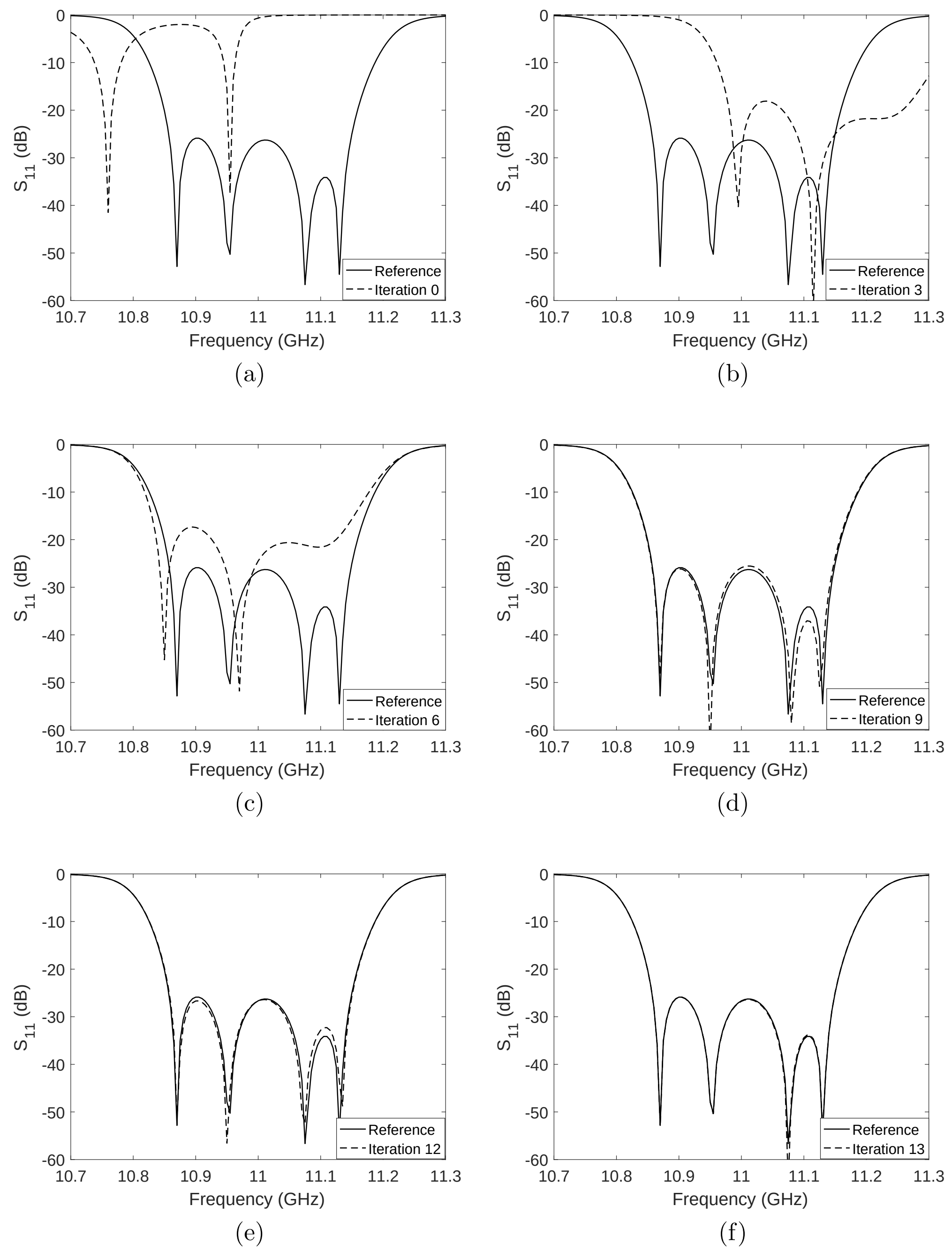

(a) (b) (c) (d) (e) (f)

Figure 4.15: Evolution of S_{11} for the waveguide filter with four dielectric posts using $\mathbf{V}_0 = \mathbf{V}^* + [0.05, 0.05, 0.05, 0.05]$ as the initial guess. (a) Iteration 0. (b) Iteration 3. (c) Iteration 6. (d) Iteration 9. (e) Iteration 12. (f) Iteration 13.

Chapter 5

Parallel FETI-DP Alogrithm for Large-Scale Electromagnetic Analysis

5.1 Introduction

Modern engineering applications, such as for phased-antenna array analysis, radar signature prediction of electrically large objects, and full-wave synthesis of on-board circuit design, tend to produce a linear system with millions or even billions of unknowns after a volumetric discretization, which is very challenging for the FEM to solve. The domain decomposition-based FETI-DP algorithm has been therefore developed to enable large-scale electromagnetic simulations [22, 23].

The FETI-DP algorithm divides an entire computational domain into many non-overlapping subdomains and enforces Robin transmission conditions at the subdomain interfaces to form an equivalent order-reduced interface problem. To accelerate the iterative convergence of the interface problem, a global coarse system, which relates only primal unknowns at the corner edges of the subdomain interfaces, is constructed and solved as a preconditioner for the interface problem. Due the complexity of the FETI-DP algorithm and the large difference between the sizes of the interface and the global coarse problems, the parallel efficiency of the previous parallel FETI-DP implementation is limited with an increasing number of computation nodes, especially when a large global coarse system is involved [23].

In this chapter, we present an efficient parallelization of the FETI-DP algorithm for large-scale electromagnetic simulations. The proposed parallelization strategy has an excellent load balance with minimized subdomain interfaces. We parallelize the solution of the interface problem by using the generalized minimal residual (GMRES) method [103] to achieve a fast convergence rate. In the GMRES method, we adopt the iterative classical Gram-Schmidt (ICGS) algorithm with a selective reorthogonalization scheme to generate the Krylov subspace so that the orthogonality of the computed basis is preserved and the issue associated with the global communication involved in orthogonalization is alleviated [122]. For the solution of the global coarse problem, we adopt another Krylov subspace method, which is a communication-avoiding biconjugate gradient stabilized (CA-BICGSTAB) method [123], to efficiently parallelize the computation and minimize the global communication overhead for explicitly forming the coarse system and updating coarse problem solutions. Based on the highly sparse pattern of the global coarse system, we further develop a sparse preconditioner to improve the convergence rate of the iterative solution. Finally, we present numerical examples to demonstrate the accuracy, scalability, and capability of our new parallel implementation of the FETI-DP algorithm by simulating the radar signature of a lossless dielectric sphere and a PEC airplane and analyzing the radiation pattern of a large Vivaldi antenna array.

5.2 FETI-DP Formulation

The BVP to be considered is governed by the vector wave equation with the first-order ABC. The ABC is employed here for the sake of simplicity, and other types of boundary conditions, such as PEC, PMC, and wave port boundary conditions [81], can be easily incorporated as well. With domain decomposition, the computational domain V is decomposed into many subdomains V^s $(s = 1, 2, \ldots, N_\mathrm{s})$, whose surfaces are denoted as S^s. For each S^s, the portion that interfaces with neighboring subdomains is denoted as Γ^s. To make the subdomain interfaces as transparent as possible for the electric field, we enforce the second-order transverse-electric transmission condition (SOTC-TE) at subdomain interfaces [25, 26, 28, 29]:

$$\hat{n}^s \times \left(\frac{1}{\mu_\mathrm{r}}\nabla \times \mathbf{E}^s\right) + \alpha^s \hat{n}^s \times (\hat{n}^s \times \mathbf{E}^s) - \beta^s \nabla \times [\hat{n}^s (\nabla \times \mathbf{E}^s)_n] = \mathbf{\Lambda}^s \quad \text{on}\, \Gamma^s. \tag{5.1}$$

The parameter α^s is set as $\alpha^s = \mathrm{j}k_0\sqrt{\epsilon_\mathrm{r}^{sq}\mu_\mathrm{r}^{sq}}$ for the interface between the sth and qth subdomains, where ϵ_r^{sq} and μ_r^{sq} are respectively the average relative permittivity and permeability given by $\epsilon_\mathrm{r}^{sq} = (\epsilon_\mathrm{r}^{s}+\epsilon_\mathrm{r}^{q})/2$ and $\mu_\mathrm{r}^{sq} = (\mu_\mathrm{r}^{s}+\mu_\mathrm{r}^{q})/2$. The parameter β^s can be determined based on the smallest mesh size and the order of basis functions employed on the subdomain interfaces to account for all the evanescent modes supported by the interface mesh. More specifically, $\beta^s = -\mathrm{j}/(k_0\sqrt{\epsilon_\mathrm{r}^{sq}\mu_\mathrm{r}^{sq}}+\tilde{k})$, $\tilde{k} = -\mathrm{j}\sqrt{k_\mathrm{max}^2 - k_0^2\epsilon_\mathrm{r}^{sq}\mu_\mathrm{r}^{sq}}$, and $k_\mathrm{max} = \pi/h_\mathrm{min}$, where h_min denotes the smallest mesh size on the subdomain interface [25, 26, 28].

With the BVP defined above, the finite element discretization of the subdomain V^s yields the matrix equation

$$\begin{bmatrix} K_\mathrm{ii}^s & K_\mathrm{ib}^s & K_\mathrm{ic}^s \\ K_\mathrm{bi}^s & K_\mathrm{bb}^s + M_\mathrm{bb}^s & K_\mathrm{bc}^s \\ K_\mathrm{ci}^s & K_\mathrm{cb}^s & K_\mathrm{cc}^s \end{bmatrix} \begin{Bmatrix} E_\mathrm{i}^s \\ E_\mathrm{b}^s \\ E_\mathrm{c}^s \end{Bmatrix} = \begin{Bmatrix} f_\mathrm{i}^s \\ f_\mathrm{b}^s \\ f_\mathrm{c}^s \end{Bmatrix} - \begin{Bmatrix} 0 \\ \lambda_\mathrm{b}^s + M_\mathrm{bc}^s E_\mathrm{c}^s \\ \lambda_\mathrm{c}^s \end{Bmatrix}, \tag{5.2}$$

where the finite element submatrices and subvectors are defined as

$$\begin{aligned}
[K_\mathrm{uv}^s] =& \int_{V^s} \left[\frac{1}{\mu_\mathrm{r}}\{\nabla \times \mathbf{N}_\mathrm{u}^s\} \cdot \{\nabla \times \mathbf{N}_\mathrm{v}^s\}^\mathrm{T} - k_0^2\epsilon_\mathrm{r}\{\mathbf{N}_\mathrm{u}^s\} \cdot \{\mathbf{N}_\mathrm{v}^s\}^\mathrm{T}\right] \mathrm{d}V \\
&+ \mathrm{j}k_0 \int_{S^s \cap S_\mathrm{o}} \{\hat{n}^s \times \mathbf{N}_\mathrm{u}^s\} \cdot \{\hat{n}^s \times \mathbf{N}_\mathrm{v}^s\}^\mathrm{T} \mathrm{d}S, \\
[M_\mathrm{bv}^s] =& \int_{\Gamma^s} \left[\alpha^s\{\hat{n}^s \times \mathbf{N}_\mathrm{b}^s\} \cdot \{\hat{n}^s \times \mathbf{N}_\mathrm{v}^s\}^\mathrm{T} + \beta^s\{\nabla \times \mathbf{N}_\mathrm{b}^s\}_n \cdot \{\nabla \times \mathbf{N}_\mathrm{v}^s\}_n^\mathrm{T}\right] \mathrm{d}S, \\
\{f_\mathrm{u}^s\} =& -\mathrm{j}k_0 \int_{S^s \cap S_\mathrm{o}} \{\hat{n} \times \mathbf{N}_\mathrm{u}^s\} \cdot \left(\eta_0 \mathbf{H}^\mathrm{inc} - \hat{n} \times \mathbf{E}^\mathrm{inc}\right) \mathrm{d}S, \\
\{\lambda_\mathrm{b}^s\} =& \int_{\Gamma^s} \{\mathbf{N}_\mathrm{b}^s\} \cdot \mathbf{\Lambda}^s \mathrm{d}S, \\
\{\lambda_\mathrm{c}^s\} =& \mathrm{j}k_0\eta_0 \int_{\Gamma^s} \{\hat{n}^s \times \mathbf{N}_\mathrm{c}^s\} \cdot \mathbf{H} \mathrm{d}S.
\end{aligned} \tag{5.3}$$

In (5.3), both of the subscripts u and v can be i, b, and c. We adopt the i, b, and c notations to represent the interior unknowns which are not associated with any subdomain interfaces, the interface unknowns which are associated with interfaces that are shared by two subdomains, and the corner unknowns which are associated with edges that are shared by at least three subdomains, respectively. Two sets of interface unknowns (Lagrange multipliers) are used for each interface and each subdomain maintains its own interface unknowns.

From (5.2), two equations involving the interface and corner unknowns on the subdomain interface can be obtained:

$$\begin{aligned}
\{E_\mathrm{b}^s\} &= [R_\mathrm{br}^s]\{E_\mathrm{r}^s\} \\
&= [R_\mathrm{br}^s][K_\mathrm{rr}^s]^{-1}\left(\{f_\mathrm{r}^s\} - [R_\mathrm{br}^s]^\mathrm{T}\{\lambda_\mathrm{b}^s\} - \left([K_\mathrm{rc}^s] + [R_\mathrm{br}^s]^\mathrm{T}[M_\mathrm{bc}^s]\right)\{E_\mathrm{c}^s\}\right),
\end{aligned} \tag{5.4}$$

$$\begin{aligned}&\left([K^s_{\mathrm{cc}}]-[K^s_{\mathrm{cr}}][K^s_{\mathrm{rr}}]^{-1}\left([K^s_{\mathrm{rc}}]+[R^s_{\mathrm{br}}]^{\mathrm{T}}[M^s_{\mathrm{bc}}]\right)\right)\{E^s_{\mathrm{c}}\}\\&\quad=\{f^s_{\mathrm{c}}\}-\{\lambda^s_{\mathrm{c}}\}-[K^s_{\mathrm{cr}}][K^s_{\mathrm{rr}}]^{-1}\left(\{f^s_{\mathrm{r}}\}-[B^s_{\mathrm{br}}]^{\mathrm{T}}\{\lambda^s_{\mathrm{b}}\}\right),\end{aligned}\tag{5.5}$$

where $[R^s_{\mathrm{br}}]$ is a sparse Boolean matrix to extract the interface unknowns $\{E^s_{\mathrm{b}}\}$ out of the unknowns $\{E^s_{\mathrm{r}}\}$, which is defined as $\{E^s_{\mathrm{r}}\} = \{E^s_{\mathrm{i}}\ E^s_{\mathrm{b}}\}^{\mathrm{T}}$. Other matrices and vectors are defined as

$$\begin{aligned}[K^s_{\mathrm{rr}}]&=\begin{bmatrix}K^s_{\mathrm{ii}} & K^s_{\mathrm{ib}}\\ K^s_{\mathrm{bi}} & K^s_{\mathrm{bb}}+M^s_{\mathrm{bb}}\end{bmatrix},\\ [K^s_{\mathrm{rc}}]&=\begin{bmatrix}K^s_{\mathrm{ic}}\\ K^s_{\mathrm{bc}}\end{bmatrix},\\ [K^s_{\mathrm{cr}}]&=\begin{bmatrix}K^s_{\mathrm{ci}} & K^s_{\mathrm{cb}}\end{bmatrix},\\ \{f^s_{\mathrm{r}}\}&=\begin{Bmatrix}f^s_{\mathrm{i}}\\ f^s_{\mathrm{b}}\end{Bmatrix}.\end{aligned}\tag{5.6}$$

Assembling (5.5) over all subdomains yields a global corner-related finite element system

$$[\tilde{K}_{\mathrm{cc}}]\{E_{\mathrm{c}}\}=\{\tilde{f}_{\mathrm{c}}\}+[\tilde{K}_{\mathrm{cb}}]\{\lambda_{\mathrm{b}}\},\tag{5.7}$$

where

$$\begin{aligned}\left[\tilde{K}_{\mathrm{cc}}\right]&=\sum_{s=1}^{N_{\mathrm{s}}}\left[\tilde{K}^s_{\mathrm{cc}}\right]=\sum_{s=1}^{N_{\mathrm{s}}}[B^s_{\mathrm{c}}]^{\mathrm{T}}([K^s_{\mathrm{cc}}]-[K^s_{\mathrm{cr}}][K^s_{\mathrm{rr}}]^{-1}([K^s_{\mathrm{rc}}]+[R^s_{\mathrm{br}}]^{\mathrm{T}}[M^s_{\mathrm{bc}}]))[B^s_{\mathrm{c}}],\\ [\tilde{K}_{\mathrm{cb}}]&=\sum_{s=1}^{N_{\mathrm{s}}}[\tilde{K}^s_{\mathrm{cb}}]=\sum_{s=1}^{N_{\mathrm{s}}}[B^s_{\mathrm{c}}]^{\mathrm{T}}[K^s_{\mathrm{cr}}][K^s_{\mathrm{rr}}]^{-1}[R^s_{\mathrm{br}}]^{\mathrm{T}}[Q^s],\\ \{\tilde{f}_{\mathrm{c}}\}&=\sum_{s=1}^{N_{\mathrm{s}}}\{\tilde{f}^s_{\mathrm{c}}\}=\sum_{s=1}^{N_{\mathrm{s}}}[B^s_{\mathrm{c}}]^{\mathrm{T}}(\{f^s_{\mathrm{c}}\}-[K^s_{\mathrm{cr}}][K^s_{\mathrm{rr}}]^{-1}\{f^s_{\mathrm{r}}\}).\end{aligned}\tag{5.8}$$

In (5.8), the Boolean matrix $[B^s_{\mathrm{c}}]$ is to extract the corner unknowns $\{E^s_{\mathrm{c}}\}$ in subdomain s from the global corner unknown $\{E_{\mathrm{c}}\}$, and $[Q^s]$ is a projection Boolean matrix to select the subdomain dual unknown $\{\lambda^s_{\mathrm{b}}\}$ from the global dual-unknown $\{\lambda_{\mathrm{b}}\}$. The matrix $[\tilde{K}_{\mathrm{cc}}]$ is a sparse nonsymmetric matrix representing the global corner unknown related system. Note that $\{\lambda^s_{\mathrm{c}}\}$ in all subdomains are canceled out by $\sum_{s=1}^{N_{\mathrm{s}}}[B^s_{\mathrm{c}}]^{\mathrm{T}}\{\lambda^s_{\mathrm{c}}\}=0$, after enforcing the Neumann continuity condition at the corner.

To couple the fields across the subdomain interfaces, we enforce the tangential continuity for the electric and magnetic fields in a weak sense through (5.1):

$$\mathbf{\Lambda}_{\mathrm{b}}^{s}+\mathbf{\Lambda}_{\mathrm{b}}^{q}=(\alpha^{s}+\alpha^{q})\hat{n}^{s}\times(\hat{n}^{s}\times\mathbf{E}_{\mathrm{b}}^{s})-(\beta^{s}+\beta^{q})\nabla\times[\hat{n}^{s}(\nabla\times\mathbf{E}_{\mathrm{b}}^{s})_{n}]\quad\text{on}\,\Gamma^{sq}.\tag{5.9}$$

Taking the sth subdomain as reference, we test (5.9) with $\{\mathbf{N}_{\mathrm{b}}^{s}\}$ and integrate over Γ^{sq} to obtain

$$\{\lambda_{\mathrm{b}}^{s}\}_{q}+\{\lambda_{\mathrm{b}}^{q}\}_{s}=-2[M_{\mathrm{bc}}^{q}]_{s}\{E_{\mathrm{c}}^{q}\}_{s}-2[M_{\mathrm{bb}}^{q}]_{s}\{E_{\mathrm{b}}^{q}\}_{s}.\tag{5.10}$$

Note that $\{\bullet\}_{s}$ and $[\bullet]_{s}$ are the subvector and submatrix of vector $\{\bullet\}$ and matrix $[\bullet]$, respectively, with unknowns defined on Γ^{s}. To derive (5.10), a conformal mesh is assumed such that the following relations hold on Γ^{sq}: $\alpha^{s}=\alpha^{q}$, $\beta^{s}=\beta^{q}$, $\hat{n}^{s}=-\hat{n}^{q}$, $\{\mathbf{N}_{\mathrm{b}}^{s}\}=\{\mathbf{N}_{\mathrm{b}}^{q}\}$, and $\{E_{\mathrm{c}}^{q}\}_{s}=\{E_{\mathrm{c}}^{s}\}_{q}$. Equation (5.10) can be reduced by eliminating $\{E_{\mathrm{b}}^{q}\}$ using (5.4) and the result is

$$\{\lambda_{\mathrm{b}}^{s}\}_{q}+\left([T_{s}^{q}]-2[F_{\mathrm{bb}}^{q}]_{s}\right)\{\lambda_{\mathrm{b}}^{q}\}+2\left([M_{\mathrm{bc}}^{q}]_{s}[B_{\mathrm{c}}^{q}]_{s}-[F_{\mathrm{bc}}^{q}]_{s}\right)\{E_{\mathrm{c}}\}=-2[M_{\mathrm{bb}}^{q}]_{s}\{d_{\mathrm{b}}^{q}\}_{s},\tag{5.11}$$

where

$$\begin{aligned}[F_{\mathrm{bb}}^{q}]=&[M_{\mathrm{bb}}^{q}][R_{\mathrm{br}}^{q}][K_{\mathrm{rr}}^{q}]^{-1}[R_{\mathrm{br}}^{q}]^{\mathrm{T}},\\ [F_{\mathrm{bc}}^{q}]=&[M_{\mathrm{bb}}^{q}][R_{\mathrm{br}}^{q}][K_{\mathrm{rr}}^{q}]^{-1}([K_{\mathrm{rc}}^{q}]+[R_{\mathrm{br}}^{q}]^{\mathrm{T}}[M_{\mathrm{bc}}^{q}])[B_{\mathrm{c}}^{q}],\\ \{d_{\mathrm{b}}^{q}\}=&[R_{\mathrm{br}}^{q}][K_{\mathrm{rr}}^{q}]^{-1}\{f_{\mathrm{r}}^{q}\},\end{aligned}\tag{5.12}$$

and $[T_{s}^{q}]$ is a projection Boolean matrix employed to extract the interface unknowns defined on Γ^{sq} from those defined on Γ^{q}.

Now we assemble (5.11) for all the subdomains to obtain the global interface system

$$[\tilde{K}_{\mathrm{bb}}]\{\lambda_{\mathrm{b}}\}+[\tilde{K}_{\mathrm{bc}}]\{E_{\mathrm{c}}\}=\{\tilde{f}_{\mathrm{b}}\},\tag{5.13}$$

where

$$\begin{aligned}\left[\tilde{K}_{\mathrm{bb}}\right]=&[I]+\sum_{s=1}^{N_{\mathrm{s}}}[Q^{s}]^{\mathrm{T}}\sum_{q\in\mathrm{neighbor}(s)}[T_{q}^{s}]^{\mathrm{T}}([T_{s}^{q}]-2[F_{\mathrm{bb}}^{q}]_{s})[Q^{q}],\\ [\tilde{K}_{\mathrm{bc}}]=&2\sum_{s=1}^{N_{\mathrm{s}}}[Q^{s}]^{\mathrm{T}}\sum_{q\in\mathrm{neighbor}(s)}[T_{q}^{s}]^{\mathrm{T}}\left([M_{\mathrm{bc}}^{q}]_{s}[B_{\mathrm{c}}^{q}]_{s}-[F_{\mathrm{bc}}^{q}]_{s}\right),\\ \{\tilde{f}_{\mathrm{b}}\}=&-2\sum_{s=1}^{N_{\mathrm{s}}}[Q^{s}]^{\mathrm{T}}\sum_{q\in\mathrm{neighbor}(s)}[T_{q}^{s}]^{\mathrm{T}}[M_{\mathrm{bb}}^{q}]_{s}\{d_{\mathrm{b}}^{q}\}_{s}.\end{aligned}\tag{5.14}$$

By combining (5.7) and (5.13) to eliminate $\{E_\mathrm{c}\}$, a global interface equation for $\{\lambda_\mathrm{b}\}$ is derived:

$$\left([\tilde{K}_\mathrm{bb}] + [\tilde{K}_\mathrm{bc}][\tilde{K}_\mathrm{cc}]^{-1}[\tilde{K}_\mathrm{cb}]\right)\{\lambda_\mathrm{b}\} = \{\tilde{f}_\mathrm{b}\} - [\tilde{K}_\mathrm{bc}][\tilde{K}_\mathrm{cc}]^{-1}\{\tilde{f}_\mathrm{c}\}, \tag{5.15}$$

which can be solved by using a Krylov subspace method. After $\{\lambda_\mathrm{b}\}$ is solved, $\{E_\mathrm{c}\}$ can be obtained from (5.7) and the electric field inside each subdomain can be obtained by solving (5.4). Once the electric field is computed everywhere, the interested quantities such as the RCS and radiation patterns can be evaluated.

5.3 Parallel Implementation

For large-scale engineering problems, we have to parallelize the FETI-DP algorithm to harness the power of computer clusters so that the solution can be obtained within a reasonable time. In this section, the parallel implementation of the FETI-DP algorithm is described. The preprocessing part, which consists of mesh partition and job distribution, is discussed first since it is vital to achieve a high parallel efficiency. This is followed by a detailed discussion of the parallelization of the interface and coarse problems. Although the presented formulation is restricted to conformal meshes for the sake of clarity, the proposed parallel strategy can be readily extended to mesh-nonconformal and/or geometry-nonconformal problems [27, 28].

5.3.1 Parallel Preprocessing

In parallel computation, there are two key factors that affect the scalability: load balance and communication overhead. The load balance can be achieved by decomposing the original computational domain into many subdomains which have similar sizes and shapes. While it is clear that subdomains with different sizes undermine the load balance, it it less obvious that subdomains with various shapes can deteriorate the load balance as well. To see this, let us compare the memory requirements and computation times for factorizing the system matrices of the three subdomains with geometrical configurations illustrated in Fig. 5.1. The volumes of the subdomains are exactly the same although their shapes are very different. Specifically, the subdomain (a) has a dimension of $0.2\lambda_0 \times 0.2\lambda_0 \times 12.8\lambda_0$, the subdomain (b) has a dimension of $1.6\lambda_0 \times 1.6\lambda_0 \times 0.2\lambda_0$, and the subdomain (c) has a dimension of $0.8\lambda_0 \times 0.8\lambda_0 \times 0.8\lambda_0$. A mesh size of $0.1\lambda_0$ is used for discretization and each of the subdomain is discretized into 2,560 tetrahedra. The system matrices are factorized by the direct solver PARDISO [105]. Figure 5.2 shows the numbers of DoFs, peak memory consumptions, and factorization times for the three subdomain system matrices with H(curl) conforming basis functions having an order ranging from 1 to 4. It is apparent that even though the subdomains have similar numbers of DoFs, the computational expenses vary significantly. In fact, the factorization times for these three cases are different by more than 5 times when 4th-order basis functions are used. This large difference in factorization times is due to the different sparse patterns of the subdomain matrices because of their different shapes. Therefore, to achieve a good load balance, not only the numbers of DoFs of the subdomains, but also their shapes, should be similar. Once the load balance is achieved, the communication overhead is mainly related to the neighboring communication and this can be reduced by minimizing subdomain interfaces. Theoretically, an effective mesh decomposer should generate subdomains with similar sizes and shapes as well as minimize subdomain interfaces. Unfortunately, the domain partition problem is NP-complete [124] and therefore to find an optimal partition is extremely time-consuming. In this work, we adopt METIS to decompose the original computational domain because of its fast processing speed and high quality of generated subdomains [125].

The efficiency of the FETI-DP algorithm is also closely related to subdomain sizes or the number of DoFs in each subdomain. For larger subdomain sizes, the subdomain interfaces are generally reduced and hence fewer resources are required to solve the interface problem. However, the computational cost involved in the factorization of the subdomain matrices increases with respect to the subdomain sizes. Similarly, for subdomains with smaller sizes, although the computation time and memory consumption for factorization decrease, the resources required by the interface problem are increased. It is observed that subdomains with a number of DoFs between 7,000 $\sim$ 25,000 generally gives the most efficient FETI-DP solution [23]. Note that a computing architecture with a different balance of computational, memory, and communication resources than conventional architectures may result in a different optimal number of DoFs per subdomain.

Another issue associated with the efficient parallelization of the FETI-DP algorithm at the preprocessing stage is to distribute subdomains to processors. As discussed in the previous paragraph, the subdomain sizes cannot be too large. For electrically large problems, the original computational domain would be divided into a large number of subdomains which can easily exceed the number of processors. Therefore, it is necessary to assign subdomains in close proximity to the same processor in order to minimize the inter-processor communication. In our implementation, a graph, whose nodes represent subdomain numbers and edges represent subdomain connectivity, is constructed. The graph is then partitioned by METIS into N_{p} parts, where N_{p} is the number of processors used in the parallel computation. After that, the subdomains in each part of the graph are assigned to the same processor.

Once the subdomains are distributed to the processors, the following matrices and vectors can be calculated in each processor without any communication:

- Subdomain system matrices: $[K^s_{\mathrm{rr}}]$, $[K^s_{\mathrm{rc}}]$, $[K^s_{\mathrm{cr}}]$, and $[K^s_{\mathrm{cc}}]$.
- Subdomain projection matrices: $[M^s_{\mathrm{bb}}]$ and $[M^s_{\mathrm{bc}}]$.
- Subdomain intermediate matrices: $[K^s_{\mathrm{rr}}]^{-1}$, $[\tilde{K}^s_{\mathrm{cc}}]$, $[\tilde{K}^s_{\mathrm{cb}}]$, $[F^s_{\mathrm{bb}}]$, and $[F^s_{\mathrm{bc}}]$.
- Subdomain excitation vectors: $\{f^s_{\mathrm{r}}\}$, $\{f^s_{\mathrm{c}}\}$, $\{\tilde{f}^s_{\mathrm{c}}\}$, and $\{d^s_{\mathrm{b}}\}$.

5.3.2 Parallel Interface Problem Implementation

The interface problem (5.15) is generally partially dense, partially sparse, and indefinite. For large problems, it is desirable to solve it using an iterative method in parallel. To evaluate the required matrix-vector multiplication (MVP)

$$\{\delta\} = \left([\tilde{K}_{\mathrm{bb}}] + [\tilde{K}_{\mathrm{bc}}][\tilde{K}_{\mathrm{cc}}]^{-1}[\tilde{K}_{\mathrm{cb}}]\right)\{\lambda_{\mathrm{b}}\}, \tag{5.16}$$

we first split the MVP into four sub-MVPs:

$$\begin{aligned}
\{t\} &= [\tilde{K}_{\mathrm{cb}}]\{\lambda_{\mathrm{b}}\}, \\
\{u\} &= [\tilde{K}_{\mathrm{cc}}]^{-1}\{t\}, \\
\{v\} &= [\tilde{K}_{\mathrm{bc}}]\{u\}, \\
\{w\} &= [\tilde{K}_{\mathrm{bb}}]\{\lambda_{\mathrm{b}}\},
\end{aligned} \tag{5.17}$$

where $\{\lambda_{\mathrm{b}}\}$, $\{t\}$, $\{u\}$, $\{v\}$, and $\{w\}$ are global vectors that will never be explicitly formed. We adopt these notations merely for the sake of convenient expressions. With these, the global MVP can then be determined by

$$\{\delta\} = \{w\} + \{v\}. \tag{5.18}$$

To illustrate the parallel MVP implementation, we further define local vectors $\{t^p\}$, $\{u^p\}$, $\{v^p\}$, and $\{w^p\}$ on processor p, which correspond to the global vectors $\{t\}$, $\{u\}$, $\{v\}$, and $\{w\}$, respectively. To calculate $\{t\}$ on a distributed machine, each processor carries out the local MVP with the local $[\tilde{K}_{\mathrm{cb}}]$ and the local dual interface unknowns $\{\lambda_{\mathrm{b}}\}$. In order to obtain a complete $\{t^p\}$, a summation reduction and a redistribution operation have to be performed for those corner unknowns shared by different processors. The communication cost for this part is negligible since the message length is small and the data exchange is restricted to a few neighboring subdomains. Once $\{t\}$ is determined, the intermediate vector $\{u\}$ can be evaluated by solving the global coarse system. The efficient calculation of $\{u\}$ in parallel involves more effort and will be discussed in the next subsection.

The evaluation of $\{v\}$ and $\{w\}$ involves computing the $\sum_{q\in\mathrm{neighbor(s)}}[T_q^s]^{\mathrm{T}}$ operator, which requires data exchanges between neighboring subdomain interfaces. Fortunately, the mesh partition and job distribution scheme in the preprocessing part assigns subdomains in close proximity to the same processor. Hence, most of the data exchanges occur inside a processor instead of across different processors. To further reduce the communication overhead, these data exchanges are implemented using non-blocking communication message passing interface (MPI) functions to overlap communication with computation.

The large, indefinite, and nonsymmetric interface problem poses a grand challenge even for the Krylov subspace based iterative solvers. In this work, the GMRES method is implemented for solving (5.15) because of its robustness and fast convergence. For the parallel GMRES method, a well-known bottleneck of efficiency is the dot-product calculation required for the construction of the Krylov subspace. In our implementation, the ICGS scheme is implemented to maintain the orthogonality quality of the Krylov subspace and to reduce the amount of global communication involved in the computation of the dot product [122].

5.3.3 Parallel Coarse Problem Implementation

The evaluation of $\{u\}$, which is equivalent to solving $[\tilde{K}_{\text{cc}}]\{u\} = \{t\}$, is also known as the global coarse problem [3]. The main difference between the global coarse problem and the global interface problem, besides the rank of the system matrices, is the definition of DoFs. In the interface problem, each dual DoF uniquely belongs to a subdomain, which makes it easy to distribute the dual DoFs among processors. However, in the global coarse problem, the corner DoFs are primal DoFs associated with corner edges that are shared by more than two subdomains. Because of this overlap of local corner DoFs in the adjacent subdomains, efficient parallelization of an iterative solver to solve the global coarse problem is not straightforward.

In the past, the coarse problem in the FETI-DP algorithm is mainly solved by a direct solver [23,59,60]. Depending on the size of the coarse problem, two direct solution approaches are commonly implemented. The first approach, which we refer to as the direct serial scheme (DSS), stores a copy of $[\tilde{K}_{\text{cc}}]$ locally and then factorizes the matrix repeatedly in each processor. Since every processor maintains a complete factorization, only one MPI *allreduce* has to be performed in an interface MVP, which obtains the corner DoFs from all processors and then redistributes them. The disadvantage of this method is that the factorization is performed completely in serial and repeated by all processors, which significantly undermines the efficiency of the FETI-DP algorithm unless the factorization and forward/backward substitution times are negligible. The other approach, which we refer to as the direct parallel scheme (DPS), solves the global coarse problem through a parallel sparse direct solver. For coarse systems with relatively large sizes where the DSS is no longer effective, the DPS is normally implemented as an alternative.

Unfortunately, due to the difference of several orders of magnitude in the matrix sizes of the coarse and interface systems, the coarse problem usually requires far fewer processors than the interface problem in order to be solved efficiently. This issue not only complicates the DPS implementation but also requires an algorithm to determine an optimal number of processors needed to be assigned to the parallel direct solver. Even if this issue can be resolved, the global communication overhead of forming the global corner matrix $[\tilde{K}_{\text{cc}}]$ and the relatively poor parallel performance of direct solvers, especially the forward/backward substitution operations, compromise significantly the parallel efficiency when a large number of processors are employed for parallel computation.

In this work, we design a parallel iterative scheme (PIS) which is tailored for the coarse problem. In the parallel scheme, processor p maintains its local corner system, the local corner DoFs $\{u^p\}$ to update the local MVP $\{t^p\}$, and another set of the corner DoFs $\{u^p\}'$ to compute the dot product, where $\{u^p\}'$ is a subset of $\{u^p\}$. Since the global corner matrix $[\tilde{K}_{\text{cc}}]$ is never explicitly formed and the construction of local corner matrices needs no data exchanges, the communication overhead can be reduced significantly as opposed to using a direct solver. To perform the MVP, only neighboring communication is required, which can be efficiently carried out by non-blocking communication techniques.

Because of the two sets of DoFs we introduced in the coarse problem, it is rather difficult to incorporate the parallel GMRES method developed for the interface problem to solve the coarse problem. Fortunately, the coarse problem is relatively well-conditioned and the BICGSTAB method [126] can give a satisfactory convergence rate. The drawback of the BICGSTAB method when parallelized on a large number of processors is the excessive global communication. To achieve a high parallel efficiency for solving the global coarse problem, we adopt the CA-BICGSTAB method [123], which performs one global communication in l MVPs instead of four in every MVP in the BICGSTAB method, where l is a user defined integer, which is chosen to be 2 in our simulations. For completeness, the adopted CA-BICGSTAB method is listed in Algorithm 1.

Since the global coarse problem has to be iteratively solved in each interface MVP, the convergence of the coarse problem significantly affects the efficiency and scalability of the FETI-DP algorithm. Several auxiliary

Algorithm 1 Communication-avoiding BICGSTAB (CA-BICGSTAB) method [123]

```
Require: Initial approximation $x_0$ for solving $Ax = b$, let $p_0 := r_0 := b - Ax_0$
Choose $\tilde{r}$ arbitrarily such that $\delta_0 := (\tilde{r}, r_0) \neq 0$
Compute the Boolean matrix $T_{4l+1,4l+1}$ with $T_{i,i-1} = 1$ where $i = 2, \dots, 2l+1, 2l+3, \dots, 4l+1$.
for $m := 0, l, 2l, \dots,$ until convergence do
    Compute $V$ with columns a basis for $\mathcal{K}_{2l+1}(A, p_m) + \mathcal{K}_{2l}(A, r_m)$
    Compute $[G, g] := V^{\mathrm{T}}[V, \tilde{r}]$
    Initialize $a_0 := [1, 0_{1,4l}]^{\mathrm{T}}$, $c_0 := [0_{1,2l+1}, 1, 0_{1,2l-1}]^{\mathrm{T}}$, and $e_0 := 0_{4l+1,1}$
    for $j := 0$ to $l - 1$ do
        $\alpha_{m+j} := (g, c_j)/(\tilde{r}, Ta_j)$
        $t_j := c_j - \alpha_{m+j} T a_j$
        Check $\|q_j\|_2 := (t_j, G t_j)^{1/2}$ for convergence
        $\omega_{m+j} := (t_j, GTt_j)/(Tt_j, Tt_j)$
        $e_{j+1} := e_j + \alpha_{m+j} a_j + \omega_{m+j} t_j$
        $c_{j+1} := t_j - \omega_{m+j} T t_j$
        Check $\|r_{j+1}\|_2 := (c_{j+1}, G c_{j+1})^{1/2}$ for convergence
        $\beta_{m+j} := \alpha_{m+j}/\omega_{m+1}(g, c_{j+1})/(g, c_j)$
        $a_{j+1} := c_{j+1} + \beta_{m+j}(a_j - \omega_{m+j} T a_j)$
    end for
    $[p_{m+l}, r_{m+l}, x_{m+l} - x_m] := V[a_l, c_l, e_l]$
end for
```

wave-based coarse problem preconditioners have been developed for solving Helmholtz problems [127,128] and recently a global plane wave deflation preconditioner has been proposed to improve the iterative convergence of the coarse problem by alleviating the influences of the cutoff and/or near cutoff modes in the vicinity of domain interfaces [129]. Although these preconditioners are quite effective, the construction and application to the coarse problem introduce some communication overhead which eventually compromises the parallel efficiency with a large number of processors. In this thesis, we propose a simple yet effective preconditioner, which is constructed directly from the global corner matrix, to improve the iterative convergence of the coarse problem. The global corner matrix $[\tilde{K}_{\text{cc}}]$, which is similar to the higher-order FEM matrix generated by super elements with DoFs associated with edges, exhibits a highly sparse pattern and block diagonally dominant entries. To utilize these properties, a diagonal preconditioner

$$[M] = \text{diag}\left([\tilde{K}_{\text{cc}}]\right) \tag{5.19}$$

is constructed to improve the convergence rate of the CA-BICGSTAB method without introducing any communication overhead.

5.4 Numerical Results

To demonstrate the accuracy, scalability, and capability of the proposed parallel strategy, the problems of electromagnetic scattering of a lossless dielectric sphere, a PEC airplane, and radiation of a Vivaldi antenna array are simulated in this section. The subdomain system matrices are factorized by the direct sparse solver PARDISO. The interface problems are solved by the GMRES method with a projection size of 30 and a stopping criterion of 10^{-3}. The coarse problems are solved using the DSS, DPS, and the proposed parallel scheme for performance comparison. The direct solver used in the DSS and DPS is also PARDISO, which is one of the most efficient direct solvers. For the proposed scheme, the CA-BICGSTAB method with a stopping criterion of 10^{-4} and initial guesses of zero is adopted. The computations are carried out in double float precision on a Cisco cluster with each node configured with 256 GB memory and 2 Intel Xeon E5-2680 v2 CPUs.

5.4.1 Lossless Dielectric Sphere

A well-known fact for the FEM is that its iterative solution of an EM problem involving lossless dielectric objects is very expensive because a large number of iterations is required. Since the parallel scheme we proposed for the global coarse problem solves the problem iteratively, it is very important to investigate the efficiency and scalability of the proposed method in solving these challenging problems where the convergence is difficult to achieve.

The problem considered is electromagnetic scattering by a lossless dielectric sphere with $\epsilon_{\mathrm{r}} = 4$ and a radius of $2\lambda_0$, enclosed by a cubic air box with an edge length of $10\lambda_0$, where λ_0 is the free-space wavelength. The computational domain is first discretized into 713,270 curvilinear tetrahedral elements and then partitioned into 400 subdomains using METIS. The third-order hierarchal vector basis functions are adopted to expand the electrical field and the dual unknowns on the subdomain interfaces, which finally yields 35,145 corner DoFs, 943,563 dual DoFs, and 14,319,180 total DoFs. The problem geometry, METIS partitioned subdomains, and corner edges are depicted in Fig. 5.3, where 20 colors are used to represent the subdomains and to ensure that neighboring subdomains have different colors.

The computational statistics for the simulations using three different corner parallelization schemes, i.e. DSS, DPS-ν, and PIS, are listed in Table 5.1, where ν is the number of cores used in the DPS. For each problem, we use various cores for the DPS simply to determine the most efficient DPS since the performance of the DPS is problem and iteration (the forward/backward substitutions are less scalable than the factorization) dependent. In Table 5.1, the time for the tearing part contains subdomain system matrix and vector assembly time, subdomain factorization time, and intermediate matrix and vector calculation time. The corner preprocessing time contains the time for reducing and factorizing the global corner system, which is zero for the PIS. The self-explanatory corner solution time, interface solution time, and total random access memory (RAM) consumed are also included in Table 5.1. For all the computational statistics presented in Table 5.1, the diagonal preconditioner is used and its negligible construction time is contained in the corner solution time.

It can be seen from Table 5.1 that the proposed PIS requires the least total RAM consumption and solution time for almost all the test cases. In contrast, the DSS is the most computationally expensive scheme due to the relatively large corner system. The performance of the DPS-ν is processor dependent and is optimal when $\nu = 16$. The total solution time and parallel efficiency versus the number of computing cores are depicted in Fig. 5.4, where the parallel efficiency is calculated using a baseline of the total solution time of 16 cores. The parallel efficiency, defined in a strong scaling fashion by fixing the problem size and increasing the number of computing cores, is given by

$$\text{Parallel efficiency} = \frac{qT_q^{\min}}{pT_p} \times 100\%, \tag{5.20}$$

where $T_q^{\min}$ is the smallest runtime on q cores (in this case, $q = 16$ and the parallel scheme is the DPS-16) and T_p is the runtime using p cores with various parallel schemes. Although METIS does not produce subdomains with the same size or shape, we still achieve a parallel efficiency of 70% when 400 cores are employed in the parallel computation and the PIS is used to solve the corner problem. Figure 5.5a compares the computed bistatic RCS values for the HH and VV polarizations with those obtained from Mie series solutions, showing good agreement. The convergence history of the interface problem and the first corner problem with and without the proposed diagonal preconditioner is shown in Fig. 5.5b. The GMRES solution of the interface problem converges in 192 iterations for all the three coarse problem parallel schemes whether or not the diagonal preconditioner is applied. Without the diagonal preconditioner, the number of iterations for each coarse problem solution is about 388 and the total solution time using the PIS with 400 cores employed in the parallel computing is 163.2 seconds, but when the preconditioner is turned on, these two numbers are reduced to 38 and 66.6, respectively.

5.4.2 PEC Airplane

The second example is the simulation of electromagnetic scattering by a PEC airplane, as shown in Fig. 5.6, which has a body length of $35\lambda_0$ and a wing span of approximately $38\lambda_0$. The ABC is placed $3\lambda_0$ away from the nearest parts of the airplane, thus creating a total computational domain with a size of $41\lambda_0 \times 44\lambda_0 \times 17\lambda_0$. The vertical polarized plane wave is incident toward the nose of the airplane with a frequency of 0.3 GHz. The computational domain is decomposed into 4,096 subdomains by METIS and the partitioned subdomains and corner edges are illustrated in Fig. 5.7. With a mesh size of $0.3\lambda_0$ to discretize the computational domain and third-order vector basis functions to expand the electric field, this problem yields 321,618 corner DoFs, 6,545,181 interface dual DoFs, and 79,120,149 total DoFs.

The detailed computational statistics for the simulation are listed in Table 5.2. Because the corner system for the FETI-DP with the SOTE-TC is nonsymmetric due to the introduction of the matrix $\{M^s_{\mathrm{bc}}\}$ and the matrix size is relatively large for this problem, the DSS scheme, which keeps a local copy of the global coarse matrix and its factorization in each processor, is too memory expensive and cannot be carried out with 512 cores. For parallel computing with 64 cores, neither of the two direct solver based corner solution schemes can be carried out with the available memory. When the number of computing cores increases to 128, the DPS-32 and DPS-64 schemes start to work. As the number of cores increases to 256, the DPS-128 becomes feasible. It is apparent in Table 5.2 that both the total solution time and the total RAM consumption for the PIS are only about 1/5 of those used by the DPSs.

The total solution time and parallel efficiency versus the number of computing cores are shown in Fig. 5.8, where the parallel efficiency is calculated using a baseline of the total solution time of 64 cores. Even though the airplane model is rather geometrically complex, our parallelized FETI-DP algorithm using the PIS still achieves a good load-balance and a parallel efficiency of about 80% when 512 cores are used for parallel computation, which is much higher than those of the direct solver based parallel corner solution schemes.

The computed bistatic RCS curve for the VV polarization using the parallel FETI-DP algorithm is plotted in Fig. 5.9a, where the plane wave is incident from the backside. The convergence history of the interface problem and the first corner problem with and without the proposed diagonal preconditioner is shown in Fig. 5.9b. The GMRES solution of the interface problem converges in 149 iterations irrespective of corner solution schemes. Without the diagonal preconditioner, the number of iterations for each coarse problem solution is about 354 and the total solution time using the PIS with 512 cores employed in the parallel computing is 546.9 seconds, and when the preconditioner is turned on, these two number are reduced to 26 and 187.6, respectively.

Finally, to demonstrate the capability of our parallel scheme for very large problems, we double the frequency and refine the mesh with a mesh size of $0.15\lambda_0$. The computational domain is decomposed into 8,192 subdomains by METIS. Again, the third-order vector basis functions are adopted to expand the electric field and dual DoFs. With such a discretization, this problem yields 1,090,398 corner DoFs, 34,661,595 interface dual DoFs, and 612,666,975 total DoFs. The computation is carried out on 64 compute nodes where 32 of them are the same as those used in the previous test cases and the remaining 32 nodes are configured with Intel Xeon E5-2680 v3 CPUs with each node having 256 GB memory installed on board. With 1,024 cores employed for parallel computing, the total solution time is 9,665.6 seconds and the total RAM consumption is 10,778.6 GB. The calculated bistatic RCS with VV polarization in the XOY plane is given in Fig. 5.10a. The convergence history for the interface problem and the first corner problem is shown in Fig. 5.10b. The interface problem converges to a residue of 10^{-3} in 288 iterations. With the diagonal preconditioner turned on, the first corner problem takes only 52 MVPs to converge to a residue of 10^{-4}.

5.4.3 Vivaldi Antenna Array

The third example is designed to explore the scalability of the proposed parallel strategy to deal with large-scale antenna array radiation problems. A 96×96 Vivaldi array, mounted on an infinite ground plane and fed by a TEM mode at 3 GHz at the coaxial ports, is simulated using different numbers of cores. The geometrical configuration of the Vivaldi antenna array element is shown in Fig. 5.11. The length, width, and thickness of the substrate are 33.3 mm, 34.0 mm, and 1.27 mm, respectively. The lossless substrate has a relative permittivity of 6.0, and the radius of the hollow circle is 2.5 mm. The half width of the slot line varies with z according to an exponential function given by $w(z) = 0.25e^{0.123z}$. The excitation is a TEM mode through a coax feed with an inner radius 0.375 mm and an outer radius 0.875 mm from the ground. The dielectric filling of the coax feed is assumed to be air. The antenna array is arranged periodically in the x- and y-directions and the periodic lengths are 36 mm in both directions. The detailed configuration of the Vivaldi antenna can be found in [27]. First-order vector basis functions are used in the simulation, which yields 108,300 corner DoFs, 4,218,000 dual DOFs, and 162,761,436 total DoFs, respectively.

The detailed computational statistics are listed in Table 5.3. It is observed from the table that the proposed parallel scheme performs better than the direct solver based corner solution schemes in terms of total solution time and total RAM consumption. The total solution time and parallel efficiency versus the number of computing cores are shown in Fig. 5.12, where the parallel efficiency is calculated using a baseline of the total solution time of 64 cores with the PIS used as corner problem solver. Because of the excellent load-balance and tailored parallel corner solver, the achieved parallel efficiency using the PIS is about 98.2% even when 512 cores are used for parallel computation. The normalized radiation patterns in the E- and H-planes, computed using the parallel FETI-DP algorithm, are plotted in Fig. 5.13a. The convergence history for the interface problem and the first corner problem is shown in Fig. 5.13b. The interface problem converges to a residue of 10^{-3} in 36 iterations irrespective of corner problem solvers. Without the diagonal preconditioner, the number of iterations for each coarse problem solution is about 14 and the total solution time using the PIS with 512 cores employed for parallel computing is 56.3 seconds, and when the preconditioner is turned on, these two numbers are reduced to 13 and 56.1, respectively. The diagonal preconditioner is not effective in this example because the corner system is already well conditioned.

5.5 Summary

In this chapter, we presented an efficient parallelization of the FETI-DP algorithm for large-scale electromagnetic simulations. For the parallel preprocessing, we discussed partitioning the mesh into subdomains with similar sizes and shapes in order to achieve a good load balance, and distributing the subdomains in close proximity to the same processor to minimize inter-processor communication. We then described a parallel GMRES algorithm to solve the global interface problem iteratively, enhanced with the ICGS orthogonalization scheme to reduce global communication. For the global coarse problem, we adopted a parallel CA-BICGSTAB method to reduce global communication. Based on the highly sparse pattern of the global coarse system, we developed a diagonal preconditioner to improve the iterative convergence. In both GMRES and CA-BICGSTAB iterative solutions, we employed the nonblocking communication approach to alleviate neighboring communication overhead. Finally, we presented three numerical examples to demonstrate the accuracy, scalability, and capability of our new parallelized FETI-DP algorithm for electromagnetic modeling of general objects and antenna arrays.

5.6 Figures and Tables

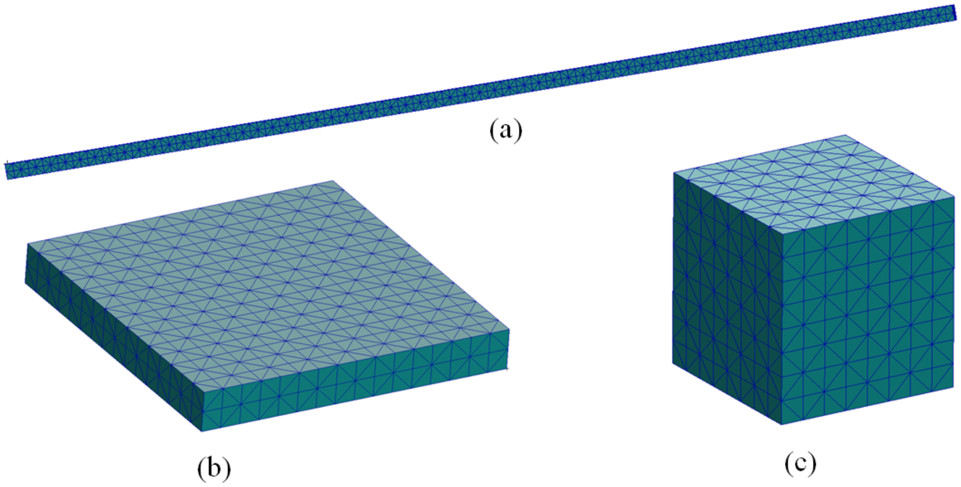

Figure 5.1: Subdomains with the same number of elements but different shapes. (a) Subdomain size is $0.2\lambda_0 \times 0.2\lambda_0 \times 12.8\lambda_0$. (b) Subdomain size is $1.6\lambda_0 \times 1.6\lambda_0 \times 0.2\lambda_0$. (c) Subdomain size is $0.8\lambda_0 \times 0.8\lambda_0 \times 0.8\lambda_0$.

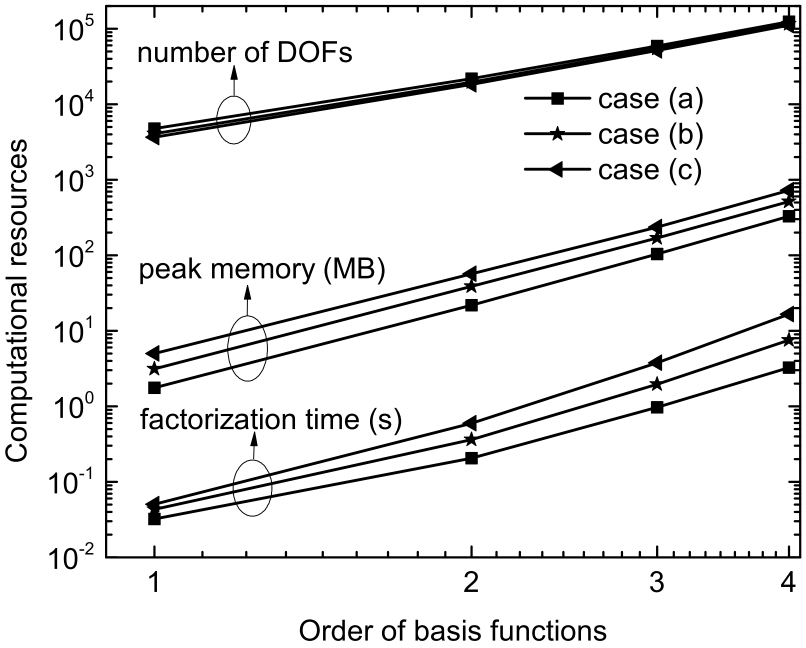

Figure 5.2: Comparison of the computational expenses for the three subdomains shown in Fig. 5.1, with the order of basis functions ranging from 1 to 4.

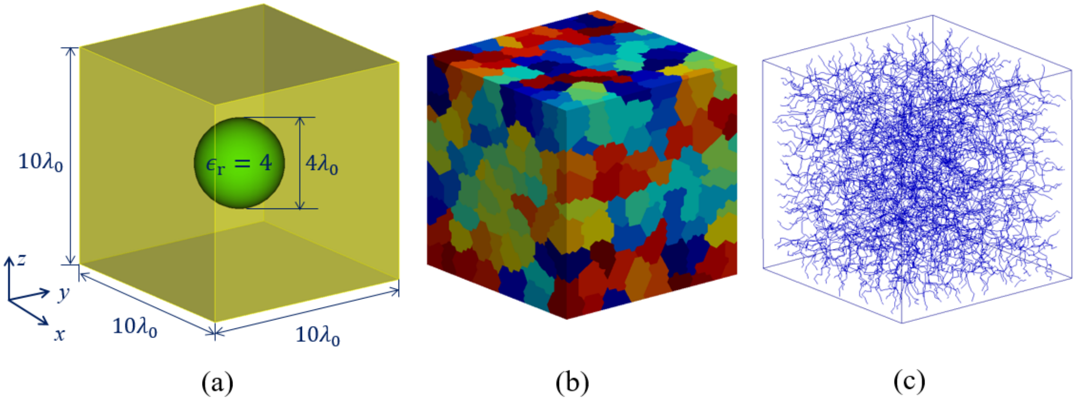

Figure 5.3: (a) Geometrical configuration of a dielectric sphere in a cubic box. (b) METIS generated 400 subdomains. (c) Corner edges shared by more than two subdomains.

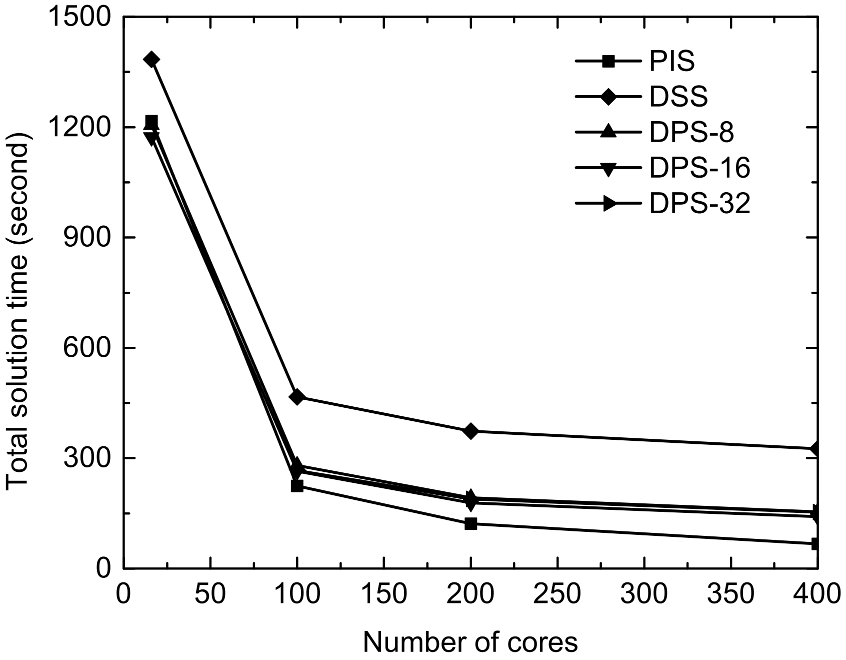

(a)

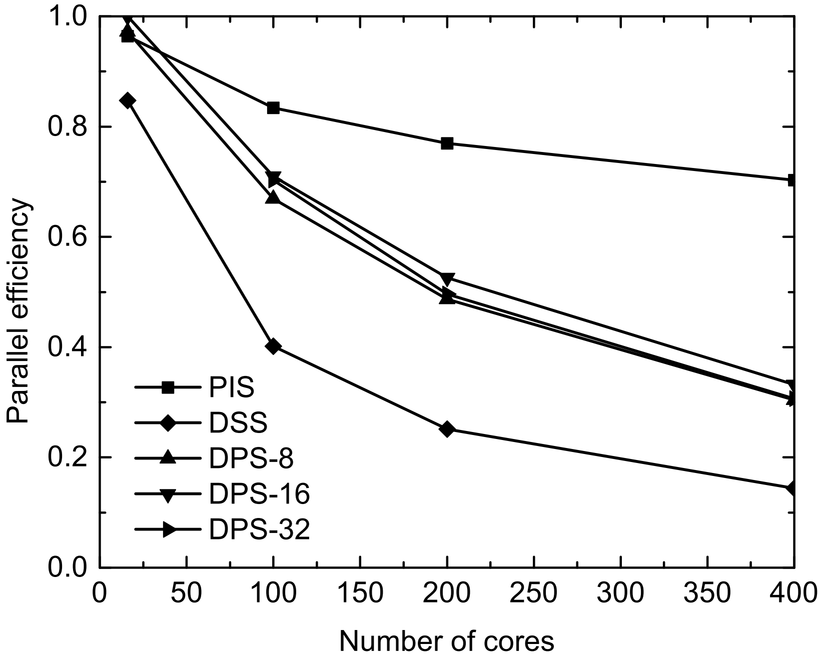

(b)

Figure 5.4: Total solution time and parallel efficiency for the simulation of the lossless dielectric sphere scattering problem with 400 subdomains. (a) Total solution time. (b) Parallel efficiency.

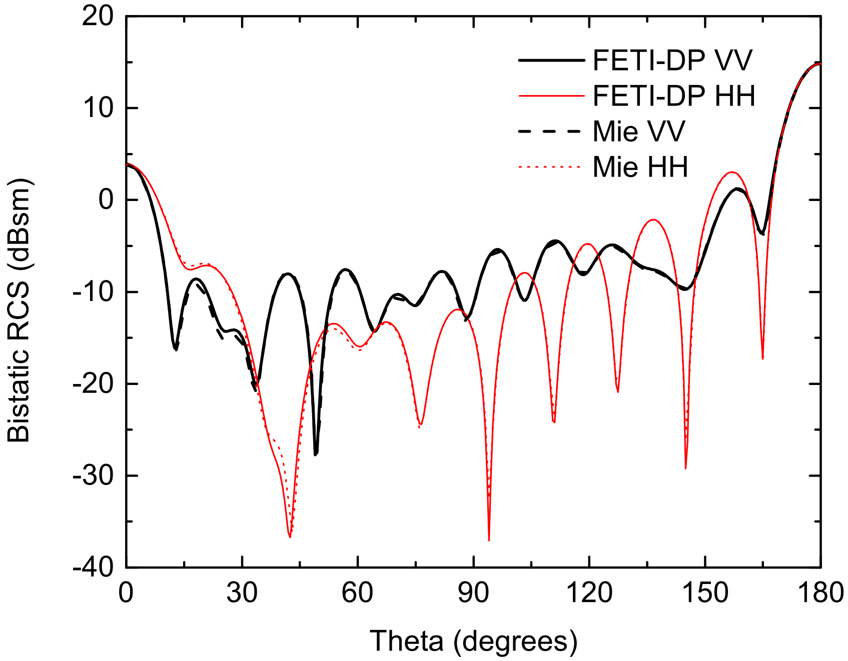

(a)

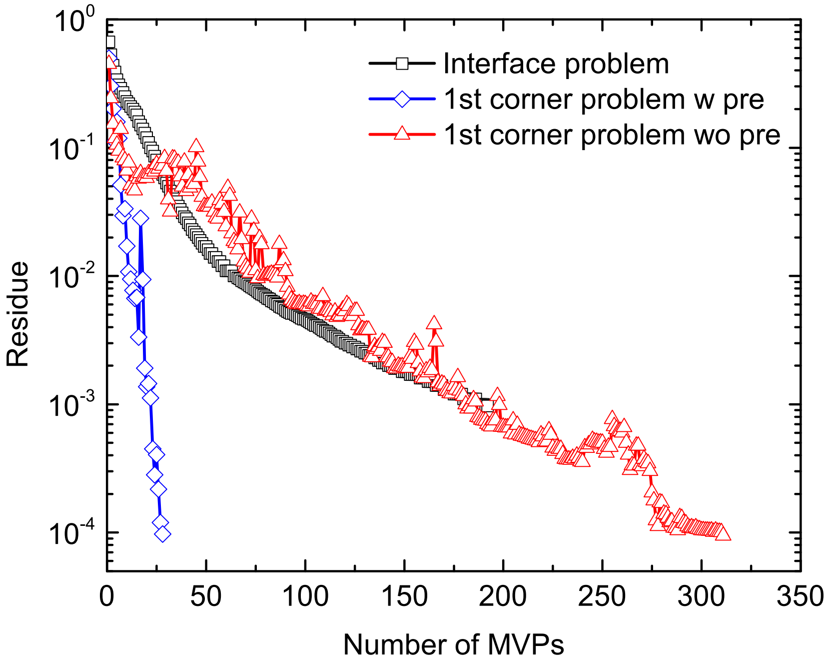

(b)

Figure 5.5: Bistatic RCS and convergence history for the simulation of the lossless dielectric sphere scattering problem with 400 subdomains. (a) Bistatic RCS. (b) Convergence history.

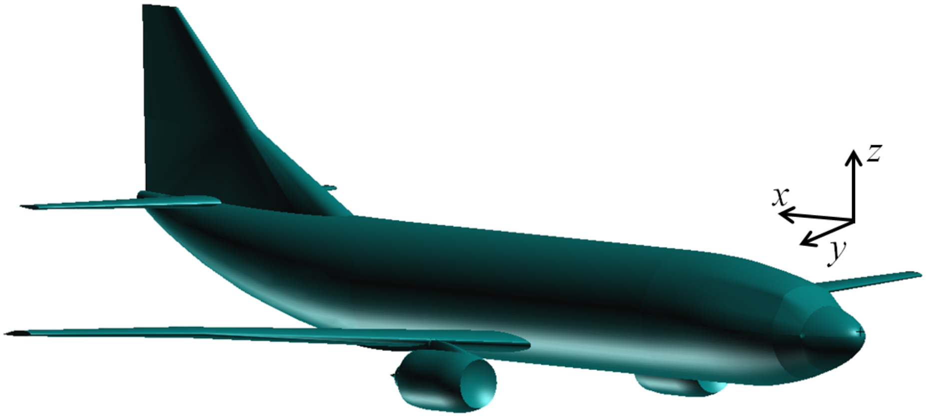

Figure 5.6: Geometrical configuration of the airplane model. The airplane has a body length of $35\lambda_0$ and a wing span of approximately $38\lambda_0$. The ABC is placed $3\lambda_0$ away from the nearest parts of the airplane, thus creating a total computational domain having a size of $41\lambda_0 \times 44\lambda_0 \times 17\lambda_0$.

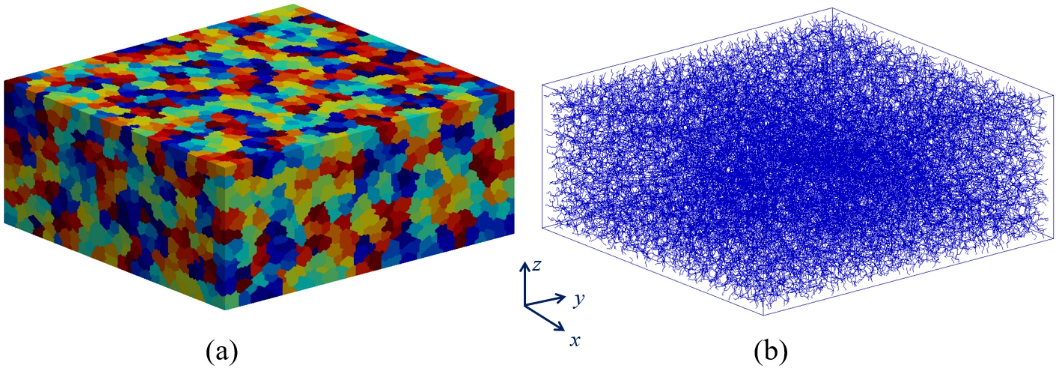

Figure 5.7: Illustrations of the METIS partitioned subdomains and corner edges. (a) METIS generated 4,096 subdomains. (c) Corner edges shared by more than two subdomains.

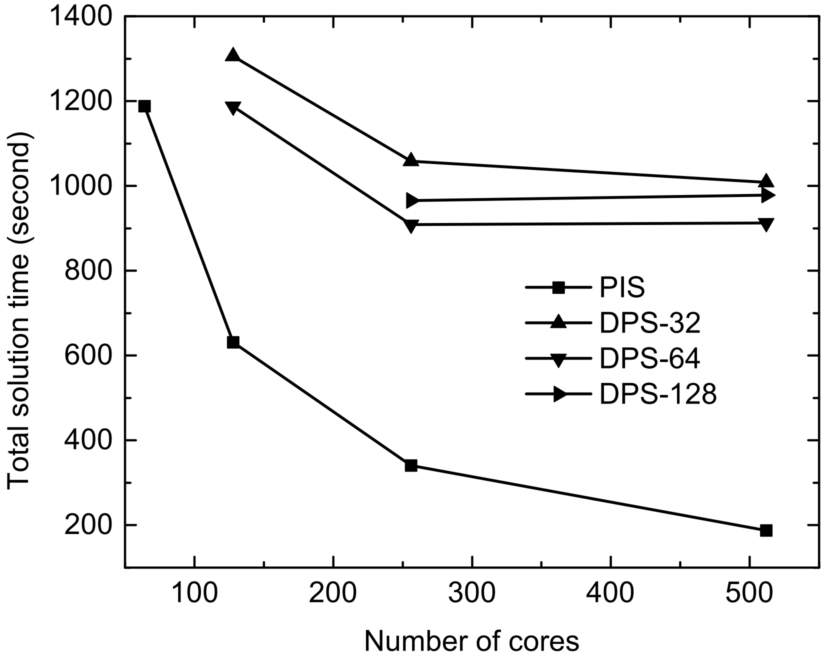

(a)

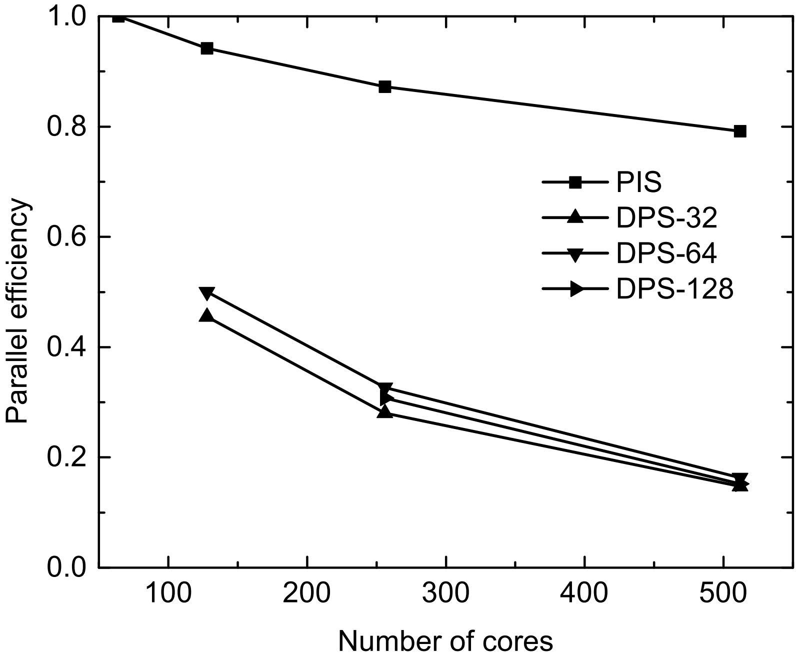

(b)

Figure 5.8: Total solution time and parallel efficiency for the simulation of the PEC airplane scattering problem with 4,096 subdomains. (a) Total solution time. (b) Parallel efficiency.

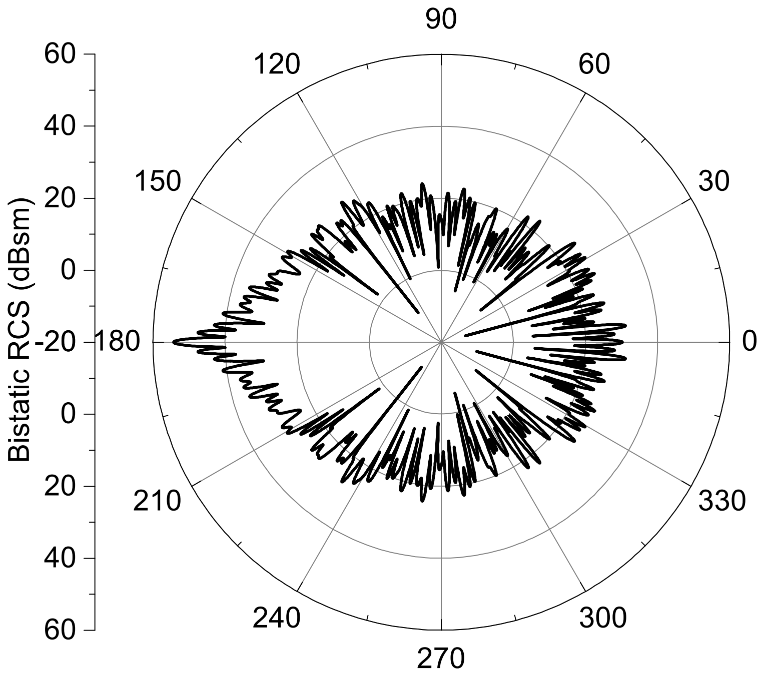

(a)

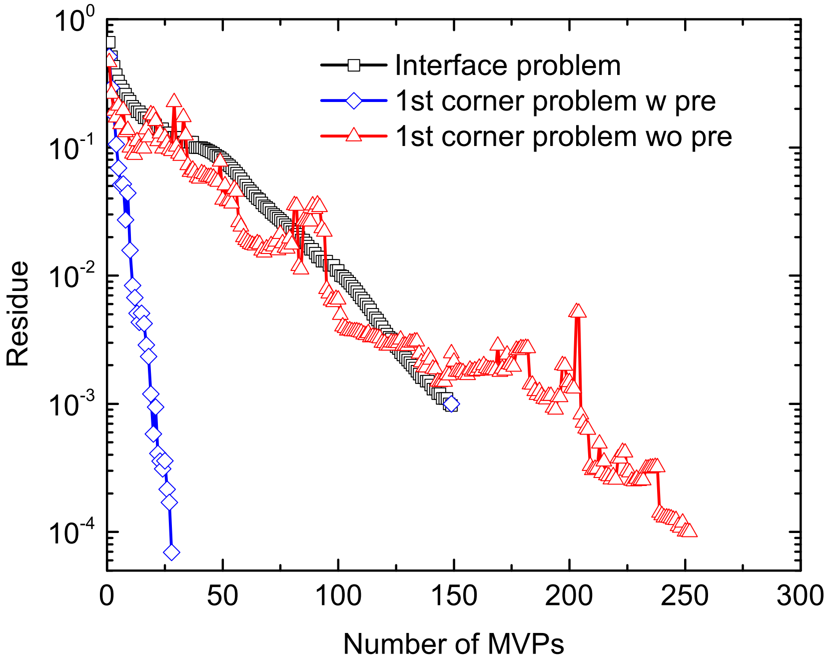

(b)

Figure 5.9: Bistatic RCS and convergence history for the simulation of the PEC airplane scattering problem with 4096 subdomains. (a) Bistatic RCS. (b) Convergence history.

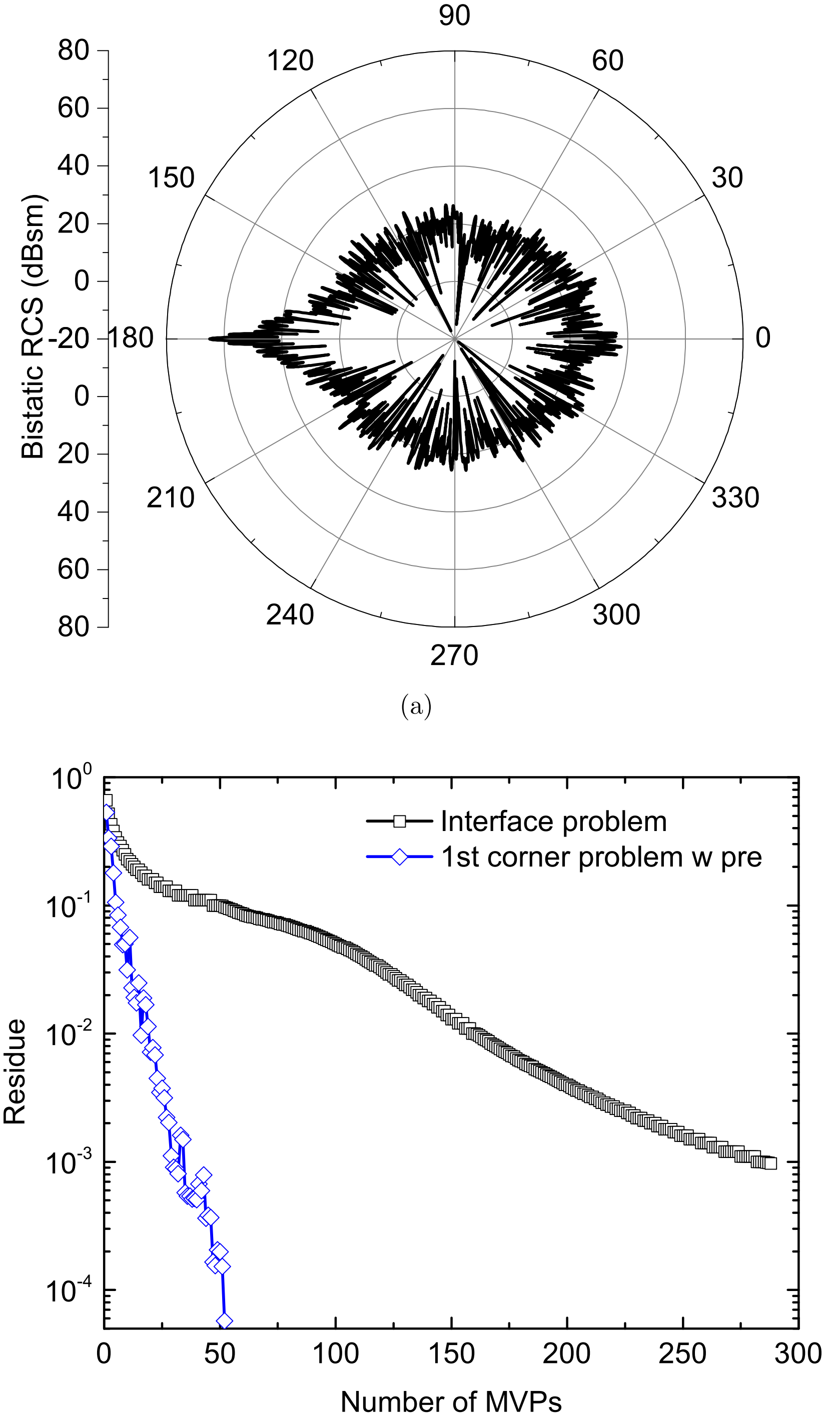

(a)

(b)

Figure 5.10: Bistatic RCS and convergence history for the simulation of the PEC airplane scattering problem with a refined mesh and 8,192 subdomains. (a) Bistatic RCS. (b) Convergence history.

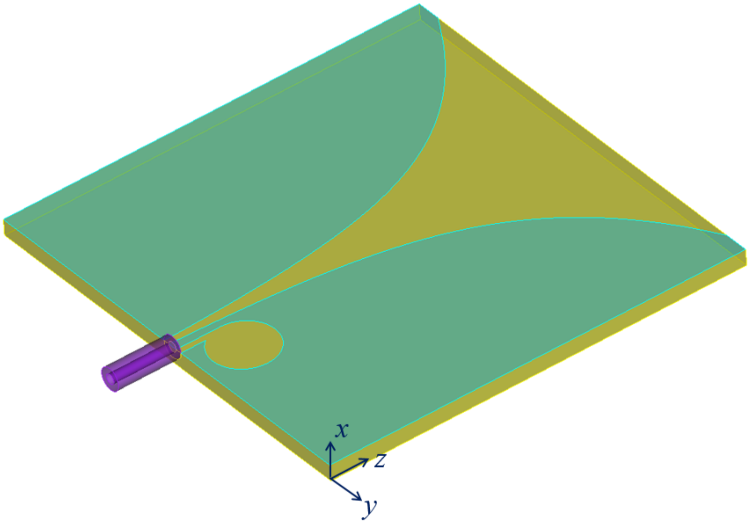

Figure 5.11: Geometrical configuration of the Vivaldi antenna array element.

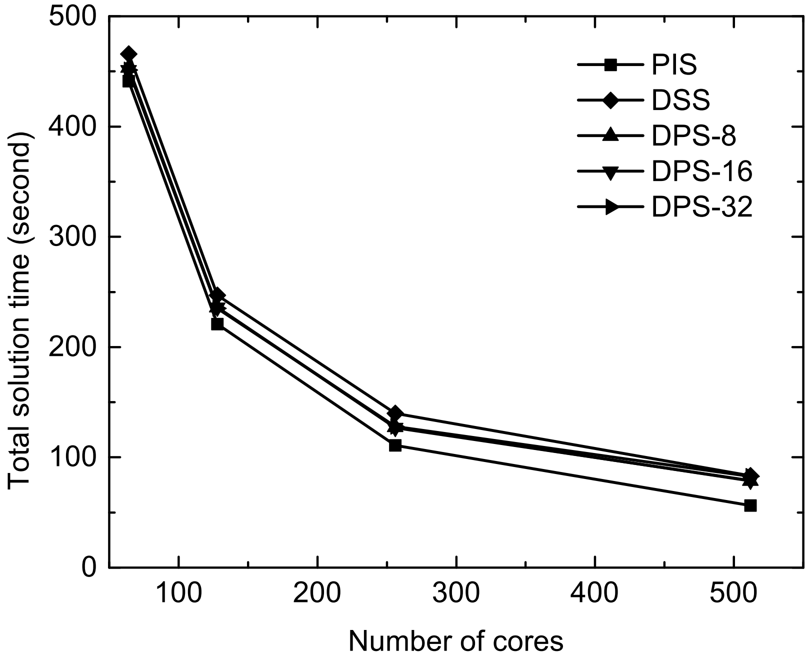

(a)

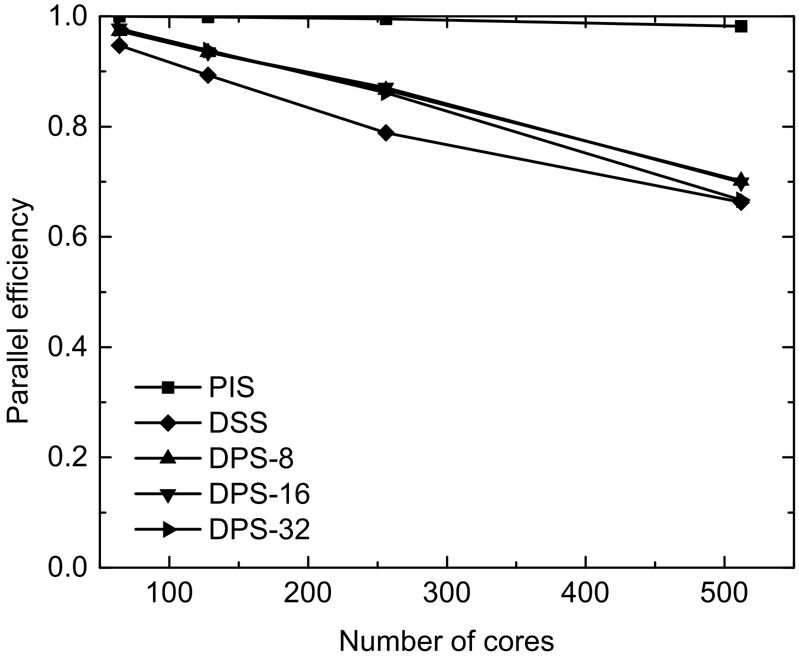

(b)

Figure 5.12: Total solution time and parallel efficiency for the simulation of the antenna radiation problem with 9,216 subdomains. (a) Total solution time. (b) Parallel efficiency.

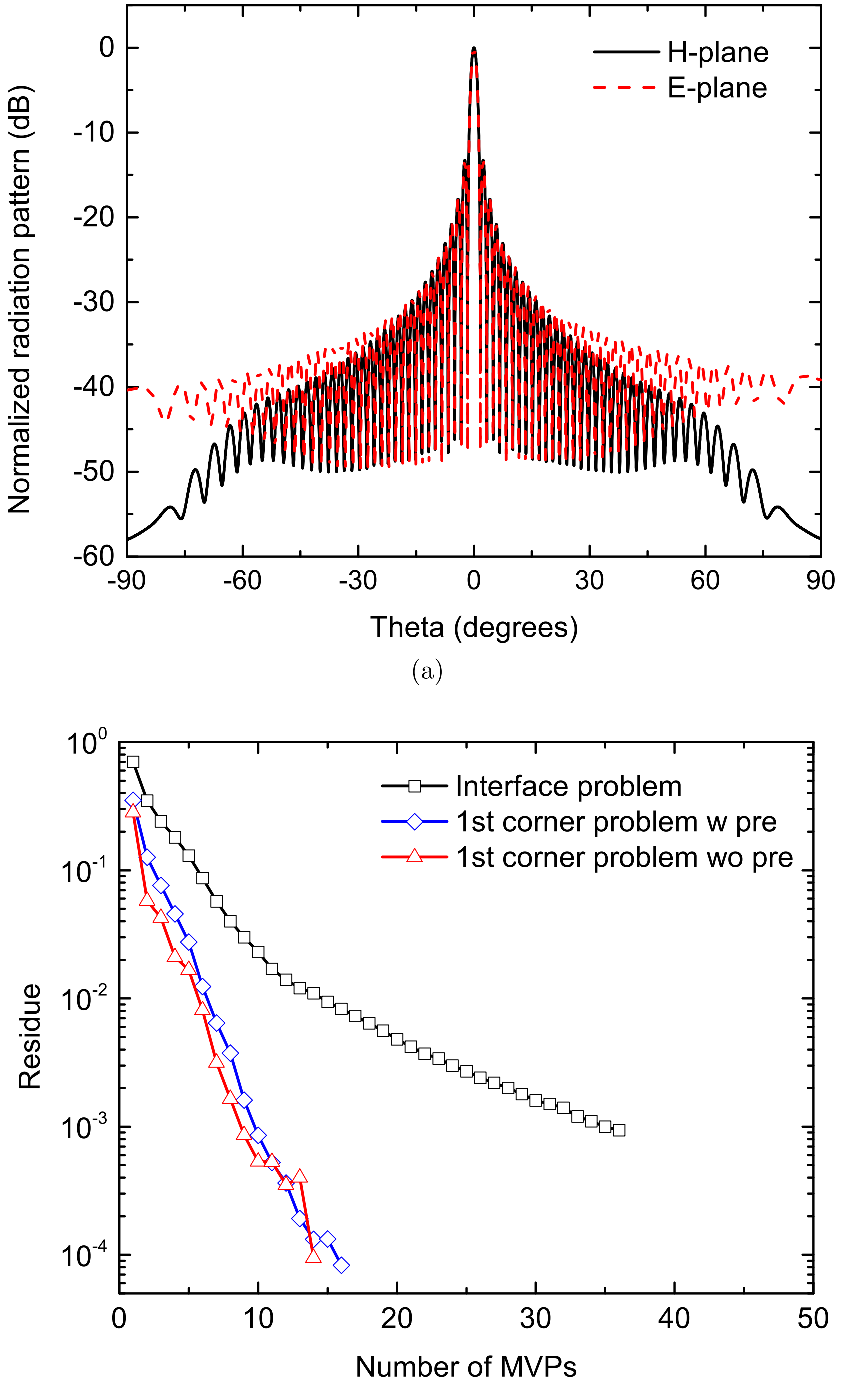

(a)

(b)

Figure 5.13: Radiation pattern and convergence history for the simulation of the 96 × 96 Vivaldi antenna array radiation problem with 9,216 subdomains. (a) Normalized radiation patterns in the E- and H-planes. (b) Convergence history.

Table 5.1: Computational statistics for the simulation of a lossless dielectric sphere. The units for time and RAM are second and GB, respectively.

Cores	Schemes	Tearing	Preproc	Corner	Interface	RAM
16	PIS	834.0	0	84.5	297.2	105.9
	DSS	830.4	163.6	97.7	291.5	181.5
	DPS-8	826.8	39.8	48.5	290.8	123.6
	DPS-16	820.6	31.7	29.5	290.5	135.2
100	PIS	152.2	0	23.8	48.8	125.3
	DSS	153.1	164.6	97.4	51.2	568.9
	DPS-8	150.5	41.8	38.9	49.1	175.3
	DPS-16	150.4	32.9	32.1	48.9	180.9
	DPS-32	150.6	28.5	38.5	49.2	198.7
200	PIS	81.7	0	15.0	25.2	148.6
	DSS	82.4	164.9	97.6	27.3	1,036.7
	DPS-8	81.2	43.0	42.3	26.1	219.5
	DPS-16	82.0	33.9	36.5	26.0	240.4
	DPS-32	82.2	30.2	50.1	26.4	260.2
400	PIS	42.7	0	10.7	13.2	194.4
	DSS	43.6	164.6	97.6	16.4	1,961.2
	DPS-8	43.1	46.5	48.5	15.9	295.7
	DPS-16	43.2	37.3	44.8	15.9	303.8
	DPS-32	43.2	32.5	61.3	16.1	331.6

Table 5.2: Computational statistics for the simulation of a PEC airplane. The units for time and RAM are second and GB, respectively.

Cores	Schemes	Tearing	Preproc	Corner	Interface	RAM
64	PIS	809.8	0	110.2	268.2	575.9
128	PIS	429.0	0	66.3	135.5	642.9
	DPS-32	445.5	507.3	198.1	155.1	1,350.9
	DPS-64	462.0	389.5	182.1	153.3	1,637.8
256	PIS	226.9	0	44.5	69.1	778.1
	DPS-32	233.7	517.2	226.3	81.3	2,349.1
	DPS-64	232.2	381.5	213.6	81.4	2,577.9
	DPS-128	231.6	321.4	326.9	85.7	3,030.0
512	PIS	118.8	0	33.2	35.6	1,046.8
	DPS-32	125.2	601.1	233.3	48.9	4,867.2
	DPS-64	124.9	444.4	291.4	51.6	5,104.3
	DPS-128	122.5	390.4	413.5	51.8	5,508.2

Table 5.3: Computational statistics for the radiation analysis of the 96 × 96 Vivaldi antenna array. The units for time and RAM are second and GB, respectively.

Cores	Schemes	Tearing	Preproc	Corner	Interface	RAM
64	PIS	352.8900	0	2.332063	85.9429	572.973
	DSS	353.5815	17.5509	8.192367	86.2966	689.200
	DPS-8	353.7420	7.0230	6.368232	86.1198	577.381
	DPS-16	352.8243	7.0271	5.463646	85.7934	579.856
	DPS-32	353.2942	6.7688	5.137395	86.1316	585.458
128	PIS	176.3970	0	1.426960	42.9950	613.484
	DSS	176.8389	17.7447	8.182873	44.1861	845.940
	DPS-8	177.0296	7.7915	7.405171	43.6508	618.002
	DPS-16	176.5317	8.4699	7.473077	43.4259	626.055
	DPS-32	176.7146	7.9734	6.946350	43.3867	626.065
256	PIS	88.2693	0	0.912756	21.6059	694.211
	DSS	88.6631	17.6649	8.163121	25.3189	1,159.12
	DPS-8	88.7056	7.7423	8.490517	22.3531	698.801
	DPS-16	88.5287	7.4408	8.521982	22.1860	701.283
	DPS-32	88.4724	7.1301	10.168981	22.2799	706.866
512	PIS	44.3770	0	0.921072	10.8632	856.344
	DSS	44.6863	18.2575	8.184400	12.0435	1,785.54
	DPS-8	44.7830	9.5801	12.036145	12.1694	861.048
	DPS-16	44.7675	8.6039	13.417057	12.1601	863.484
	DPS-32	44.7571	9.9491	15.724576	12.2621	869.052

Chapter 6

Scattering from Objects on a Stratified Medium

6.1 Introduction

Scattering analysis of objects above, straddling, and/or embedded in a stratified medium is one of the most challenging yet important problems in the computational electromagnetics community. Typical applications of scattering from stratified media are commonly found in patch antenna design, interconnect and monolithic microwave integrated circuit simulations, biomedical imaging, nondestructive testing, target identification, geophysical exploration, and remote sensing [61–63]. Traditional modeling of such problems is often performed using integral-equation based methods with a multilayer Green's function [2, 62, 64]. Although these methods yield very accurate results, the numerical evaluation of the multilayer Green's function is very difficult and prone to convergence issues. Moreover, the integral-equation based methods are not efficient for analyzing highly inhomogeneous structures.

In this chapter, we develop an inhomogeneous ABC for the finite-element truncation. Similar to the traditional first-order ABC, the proposed inhomogeneous ABC can be easily incorporated into the existing FEM frameworks. Using the parallel FETI-DP algorithm developed in the previous chapter, the proposed boundary condition enables large-scale simulations of problems with a stratified medium. For electrically large objects, the far-field calculations can be prohibitively expensive, especially in the vectorial imaging process where far-fields need to be evaluated billions of times in order to form a sharp image for an object even with a dimension of 100-wavelength [70]. Therefore, a fast far-field calculation approach, based on the idea of MLFMA, is developed for the stratified medium. Finally, numerical examples are presented to demonstrate the solution accuracy and large-scale simulation capability of the proposed method.

6.2 Formulation

In this section, the inhomogeneous ABC in a stratified medium is derived. The fast far-field calculation using MLFMA is discussed subsequently. Since the inhomogeneous ABC can be as easily incorporated into the parallel FETI-DP algorithm as the traditional ABC, the discussion about this part is omitted.

6.2.1 Inhomogeneous ABC in a Stratified Medium

The inhomogeneous ABC for a stratified medium can be obtained simply by modifying the traditional ABC in free-space with the desired material properties

$$\begin{aligned}\hat{n} \times \left(\frac{1}{\mu_m}\nabla \times \mathbf{E}\right) &+ \mathrm{j}\omega\frac{1}{\eta_m}\hat{n} \times (\hat{n} \times \mathbf{E}) = \\ &\hat{n} \times \left(\frac{1}{\mu_m}\nabla \times \mathbf{E}^{\mathrm{inc}}\right) + \mathrm{j}\omega\frac{1}{\eta_m}\hat{n} \times (\hat{n} \times \mathbf{E}^{\mathrm{inc}}).\end{aligned} \tag{6.1}$$

Although the expression is fairly simple, the incident field $\mathbf{E}^{\mathrm{inc}}$ is no longer the plane wave in the free-space. To get the incident field analytically, let us consider an M-layer medium placed in the XY plane with the permittivity and permeability in each layer denoted by ϵ_m and μ_m ($m = 1, 2, \ldots, M$), as illustrated in Fig. 6.1. With a uniform plane wave propagating towards the origin, the solution within the mth layer, without the presence of the scatterers, can be expressed as the summation of forward and backward waves. Depending on the polarizations, $\mathbf{E}^{\mathrm{inc}}$ has different forms.

6.2.2 $\hat{\phi}$-polarization

For a $\hat{\phi}$-polarized plane wave incidence, the electric field in the mth-layer can be represented by the summation of the forward and backward waves

$$\mathbf{E}_m^{\phi} = \hat{\phi} A_m^{\phi} \left[1 + R_m^{\phi} \mathrm{e}^{-\mathrm{j}(\mathbf{k}_m^{\mathrm{r}} - \mathbf{k}_m^{\mathrm{i}})\cdot\mathbf{r}}\right] \mathrm{e}^{-\mathrm{j}\mathbf{k}_m^{\mathrm{i}}\cdot\mathbf{r}}, \tag{6.2}$$

where A_m^{ϕ} and R_m^{ϕ} are the magnitude of the forward electric field and the reflection coefficient of electric field in the mth layer, respectively, and $\mathbf{k}_m^{\mathrm{i}}$

and $\mathbf{k}_m^{\mathrm{r}}$ are the wave vectors of the forward and backward waves, which are given by

$$\mathbf{k}_m^{\mathrm{i}} = -\hat{x}k_m^x - \hat{y}k_m^y - \hat{z}k_m^z, \tag{6.3}$$

$$\mathbf{k}_m^{\mathrm{r}} = -\hat{x}k_m^x - \hat{y}k_m^y + \hat{z}k_m^z, \tag{6.4}$$

with

$$k_m^x = k_M \sin\theta\cos\phi, \tag{6.5}$$

$$k_m^y = k_M \sin\theta\sin\phi, \tag{6.6}$$

$$k_m^z = \sqrt{k_m^2 - k_M^2 \sin^2\theta}, \tag{6.7}$$

$$\eta_m = \sqrt{\mu_m/\epsilon_m}, \tag{6.8}$$

$$k_m = \omega\sqrt{\mu_m\epsilon_m}. \tag{6.9}$$

Note that the phase matching condition is used in (6.5) and (6.6). For a plane wave with $\mathrm{e}^{-\mathrm{j}\mathbf{k}\cdot\mathbf{r}}$ phase delay, we have

$$\mathbf{H} = \frac{1}{\omega\mu}\mathbf{k}\times\mathbf{E}. \tag{6.10}$$

Hence, the corresponding magnetic field in the mth layer can be written as

$$\mathbf{H}_m^{\phi} = \frac{1}{\omega\mu_m}A_m^{\phi}\left[\mathbf{k}_m^{\mathrm{i}} + \mathbf{k}_m^{\mathrm{r}}R_m^{\phi}\mathrm{e}^{-\mathrm{j}(\mathbf{k}_m^{\mathrm{r}}-\mathbf{k}_m^{\mathrm{i}})\cdot\mathbf{r}}\right]\times\hat{\phi}\mathrm{e}^{-\mathrm{j}\mathbf{k}_m^{\mathrm{i}}\cdot\mathbf{r}}. \tag{6.11}$$

By enforcing that the tangential fields be continuous across the $(m+1)$th interface between the mth and $(m+1)$th layers, we obtain the recursive formulation for R_{m+1}^{ϕ} and A_{m+1}^{ϕ}

$$R_{m+1}^{\phi} = \frac{R_{m+1,m}^{\phi} + R_m^{\phi}\mathrm{e}^{-2\mathrm{j}k_m^z z_{m+1}}}{1 + R_{m+1,m}^{\phi}R_m^{\phi}\mathrm{e}^{-2\mathrm{j}k_m^z z_{m+1}}}\mathrm{e}^{2\mathrm{j}k_{m+1}^z z_{m+1}}, \tag{6.12}$$

$$A_{m+1}^{\phi} = A_m^{\phi}\frac{\mathrm{e}^{\mathrm{j}k_m^z z_{m+1}} + R_m^{\phi}\mathrm{e}^{-\mathrm{j}k_m^z z_{m+1}}}{\mathrm{e}^{\mathrm{j}k_{m+1}^z z_{m+1}} + R_{m+1}^{\phi}\mathrm{e}^{-\mathrm{j}k_{m+1}^z z_{m+1}}}, \tag{6.13}$$

where z_{m+1} denotes the position of the interface and the Fresnel reflection coefficient $R_{m+1,m}^{\phi}$ is

$$R_{m+1,m}^{\phi} = \frac{\mu_m k_{m+1}^z - \mu_{m+1}k_m^z}{\mu_m k_{m+1}^z + \mu_{m+1}k_m^z}. \tag{6.14}$$

6.2.3 $\hat{\theta}$-polarization

For a $\hat{\theta}$-polarized plane wave incidence, the magnetic field in the mth-layer can be represented by the summation of the forward and backward waves

$$\mathbf{H}_m^\theta = \hat{\phi}\frac{1}{\eta_m}A_m^\theta \left[-1 + R_m^\theta \mathrm{e}^{-\mathrm{j}(\mathbf{k}_m^\mathrm{r} - \mathbf{k}_m^\mathrm{i})\cdot\mathbf{r}}\right]\mathrm{e}^{-\mathrm{j}\mathbf{k}_m^\mathrm{i}\cdot\mathbf{r}}, \tag{6.15}$$

where A_m^θ and R_m^θ are the magnitude of the forward magnetic field and the reflection coefficient of the magnetic field in the mth layer, respectively. Using the plane wave equation

$$\mathbf{E} = -\frac{1}{\omega\epsilon}\mathbf{k}\times\mathbf{H}, \tag{6.16}$$

the corresponding electric field in the mth layer can be written as

$$\mathbf{E}_m^\theta = \frac{1}{k_m}A_m^\theta \left[\mathbf{k}_m^\mathrm{i} - \mathbf{k}_m^\mathrm{r} R_m^\theta \mathrm{e}^{-\mathrm{j}(\mathbf{k}_m^\mathrm{r} - \mathbf{k}_m^\mathrm{i})\cdot\mathbf{r}}\right]\times\hat{\phi}\mathrm{e}^{-\mathrm{j}\mathbf{k}_m^\mathrm{i}\cdot\mathbf{r}}. \tag{6.17}$$

By enforcing that the tangential fields be continuous across the $(m+1)$th interface between the mth and $(m+1)$th layers, we obtain the recursive formulation for R_{m+1}^θ and A_{m+1}^θ

$$R_{m+1}^\theta = \frac{R_{m+1,m}^\theta + R_m^\theta \mathrm{e}^{-2\mathrm{j}k_m^z z_{m+1}}}{1 + R_{m+1,m}^\theta R_m^\theta \mathrm{e}^{-2\mathrm{j}k_m^z z_{m+1}}}\mathrm{e}^{2\mathrm{j}k_{m+1}^z z_{m+1}}, \tag{6.18}$$

$$A_{m+1}^\theta = A_m^\theta \frac{\eta_{m+1}}{\eta_m}\frac{\mathrm{e}^{\mathrm{j}k_m^z z_{m+1}} - R_m^\theta \mathrm{e}^{-\mathrm{j}k_m^z z_{m+1}}}{\mathrm{e}^{\mathrm{j}k_{m+1}^z z_{m+1}} - R_{m+1}^\theta \mathrm{e}^{-\mathrm{j}k_{m+1}^z z_{m+1}}}, \tag{6.19}$$

where z_{m+1} denotes the position of the interface and the Fresnel reflection coefficient $R_{m+1,m}^\theta$ is

$$R_{m+1,m}^\theta = \frac{\epsilon_{m+1}k_m^z - \epsilon_m k_{m+1}^z}{\epsilon_{m+1}k_m^z + \epsilon_m k_{m+1}^z}. \tag{6.20}$$

The evaluation of (6.12) and (6.18) requires the reflection coefficients at the bottom layer as initial values. If an infinite ground plane is present at $z = z_1$ in the bottom layer, we have

$$R_1^\phi = R_1^\theta = -\mathrm{e}^{2\mathrm{j}k_1^z z_1}. \tag{6.21}$$

Otherwise, if the bottom layer extends to the negative infinity, we have

$$R_1^{\phi} = R_1^{\theta} = 0. \tag{6.22}$$

6.2.4 Fast Far-Field Calculation

The proposed inhomogeneous ABC can be implemented by replacing the traditional ABC in the parallelized FETI-DP algorithm proposed in the previous chapter to enable large-scale simulations. Once the equivalent electric and magnetic surface currents are obtained, the scattered far-fields can be calculated using the multilayer Green's function. A simpler approach is to employ the *Rayleigh-Carson reciprocity theorem*

$$\int_V \mathbf{E}^{\text{sc}} \cdot \mathbf{J}_2 \mathrm{d}\mathbf{r} = \int_S (\mathbf{E}_2 \cdot \mathbf{J}_{\text{s}} - \mathbf{H}_2 \cdot \mathbf{M}_{\text{s}}) \mathrm{d}\mathbf{r} \tag{6.23}$$

in the far-field calculation, where $\mathbf{J}_2$ denotes an arbitrary electric current and $\mathbf{E}_2$ and $\mathbf{H}_2$ are the electric and magnetic fields radiated by $\mathbf{J}_2$ in the presence of the multilayer media. Choosing an infinitesimal electric current element, either θ-polarized or ϕ-polarized, and placing it at the observation point in the far zone, we can compute the electric field $\mathbf{E}_m^{\theta,\phi}$ and the magnetic field $\mathbf{H}_m^{\theta,\phi}$ in the presence of the multilayer media without the scatterers, where $\mathbf{E}_m^{\theta}$ and $\mathbf{H}_m^{\theta}$ are due to the θ-polarized electric current element, and $\mathbf{E}_m^{\phi}$ and $\mathbf{H}_m^{\phi}$ are due to the ϕ-polarized electric current element. In the backscatter case, $\mathbf{E}_m^{\theta}$, $\mathbf{H}_m^{\theta}$, $\mathbf{E}_m^{\phi}$, and $\mathbf{H}_m^{\phi}$ are given in (6.17), (6.15), (6.2), and (6.11), respectively. Hence, from the reciprocity theorem, we can obtain the scattered far-field in the free-space as

$$E_{\theta,\phi}^{\text{sc}}(\mathbf{r}) = -\mathrm{j}\frac{k_0\eta_0}{4\pi r} \int_S \left[\mathbf{J}_{\text{s}} \cdot \mathbf{E}_m^{\theta,\phi} - \mathbf{M}_{\text{s}} \cdot \mathbf{H}_m^{\theta,\phi}\right] \mathrm{d}\mathbf{r}'. \tag{6.24}$$

The direct evaluation of (6.24) can be prohibitively expensive for electrically large objects, since it requires $O(PQ)$ operations, where P and Q respectively represent the number of field and source points on the far-field plane and the inhomogeneous ABC surface S. To speed up the far-field calculation, the MLFMA was adopted to reduce the computational complexity to $O(P \log Q)$ [2]. In the context of MLFMA, the surface S is enclosed by a box, which is then partitioned into eight sub-boxes. Each sub-box is recursively partitioned until the smallest boxes are about one quater-wavelength in size. The boxes with the same size are grouped as a level, with level 0 and L representing the largest and smallest box(es), respectively. Inside each smallest box, the radiation patterns, produced by the equivalent electric current $\mathbf{J}_\mathrm{s}$ and magnetic current $\mathbf{M}_\mathrm{s}$, are gathered to the box center $\mathbf{r}_m$. After that, the radiation patterns at the current box center $\mathbf{r}_m$ are gathered to the center of their parent box $\mathbf{r}_m^\mathrm{p}$ by multiplying the phase shifting $\mathrm{e}^{\mathrm{j}\mathbf{k}\cdot(\mathbf{r}_m-\mathbf{r}_m^\mathrm{p})}$. This radiation pattern gathering process keeps going until the center of the largest cube is reached. Finally, the scattered far-fields can be very efficiently obtained by the spectral interpolation of the radiation patterns at the largest cube center.

It is worth mentioning that the spectral sampling rate in each level of the boxes is significantly higher than the traditional MLFMA developed for free-space scattering analysis due to the highly oscillating $R_m^{\theta,\phi}$ terms, especially when the thick dielectric layers are encountered. The high spectral sampling rate in the inhomogeneous MLFMA inevitably undermines the efficiency of far-field calculation. Fortunately, for a specific working frequency and structure of the stratified medium, $R_m^{\theta,\phi}$ are only determined by the observation angle. Hence, the efficient far-field calculation can be decomposed into two parts: the forward wave contribution and backward wave contribution. The forward wave contribution is calculated the same as the traditional MLFMA. The backward wave contribution is carried out in two steps. In the first step, the $R_m^{\theta,\phi}$ terms are not considered during the aggregation process so that the spectral sampling rate is kept the same as the traditional MLFMA's sampling rate. In the second step, after aggregating to the top level, the interpolated radiation patterns at the desired observation angle are multiplied by $R_m^{\theta,\phi}$ to produce the correct far fields.

6.3 Numerical Results

In this section, three verification examples are first presented to demonstrate the solution accuracy of our proposed method. After verifications, an electrically large example is simulated to show the capability of the proposed method for a large-scale scattering analysis with the presence of a stratified medium.

6.3.1 A PEC Sphere above an Infinite Ground Plane

The first verification example is the scattering from a PEC sphere above an infinite ground plane, as shown in Fig. 6.2. The sphere has a radius of 0.2 m and is 0.3 m above the ground. An inhomogeneous ABC box with edge length of 1.0 m is used to truncate the computational domain. The incident plane wave propagates towards the negative z-direction at frequency 1 GHz. With a mesh size of 0.15 m, the computational domain is discretized into 4,003 curvilinear tetrahedral elements. The parallel FETI-DP algorithm is used to simulate this example on six cores with each core handling one subdomain. The convergence histories for the $\phi\phi$- and $\theta\theta$-polarizations are given in Fig. 6.3, which both converge to 10^{-3} in 25 iterations. The calculated bistatic RCS results are plotted in Fig. 6.4, both showing a good agreement with FEKO's simulation results.

6.3.2 A Dielectric Sphere on a Stratified Medium

The second verification example is a dielectric sphere sitting on a two-layered medium, whose geometrical configurations are given in Fig. 6.5. The dielectric sphere, with a radius of 1 m and a relative permittivity of 4.0, is surrounded by an air box with dimensions of 8 m × 8 m × 5 m. Beneath the dielectric sphere is a two-layered medium with each layer having a thickness of 1 m. The relative permittivity for the bottom layer is $6.5 - \mathrm{j}0.6$ and 2.56 for the other layer. The working frequency is set to 100 MHz. The computational domain is discretized into 170,969 curvilinear tetrahedral elements with a mesh size about 0.5λ. The calculations were performed by the parallel FETI-DP code with 24 cores and 96 subdomains. The convergence histories for the two different polarizations with and without an infinite ground plane are depicted in Fig. 6.6. Because the ground plane increases the multi-reflections between layers, a slowdown in the convergence rate is observed for the cases with an infinite ground plane. The bistatic RCS figures with and without the presence of the ground plane are shown in Figs. 6.7 and 6.8, respectively. As can be seen, all the figures show an excellent agreement with FEKO's simulation results.

6.3.3 A Dielectric Cuboid over a Stratified Medium

The final verification example is a dielectric cuboid over a stratified medium, as given in Fig. 6.9. The cuboid, with the relative permittivity of 4.0 and dimensions of 2 m × 2 m × 0.5 m, is placed 0.1 m above a two-layered medium. The top layer ($\epsilon_\mathrm{r} = 2.56$) of the stratified medium is 1 m thick and the bottom layer ($\epsilon_\mathrm{r} = 6.5 - \mathrm{j}0.6$) is 1.5 m thick. The computational domain is truncated by an inhomogeneous ABC with the dimensions of 5 m × 5 m × 4.6 m. The incident plane wave illuminates the scatterer in the normal direction at 300 MHz. The computational domain is discretized into 138,368 curvilinear tetrahedral elements and then partitioned into 96 subdomains for the parallel FETI-DP computation. The convergence histories are plotted in Fig. 6.10 for the two different polarizations with and without an infinite ground plane. Since the bottom layer is lossy and thick, the infinite ground plane has small effect on the convergence rate. The bistatic RCS figures with and without the presence of the ground plane are respectively plotted in Figs. 6.11 and 6.12, all overlapping with the corresponding FEKO's simulation results. Because the fields are significantly attenuated when they reach to the position of the infinite ground plane, we see very close agreement between the RCS results with and without the ground plane.

6.3.4 Scattering from a Microring Resonator

After three verification examples, we simulate a mircoring resonator to demonstrate the capability of our proposed method in handling large-scale scattering analysis with the presence of a stratified medium. The ring resonator, as illustrated in Fig. 6.13, has an inner radius of 4.5 μm and an outer radius of 5.5 μm. The top layer of the ring is made of $\mathrm{Si_3N_4}$ with a thickness of 0.4 μm. The bottom layer of the ring is made of $\mathrm{SiO_2}$ with a thickness of 0.1 μm. The waveguide bus, with a 1-um width, has exactly the same configurations as the ring in the vertical direction. The smallest distance between the ring and the bus is 0.55 μm. Both the ring and the bus are sitting on a two-layered dielectric substrate, with the top ($\mathrm{SiO_2}$) and bottom (Si) layers measuring at 2.9 μm and 0.1375 μm in the vertical direction, respectively. The air box on the top of the $\mathrm{SiO_2}$ substrate has a thickness of 1.05 μm. The entire computational domain, which is enclosed by the inhomogeneous ABC, is 14 μm × 15.5 μm × 4.0875 μm.

With the interested free-space wavelength of 0.55 μm, this example yields 5,121,590 curvilinear tetrahedral elements and 101,706,582 total DoFs when third-order vector basis functions are adopted to represent the unknown field. With 1,920 subdomains and 240 cores employed in the parallel computing, the computational times for the $\phi\phi$- and $\theta\theta$-polarizations are 14.1 and 16.9 minutes, respectively. The peak memory consumption for both cases is 1.04 TB. The convergence histories are plotted in Fig. 6.14; both converged to 10^{-3} in less than 250 iterations. The calculated bistatic RCS results for the $\phi\phi$- and $\theta\theta$-polarizations are depicted in Fig. 6.15. As is apparent there, the MLFMA accelerated far-field calculation produces the same results as the direct evaluation of (6.24) even for such a large-scale problem.

6.4 Summary

In this chapter, we presented an inhomogeneous ABC to efficiently perform scattering analysis with the presence of a stratified medium. We derived the analytical expressions for the incident field in the right-hand side of the inhomogeneous ABC. We adopted the parallel FETI-DP algorithm to enable large-scale electromagnetic simulations. We also developed an MLFMA-based fast far-field calculation approach to reduce the computational complexity when a large number of far-field points need to be evaluated. We then presented three verification examples to demonstrate the solution accuracy of our proposed method. Finally, we presented an electrically large example to demonstrate the capability of this method for large-scale electromagnetic modeling of objects in a stratified medium.

6.5 Figures

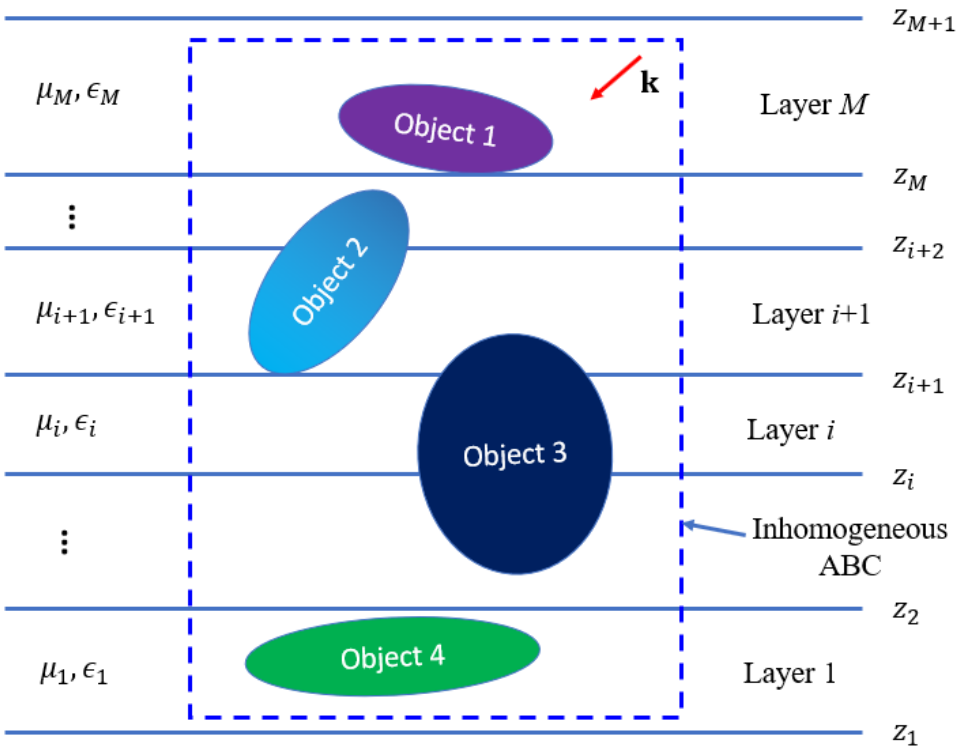

Figure 6.1: Scattering analysis of objects in a stratified medium.

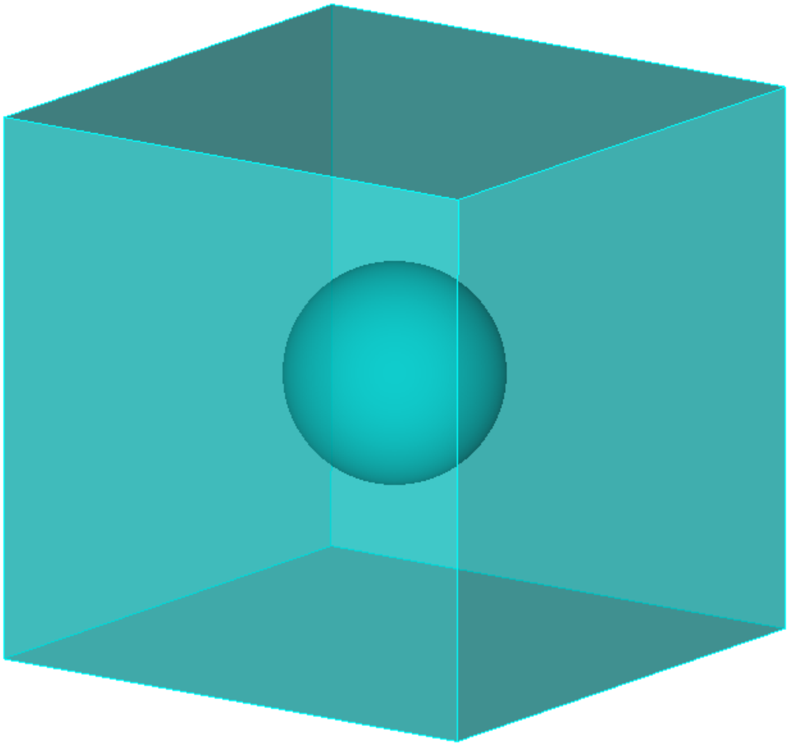

Figure 6.2: A PEC sphere above an infinite ground plane.

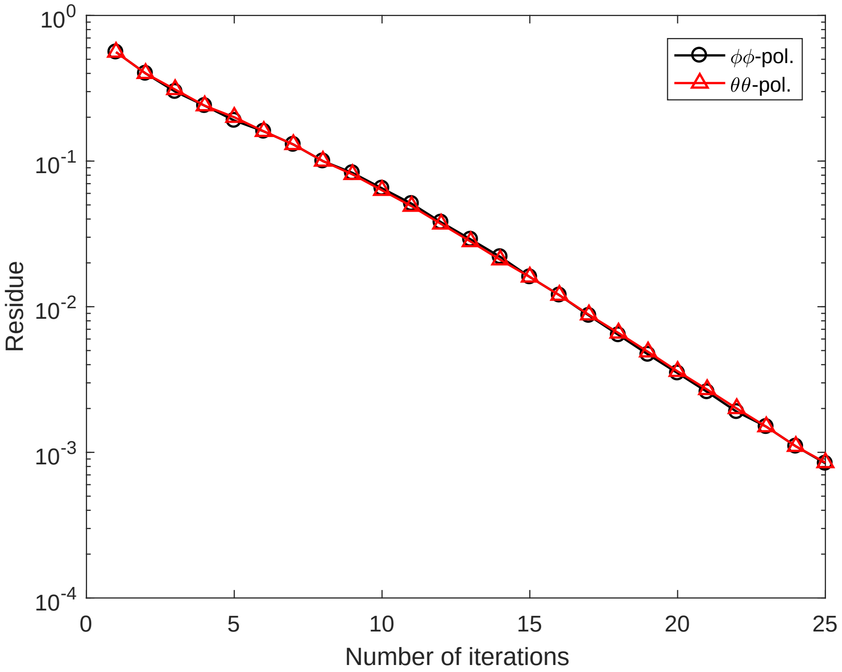

Figure 6.3: Convergence history for the simulation of the PEC sphere above an infinite ground plane.

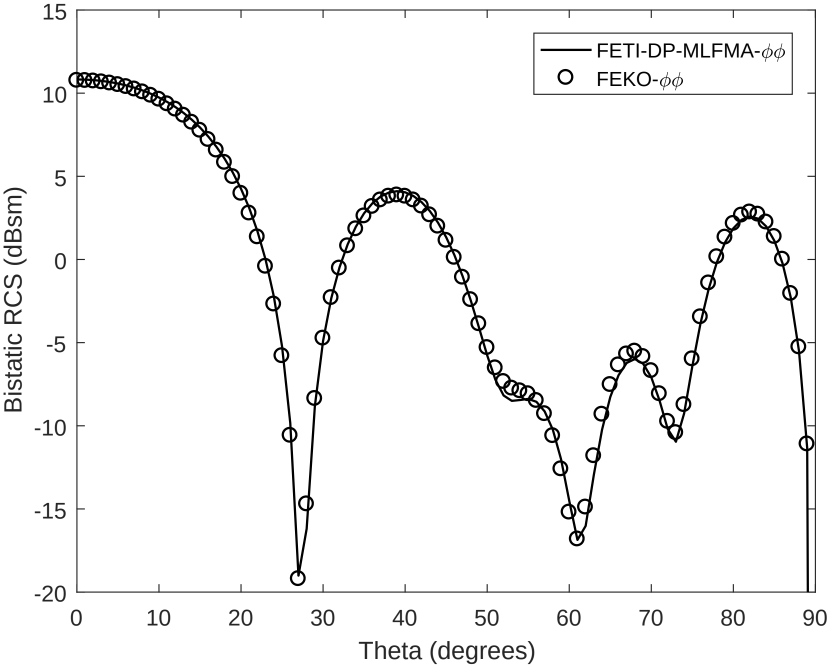

(a)

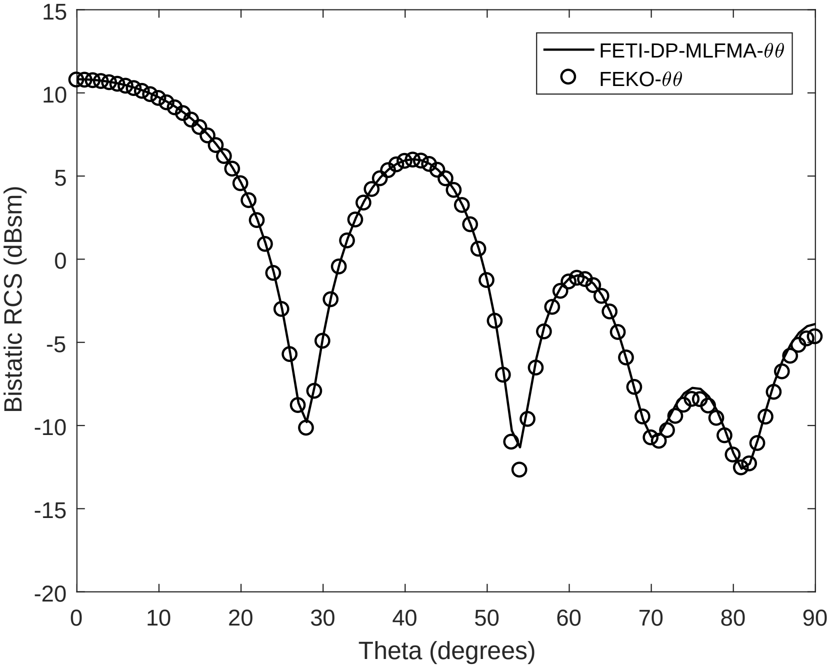

(b)

Figure 6.4: Bistatic RCS of the PEC sphere above an infinite ground plane. (a) $\phi\phi$ polarization. (b) $\theta\theta$ polarization.

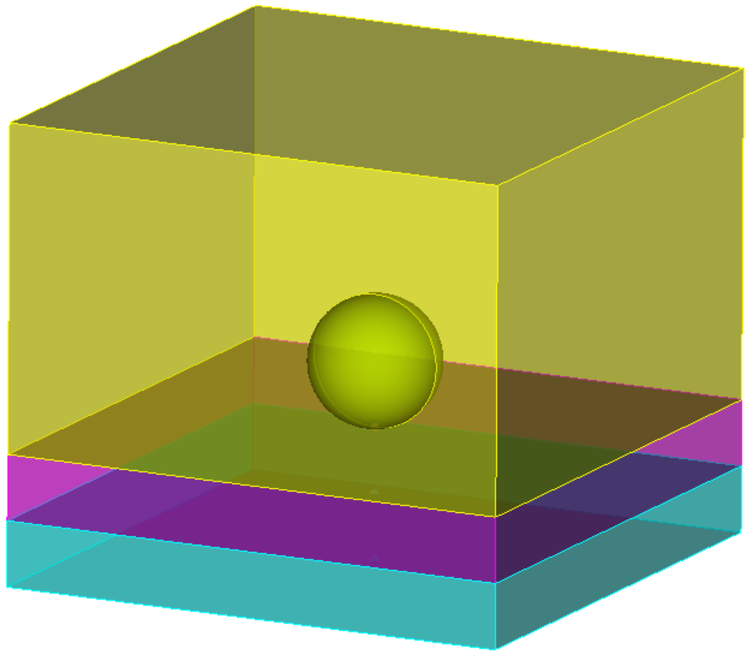

Figure 6.5: A dielectric sphere on a two-layered medium.

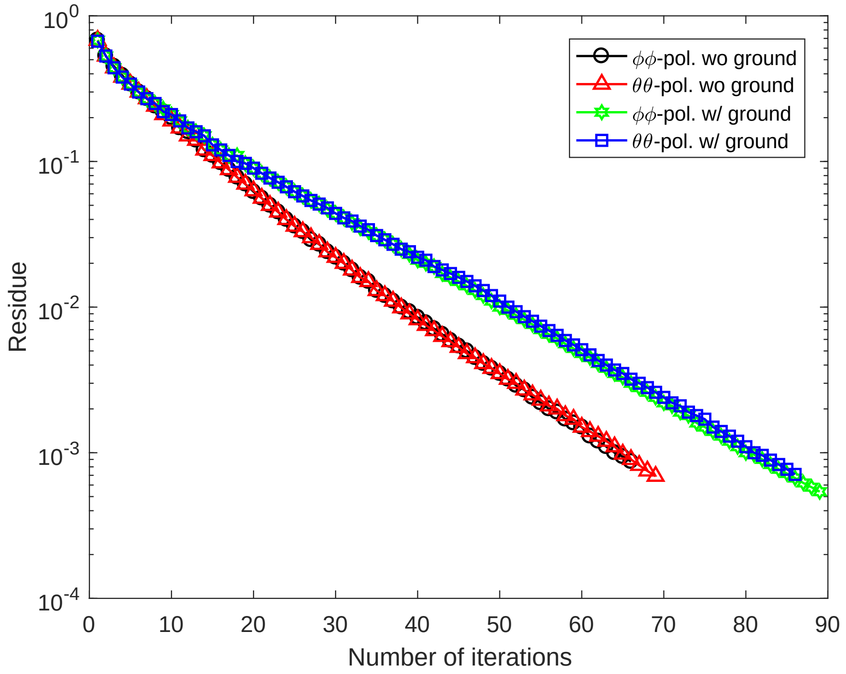

Figure 6.6: Convergence history for the simulation of the dielectric sphere on a two-layered medium.

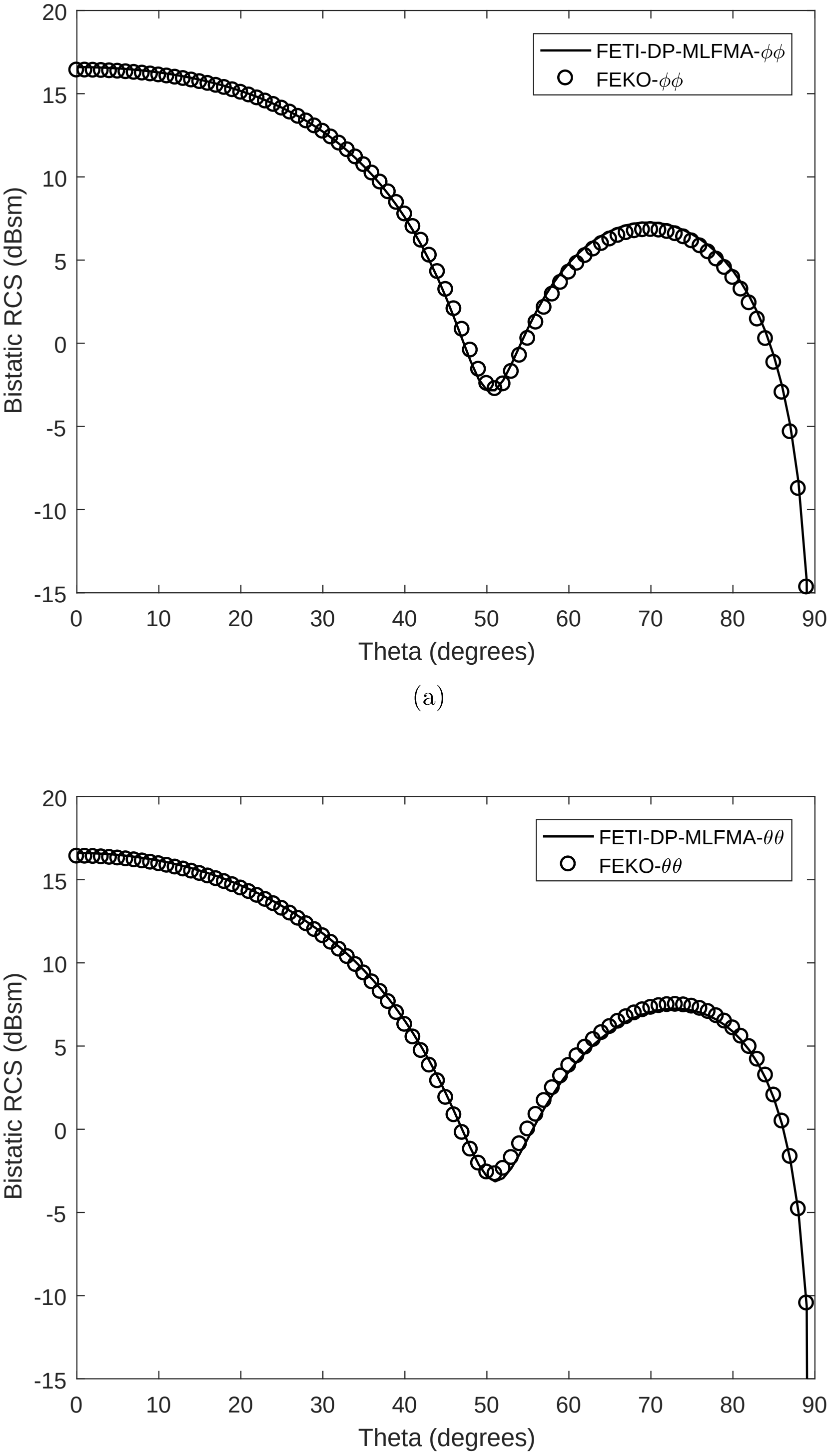

(a)

(b)

Figure 6.7: Bistatic RCS of the dielectric sphere on a two-layer medium. (a) $\phi\phi$ polarization. (b) $\theta\theta$ polarization.

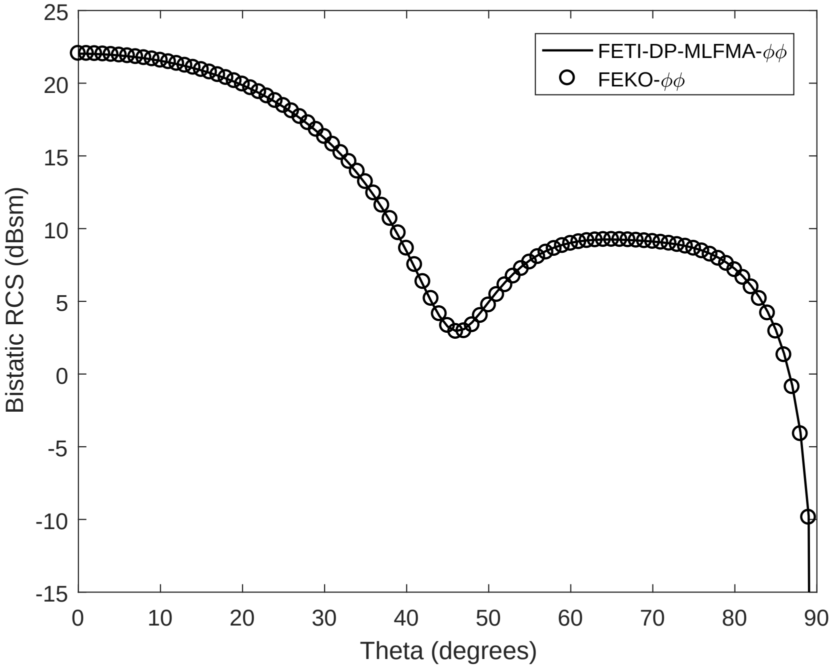

(a)

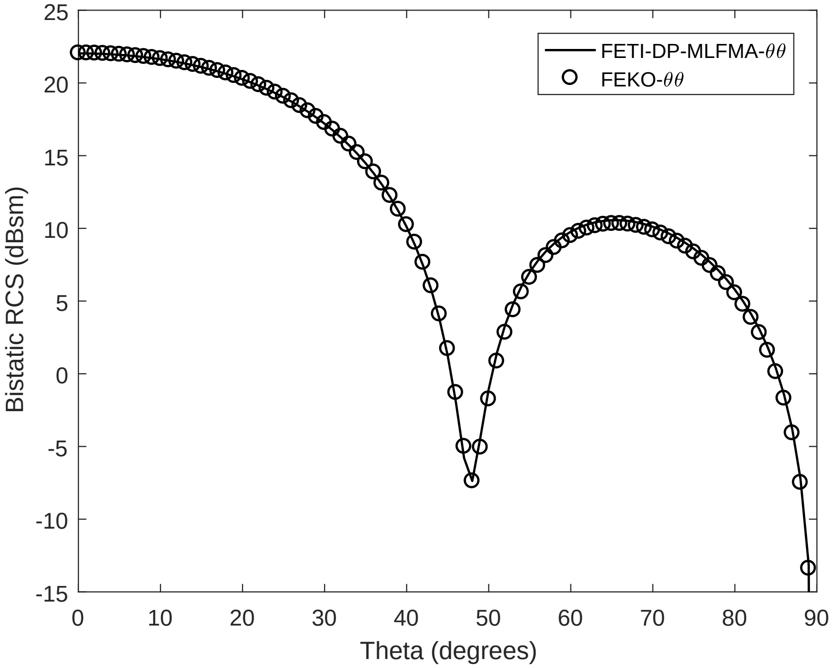

(b)

Figure 6.8: Bistatic RCS of the dielectric sphere on a two-layer medium with an infinite ground plane. (a) $\phi\phi$ polarization. (b) $\theta\theta$ polarization.

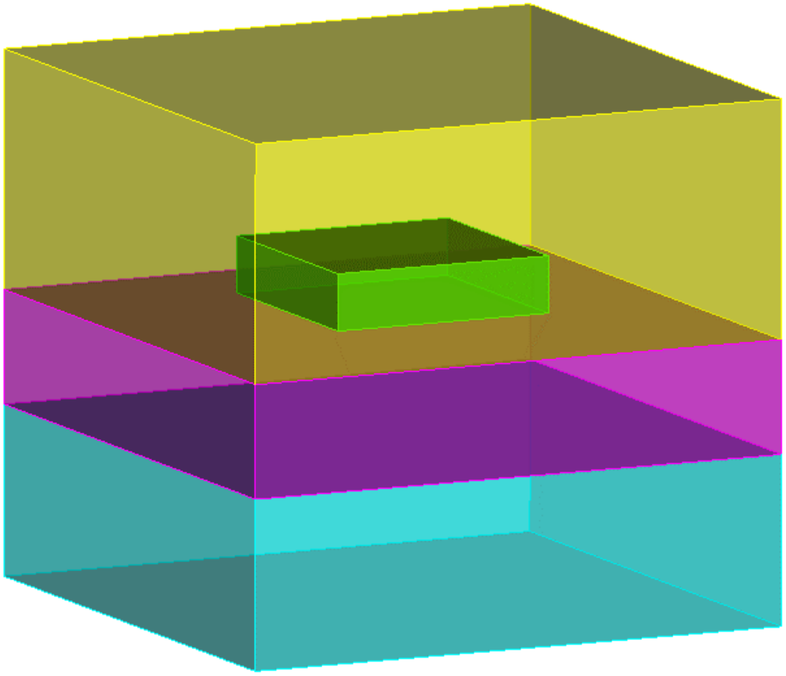

Figure 6.9: A dielectric cuboid over a two-layered medium.

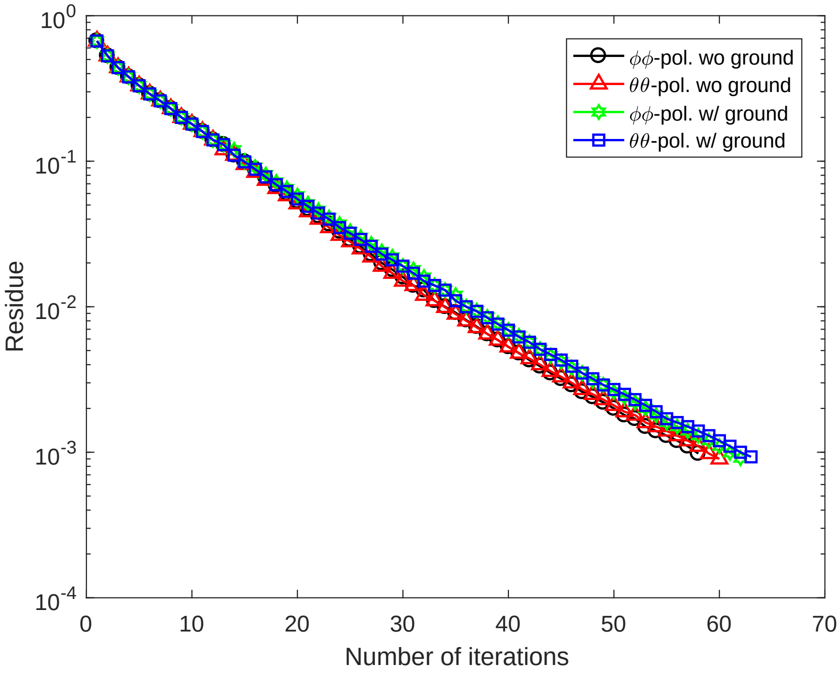

Figure 6.10: Convergence history for the simulation of the dielectric cuboid over a two-layered medium.

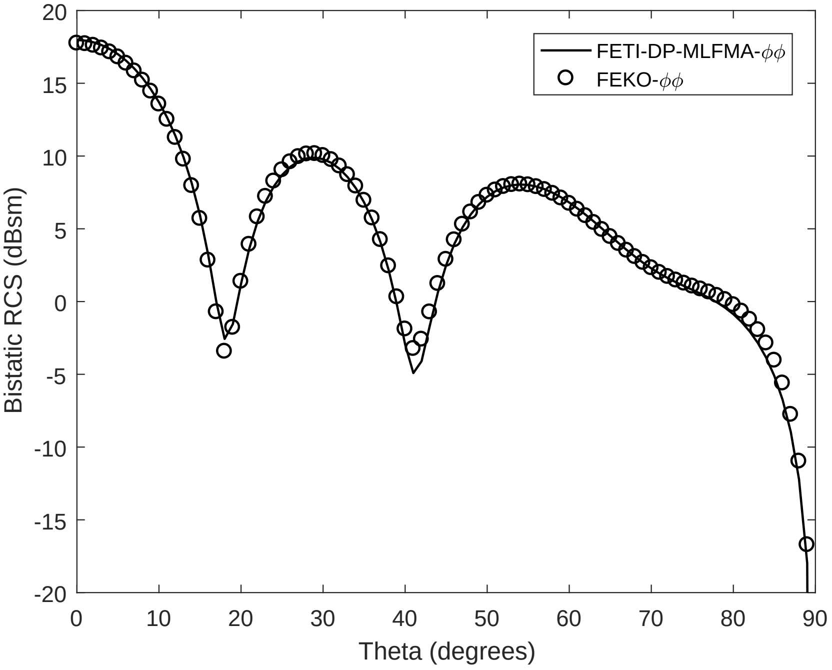

(a)

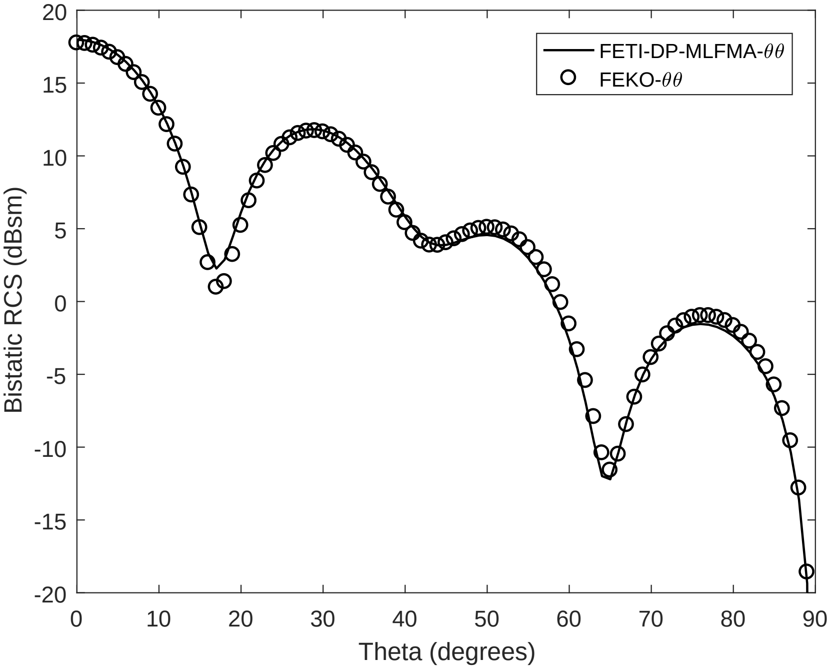

(b)

Figure 6.11: Bistatic RCS of the dielectric cuboid over a two-layer medium. (a) $\phi\phi$ polarization. (b) $\theta\theta$ polarization.

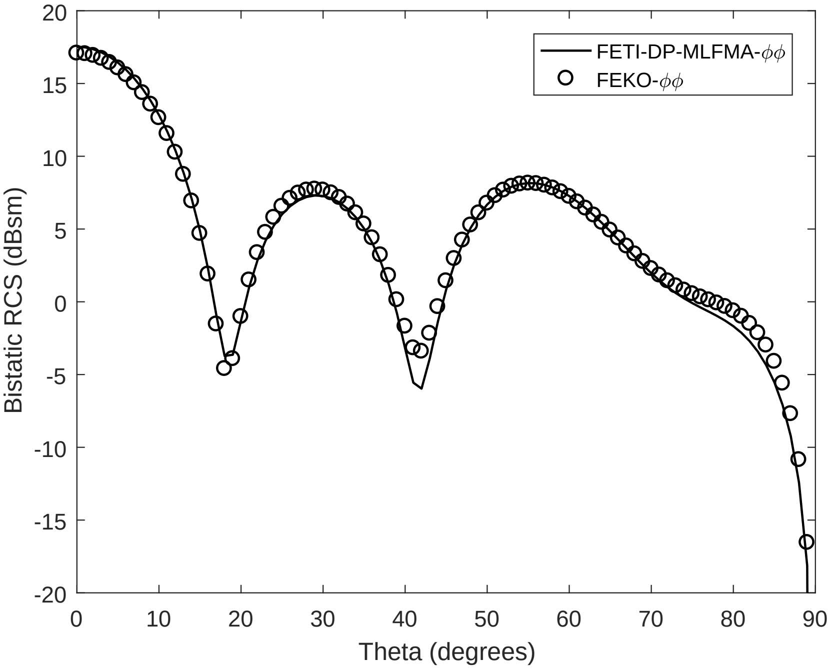

(a)

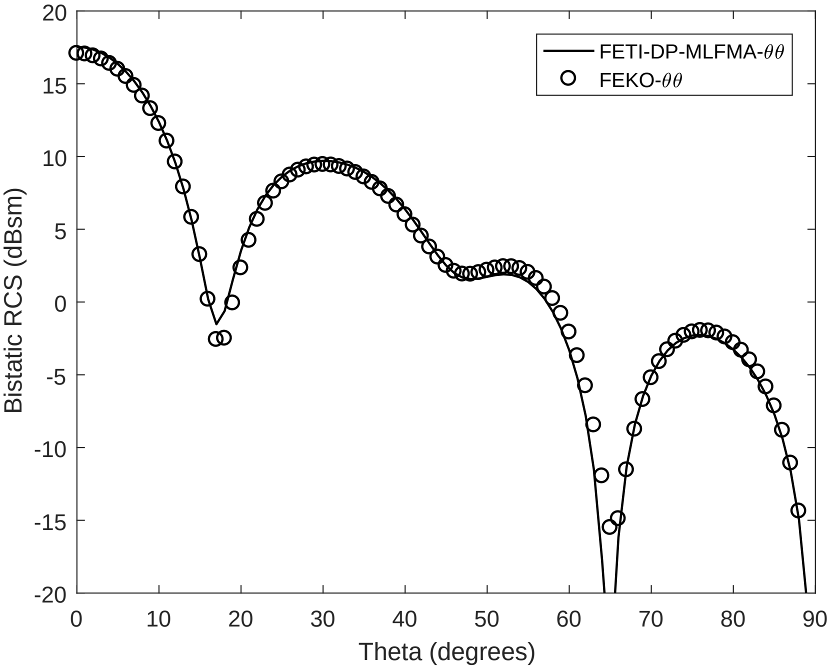

(b)

Figure 6.12: Bistatic RCS of the dielectric cuboid over a two-layered medium with an infinite ground plane. (a) $\phi\phi$ polarization. (b) $\theta\theta$ polarization.

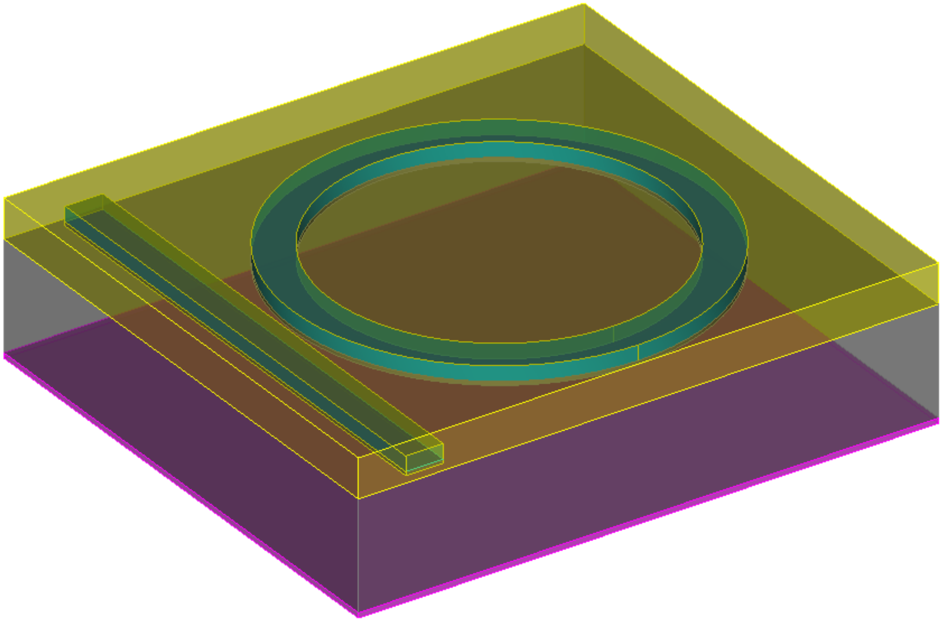

Figure 6.13: A microring resonator on a two-layered substrate.

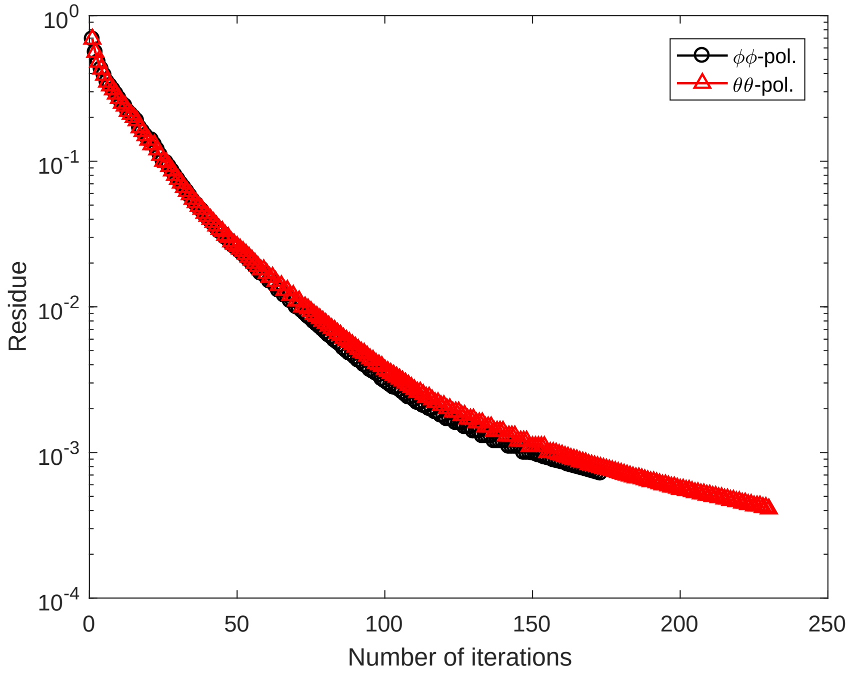

Figure 6.14: Convergence history for the simulation of the microring resonator on a two-layered substrate.

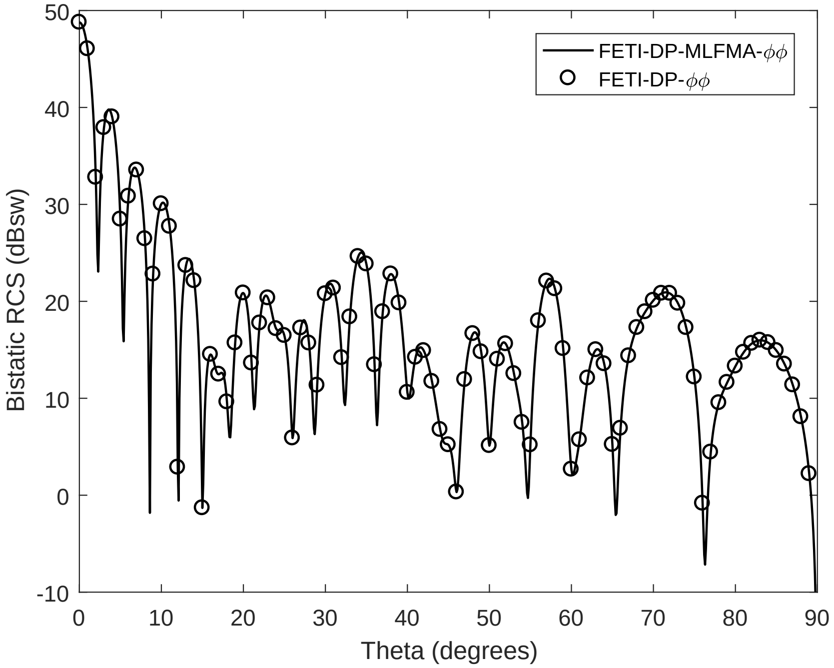

(a)

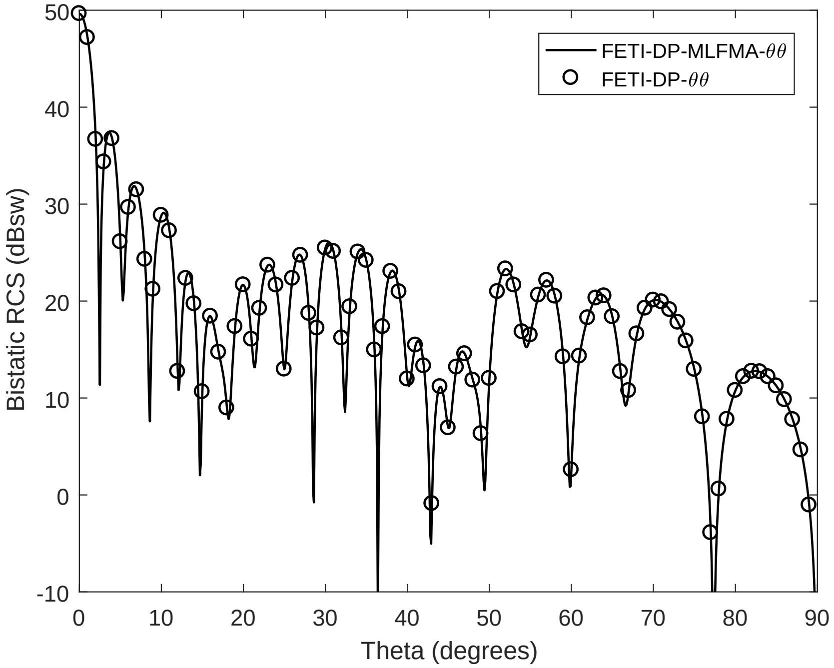

(b)

Figure 6.15: Bistatic RCS of the microring resonator. (a) $\phi\phi$ polarization. (b) $\theta\theta$ polarization.

Chapter 7

Vectorial Imaging of Electrically Large Objects in Coherent Optical Microscopes

7.1 Introduction

Optical microscope systems are widely used in scientific research and industrial applications. Examples span many fields including medical imaging [65,66], cell biology [130], optical lithography [67], semiconductor inspection [68] and metrology [69], and material characterization [131]. To design an imaging system that is optimized for these diverse applications, it is necessary to understand how to calculate the image of an arbitrary scattering object. It is now well-understood that for the case of a small numerical aperture (NA) objective (NA<0.6), paraxial approximation is adequate to be applied in mimicking the wave propagation through an optical system [132]. The paraxial limitation is a result of using the Fresnel approximation and a thin lens model; thus, it allows fast numerical computation through use of the fast Fourier transform (FFT) algorithm [133]. However, the high NA objective lenses used widely in modern optical systems cannot be adequately described by the scalar diffraction theory. Instead, a rigorous vectorial imaging model is required.

To model the vectorial images of objects, several approaches have been proposed. Judkins and Ziolkowski introduced a 2-D model that employed the finite-difference time-domain (FDTD) method to model a Gaussian beam scattered by conducting thin film gratings, after which the scattered field was analyzed by a Fraunhoffer based near- to far-field transform [134]. Liu et al. calculated the incident light and near- to far-field transform using Fresnel diffraction [135]. Török et al. proposed to perform a vectorial far-field transformation on an arbitrary field followed by the application of Debye-Wolf integral [70]. However, each approach above lacks a degree of rigor or generality. Recently, Munro and Török [137] proposed a comprehensive and rigorous vectorial imaging model that is capable of computing the image of an arbitrary object in both transmission and reflection modes. This model, which consists of the illumination light modeling, the numerical computation of scattered field with respect to the object, the near- to far-field transformation and field re-sampling by the m-theory [136], and the image calculation based on geometrical optics approximation and Debye-Wolf integral, paves an intuitive way for researchers to understand the underlying physics. However, the introduced FDTD method used for modeling the light scattering by the object and the m-theory and Debye-Wolf induced an extremely massive number of integrals of Bessel functions, which inevitably give rise to the huge expenditure of computing resources even when dealing with electrically small objects. These inherent drawbacks tremendously hinder the widespread application of this vectorial imaging model in various areas; examples include computational lithography [138, 139] and large-scale optical wafer inspection and metrology [68, 140–144].

For this topic, we propose an elegant scheme to renovate the cumbersome vectorial imaging model step by step. Specifically, the scattered near-fields of an object are computed by the domain decomposition based FETI-DP algorithm. With a Robin-type SOTC-TE to ensure transparent energy flows between subdomain interfaces and a global coarse corner system to improve the iterative convergence of the FETI-DP solution, this method has numerically proven to be very accurate, efficient, and stable. Combined with the developed parallel scheme in Chapter 5, the FETI-DP method is able to solve problems with tens of millions DoFs on computer clusters with more than 1000 cores. The obtained near-fields are then processed by the MLFMA [2] to produce the far-fields at a computational cost of $O(N_f \log N_n)$ instead of the traditional $O(N_n N_f)$, where N_n and N_f are the number of near- and far-field points, respectively. The evaluated far-fields are treated as multiple equivalent magnetic dipoles (EMDs), with their images calculated by the Debye-Wolf integral. The time-consuming integration of the highly oscillating Bessel functions involved in the Debye-Wolf integral, especially when the object is electrically large, is accelerated by a fast linear interpolation, which not only significantly reduces the memory overhead but also improves the overall computation speed by thousands of times.

The remainder of this chapter is organized as follows. Section 7.2 introduces the formulations in computing the image of an arbitrary object.

Since the parallel FETI-DP algorithm for the near-field simulation and the MLMFA for the fast near-field to far-field transformation are already covered in the previous chapters, here we only describe the imaging formulation using the Debye-Wolf integral and its acceleration via a linear interpolation. In Section 7.3, we present several examples to demonstrate the capability and efficiency of the proposed comprehensive scheme in imaging of electrically large objects. Finally we draw the conclusions in Section 7.4.

7.2 Formulation

7.2.1 CCD Imagery from Far-Fields

Given a typical 4f system, as illustrated in Fig. 7.1, the image field $\mathbf{E}$ at position $\mathbf{r}_{\mathrm{d}} = (x_{\mathrm{d}}, y_{\mathrm{d}}, z_{\mathrm{d}})$ on the CCD plane due to an EMD $\mathbf{p}$ positioned at $\mathbf{r}_{\mathrm{p}} = (x_{\mathrm{p}}, y_{\mathrm{p}}, z_{\mathrm{p}})$ on the far-field plane can be calculated using the Debye-Wolf integral [70]

$$E_x = p_x \left[I_0(r) + I_2(r) \cos 2\phi \right] + p_y I_2(r) \sin 2\phi, \tag{7.1}$$

$$E_y = p_y \left[I_0(r) - I_2(r) \cos 2\phi \right] + p_x I_2(r) \sin 2\phi, \tag{7.2}$$

$$E_z = 2\mathrm{j} \left[p_x I_1(r) \cos \phi + p_y I_1(r) \sin \phi \right], \tag{7.3}$$

where

$$r = \sqrt{(x_{\mathrm{d}} - \beta x_{\mathrm{p}})^2 + (y_{\mathrm{d}} - \beta y_{\mathrm{p}})^2}, \tag{7.4}$$

$$\sin \phi = \frac{y_{\mathrm{d}} - \beta y_{\mathrm{p}}}{r}, \tag{7.5}$$

$$\cos \phi = \frac{x_{\mathrm{d}} - \beta x_{\mathrm{p}}}{r}, \tag{7.6}$$

with β being the magnification factor, which is given by

$$\beta = -\frac{f_2}{f_1} = -\frac{\sin \theta_1}{\sin \theta_2}. \tag{7.7}$$

In (7.1)-(7.3), the three integrations $I_0(r)$, $I_1(r)$, and $I_2(r)$ are respectively given by

$$I_0(r) = \int_{\pi-\alpha}^{\pi} s(\theta_2)(\cos\theta_1 + \cos\theta_2)J_0(kr\sin\theta_2)\mathrm{d}\theta_2, \tag{7.8}$$

$$I_1(r) = \int_{\pi-\alpha}^{\pi} s(\theta_2)\sin\theta_2 J_1(kr\sin\theta_2)\mathrm{d}\theta_2, \tag{7.9}$$

$$I_2(r) = \int_{\pi-\alpha}^{\pi} s(\theta_2)(\cos\theta_1 - \cos\theta_2)J_2(kr\sin\theta_2)\mathrm{d}\theta_2, \tag{7.10}$$

where

$$s(\theta_2) = \sqrt{\frac{\cos\theta_2}{\cos\theta_1}}\sin\theta_2 \mathrm{e}^{-\mathrm{j}k(z_\mathrm{d}\cos\theta_2 - z_\mathrm{p}\cos\theta_1)}, \tag{7.11}$$

and α is related to the magnification factor and numerical aperture by

$$-\beta\sin\alpha = \mathrm{NA}. \tag{7.12}$$

7.2.2 Linear Interpolation-Based Fast Integration

The three integrations $I_0(r)$, $I_1(r)$, and $I_2(r)$ are very challenging to evaluate because of their highly oscillating kernels, especially for an electrically large object in a high-NA system. Moreover, each of these integrations needs to be evaluated with different r for MN times, where M is the number of far-field sampling points and N is the number of the CCD image sampling points. Here, the integration at a given r is performed using adaptive high-order Gauss quadrature so that a high-precision result can be achieved. To avoid the direct evaluation of (7.8)-(7.10), an efficient linear interpolation technique is adopted. Specifically, for a given problem, the maximum r can be predetermined using (7.4). Since Bessel functions vary on the order of $\sin(x)$, where x is is the argument, the total number of equidistant interpolation points is given by

$$N_\text{interp} = 30\frac{r_\text{max}k\sin\alpha}{2\pi}, \tag{7.13}$$

where 30 is the sampling points per period.

7.3 Numerical Results

In this section, we present two examples to verify our CCD imaging code, followed by several electrically large examples to fully demonstrate the capability of the proposed method.

7.3.1 Resolution Limit Study

The first verification example is to investigate the resolution limit. The geometries considered here are two sub-wavelength dielectric spheres placed in free space, each with a radius of $\lambda_0/15$ and a relative permittivity of 4.0, as illustrated in Fig. 7.2. The spheres are enclosed by an ABC with dimensions of $1.0\lambda_0 \times 3.0\lambda_0 \times 1.0\lambda_0$. The sampling rate of the far-field points is $1/\lambda_0$ at the plane that is $1000\lambda_0$ above the scatterers. The 4f system used in this example has a NA of 0.85.

The generated CCD images for the two sub-wavelength dielectric spheres with different center-to-center distances ($d = 0.5\lambda_0$, $1.0\lambda_0$, and $2.0\lambda_0$) under the θ-polarized plane wave illumination are given in Fig. 7.3, together with the power intensity plots along line $x = 0$. As shown in those figures, the CCD imagery cannot distinguish the two spheres when the center-to-center distance is $0.5\lambda_0$. At $d = 1.0\lambda_0$, the two spheres on the CCD image are well detected. As d increases to $2.0\lambda_0$, we observe that the hot spots are farther apart. The artifact at the center of the CCD image is believed due to interference.

7.3.2 An L-Shaped PEC Object

The second verification example is the CCD imaging of an L-shpaed PEC object. As shown in Fig. 7.4, the smallest and largest features of that object are $1\lambda_0$ and $3\lambda_0$, respectively. According to our previous resolution limit study, this L-shaped PEC object should be well resolved in the CCD image. Figure 7.5 shows the calculated far-field plot and the CCD image. As expected, the L-shaped geometry is clearly shown in the CCD image. The flipped image is due to the 4f system.

7.3.3 A PEC UI Logo

After two verification examples with relatively small electrical sizes, we start to investigate the capability of our proposed method in imaging electrically large objects. To this end, A PEC UI logo, as depicted in Fig. 7.6, is modeled here. The electrical sizes of this object are $66\lambda_0 \times 86\lambda_0$, with the smallest feature having a dimension of $1\lambda_0$. The computation time is 11 hours with 1,900 cores employed in the parallel computing. The generated CCD image, which is flipped in order to compare more easily with the physical geometry, is given in Fig. 7.7, showing all details of the real structure.

7.3.4 A PEC USAF Target

The next electrically large example is a PEC USAF target, fabricated for testing the resolution of optical imaging systems. The target, as illustrated in Fig. 7.8, is $100\lambda_0$ in length and width. The finest feature dimension is $0.28\lambda_0$. With 1,700 cores employed for computation, the total solution time is 19 hours. The calculated CCD image, flipped in the x and y directions, is depicted in Fig. 7.9. As is apparent there, the CCD image is a good representation of the physical structure, even though the finest features cannot be resolved.

7.3.5 Sub-Wavelength Defect Detection of Nanopatterned Semiconductor Wafer

After two verifications of electrically large examples, it is time to apply the developed method to engineering problems for sub-wavelength defect detection of a semiconductor wafer with nanopatterns. A defect present in nanopatterns significantly affects the functionality of the whole system. Optical microscopy is an effective and nondestructive inspection technique to be performed during nanofabrication in order to maintain a high yield. Understanding its sensitivity through numerical simulation can provide guidance for designing an optimized inspection system.

The problem considered, as shown in Fig. 7.10, is a wafer with polysilicon nanopatterns (grey) and a single isolated polysilicon defect (red) of size 20 nm by 160 nm on a silicon substrate (blue). The coordinates of the defect center are $x = 400$ nm and $y = 800$ nm. The nanopatterns, which are periodic, consist of two different lines that are 20 nm in width, 120 or 260 nm in length, and 110 nm in height. The lines are arranged to form a 0.8 μm by 0.8 μm unit cell, which repeats in a rhombic lattice pattern to form a two-dimensional array [68]. The simulation domain has an area of 6.4 μm by 6.4 μm. The refractive indices of the polysilicon and silicon substrate ($6.4\mu\text{m}\times6.4\mu\text{m}\times0.1\mu\text{m}$) are $4.84-\text{j}0.64$ and $5.48-\text{j}0.25$, respectively, at the wavelength of 532 nm. A rectangular box ($6.4\mu\text{m}\times6.4\mu\text{m}\times0.4\mu\text{m}$) is placed over the substrate, where an absorbing boundary condition is assigned for truncation. The entire domain is discretized into 1,689,312 curvilinear tetrahedra and partitioned into 128 subdomains. Third-order hierarchal vector bases are adopted to expand the unknown electric field and dual variable, which yields 32,196,297 unknowns to approximate the electric field.

Figures 7.11a and 7.11b show the log-scaled far-field power of the nanopatterned wafer without and with a defect. The far-field power difference is plotted in Fig. 7.11c. The signal-to-noise ratio (SNR), defined as the power of the field difference over the power of a defect-free wafer, is about 10^{-8}, which is too small for practical detection. Even if an extremely sensitive device can cope with this small SNR, it is impossible to accurately locate the defect because of the spread hot spot in Fig. 7.11c. The SNR can be significantly enhanced by a 4f system. Figures 7.12a and 7.12b show the CCD images in terms of the magnitude of the electric field for the nanopatterned wafer without and with a defect. Although they look almost identical, their images differ, as is depicted in Fig. 7.12c, which clearly shows the location of the defect. Moreover, the SNR is about 10^{-2}, which is large enough for use in real applications.

7.4 Summary

In this chapter, we proposed a systematic scheme to efficiently model a 4f system with the vectorial imaging technique. We adopted the parallel FETI-DP algorithm to solve the near-field of electrically large objects and an MLFMA accelerated near-field to far-field transformation to significantly reduce the computational cost. After that, we developed a linear interpolation technique to speed up the evaluation of the Debye-Wolf integrals in the imaging formulation. We then numerically studied the resolution limit and presented three verification examples to demonstrate the accuracy and large-scale imaging capability of the proposed scheme. Finally, we presented the imaging of a nanopatterned semiconductor wafer to illustrate the potential of this scheme in detecting sub-wavelength defects.

7.5 Figures

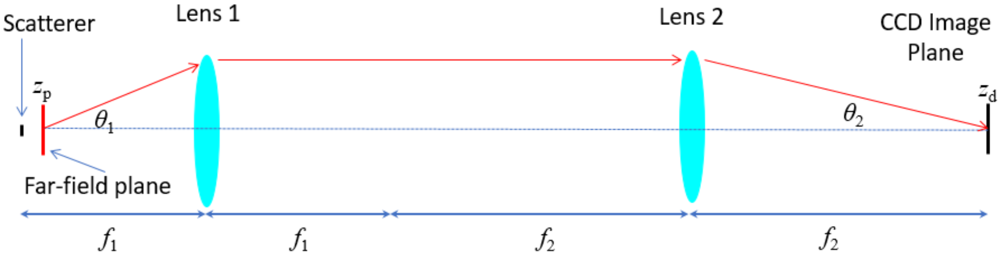

Figure 7.1: Schematic diagram of a typical 4f system.

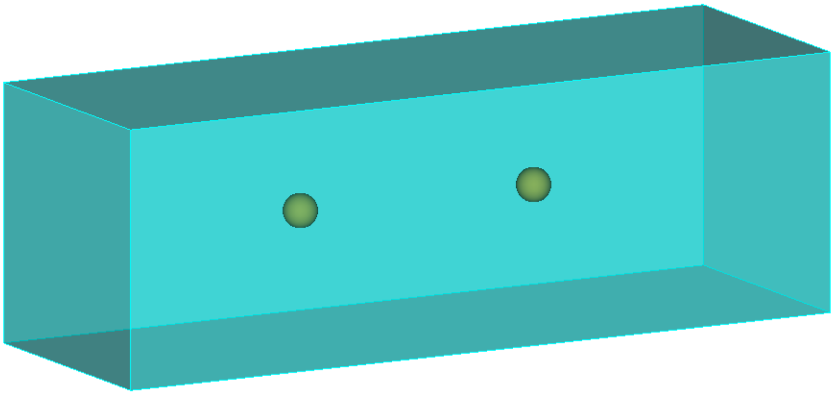

Figure 7.2: Geometry for two sub-wavelength dielectric spheres in the free space.

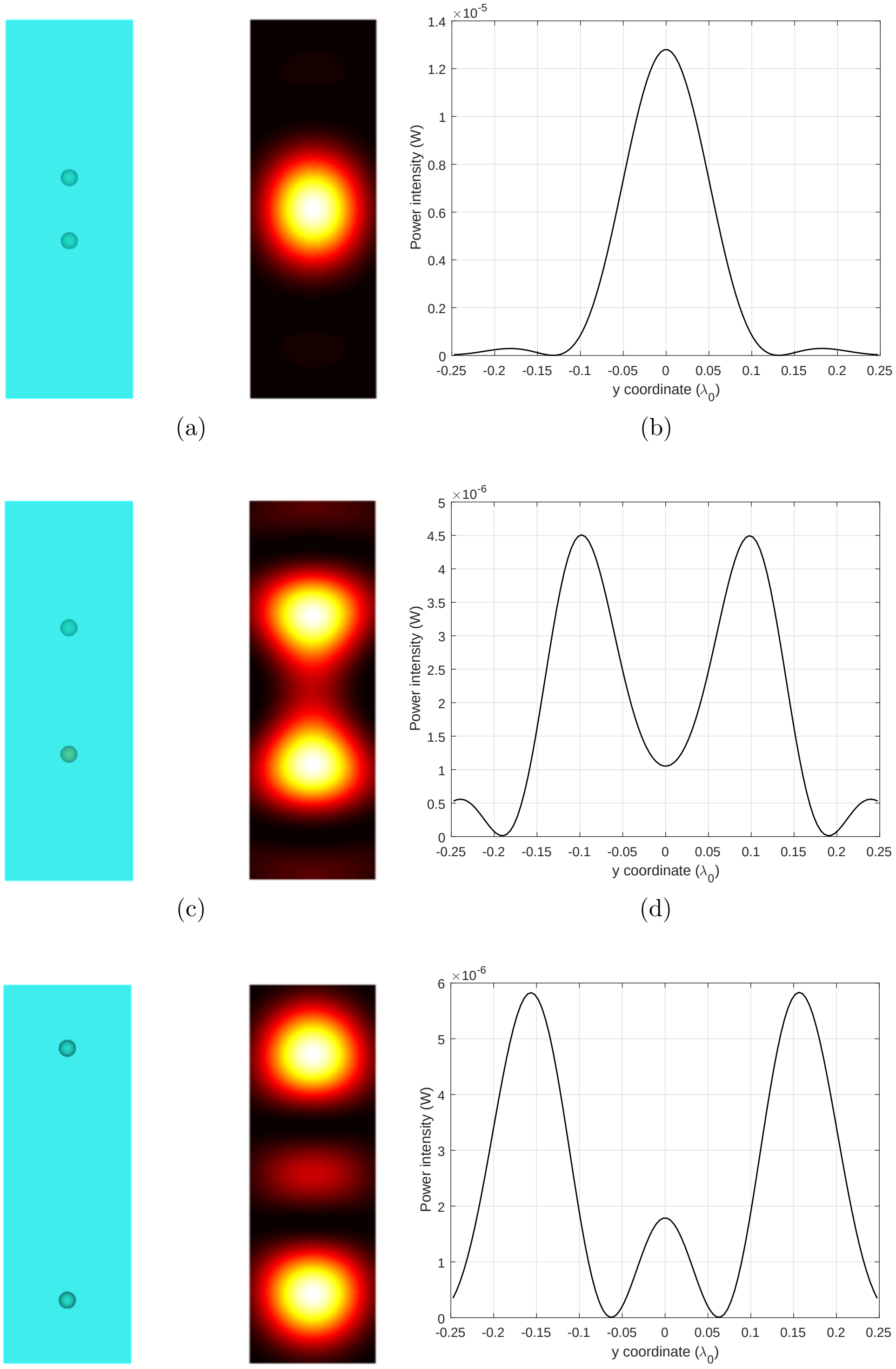

(a) (b)

(c) (d)

(e) (f)

Figure 7.3: CCD images and power intensity plots for the two sub-wavelength dielectric spheres with difference center-to-center distances. (a) and (b) $d = 0.5\lambda_0$. (c) and (d) $d = 1.0\lambda_0$. (e) and (f) $d = 2.0\lambda_0$.

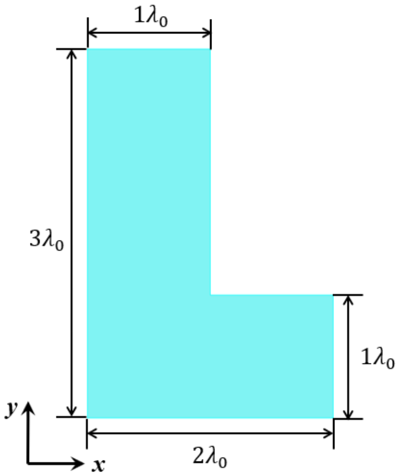

Figure 7.4: An L-shaped PEC object.

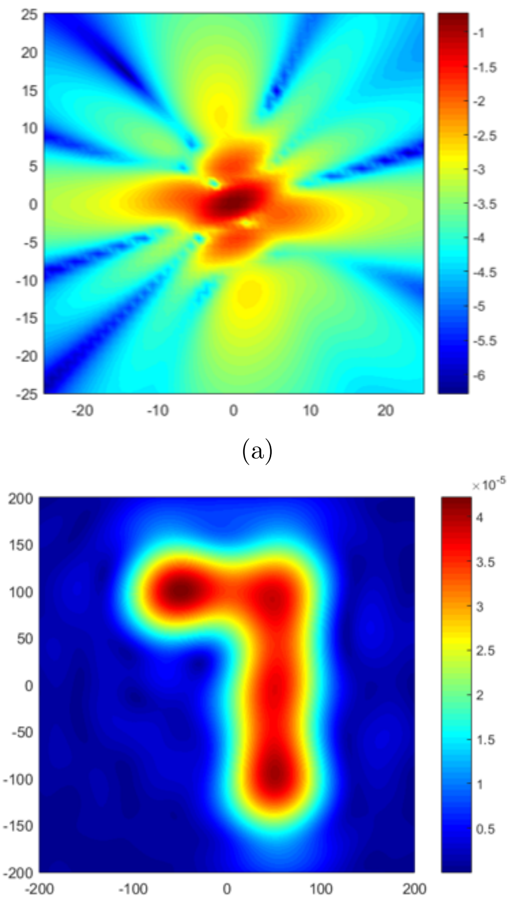

(a)

(b)

Figure 7.5: Far-field and CCD image of the L-shaped PEC object. The unit for the x and y coordinates is λ_0. (a) Log-scaled far-field power. (b) CCD image.

Figure 7.6: Geometry of the UI logo.

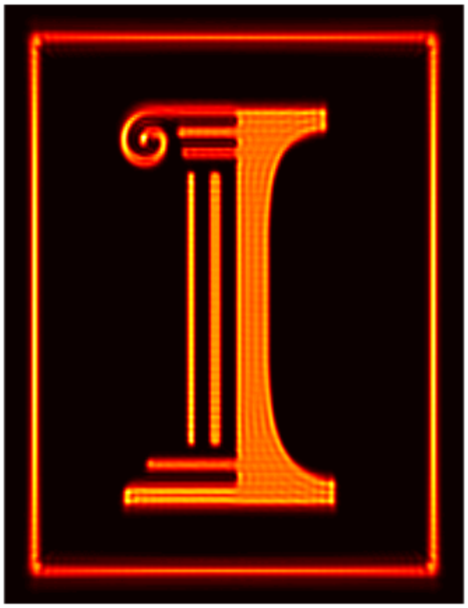

Figure 7.7: CCD image of the UI logo.

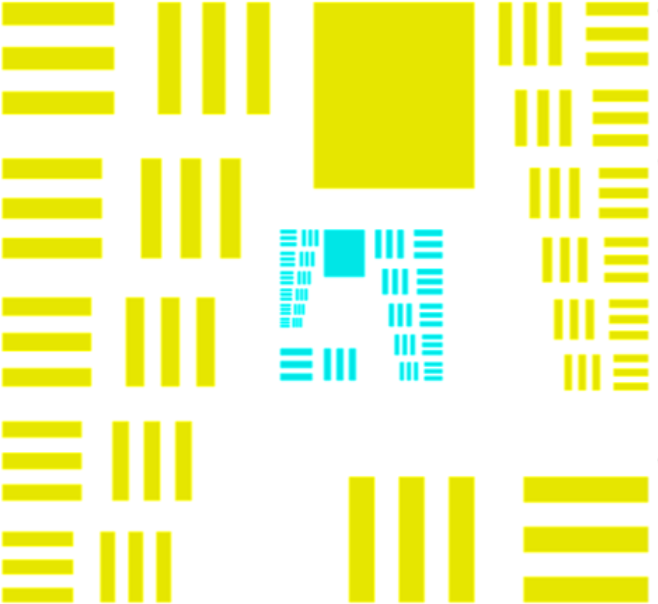

Figure 7.8: Geometry of the USAF target.

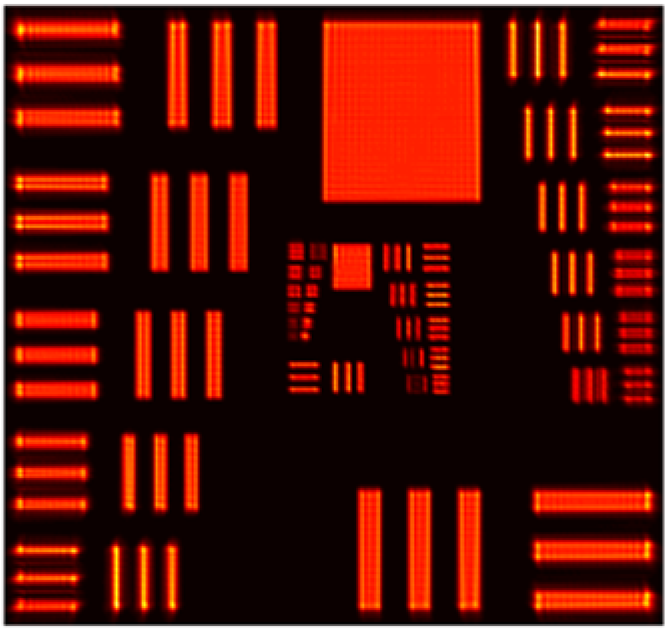

Figure 7.9: CCD image of the USAF target.

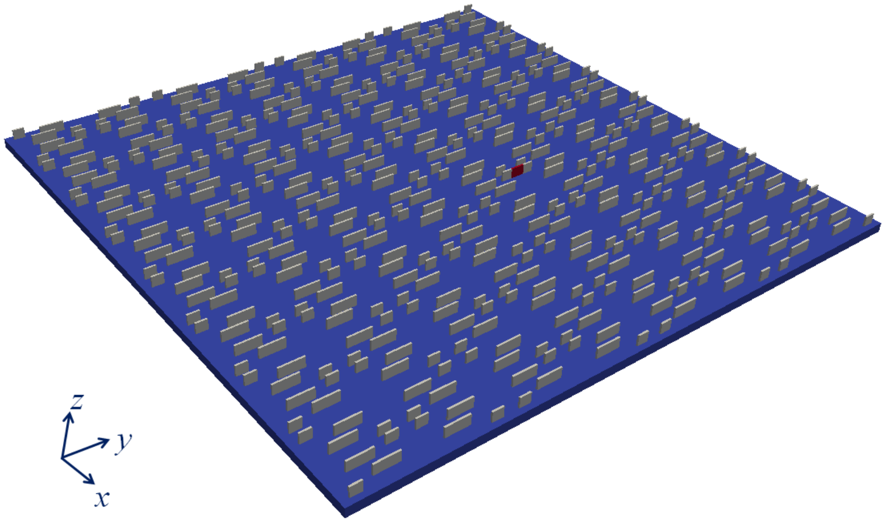

Figure 7.10: Geometry of a nanopatterned semiconductor wafer with a defect (red).

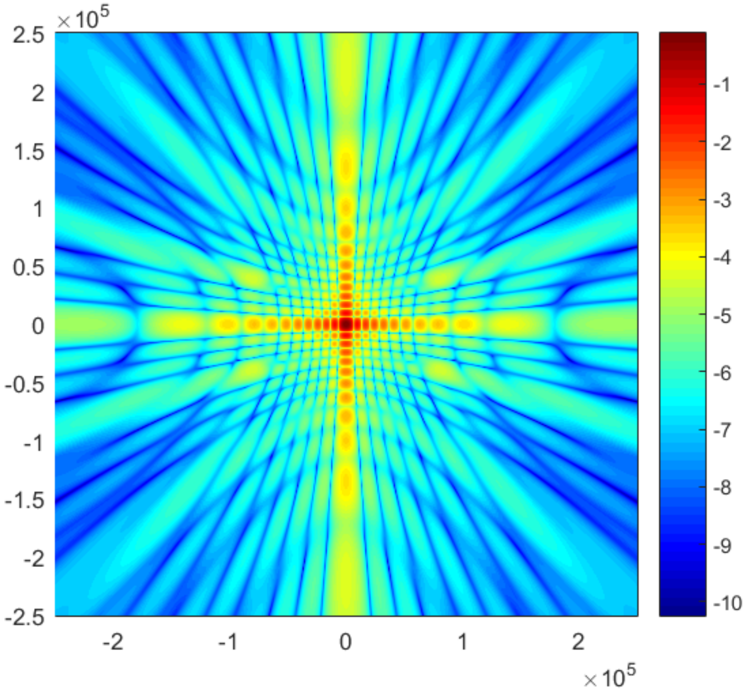

(a)

Figure 7.11: Log-scaled far-field power for the nanopatterned semiconductor wafer. The unit for the x and y coordinates is μm and the unit for the color bars is dB. (a) Wafer without a defect. *(cont.)*

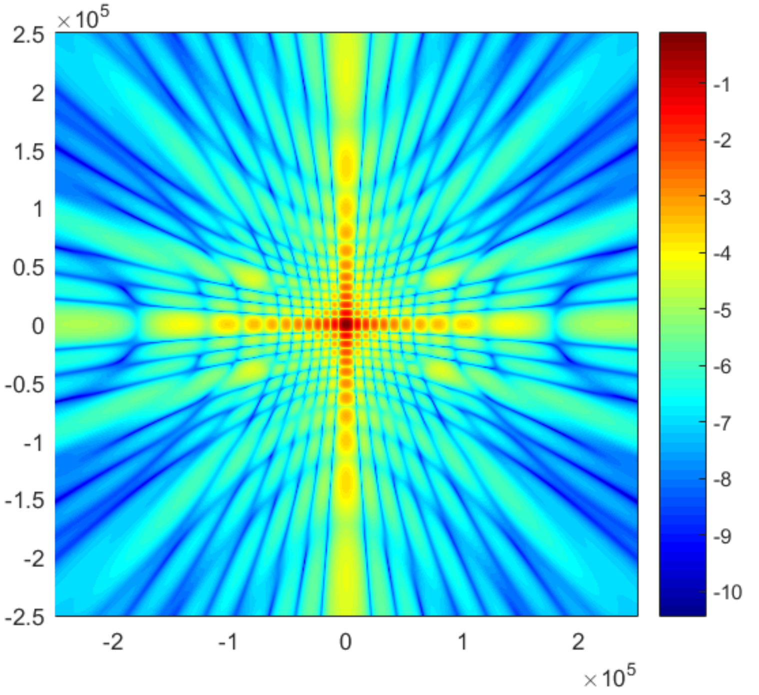

(b)

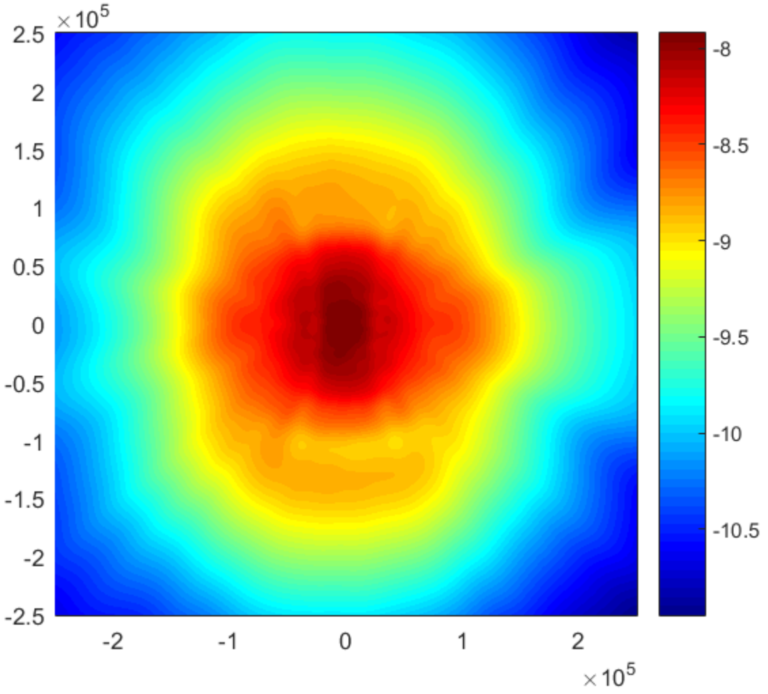

(c)

Figure 7.11 continued: (b) Wafer with a defect. (c) Difference between (a) and (b).

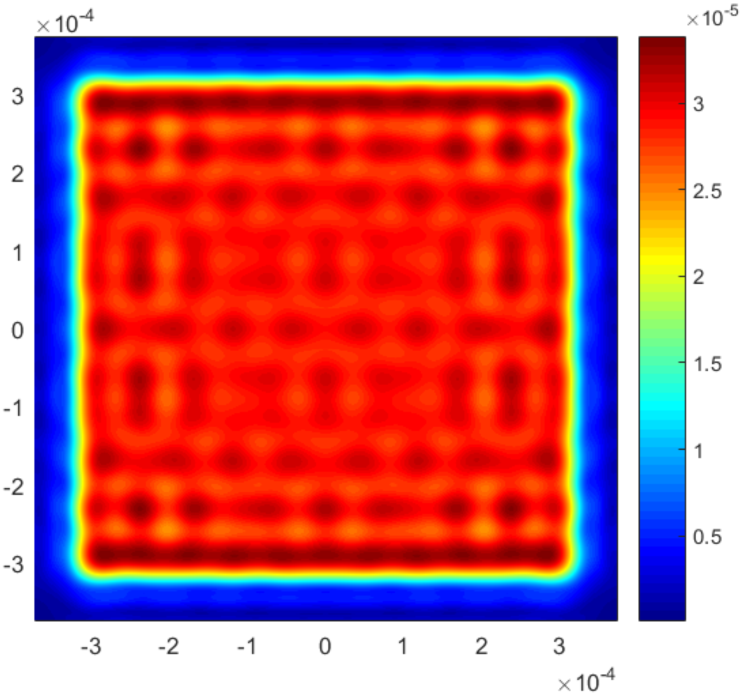

(a)

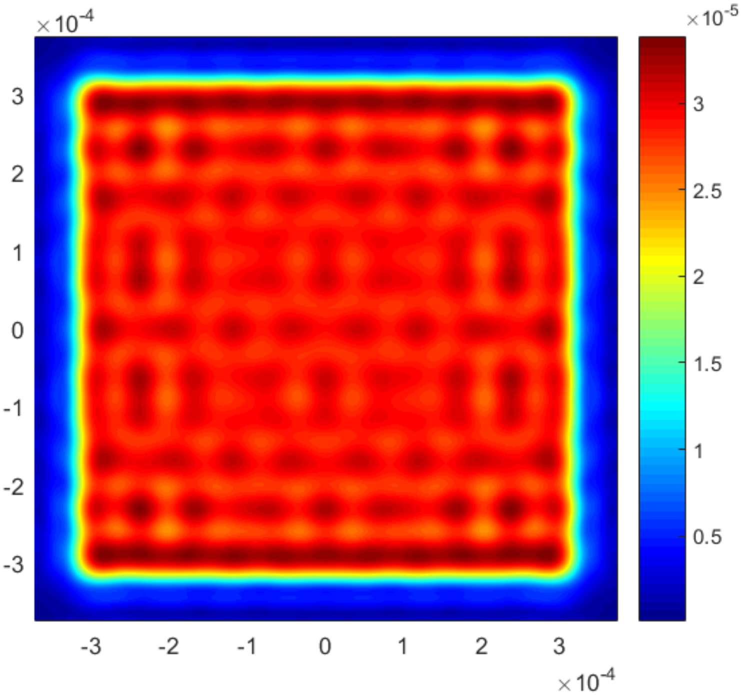

(b)

Figure 7.12: CCD images for the nanopatterned semiconductor wafer. The unit for the x and y coordinates is m. The unit of the color bars is volt per meter. (a) Wafer without a defect. (b) Wafer with a defect. *(cont.)*

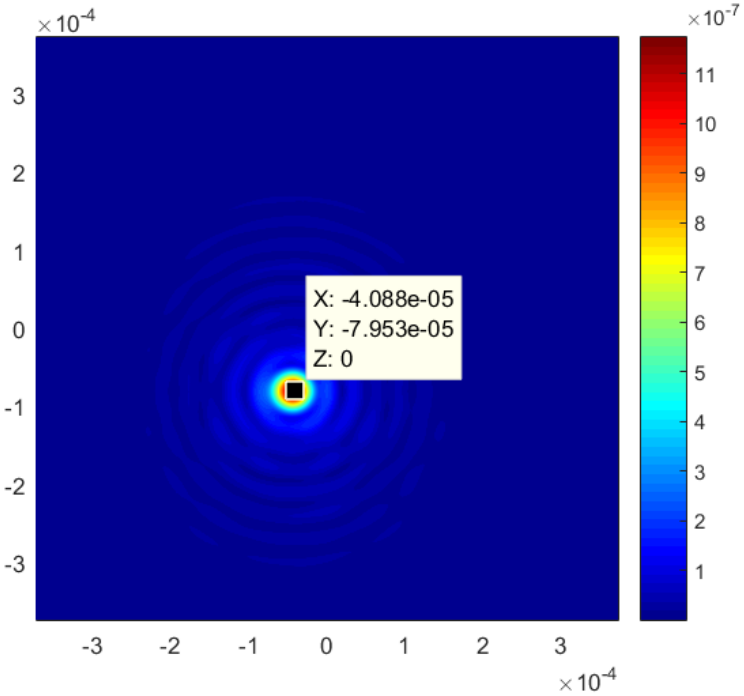

Figure 7.12 continued: (c) Difference between (a) and (b).

Chapter 8

FETD-GSM for Waveguide Devices

8.1 Introduction

Accurate and efficient broadband modeling of resonant waveguide structures can significantly facilitate the design and optimization of microwave and millimeter-wave devices, such as filters, multiplexers, and power dividers [71], and hence has been an important topic in the computational electromagnetics community for decades [3, 10, 71–81]. Early development of waveguide device analysis was based on the equivalent circuit theory, where waveguide discontinuities/junctions were represented by resistors, capacitors, inductors, and transformers with the consideration of only the fundamental mode, and the network synthesis theory was then applied to analyze the lumped circuit model [71–73]. Despite its simplicity and minimal computational effort, the equivalent circuit theory suffered from serious accuracy problems mainly because of the neglect of higher-order modes induced in the proximity of discontinuities. The consequence of low accuracy in the prototype design inevitably led to the time-consuming *trial-and-error* adjustments. To improve the solution accuracy, the MM method was proposed to take into account higher-order mode coupling effects, junction effects, and finite thickness of inclusions [74, 75]. With the field inside the computational domain expanded by waveguide modes and tangential continuity enforced at discontinuities, the MM method was shown to be highly accurate with a low computational cost and it quickly dominated in waveguide device modeling [74–78]. However, due to the difficulty of deriving analytical waveguide modes, the MM method has found most applications in canonical geometries, such as rectangular, circular, coaxial circular, and elliptical waveguides. Even though numerical waveguide modes can be evaluated for noncanonical geometries by solving an eigenvalue problem, the MM method generally suffers from the well-known convergence problem [74].

In the past few years, benefitting from the significant improvement of computing facilities and fast development of full-wave numerical methods, a large volume of research literature has been devoted to advanced hybrid algorithms that combine the efficiency of the MM method and flexibility of the finite-element (FE), finite-difference (FD), and method of moments (MoM) techniques [79,80]. To simulate a realistic waveguide device with a high complexity using these hybrid algorithms, the device is usually first divided into several building blocks; each block is then modeled by a FE, FD, or MoM technique and represented by a GSM; and finally all GSMs are cascaded to form the global GSM of the full device. Although these high-fidelity algorithms can handle building blocks with arbitrarily shaped cross-sections and rather complicated internal structures and materials, the broadband analysis is usually very time-consuming since the space discretization techniques are typically performed in the frequency domain. The asymptotic waveform evaluation (AWE) [145], which was originally developed for high-speed circuit analysis with a lower-order approximation of the system response to reduce computational complexity, has been adopted to alleviate the tedious frequency-sweep problem [2]. However, the AWE is also generally acknowledged for its spurious ringing and accuracy issues [146, 147].

An alternative to fast frequency sweep for a broadband characterization is to employ a time-domain algorithm such as the FDTD [148], the FETD [3, 81], and the time-domain integral equation (TDIE) method [149, 150] to perform a simulation directly in the time domain and then convert the time-domain solution into the frequency domain by the FFT afterwards. This approach is highly efficient for nonresonant devices. But for highly resonant devices, it requires an extremely large number of time marching steps because of a very slow decay of energy trapped in the devices. Although some signal processing techniques, such as Prony's method [151, 152], autoregressive method [153], and Padé approximation [154], can be employed to extract late-time responses to avoid their direct calculation, a sufficient number of time marching steps is still required to allow the waves propagating through an entire device a few times to capture the resonant characteristics of the device. Furthermore, the solution is limited by the accuracy of the parameters extracted from the calculations performed. Note that for an implicit algorithm such as the FETD and TDIE, one has to solve a global system matrix in each time step. Since the solution time is not linearly proportional to the size of the system matrix, the total computation time can increase significantly when the device to be simulated is electrically large. The alternating-direction-implicit FDTD (ADI-FDTD) [155], which solves a tridiagonal system equation without too restrictive a stability requirement, on the other hand, seems to be a good candidate. Unfortunately, in addition to its relatively poor accuracy of geometrical modeling, the ADI-FDTD has been shown to be a dissipative algorithm and some terms of its truncation error grow with the square of the time increment multiplied by the spatial derivatives of the field, which give rise to a large numerical error when the time step is beyond the Courant limit even though the key temporal features may be adequately resolved [148, 156].

In this chapter, we propose an accurate and efficient hybrid algorithm that combines the rigorous full-wave FETD method [3, 10, 81] with the GSM technique to alleviate the aforementioned issues. We first decompose the original resonant device into several subdomains and apply the time-domain WPBC [10] to the subdomain interfaces so that there is no strong resonance in the subdomains and consequently there is no need for an excessively large number of time marching steps to capture late-time responses. With curvilinear tetrahedral elements to discretize waveguide geometries and internal inclusions with high fidelity, higher-order basis functions to effectively reduce numerical dispersion errors, and WPBC to perfectly absorb any desired waveguide modes at subdomain interfaces with arbitrary shapes, the FETD analysis of the subdomains can be accurately and efficiently performed. The subdomains are then represented by broadband GSMs, which are evaluated from the FFT of the time-domain results. Finally, we cascade the extracted subdomain GSMs to obtain the global broadband GSM for the entire structure. Since the subdomains are fully decoupled, the proposed algorithm enables the use of nonconformal meshes and parallel computing to respectively reduce the mesh generation burden and effectively speed up simulations. Although the WPBC adopted in this chapter requires homogeneous subdomain interfaces, where the supported waveguide modes may consist of transverse electromagnetic (TEM), transverse electric (TE), and transverse magnetic (TM) waves, the proposed FETD-GSM methodology is applicable to more general waveguides with hybrid modes and even with frequency-dependent materials loaded when perfectly matched layers (PML) [3] are used to truncate subdomain interfaces.

The rest of the chapter is organized as follows. In Section 8.2, we formulate the WPBC truncated FETD equations and the modal analysis of an arbitrary cross-section. After that, we discuss the calculation and cascading of GSMs. We then present three engineering applications for accuracy and efficiency demonstration of the proposed hybrid algorithm in Section 8.3. Finally, we conclude in Section 8.4.

8.2 Formulation

The proposed hybrid algorithm combines the FETD method and GSM technique to efficiently analyze resonant devices. In this section, we present the formulation and implementation details for the FETD method equipped with the WPBC as truncation for subdomain interfaces, numerical modal analysis of an arbitrary cross-section, and the cascading of adjacent subdomain GSMs with various number of ports. We also include the expressions of high-order interpolatory nodal bases and hierarchal vector bases adopted in the modal analysis and the FETD method, respectively, for completeness.

8.2.1 Finite-Element Time-Domain Method

Consider a source-free computational domain with material properties specified by permittivity ϵ, permeability μ, and conductivity σ. The time-domain vector wave equation that governs the electric field $\mathbf{E}(\mathbf{r}, t)$ can be expressed as [3]

$$\nabla \times \left(\frac{1}{\mu}\nabla \times \mathbf{E}\right) + \epsilon\frac{\partial^2 \mathbf{E}}{\partial t^2} + \sigma\frac{\partial \mathbf{E}}{\partial t} = 0. \tag{8.1}$$

To ensure a unique solution, proper boundary conditions have to be prescribed at the surface S that bounds the computational domain, among which the Dirichlet and Robin boundary conditions are the most common ones:

$$\hat{n} \times \mathbf{E} = 0, \qquad \mathbf{r} \in S_{\mathrm{D}}, \tag{8.2}$$

$$\hat{n} \times \left(\frac{1}{\mu}\nabla \times \mathbf{E}\right) + P(\mathbf{E}) = \mathbf{U}^{\mathrm{inc}}, \quad \mathbf{r} \in S_{\mathrm{R}}, \tag{8.3}$$

where $\hat{n}$ is the outward unit normal vector of S, $P(\mathbf{E})$ denotes a functional of $\mathbf{E}$, and $\mathbf{U}^{\text{inc}}$ represents the boundary excitation. For microwave and millimeter-wave device simulations, the WPBC is preferred because it provides perfect absorbtion of waveguide modes without introducing extra degrees of freedom (DoFs), and therefore it is more accurate than absorbing boundary conditions (ABC) and more efficient than PML [3, 10, 81]. The WPBC can be expressed in the form of (8.3) with

$$P(\mathbf{E}) = -\sum_{m=1}^{\infty} \mathbf{e}_m \int_{S_{\mathrm{R}}} \mathbf{e}_m \cdot \left[\frac{\partial \mathbf{E}}{c\partial t} + \mathcal{L}_m(t) * \mathbf{E} \right] \mathrm{d}\mathbf{r}, \tag{8.4}$$

$$\mathbf{U}^{\text{inc}} = \hat{n} \times \left(\frac{1}{\mu} \nabla \times \mathbf{E}^{\text{inc}} \right) + P(\mathbf{E}^{\text{inc}}), \tag{8.5}$$

where $\mathbf{e}_m$ represents the mth waveguide mode, which can be TEM, TE, or TM, $c = 1/\sqrt{\mu\epsilon}$ is the speed of light in medium, $\mathbf{E}^{\text{inc}}$ is typically a time-domain incident mode, and the time-domain function $\mathcal{L}_m(t)$ associated with the mth mode is defined as

$$\mathcal{L}_m(t) = \frac{k_{\mathrm{c}m}}{t} \begin{cases} J_1(\kappa) u(t) & \text{TE modes,} \\ \left[J_1(\kappa) - \kappa J_0(\kappa) \right] u(t) & \text{TM modes,} \end{cases} \tag{8.6}$$

in which $k_{\mathrm{c}m}$ is the mth cutoff wavenumber, $u(t)$ denotes the unit step function, and $J_n(\kappa)$ represents the Bessel function of order n with the argument $\kappa = k_{\mathrm{c}m} ct$.

To solve the governing equation (8.1) together with the boundary conditions defined in (8.3), the electric field $\mathbf{E}(\mathbf{r}, t)$ is first spatially discretized as

$$\mathbf{E}(\mathbf{r}, t) = \sum_{j=1}^{N} \mathbf{N}_j e_j(t), \tag{8.7}$$

where N is the number of DoFs, $e_j(t)$ is the jth DoF at time t, and $\mathbf{N}_j$ is the jth vector basis function, whose expression will be discussed in detail later.

In the FETD formulation, the Galerkin method is usually adopted, where

$\mathbf{N}_i$ is used to test the governing equation (8.1) to yield the weak-form

$$\begin{aligned}&\int_V \left[\frac{1}{\mu}(\nabla \times \mathbf{N}_i)\cdot(\nabla \times \mathbf{E}) + \epsilon \mathbf{N}_i \cdot \frac{\partial^2 \mathbf{E}}{\partial t^2}\right] \mathrm{d}\mathbf{r} \\ &+ \int_V \sigma \mathbf{N}_i \cdot \frac{\partial \mathbf{E}}{\partial t} \mathrm{d}\mathbf{r} = \oint_S \hat{n} \cdot \left(\mathbf{N}_i \times \frac{1}{\mu}\nabla \times \mathbf{E}\right) \mathrm{d}\mathbf{r}.\end{aligned} \tag{8.8}$$

By substituting the spatial discretization (8.7) into (8.8) and utilizing the boundary conditions defined in (8.3)–(8.5), a matrix representation is derived as

$$\begin{aligned}&[T]\,\frac{\mathrm{d}^2\{e\}}{\mathrm{d}t^2} + [B]\frac{\mathrm{d}\{e\}}{\mathrm{d}t} + [S]\{e\} \\ &\qquad + \sum_{m=1}^{\infty}[Q^m]\mathcal{L}_m(t) * \{e\} = \{f\},\end{aligned} \tag{8.9}$$

where

$$T_{ij} = \int_V \epsilon \mathbf{N}_i \cdot \mathbf{N}_j \mathrm{d}\mathbf{r}, \tag{8.10}$$

$$S_{ij} = \int_V \frac{1}{\mu}(\nabla \times \mathbf{N}_i)\cdot(\nabla \times \mathbf{N}_j)\mathrm{d}\mathbf{r}, \tag{8.11}$$

$$B_{ij} = \int_V \sigma \mathbf{N}_i \cdot \mathbf{N}_j \mathrm{d}\mathbf{r} + \frac{1}{\mu c}\sum_{m=1}^{\infty} \Phi_{im}\Phi_{jm}, \tag{8.12}$$

$$Q_{ij}^m = \frac{1}{\mu}\Phi_{im}\Phi_{jm}, \tag{8.13}$$

$$f_i = \frac{2}{\mu}\Phi_{im}\left[\frac{\mathrm{d}}{c\mathrm{d}t}f^{\mathrm{inc}}(t) + \mathcal{L}_m(t) * f^{\mathrm{inc}}(t)\right]. \tag{8.14}$$

In (8.13) and (8.14), Φ_{im} is defined as the projection of the mth mode onto the ith vector basis function

$$\Phi_{im} = \int_{S_{\mathrm{R}}} \mathbf{N}_i \cdot \mathbf{e}_m \mathrm{d}\mathbf{r}, \tag{8.15}$$

and the temporal incidence $f^{\mathrm{inc}}(t)$ is defined as a modulated Gaussian pulse

$$f^{\mathrm{inc}}(t) = \exp\left[-(t-t_0)^2/\tau^2\right]\cos\left[2\pi f_0(t-t_0)\right], \tag{8.16}$$

where f_0 is the central frequency, t_0 is the time delay, and τ is a bandwidth-related constant. To resolve the temporal variation, $f^{\mathrm{inc}}(t)$ is uniformly discretized with a time step $\Delta t = 1/(60 f_0)$. Furthermore, τ is specified as

$1.25/f_0$ to carry out a broadband simulation. The time delay t_0 is set as $6/f_0$ such that the incidence has a vanishing value at $t = 0$.

Finally, it remains to temporally discretize the time-domain variables $e_j(t)$ to formulate a time-marching scheme. The Newmark-beta method [157], which uses central differencing for the first and second derivatives and a weighted average for the undifferentiated quantities, is best suited for this purpose because it has a second-order accuracy and unconditional stability. With the application of the Newmark-beta method, a fully discretized matrix equation is generated:

$$[K^0]\{e\}^{n+1} = \{b\}^n - [K^1]\{e\}^n - [K^2]\{e\}^{n-1}, \tag{8.17}$$

where

$$\begin{aligned}
\left[K^0\right] &= \frac{1}{\Delta t^2}[T] + \frac{1}{2\Delta t}[B] + \frac{1}{4}[S] + \frac{1}{4}\sum_{m=1}^{\infty}[Q^m]\mathcal{L}_m^0, && (8.18)\\
\left[K^1\right] &= \frac{1}{\Delta t^2}[T] + \frac{1}{2}[S], && (8.19)\\
\left[K^2\right] &= \frac{1}{\Delta t^2}[T] - \frac{1}{2\Delta t}[B] + \frac{1}{4}[S], && (8.20)\\
\{b\}^n &= \{f\}^n - \frac{1}{4}\sum_{m=1}^{\infty}[Q^m]\left(\mathcal{L}_m^{n,s} + 2\mathcal{L}_m^n\right) * \{e\}^n \\
&\quad - \frac{1}{4}\sum_{m=1}^{\infty}[Q^m]\mathcal{L}_m^{n-1} * \{e\}^{n-1}. && (8.21)
\end{aligned}$$

In the above equations, $\mathcal{L}_m^n$ is an n-entry time-domain sequence discretized from $\mathcal{L}_m(t)$ and $\mathcal{L}_m^{n,s}$ is defined as the sequence of $\mathcal{L}_m^{n+1}$ with its first entry $\mathcal{L}_m^0$ removed. More specifically, $\mathcal{L}_m^{n,s}$ satisfies the following relationship:

$$\mathcal{L}_m^{n+1} = \{\mathcal{L}_m^0, \mathcal{L}_m^{n,s}\}. \tag{8.22}$$

It is worth mentioning that since the subsystem matrices $[Q^m]$ contributed by the WPBC are fully populated, $[K^0]$ and $[K^1]$ are partially sparse and partially dense. Fortunately, the number of DoFs on the ports is far smaller than the total number of DoFs. Together with the symmetry of the system matrices, (8.17) can still be efficiently solved by a sparse direct solver [104, 105]. The computational efficiency can be improved if only one propagating mode is excited at a waveguide port, as is the case for most waveguide device analyses, where the devices are designed to work at the fundamental mode. For such a scenario, an ABC-like boundary condition is derived by utilizing the relationship between the electric and magnetic modal fields, which becomes

$$\begin{aligned} P(\mathbf{E}) =&\hat{n} \times \hat{n} \times \left[\frac{\partial \mathbf{E}}{c\partial t} + \mathcal{L}_m(t) * \mathbf{E}\right], \qquad (8.23) \\ \mathbf{U}^{\text{inc}} =&\hat{n} \times \left(\frac{1}{\mu}\nabla \times \mathbf{E}^{\text{inc}}\right) + P(\mathbf{E}^{\text{inc}}) \\ =&\frac{2}{\mu}\mathbf{e}_m \left[\frac{\mathrm{d}}{c\mathrm{d}t} f^{\text{inc}}(t) + \mathcal{L}_m(t) * f^{\text{inc}}(t)\right]. \qquad (8.24) \end{aligned}$$

The convolution in the right-hand-side (RHS) calculation in (8.21) remains time-consuming when a large number of time steps is involved since a direct evaluation requires $O(N_t^2)$ operations, where N_t is the number of temporal unknowns. Fortunately, the recursive FFT, which subdivides the time-domain sequences recursively into small intervals and exploits FFT to speed up convolutions between intervals whenever possible, could be applied to alleviate this issue with a computational complexity of $O(N_t \log^2 N_t)$ [158–160].

8.2.2 Modal Profiles

The implementation of WPBC needs modal profiles evaluated at the waveguide cross-sections. Although analytical modal profiles for canonical waveguide structures have been well established [3,75–78,81], numerical modal profiles are often desirable for waveguides with an arbitrary cross-section. For a homogeneous cross-section S_{R}, the potential ϕ satisfies the scalar Helmholtz equation [161]

$$(\nabla_t^2 + k_{cm}^2)\phi = 0 \quad \text{in}\, S_{\text{R}}, \qquad (8.25)$$

where ∇_t represents the transverse gradient operator.

Depending on the structure of the cross-section, different boundary conditions have to be enforced for (8.25) to produce the desired modes. For the TEM mode, which exhibits no cut-off frequencies, i.e., $k_{cm} = 0$, the boundary condition is given by

$$\phi = V_i \quad \text{on}\, \Gamma_i, \qquad (8.26)$$

where $\Gamma = \bigcup \Gamma_i$ is the line contour of S_{R} and V_i is the prescribed potential.

The potential ϕ is discretized using high-order nodal basis functions N_i as

$$\phi = \sum_{i=1}^{N_\ell} \phi_i N_i, \tag{8.27}$$

with ϕ_i representing the ith nodal coefficient and N_ℓ denoting the number of nodal DoFs. By using the Galerkin method, a discretized linear matrix equation is derived as

$$[A]\{\phi\} = \{b\}, \tag{8.28}$$

where the nonvanishing matrix entries A_{ij} are given by

$$A_{ii} = 1 \qquad\qquad i \in \Gamma, \tag{8.29}$$

$$A_{ij} = \int_{S_\mathrm{R}} \nabla_t \phi_i \cdot \nabla_t \phi_j \mathrm{d}\mathbf{r} \quad i \notin \Gamma, \tag{8.30}$$

and the nonvanishing RHS is given by

$$b_i = V_j \quad i \in \Gamma_j. \tag{8.31}$$

For the TE and TM modes, where their boundary conditions are respectively expressed as

$$\frac{\partial \phi}{\partial n} = 0 \quad \text{for TE modes}, \tag{8.32}$$

$$\phi = 0 \quad \text{for TM modes}, \tag{8.33}$$

the matrix representation can be uniformly written as

$$[A]\{\phi\} = k_{cm}^2 [M]\{\phi\}, \tag{8.34}$$

where

$$A_{ij} = \int_{S_\mathrm{R}} \nabla_t \phi_i \cdot \nabla_t \phi_j \mathrm{d}\mathbf{r}, \tag{8.35}$$

$$M_{ij} = \int_{S_\mathrm{R}} \phi_i \phi_j \mathrm{d}\mathbf{r}. \tag{8.36}$$

Note that DoFs are not defined on boundaries for the TM modes.

The resultant system equation (8.28) and the eigenvalue problem (8.34) are solved by PARDISO [105] and FEAST [162], respectively. Once the potential is evaluated, the electric modal function can be computed from

$$\mathbf{e}_m = \begin{cases} \hat{n} \times \nabla_t \phi & \text{TE modes,} \\ -\nabla_t \phi & \text{TEM/TM modes,} \end{cases} \tag{8.37}$$

where $\mathbf{e}_m$ is normalized with the subdomain interface area

$$\int_{S_{\mathrm{R}}} \mathbf{e}_m \cdot \mathbf{e}_m \mathrm{d}\mathbf{r} = 1. \tag{8.38}$$

It is well known that (8.34) suffers from the mode ambiguity issue even for nondegenerate modes. More specifically, if eigenvector $\{\phi\}$ is associated with $k_{\mathrm{c}m}$, so is $\{-\phi\}$. The problem becomes even worse for a circular cross-section where an eigenvector rotated by an arbitrary angle is still associated with the same eigenvalue. The mode ambiguity will lead to incorrect solutions for the proposed FETD-GSM algorithm where ports sharing the same cross-section are required to have the same modal profiles. To obviate the ambiguity issue, the modal profiles at a given cross-section are solved and stored in prior, and accessed by the FETD-GSM solver afterwards whenever needed. As a byproduct of this remedy, the meshes for the eigensolver and FETD-GSM solver at the port cross-sections can be completely nonconformal, which makes the solvers very flexible in choosing discretizations and basis functions.

8.2.3 Basis Functions

In the aforementioned eigensolver and FETD-GSM solver, nodal and vector basis functions are employed to expand the potential and electric field, respectively. For the sake of completeness, the expressions for the two bases are listed bellow. The second-order bases are used to achieve a balance between the computational efficiency and solution accuracy for the simulation of microwave and millimeter-wave waveguide devices, where the structure typically has sharp geometrical discontinuities and dimensions on the order of a wavelength.

Interpolatory Nodal Basis Functions

Let the barycentric coordinate ξ_i represent the zero-coordinate surface of the ith edge of a triangle or ith face of a tetrahedron [5]. The second-order Lagrangian interpolation polynomial for the vertex i is

$$\phi_i = \xi_i(2\xi_i - 1), \tag{8.39}$$

and the edge middle node i is

$$\phi_i = 4\xi_j\xi_k, \tag{8.40}$$

where j and k are the corresponding edge vertices [3].

Hierarchal Vector Basis Functions

Because of their p-adaption capability, hierarchal vector bases have been very popular among the computational electromagnetics community to allow mixed basis orders within the same mesh while preserving tangential continuity [3, 4, 6, 81]. These bases provide nonoverlapping gradient and rotational subspaces for irrotational and solenoidal vectorial field components, respectively. For the mixed second-order bases, following [4], the rotational and gradient parts associated with an edge with vertices i and j are respectively given by

$$\mathbf{N}^r_{ij} = \xi_i\nabla\xi_j - \xi_j\nabla\xi_i, \tag{8.41}$$

$$\mathbf{N}^g_{ij} = \nabla(\xi_i\xi_j), \tag{8.42}$$

and the rotational basis associated with a face is expressed as

$$\mathbf{N}^r_{ijk} = \xi_i\nabla(\xi_j\xi_k) - 2\xi_j\xi_k\nabla\xi_i, \tag{8.43}$$

where i, j, and k are the face vertices.

8.2.4 Generalized Scattering Matrix

In a microwave and millimeter-wave waveguide device analysis, the key quantities to characterize device performance are scattering parameters. For waveguide devices with potentially multi-modes, the GSM is usually of interest, and its entries are defined as

$$S_{ji}^{nm} = b_n^j / a_m^i, \tag{8.44}$$

where a_m^i denotes the frequency-domain modal amplitude for the mth mode at port i and b_n^j denotes the modal amplitude for the nth mode at port j. The frequency-domain modal amplitudes are calculated by the FFT of the time-domain modal amplitudes. At port S_{R}, the mth time-domain modal amplitude $A_m(t)$ is given by

$$A_m(t) = \int_{S_{\mathrm{R}}} \mathbf{E} \cdot \mathbf{e}_m \mathrm{d}\mathbf{r}. \tag{8.45}$$

Since directly calculating the GSM of a resonant structure using a time-domain method is very time-consuming, as discussed earlier, we propose a hybrid method that partitions a resonant device into several nonresonant subdomains to be solved by the FETD method, and then cascade the subdomain GSMs to form the global GSM for the original device in the frequency domain. The cascading equation can be obtained by first separating waves at a port into incoming and outgoing waves and then matching tangential field continuity with adjacent subdomains. Depending on the partition, the cascading equation varies. Fortunately, for many waveguide devices, cascading subdomain GSMs can be categorized into three groups: a) two-port two-port cascading, b) three-port one-port cascading, and c) three-port two-port cascading, as illustrated in Fig. 8.1.

The global GSM for cascading two two-port subdomains is given by

$$\mathbf{S}_{11} = \mathbf{S}_{12}^a \mathbf{G}_{12} \mathbf{S}_{11}^b \mathbf{S}_{21}^a + \mathbf{S}_{11}^a, \tag{8.46}$$

$$\mathbf{S}_{12} = \mathbf{S}_{12}^a \mathbf{G}_{12} \mathbf{S}_{12}^b, \tag{8.47}$$

$$\mathbf{S}_{21} = \mathbf{S}_{21}^b \mathbf{H}_{21} \mathbf{S}_{21}^a, \tag{8.48}$$

$$\mathbf{S}_{22} = \mathbf{S}_{21}^b \mathbf{H}_{21} \mathbf{S}_{22}^a \mathbf{S}_{12}^b + \mathbf{S}_{22}^b, \tag{8.49}$$

where

$$\mathbf{G}_{ij} = \left[\mathbf{I} - \mathbf{S}^b_{ii}\mathbf{S}^a_{jj}\right]^{-1}, \tag{8.50}$$

$$\mathbf{H}_{ij} = \left[\mathbf{I} - \mathbf{S}^a_{ii}\mathbf{S}^b_{jj}\right]^{-1}. \tag{8.51}$$

Note that $\mathbf{I}$ is an identity matrix in (8.50) and (8.51). The global GSM for cascading a three-port subdomain with a one-port subdomain, which is very common in compact band-rejection filter designs, can be formulated as

$$\mathbf{S}_{ij} = \mathbf{S}^a_{ij} + \mathbf{S}^a_{i3}\mathbf{G}_{13}\mathbf{S}^b_{11}\mathbf{S}^a_{3j}, \tag{8.52}$$

where $1 \le i, j \le 2$. The cascading of a three-port subdomain with a two-port subdomain is of particular interest in power divider and diplexer/multiplexer designs, and is expressed as

$$\mathbf{S}_{ij} = \mathbf{S}^a_{ij} + \mathbf{S}^a_{i2}\mathbf{G}_{12}\mathbf{S}^b_{11}\mathbf{S}^a_{2j}, \tag{8.53}$$

$$\mathbf{S}_{i2} = \mathbf{S}^a_{i2}\mathbf{G}_{12}\mathbf{S}^b_{i2}, \tag{8.54}$$

$$\mathbf{S}_{2i} = \mathbf{S}^b_{21}\mathbf{H}_{21}\mathbf{S}^a_{2i}, \tag{8.55}$$

$$\mathbf{S}_{22} = \mathbf{S}^b_{22} + \mathbf{S}^b_{21}\mathbf{H}_{21}\mathbf{S}^a_{22}\mathbf{S}^b_{12}, \tag{8.56}$$

where $i, j \in \{1, 3\}$.

8.3 Numerical Results

In this section, we present three examples to demonstrate the accuracy and efficiency of the proposed hybrid FETD-GSM algorithm for a broadband full-wave analysis of resonant devices. The resonant devices are decomposed into several subdomains so that resonance in each subdomain can be eliminated or significantly suppressed. To minimize the number of modes to truncate each subdomain, which is critical to achieving high efficiency for the proposed algorithm, the decomposed interfaces are located where geometrical discontinuities are not present and hence only propagating modes and a few evanescent modes need to be considered. For each example, the same mesh size and temporal step size are used in both the conventional FETD method and FETD-GSM algorithm for performance comparison. The resultant symmetric system matrices are stored with only the upper triangular entries and factorized by the direct sparse solver PARDISO [105]. The simulations are terminated when the signal power of each mode, normalized with the peak power of the incident mode, reduces to −60 dB, where the signal power for the mth mode is defined as

$$P_m(t) = 20 \log_{10} |A_m(t)| . \tag{8.57}$$

In our numerical examples, all the computations are carried out in double float precision on a computing node configured with 256 GB memory and two Intel Xeon E5-2680 v2 CPUs in a sequential mode. The time for computing numerical modes is negligible and will not be mentioned in all the examples.

8.3.1 Dual-Mode Circular Cavity Filter

The first example is a dual-mode circular cavity filter [163]. The filter, illustrated in Fig. 8.2, consists of a circular waveguide (length: 100 mm and radius: 12 mm) which is linked to the input and output rectangular waveguide ports (19.05 mm by 9.525 mm by 10 mm) through two rectangular coupling slots (9.7 mm by 3 mm by 1 mm). The entire structure is discretized into 28,136 curvilinear tetrahedral elements with a mesh size of 2.4 mm. A broadband TE_{10} signal is chosen as excitation. To resolve the highly resonant field in the device, the temporal step size is set to 1.3 ps, which is approximately 1/60 of the period of the central frequency at 12.5 GHz. With the conventional FETD method, the recorded time-domain signal powers at the two ports are depicted in Fig. 8.3a in logarithmic scales, where the ports on the left and right sides are respectively referred to as port 1 and port 2 for simplicity. Because the energy trapped in the lossless circular waveguide decays slowly, 46,000 time marching steps have been performed to let the signal powers reduce to −60 dB.

The excessively long simulation required to fully capture the late-time response of such a resonant device significantly compromises the efficiency of the conventional FETD method. To eliminate the resonance and hence reduce the number of time marching steps, we decompose the circular cavity filter evenly into two nonresonant subdomains as illustrated in Fig. 8.2. Although four propagating modes (TE_{11}-even, TE_{11}-odd, TE_{21}, and TM_{01}) are supported at the interface when the frequency of interest rises to 15 GHz, it is apparent that only the TE_{11}-even mode can be effectively excited for the TE_{10} mode incidence. The simulated time-domain signal powers for the half structure with the TE_{10} and TE_{11}-even mode incidences respectively applied on port 1 and port 2 are plotted in Figs. 8.3b and 8.3c. As opposed to the simulation of the entire filter with 46,000 time steps, only 7,400 time steps need to be carried out to reduce the signal powers to -60 dB for the TE_{10} mode incidence and 6,400 time steps for the TE_{11}-even mode incidence. The corresponding frequency-domain responses for the two incidences are given in Fig. 8.4, with the difference between the magnitudes of S_{12} and S_{21} representing the modal power conversion loss between the TE_{10} and TE_{11}-even modes. Due to the geometrical symmetry, the GSM of the right half section can be readily obtained by swapping port 1 with port 2. By cascading the GSMs of the two subdomains, the final S_{21} for the entire filter is plotted in Fig. 8.5, together with the conventional FETD result and the measurement. The excellent agreement between these three results validates not only the accuracy of our conventional FETD method but also that of the proposed FETD-GSM algorithm.

The computational statistics of using the conventional FETD method and the proposed FETD-GSM algorithm to simulate the circular cavity filter are summarized in Table 8.1. Since the cavity filter is evenly divided into two subdomains, each subdomain has approximately half the number of DoFs of the whole structure. In fact, the WPBC introduced at the center of the filter to suppress resonance only contributes 418 DoFs, which is negligible compared with the total number of DoFs. The random access memory (RAM) consumption, which is supposed to be super-linear for general three-dimensional problems solved by a sparse direct solver, is actually linear since the structure is quasi-one-dimensional and the decomposition is along the longitudinal direction. Because the strong resonance of the circular cavity is significantly suppressed in the half structure simulation, the number of time marching steps is greatly reduced, which results in a speedup of 6.88.

8.3.2 Hybrid Folded Filter

Next, we consider the simulation of a five-pole hybrid folded filter centered at 12.6 GHz with a bandwidth of 400 MHz [164]. To provide a steep out-of-band rejection and minimize the signal interference in adjacent channels, the filter must introduce an attenuation of 35 dB in an adjacent channel separated by 130 MHz from the lower passband edge, and at least 100 dB between 8.7 and 11 GHz. Figure 8.6 shows one physical design that can satisfy all the electrical specifications with the introduction of two trisections to provide transmission zeros both close to the passband and far from it. The filter ports and cavities are implemented with standard WR-75 waveguides, and the detailed dimensions can be found in [164]. The entire structure is discretized into 119,558 curvilinear tetrahedra with an adaptive mesh size from 0.3 mm for fine features to 1.5 mm for the smooth parts. The fundamental TE_{10} mode is chosen as the excitation signal and the temporal step size is set to 1.6 ps. Figure 8.7a shows the two ports' recorded time-domain signal powers, which take 130,000 time marching steps to decrease to -60 dB.

To reduce the number of time marching steps, we decompose the hybrid folded filter into four less-resonant sections as illustrated in Fig. 8.6. The subdomain interfaces are particularly chosen at places where the fields have the least variation so that even one single TE_{10} mode is sufficient to retrieve subdomain GSMs accurately. The simulated time-domain signal powers for the four subdomains with the TE_{10} mode incidence respectively applied on port 1 and port 2 are plotted in Figs. 8.7b–8.7i. Apparently, the signal powers in the subdomains decay much faster to the threshold in less than 28 ns even for the worst case compared with the signal powers in the full structure, which require more than 200 ns. The FFT calculated subdomain GSMs are provided in Figs. 8.8a–8.8d for reference. Due to reciprocity ($\mathbf{S}_{12} = \mathbf{S}_{21}^{\mathrm{T}}$), we observe the overlap of the magnitude curves of S_{12} and S_{12}. Considering the passive and lossless nature of the subdomains, it is trivial to conclude that the magnitudes of S_{11} and S_{22} should also be equal, as is clearly demonstrated by Figs. 8.8a–8.8d. It is worth mentioning that although S_{11} and S_{22} have an equal magnitude, their values are typically different unless the structure under consideration is geometrically symmetric. After cascading the subdomain GSMs, the global S-parameters based on the FETD-GSM algorithm are plotted against the conventional FETD results and the measurements in

Fig. 8.8e, showing a good agreement.

The computational statistics of using the conventional FETD method and the proposed hybrid FETD-GSM algorithm to simulate the hybrid folded filter are listed in Table 8.2. The maximum memory footprint decreases from 7.96 GB for the whole structure to 2.85 GB for the second subdomain. Because resonance is isolated in each subdomain, the number of time marching steps is significantly reduced and a speedup of 6.59 is obtained.

8.3.3 In-Line Pure E-Plane Band-Stop Filter

The last example simulated is an in-line pure E-plane band-stop filter [165]. With band-rejection cavities coupled to the main rectangular waveguide, these compact band-stop in-line filters are essential in applications where a specific narrow frequency band needs to be strongly attenuated, for instance, to reject the spurious harmonic frequencies of the output of high-power nonlinear amplifiers. Figure 8.9 illustrates the geometrical configurations of the filter simulated in this section with its detailed dimensions listed in [165]. The entire structure is discretized into 146,476 curvilinear tetrahedra with an adaptive mesh size from 0.07 mm for fine features to 0.6 mm for the smooth parts. A broadband TE_{10} mode is used as the excitation at port 1 and the temporal step size is set to 0.57 ps. Figure 8.10a depicts the two ports' simulated time-domain signal powers, which take 103,000 time marching steps to decrease to -60 dB.

To study the efficiency of the FETD-GSM algorithm, we divide the in-line pure E-plane band-stop filter into 12 nonresonant sections (Fig. 8.9) and use a single TE_{10} mode at each waveguide port to simulate the subdomain S-parameter matrices. Due to the limited space, only the time-domain signal powers for the first three subdomains are plotted in Figs. 8.10b–8.10f, where port 3 denotes the top/bottom port of a three-port structure. Obviously, the FETD-GSM algorithm uses many fewer time marching steps to reduce the signal powers to -60 dB than the conventional FETD with the direct full structure simulation. Finally, the conventional FETD method, hybrid FETD-GSM algorithm, and HFSS calculated frequency-domain responses are compared in Fig. 8.11, showing good agreement.

The computational statistics of using the conventional FETD method and the proposed FETD-GSM algorithm to simulate the in-line pure E-plane band-stop filter are listed in Table 8.3. The maximum memory footprint decreases from 8.77 GB for the whole structure to 1.84 GB for the third subdomain. Because resonance is greatly suppressed in each subdomain, the number of time marching steps is significantly reduced, resulting in a speedup of 11.53.

8.4 Summary

In this chapter, we presented an accurate and efficient hybrid algorithm that combines the FETD method with the GSM technique to quickly characterize broadband frequency responses of highly resonant waveguide devices. To obviate the necessity of an excessive number of temporal unknowns to fully capture late-time responses, we decomposed the original resonant device into several less-resonant subdomains with the aid of an accurate WPBC at the subdomain interfaces so that an accurate FETD analysis can be efficiently performed for each subdomain. We discussed in detail the formulation and implementation of the WPBC truncated FETD method and derived equations for cascading broadband generalized scattering matrices obtained from the time-domain simulation of multi-port structures. Finally, we demonstrated the accuracy and efficiency of the proposed hybrid algorithm by modeling three engineering application examples. The proposed FETD-GSM algorithm can be extended to model more general waveguides with hybrid modes and frequency-dependent materials when the WPBC is replaced with PML.

8.5 Figures and Tables

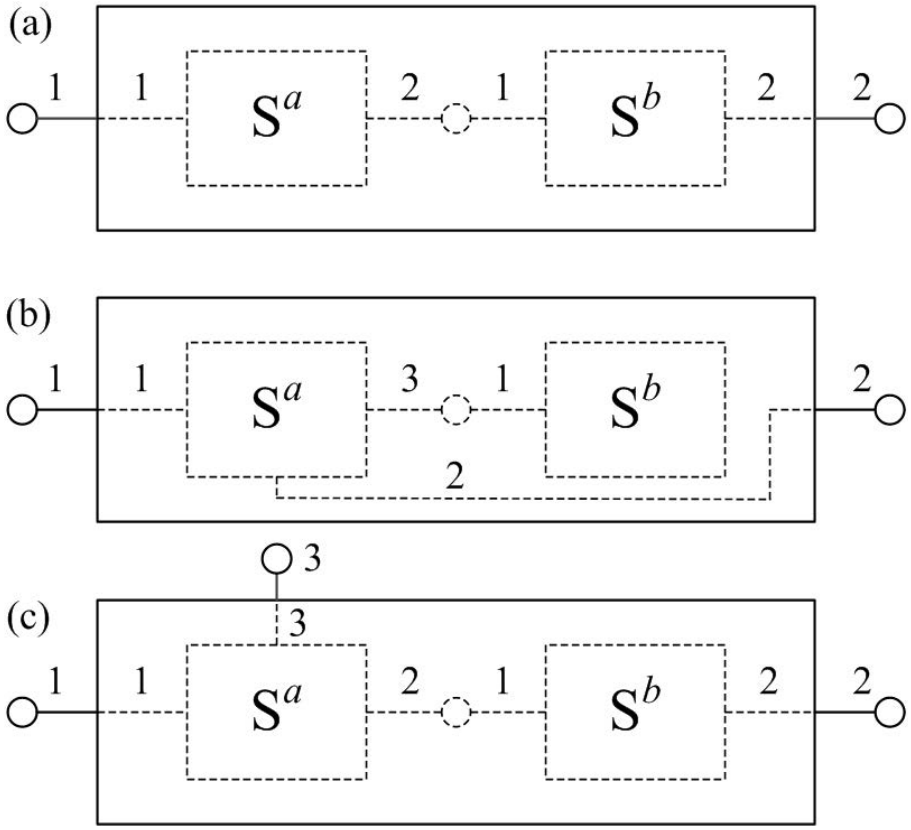

Figure 8.1: Cascading GSMs of two subdomains. (a) Two-port two-port cascading. (b) Three-port one-port cascading. (c) Three-port two-port cascading.

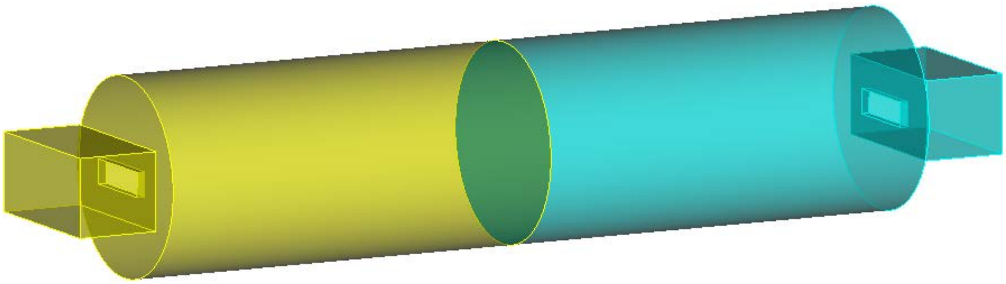

Figure 8.2: Geometry of a dual-mode circular cavity filter with WR75-waveguide input and output ports, two rectangular coupling slots, and a circular cavity. The filter is decomposed evenly into two subdomains, represented by two colors, for the FETD-GSM simulation.

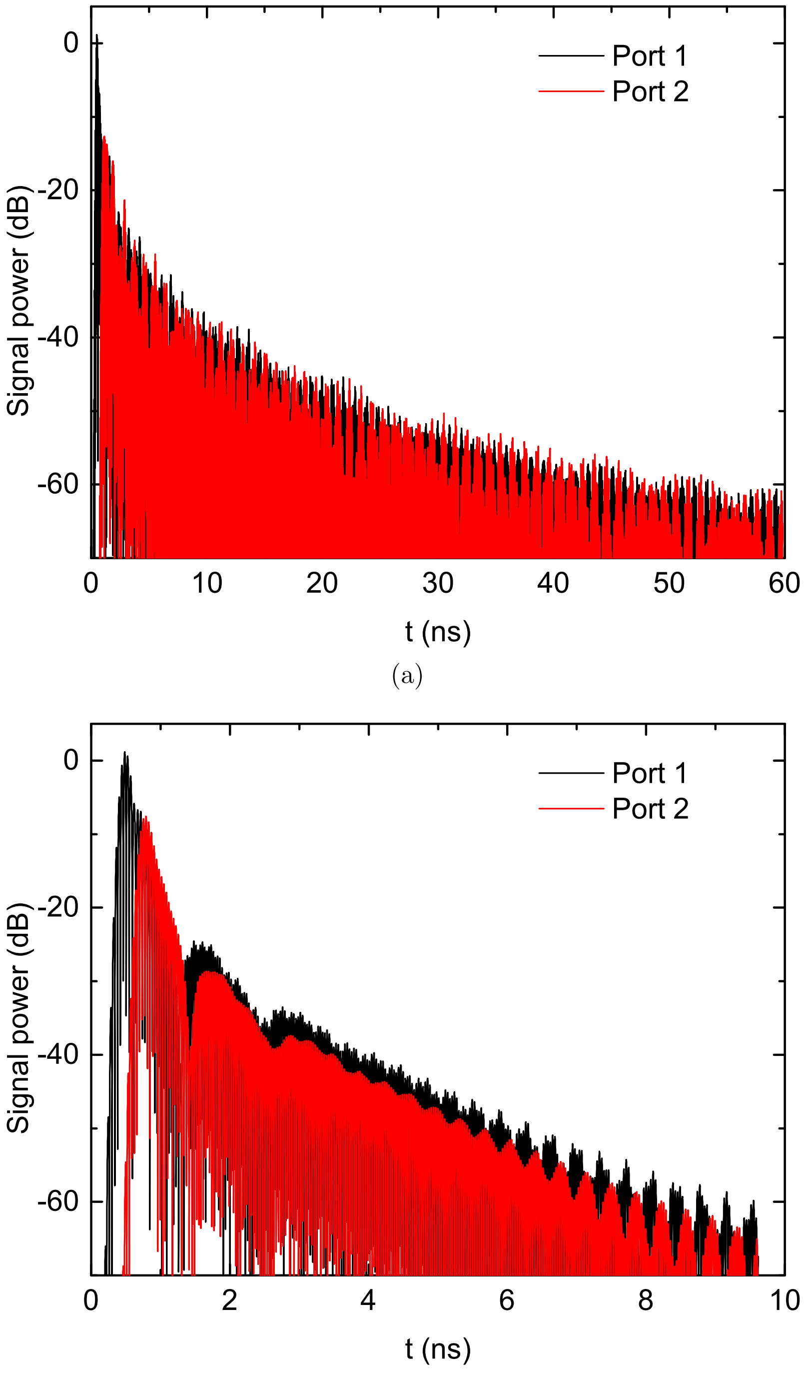

(a)

(b)

Figure 8.3: Time-domain signal powers P_m for the dual-mode circular cavity filter simulation. Port 1 and port 2 respectively denote the left port and the right port in both full structure and half structure simulations. (a) Full structure simulation with the TE_{10} mode excited at the port 1. (b) Half structure simulation with the TE_{10} mode excited at port 1. *(cont.)*

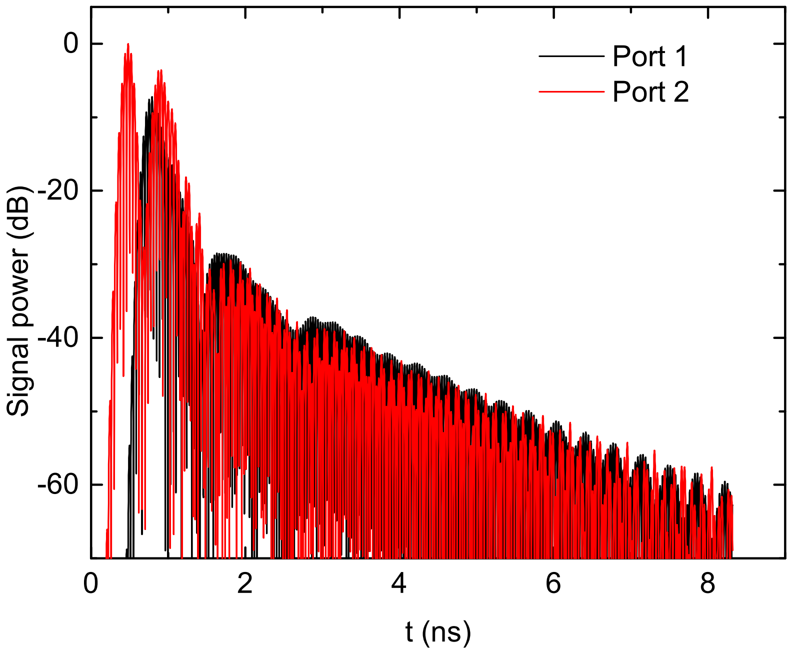

(c)

Figure 8.3 continued: (c) Half structure simulation with the TE_{11}-even mode excited at port 2.

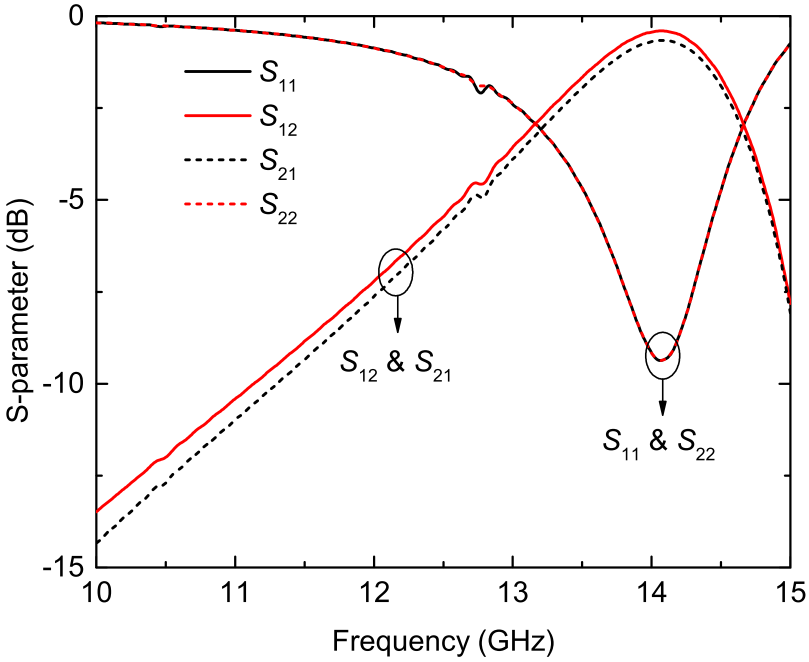

Figure 8.4: Frequency-domain responses for the half structure simulation with TE_{10} mode and TE_{11}-even mode excited at port 1 and port 2, respectively.

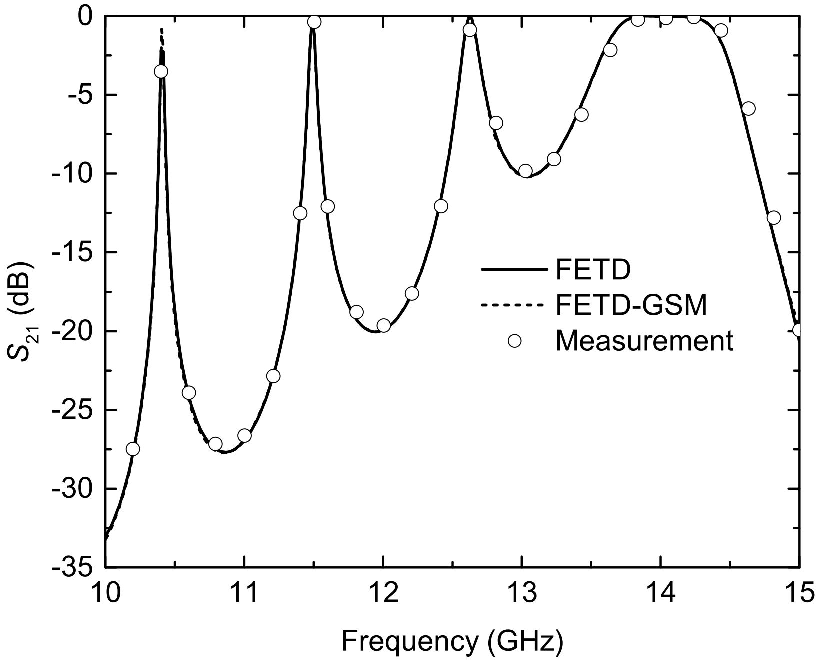

Figure 8.5: Frequency-domain responses for the dual-mode circular cavity filter.

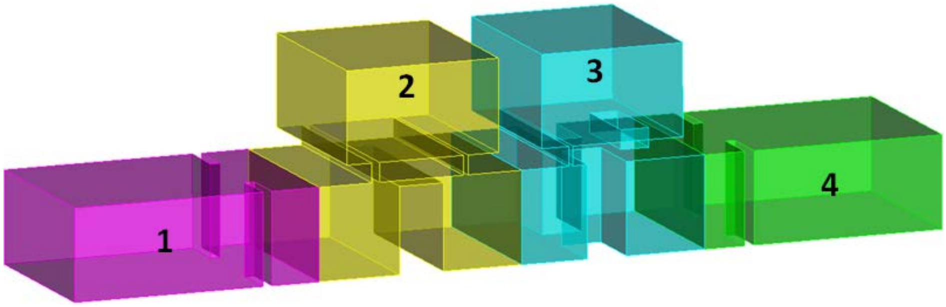

Figure 8.6: Geometry of the hybrid folded filter. The filter is decomposed into four subdomains, represented by different colors, for the FETD-GSM simulation. The subdomains are labeled as 1, 2, 3, and 4 from left to right.

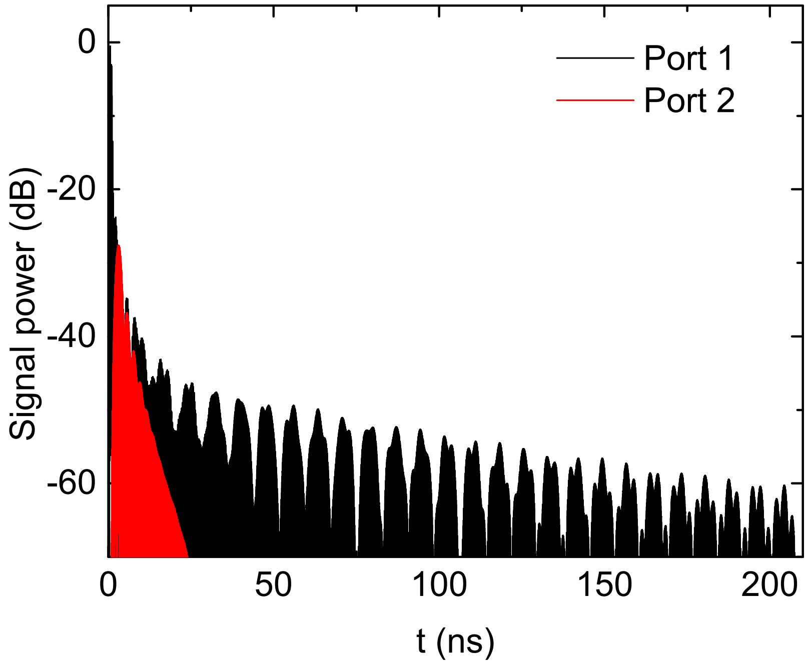

(a)

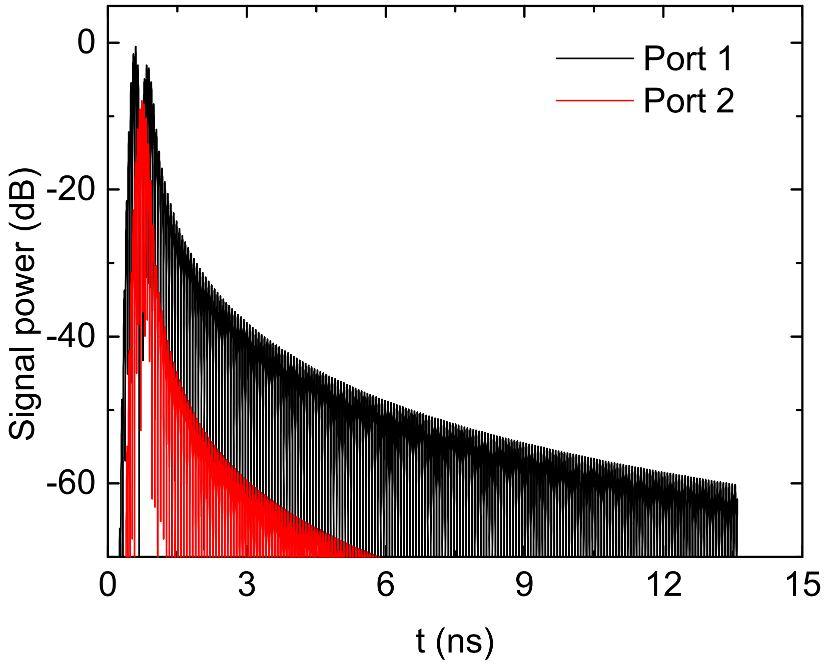

(b)

Figure 8.7: Time-domain signal powers for the hybrid folded filter simulation. Port 1 and port 2 respectively represent the left port and the right port in both full structure and subdomain simulations. (a) Full structure simulation with the TE_{10} mode excited at port 1. (b) Subdomain 1 simulation with the TE_{10} mode excited at port 1. *(cont.)*

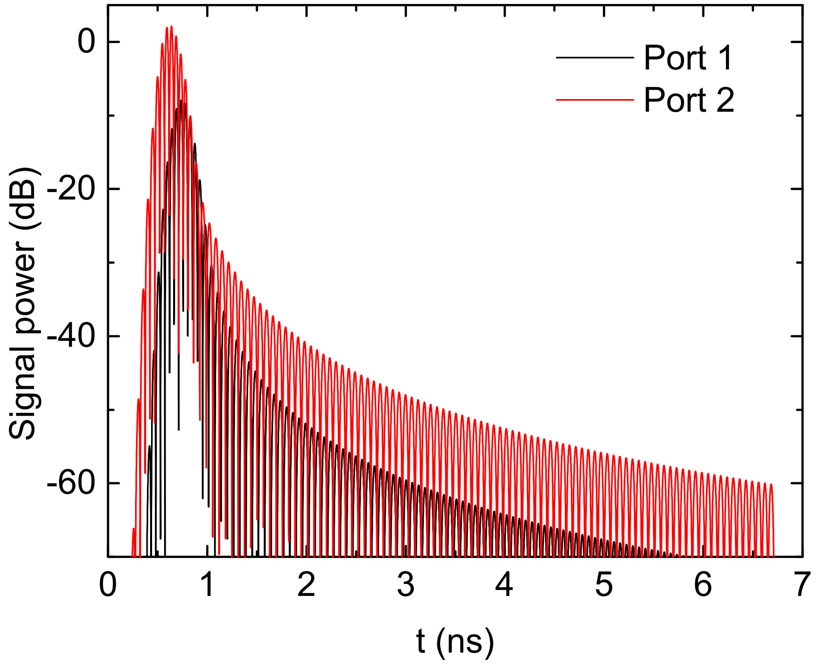

(c)

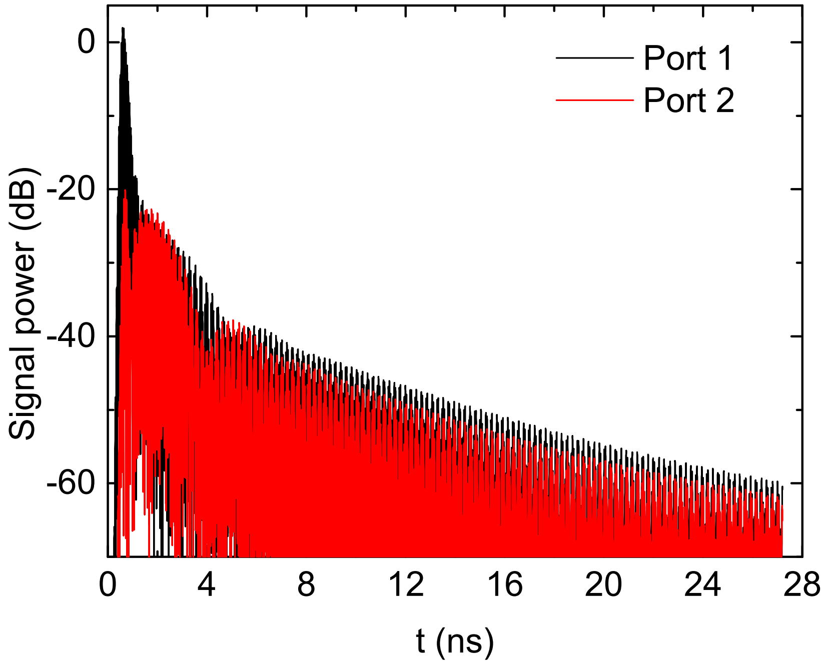

(d)

Figure 8.7 continued: (c) Subdomain 1 simulation with the TE_{10} mode excited at port 2. (d) Subdomain 2 simulation with the TE_{10} mode excited at port 1. *(cont.)*

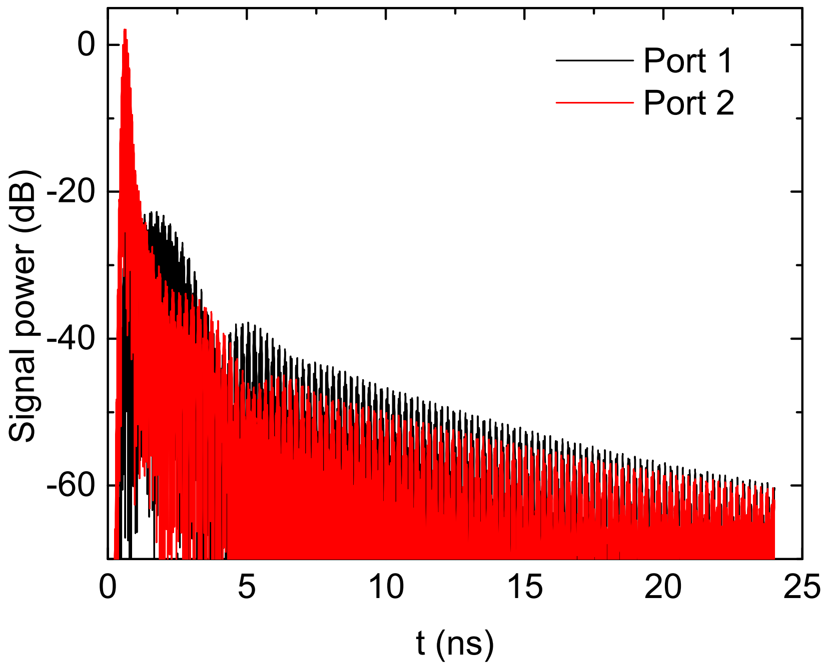

(e)

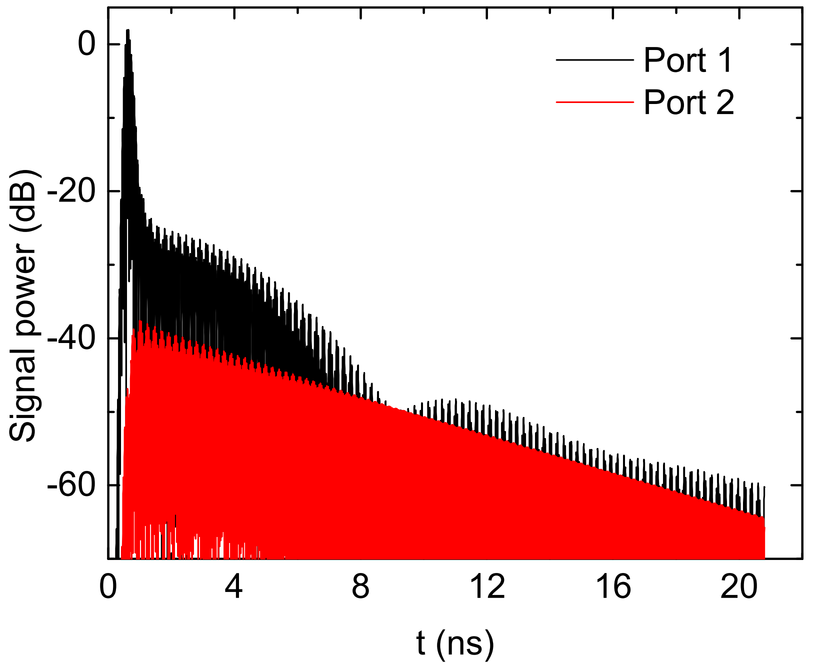

(f)

Figure 8.7 continued: (e) Subdomain 2 simulation with the TE_{10} mode excited at port 2. (f) Subdomain 3 simulation with the TE_{10} mode excited at port 1. *(cont.)*

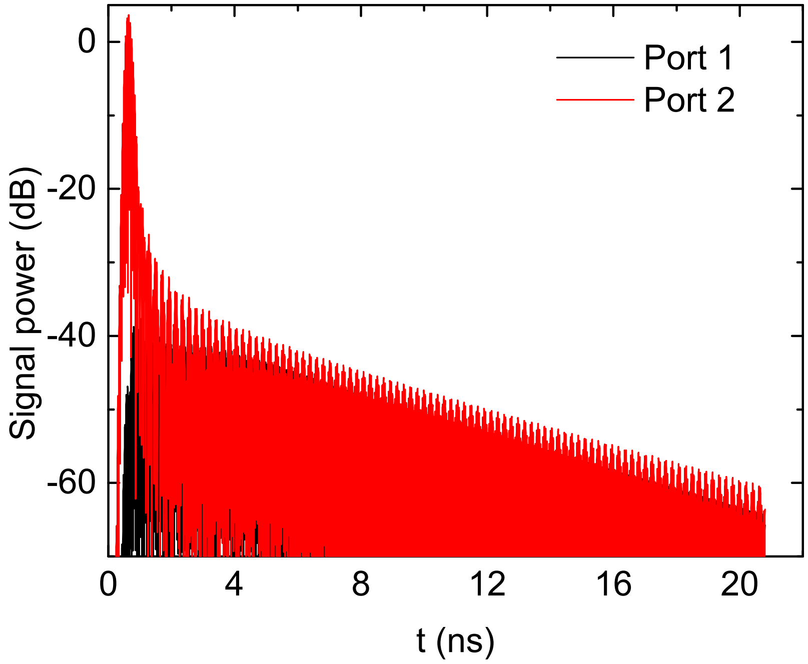

(g)

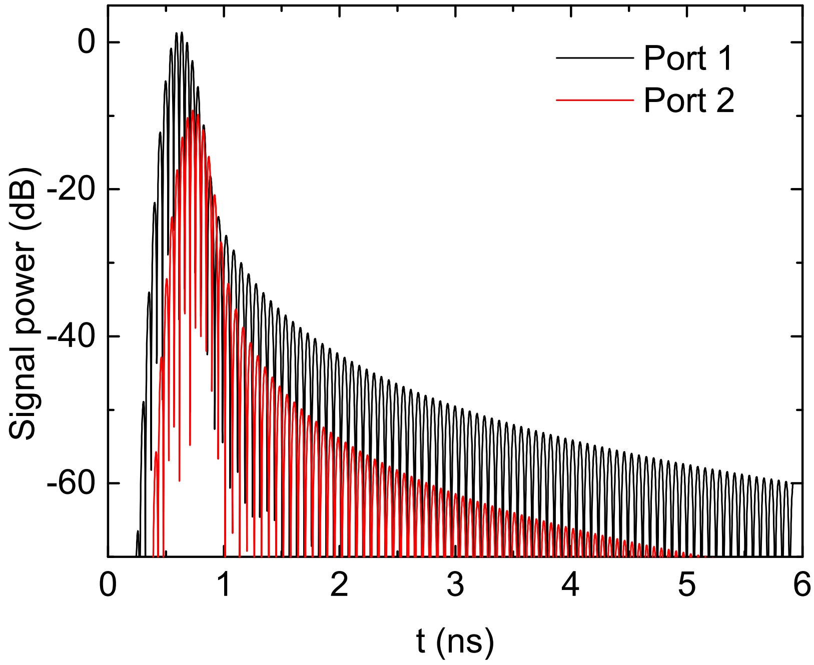

(h)

Figure 8.7 continued: (g) Subdomain 3 simulation with the TE_{10} mode excited at port 2. (h) Subdomain 4 simulation with the TE_{10} mode excited at port 1. *(cont.)*

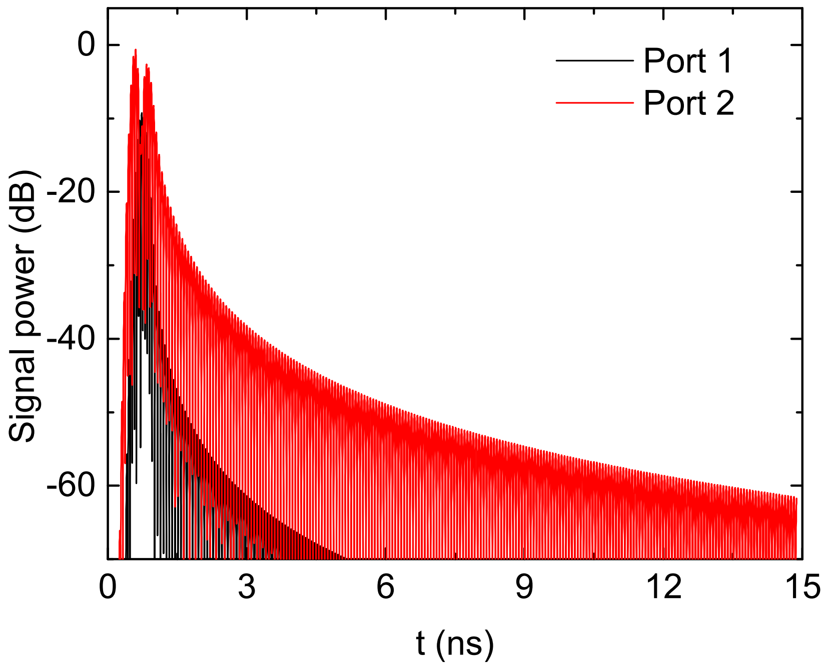

(i)

Figure 8.7 continued: (i) Subdomain 4 simulation with the TE_{10} mode excited at port 2.

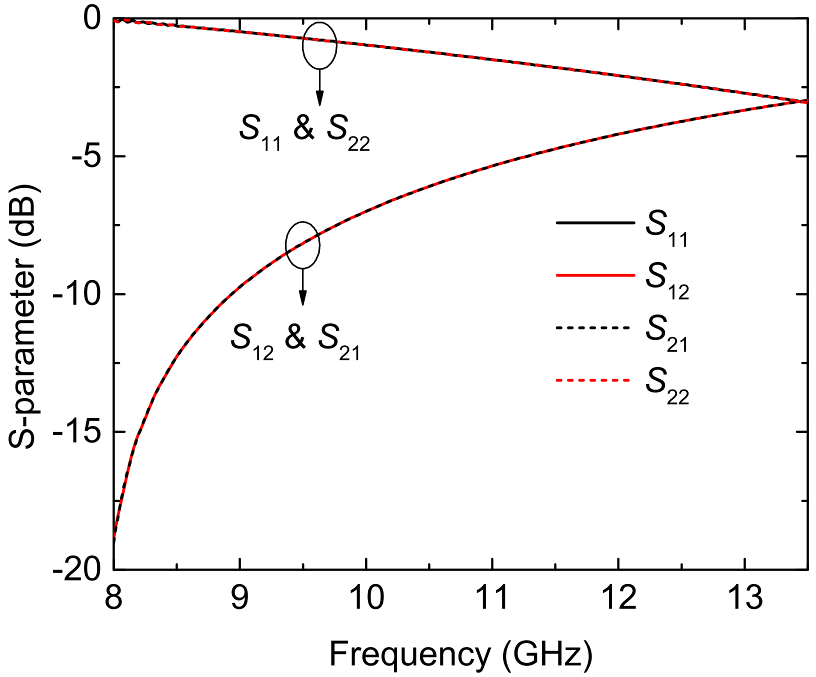

(a)

Figure 8.8: Frequency-domain responses for the hybrid folded filter. (a) Subdomain 1 responses. *(cont.)*

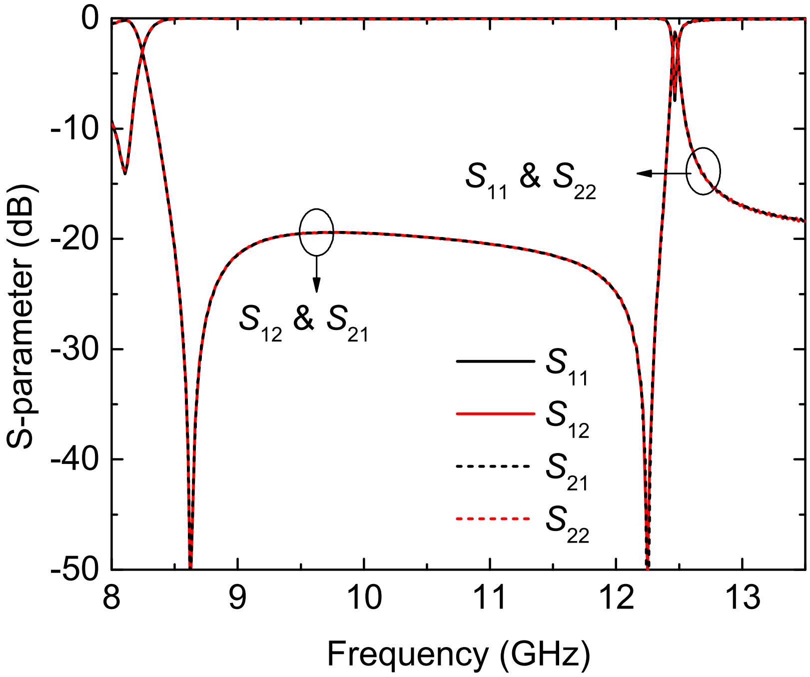

(b)

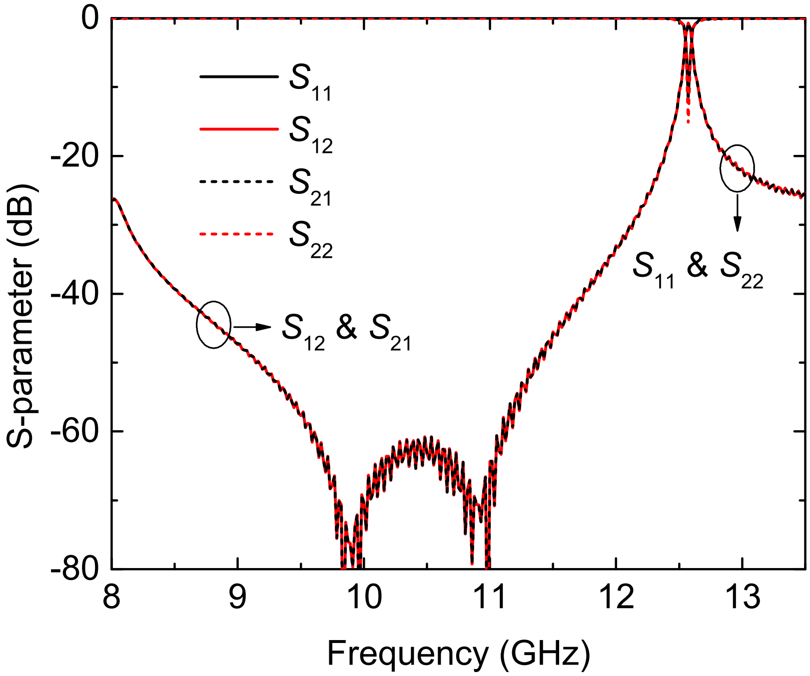

(c)

Figure 8.8 continued: (b) Subdomain 2 responses. (c) Subdomain 3 responses. *(cont.)*

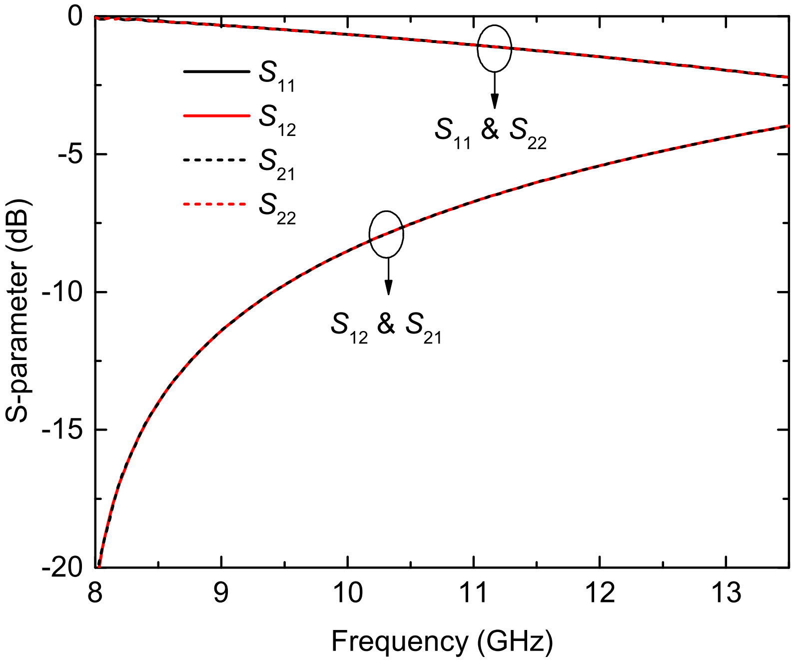

(d)

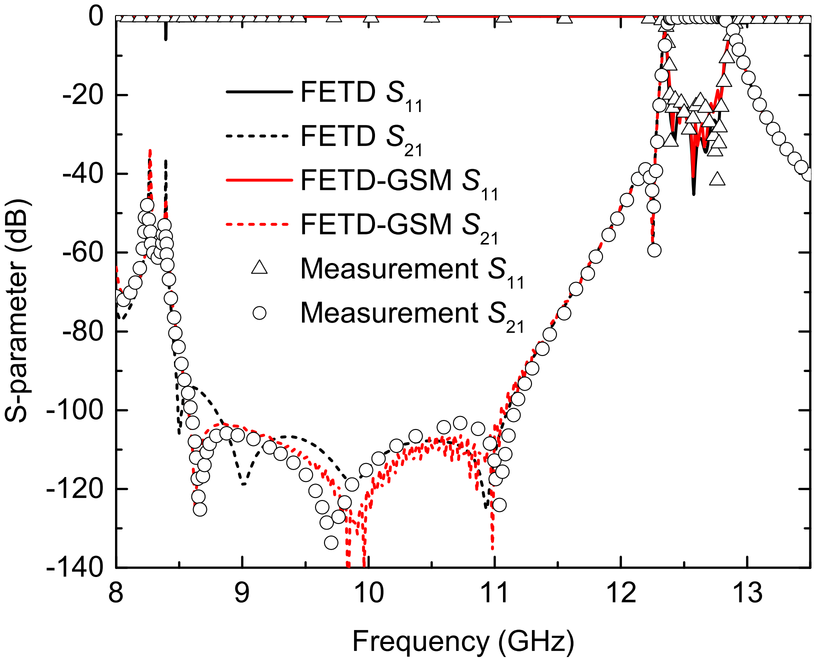

(e)

Figure 8.8 continued: (d) Subdomain 4 responses. (e) Full structure responses.

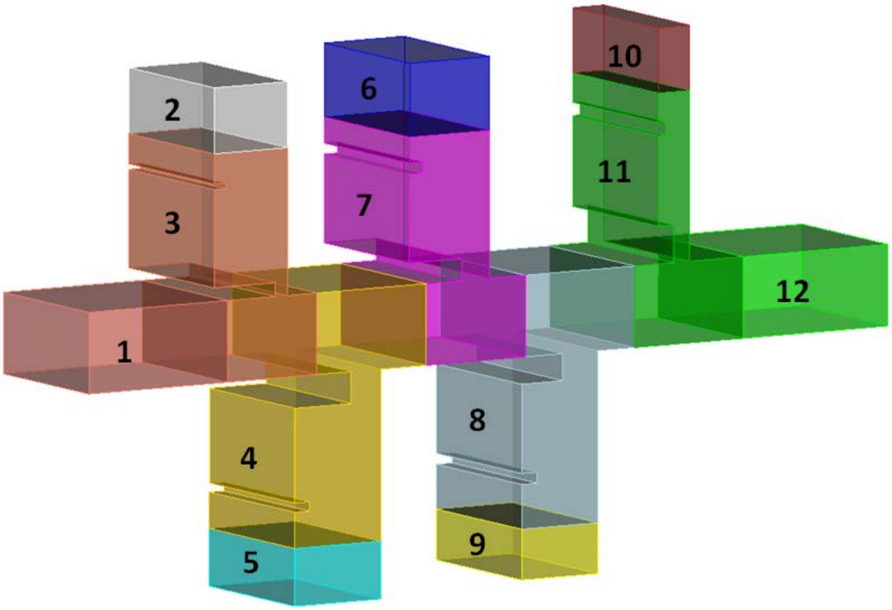

Figure 8.9: Geometry of the in-line pure E-plane band-stop filter. The filter is decomposed into 12 subdomains consisting of one-port, two-port, and three-port components.

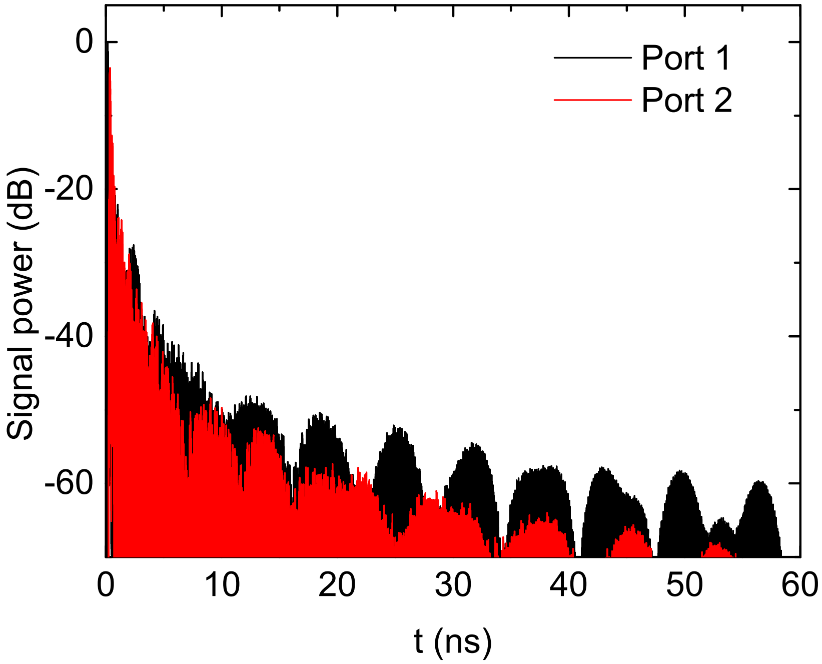

(a)

Figure 8.10: Time-domain signal powers for the in-line pure E-plane band-stop filter simulation. Port 1 and port 2 respectively represent the left port and the right port in both full structure and subdomain simulations, and port 3 denotes the top/bottom port of a three-port structure in subdomain simulations. (a) Simulation of the full structure. *(cont.)*

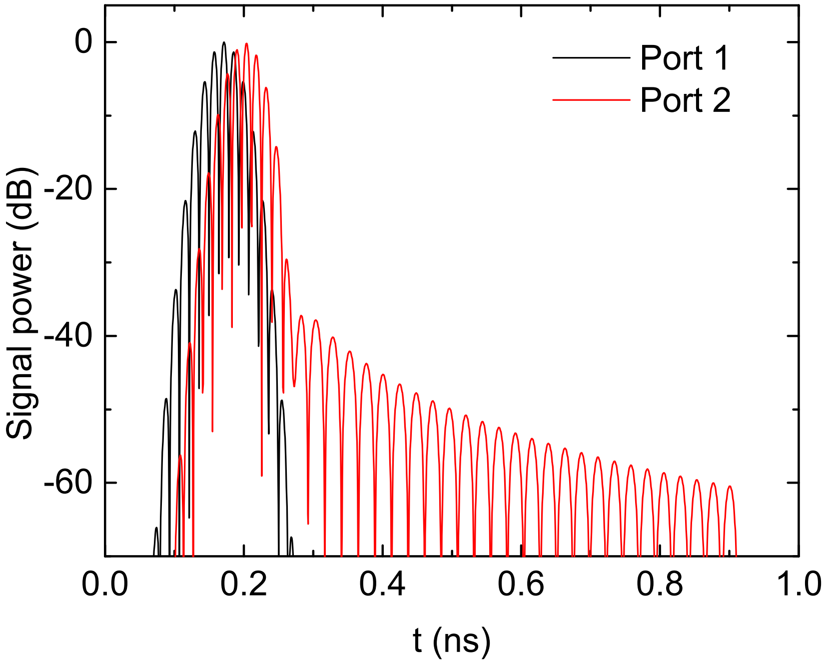

(b)

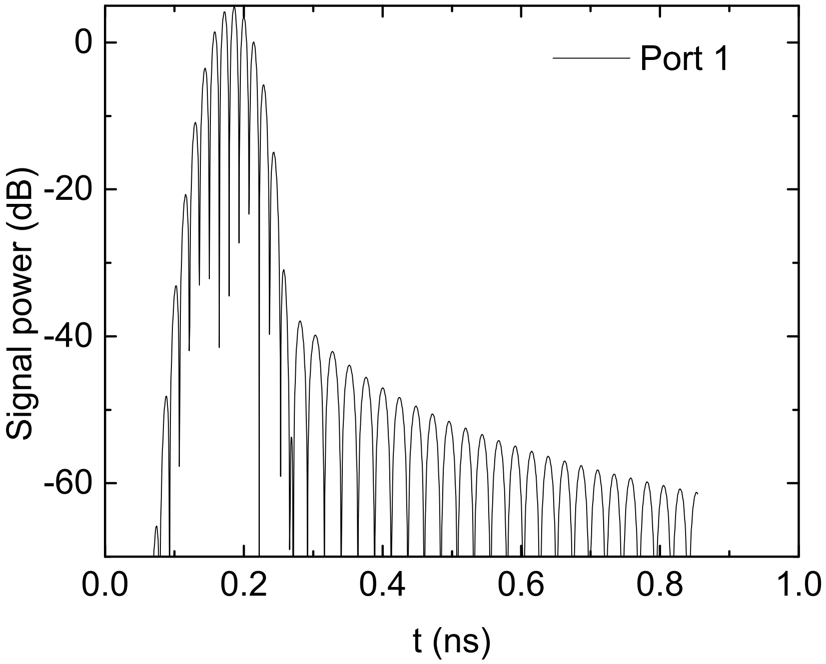

(c)

Figure 8.10 continued: (b) Simulation of subdomain 1 with incidence at port 1. (c) Simulation of subdomain 2. *(cont.)*

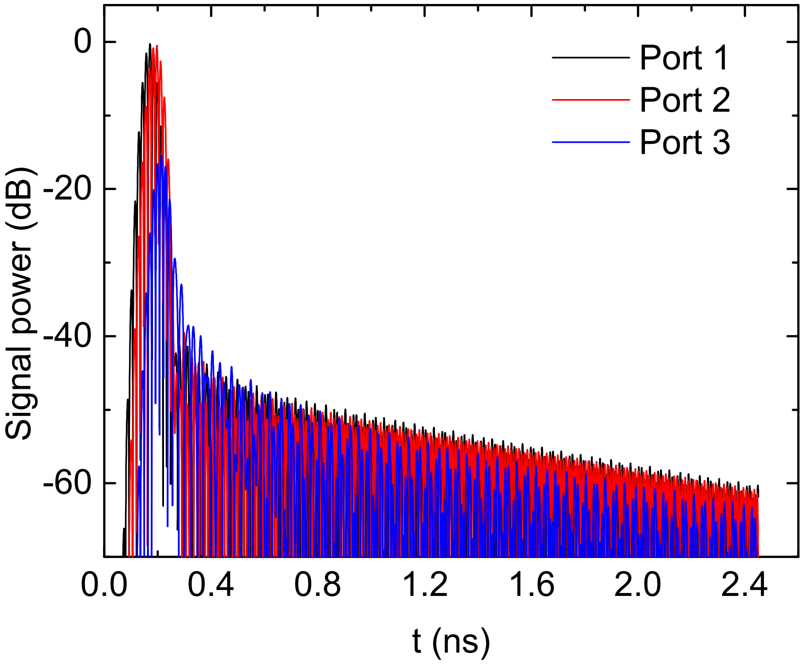

(d)

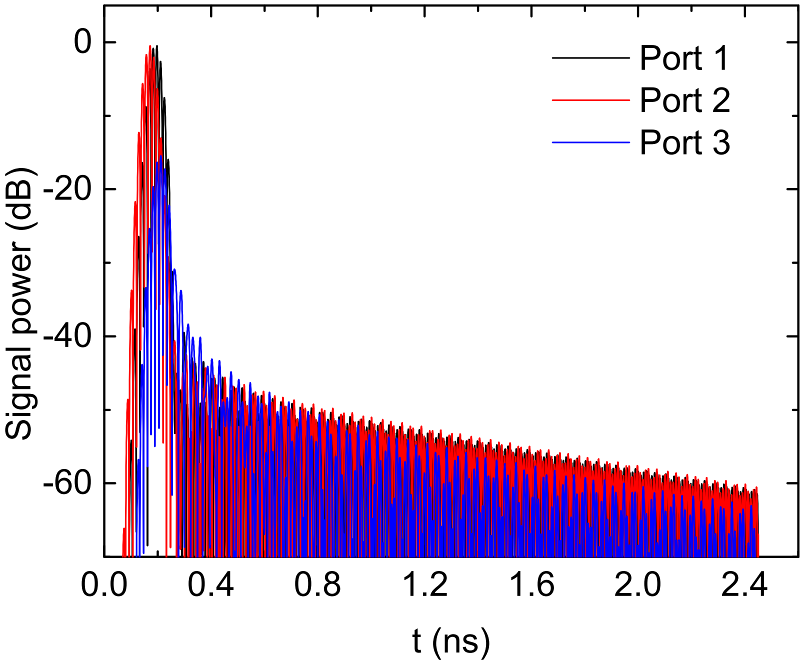

(e)

Figure 8.10 continued: (d) Simulation of subdomain 3 with the incidence applied on port 1. (e) Simulation of subdomain 3 with the incidence applied on port 2. *(cont.)*

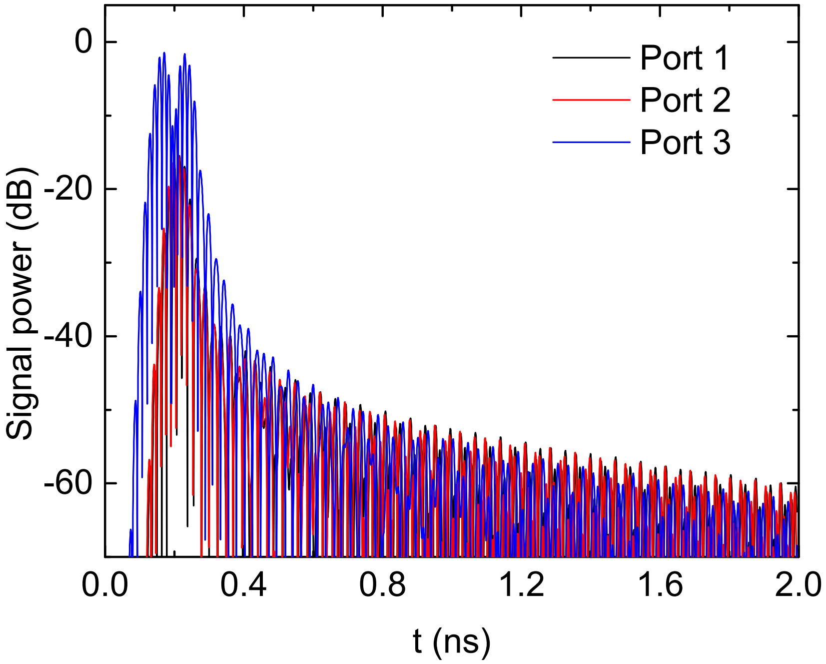

(f)

Figure 8.10 continued: (f) Simulation of subdomain 3 with the incidence applied on port 3.

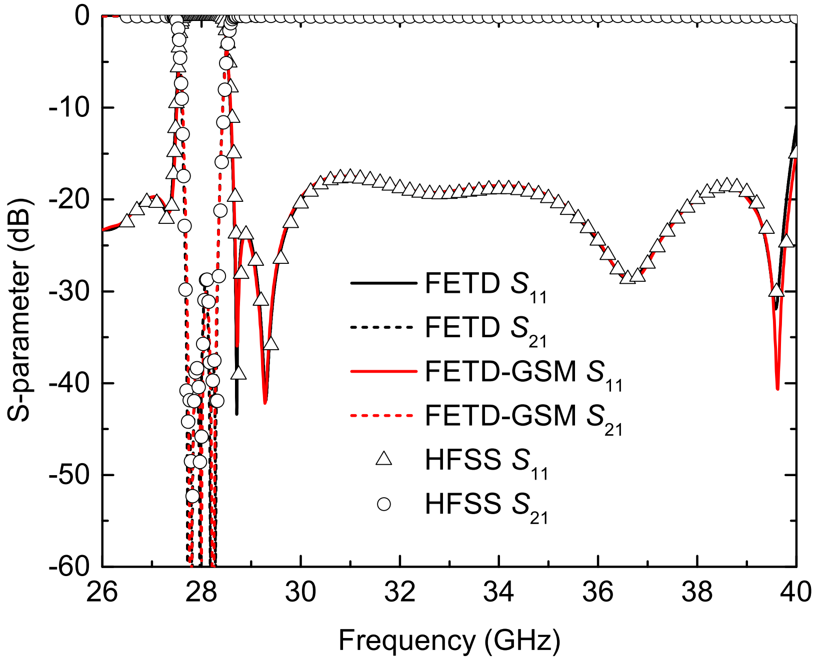

Figure 8.11: Frequency-domain responses of the in-line pure E-plane band-stop filter.

Table 8.1: Computational statistics of the circular cavity filter.

Geo/Src	DoFs	RAM (GB)	N_t	Total time (s)
Whole/Port1	188,332	1.66	46,000	7,551
Half/Port1	94,584	0.83	7,400	593
Half/Port2	94,584	0.83	6,400	505

Table 8.2: Computational statistics of the hybrid folded filter.

Geo/Src	DoFs	RAM (GB)	N_t	Total time (s)
Whole/Port1	700,516	7.96	130,000	108,360
Sub1/Port1	115,610	1.15	8,500	1,001
Sub1/Port2	115,610	1.15	4,200	460
Sub2/Port1	373,144	2.85	17,000	4,700
Sub2/Port2	373,144	2.85	15,000	4,087
Sub3/Port1	220,950	1.86	13,000	2,390
Sub3/Port2	220,950	1.86	13,000	2,393
Sub4/Port1	103,492	0.97	3,700	369
Sub4/Port2	103,492	0.97	9,300	1,035

Table 8.3: Computational statistics of the in-line pure E-plane band-stop filter.

Geo/Src	DoFs	RAM (GB)	N_t	Total time (s)
Whole/Port1	977,386	8.77	103,000	90,460
Sub1/Port1	50,052	0.51	1,600	96
Sub1/Port2	50,052	0.51	1,600	96
Sub2/Port1	23,102	0.22	1,500	37
Sub3/Port1	213,068	1.84	4,300	781
Sub3/Port2	213,068	1.84	4,300	797
Sub3/Port3	213,068	1.84	3,500	639
Sub4/Port1	132,236	1.29	3,800	518
Sub4/Port2	132,236	1.29	3,800	528
Sub4/Port3	132,236	1.29	3,200	429
Sub5/Port1	20,964	0.23	1,400	42
Sub6/Port1	26,774	0.27	1,500	47
Sub7/Port1	172,944	1.65	3,600	615
Sub7/Port2	172,944	1.65	3,600	620
Sub7/Port3	172,944	1.65	3,100	531
Sub8/Port1	159,762	1.46	2,900	431
Sub8/Port2	159,762	1.46	2,900	440
Sub8/Port3	159,762	1.46	3,000	446
Sub9/Port1	16,152	0.17	1,300	26
Sub10/Port1	9,518	0.07	1,400	8
Sub11/Port1	110,842	0.91	1,500	145
Sub11/Port2	110,842	0.91	1,600	154
Sub11/Port3	110,842	0.91	2,400	230
Sub12/Port1	51,306	0.52	1,600	95
Sub12/Port1	51,306	0.52	1,600	98

Chapter 9

FETD-GSM for Cavity Scattering

9.1 Introduction

Fast computation of electromagnetic scattering from a large and deep open cavity with high fidelity and efficiency has been a challenging problem in computational electromagnetics for the past four decades [82–100]. This problem is even more pronounced when broadband monostatic responses are desired, such as those required in ISAR imaging [166–169]. Early research was mainly focused on edge diffraction and ray tracing based high-frequency asymptotic methods to predict the RCS of a cavity with a simple structure and a large electrical size [82–85]. When cavities become geometrically complicated, these high-frequency approximations deteriorate in the solution accuracy. To circumvent this issue and enable the analysis of cavities with complex materials, rigorous full-wave numerical methods and their hybrid variants, combined with either an asymptotic technique or another full-wave method, were gradually introduced [2, 3, 86–91, 148]. Over the years, benefitting from the development of fast and efficient full-wave algorithms to reduce the memory consumption and computation cost [2, 3, 148], electromagnetic scattering from cavities with moderate electrical sizes can be modeled with a high accuracy. The reader is referred to [99] and the references therein for a comprehensive review of computational methods developed in the past for open cavity scattering analyses.

Despite this significant progress, computation of broadband monostatic RCS of a large and deep open cavity is still very challenging. In [98], a tailored direct solver was proposed to efficiently model cavity scattering using the FEBI method. The solver exploits the unique features of the FEBI system and the waveguide structure of a large and deep cavity to eliminate the interior FE unknowns starting from the bottom of the cavity and leave only the aperture unknowns in the system for a fast monostatic RCS calculation. This algorithm was later enhanced by incorporating higher-order curl-conforming basis functions to expand the unknown field [95, 97] and extended to more general cases to account for inhomogeneous coatings [96]. For a specific mesh discretization scheme, the memory consumption is solely determined by the cavity's cross-section. It is observed that the solution time scales linearly with the cavity's depth and the method is computationally efficient for cavities with a cross-section smaller than 100 square wavelengths. Unfortunately, the efficiency of this method deteriorates quickly for cavities with a larger cross-section because the solution time increases exponentially with the cross-section of the cavity. Furthermore, this method cannot be well parallelized to harness the parallel processing power of modern computer clusters and is ineffective for a broadband RCS analysis.

As an alternative approach, the domain decomposition method (DDM) has also been proposed for the scattering analysis of a large and deep cavity. A straightforward strategy is to partition the deep cavity into several subdomains along the depth direction, and then employ a full-wave solver to deal with each subdomain independently. After that, generalized admittance or scattering matrices (GAMs/GSMs) are extracted from each subdomain and cascaded to represent the behavior of the original cavity [90, 91]. However, due to its requirements for discretization and basis functions, the GAM method demonstrated potential only for fairly small and simple cavities [90]. The GSM method [91], on the other hand, removed the requirements in the GAM method by using modal bases at the subdomain interfaces. Unfortunately, its solution accuracy, especially at large incident angles, is significantly limited by the subdomain GSMs where higher-order modal effects must be simulated very accurately in order to account for modal power coupling in a general cavity. Later on, a more sophisticated DDM-based FEBI method was proposed to simulate large and deep cavities with the MLFMA acceleration [93]. Unlike the previous DDMs that completely decouple the subdomains, this method divides a cavity into several layers and eliminates the interior unknowns of each layer based on the local Schur complement to form a coupled global interface problem that involves FE unknowns on the layer-to-layer interfaces and the BI unknowns on the aperture. The coupled interface problem is then solved iteratively until a convergence criterion is satisfied. More recently, an advanced BI-based DDM was also proposed for scattering analysis of large and deep cavities [94]. By introducing surface traces of the electric and magnetic fields as unknowns, a multi-trace combined field integral equation was developed for the subdomain boundary-value problems, together with an optimized multiplicative Schwarz preconditioner to speed up the iterative convergence. Although electrically large cavities can be simulated by these full-wave DDM solvers via coupled interface problems, the iterative convergence is still an issue when the large and deep cavity is lossless (or has a small interior loss). More seriously, being a frequency-domain method the iterative solution is not efficient for the monostatic RCS calculation or for a broadband sweep.

In this chapter, we propose a hybrid algorithm that combines the FETD method [3] and GSM technique to efficiently simulate large and deep cavities by exploiting the waveguide-like structure of the open cavities and adopting waveguide modes as basis functions to expand the electric field at the cavity aperture. With the FETD transient simulations, a broadband GSM is extracted to represent the scattering characteristics of the original cavity. Since the dimensions of the GSM are significantly smaller than those of the system equation directly resulting from the FE discretizations, monostatic RCS calculations can be performed very efficiently. For the FETD simulation, the complex-frequency shifted perfectly matched layers (CFS-PML) [170] are employed as the truncation for the cavity aperture so that all the waveguide modes will be appropriately absorbed. The ABC is placed at the outmost boundaries of CFS-PMLs to further improve the absorption and increase the time marching stability. Moreover, unlike the FEBI-based methods which generate a partially full system matrix that is difficult to store and solve, the resultant system matrix from the ABC-backed CFS-PML is purely sparse, which enables the simulation of very large and deep open cavity scattering problems.

The rest of this chapter is organized as follows. In Section 9.2, we formulate the eigenvalue problems for general waveguide ports and the FETD method with ABC and CFS-PML truncations. Afterwards, we describe the calculation of the scattered field and approaches to improve the computational efficiency. In Section 9.3, we validate the proposed algorithm by comparing the simulation results of scattering from two straight cavities with measurements, and present two complicated structures to further demonstrate its solution accuracy and efficiency for the broadband wide-angle scattering simulation and ISAR imagery. Finally, we conclude in Section 9.4.

9.2 Formulation

The proposed hybrid algorithm combines the FETD method and GSM technique to efficiently analyze large and deep open cavities. In this section, we present the formulation and implementation for the numerical modal analysis of an arbitrary cross-section and the FETD method with an ABC-backed CFS-PML truncation for transient simulations. We then present the broadband monostatic RCS evaluation and ISAR imagery using a broadband GSM obtained from the FETD solution. Finally, we discuss the issue of selecting dominant scattering modes to improve the efficiency of this hybrid algorithm.

9.2.1 Modal Profiles at Waveguide Ports

The proposed method relies on the modal profiles to expand the electric field at the aperture of the cavity as well as the field at the interfaces between subdomains when a domain decomposition algorithm [117] is employed. For a general waveguide cross section S with material properties specified by the relative permittivity ϵ_{r} and permeability μ_{r}, the electric field $\mathbf{E}$ is governed by the source-free vector Helmholtz equation

$$\nabla \times \left(\frac{1}{\mu_{\mathrm{r}}} \nabla \times \mathbf{E} \right) = k_0^2 \epsilon_{\mathrm{r}} \mathbf{E}, \tag{9.1}$$

and is subject to the Dirichlet boundary condition

$$\hat{n} \times \mathbf{E} = 0 \tag{9.2}$$

on a PEC boundary, where k_0 is the free-space wavenumber and $\hat{n}$ is the outward unit normal vector on the boundary of S. Assuming that the electric field has the $\mathrm{e}^{-\gamma z}$ dependence, where γ is the propagating constant, the electric field and the ∇ operator can be decomposed into transverse and $\hat{z}$ components. A generalized eigenvalue system can then be derived from

(9.1) [171]

$$\begin{bmatrix} H + A/\Theta^2 & G \\ G^{\mathrm{T}} & B \end{bmatrix} \begin{Bmatrix} e_t \\ e_z \end{Bmatrix} = \frac{\Theta^2 + \gamma^2}{\Theta^2} \begin{bmatrix} H & G \\ G^{\mathrm{T}} & B \end{bmatrix} \begin{Bmatrix} e_t \\ e_z \end{Bmatrix}, \tag{9.3}$$

in which

$$A_{ij} = \int_S \left[\frac{1}{\mu_{\mathrm{r}}} (\nabla_t \times \mathbf{N}_i) \cdot (\nabla_t \times \mathbf{N}_j) - k_0^2 \epsilon_{\mathrm{r}} \mathbf{N}_i \cdot \mathbf{N}_j \right] \mathrm{d}\mathbf{r}, \tag{9.4}$$

$$B_{ij} = \int_S \left[\frac{1}{\mu_{\mathrm{r}}} \nabla_t \phi_i \cdot \nabla_t \phi_j - k_0^2 \epsilon_{\mathrm{r}} \phi_i \phi_j \right] \mathrm{d}\mathbf{r}, \tag{9.5}$$

$$H_{ij} = \int_S \frac{1}{\mu_{\mathrm{r}}} \mathbf{N}_i \cdot \mathbf{N}_j \mathrm{d}\mathbf{r}, \tag{9.6}$$

$$G_{ij} = \int_S \frac{1}{\mu_{\mathrm{r}}} \mathbf{N}_i \cdot \nabla_t \phi_j \mathrm{d}\mathbf{r}, \tag{9.7}$$

$$\Theta^2 = k_0^2 \mu_{\mathrm{max}} \epsilon_{\mathrm{max}}, \tag{9.8}$$

and $\mathbf{E}$ is expanded by N_V hierarchical vector bases $\mathbf{N}_i$ and N_N hierarchical nodal bases ϕ_i [4]

$$\mathbf{E} = \gamma \sum_{i=1}^{N_V} e_{t,i} \mathbf{N}_i + \hat{z} \sum_{i=1}^{N_N} e_{z,i} \phi_i. \tag{9.9}$$

Note that μ_{max} and ϵ_{max} in (9.8) are respectively the maximum relative permeability and permittivity on the waveguide port.

The resultant generalized eigenvalue problem is solved by the FEAST eigensolver [162], which adopts the idea from the density-matrix representation and contour integration technique in quantum mechanics to achieve high robustness, accuracy, and scalability. However, the eigenvalue system suffers from DC spurious modes ($\gamma = 0$ and $\{e_z\} \neq 0$), as can be observed from the second equation of (9.3). To remove the undesired spurious modes, a constraint

$$\{e_z\} = -[B]^{-1}[G^{\mathrm{T}}]\{e_t\} \tag{9.10}$$

is applied to rectify the normal electric field with the tangential component in each matrix-vector product iteration of the FEAST eigensolver.

9.2.2 FETD Method with ABC-Backed CFS-PML

Once the modal profiles at a cavity aperture are obtained, they can be used to launch modal incidences and retrieve a broadband GSM that characterizes the scattering properties of the cavity. To perform a transient simulation, we first formulate the time-domain vector wave equation with the CFS-PML materials [3]

$$\nabla \times \left[\frac{1}{\mu} \overline{\mathbf{L}}_2 \cdot (\nabla \times \mathbf{E}) \right] + \epsilon \overline{\mathbf{L}}_1 \cdot \mathbf{E} + \sigma_{\mathrm{e}} \frac{\partial \mathbf{E}}{\partial t} = -\frac{\partial \mathbf{J}_{\mathrm{imp}}}{\partial t}, \tag{9.11}$$

where $\epsilon = \epsilon_{\mathrm{r}} \epsilon_0$ and $\mu = \mu_{\mathrm{r}} \mu_0$ with ϵ_0 and μ_0 the free-space permittivity and permeability, σ_{e} denotes the material conductivity, and $\mathbf{J}_{\mathrm{imp}}$ represents the impressed current which is obtained by multiplying a modal profile by a modulated Gaussian pulse. The CFS-PML based constitutive tensors $\overline{\mathbf{L}}_1$ and $\overline{\mathbf{L}}_2$ in (9.11) are respectively given by [3]

$$\overline{\mathbf{L}}_1 = \overline{\boldsymbol{\kappa}} \cdot \left[\frac{\partial^2}{\partial t^2} \overline{\mathbf{I}} + \overline{\mathbf{J}} \frac{\partial}{\epsilon_0 \partial t} + \frac{1}{\epsilon_0^2} \overline{\mathbf{K}}_1 - \frac{1}{\epsilon_0^3} \overline{\mathbf{K}}_2 \cdot \mathrm{e}^{-\frac{\overline{\boldsymbol{\sigma}}}{\epsilon_0} t} \mathrm{u}(t) * \right], \tag{9.12}$$

$$\overline{\mathbf{L}}_2 = \overline{\boldsymbol{\kappa}}^{-1} \cdot \left[\overline{\mathbf{I}} - \frac{1}{\epsilon_0} \overline{\mathbf{J}} \cdot \mathrm{e}^{-\frac{\overline{\boldsymbol{\tau}}}{\epsilon_0} t} \mathrm{u}(t) * \right], \tag{9.13}$$

with

$$\overline{\boldsymbol{\kappa}} = \kappa (\hat{x}\hat{x} + \hat{y}\hat{y}) + \kappa^{-1} \hat{z}\hat{z}, \tag{9.14}$$

$$\overline{\mathbf{I}} = \hat{x}\hat{x} + \hat{y}\hat{y} + \hat{z}\hat{z}, \tag{9.15}$$

$$\overline{\mathbf{J}} = \sigma \kappa^{-1} (\hat{x}\hat{x} + \hat{y}\hat{y} - \hat{z}\hat{z}), \tag{9.16}$$

$$\overline{\mathbf{K}}_1 = -\alpha \sigma \kappa^{-1} (\hat{x}\hat{x} + \hat{y}\hat{y}) + \sigma \kappa^{-1} (\sigma \kappa^{-1} + \alpha) \hat{z}\hat{z}, \tag{9.17}$$

$$\overline{\mathbf{K}}_2 = -\alpha^2 \sigma \kappa^{-1} (\hat{x}\hat{x} + \hat{y}\hat{y}) + \sigma \kappa^{-1} (\sigma \kappa^{-1} + \alpha)^2 \hat{z}\hat{z}, \tag{9.18}$$

$$\overline{\boldsymbol{\sigma}} = \alpha \hat{x}\hat{x} + \alpha \hat{y}\hat{y} + (\sigma \kappa^{-1} + \alpha) \hat{z}\hat{z} \tag{9.19}$$

$$\overline{\boldsymbol{\tau}} = (\sigma \kappa^{-1} + \alpha)(\hat{x}\hat{x} + \hat{y}\hat{y}) + \alpha \hat{z}\hat{z}. \tag{9.20}$$

In (9.12) and (9.13), $\mathrm{u}(t)*$ represents the time-domain convolution with the unit step function and ϵ_0 instead of ϵ is adopted to avoid the accumulation of electric charges at material interfaces [148]. Note in (9.14)-(9.20) that the CFS-PML is placed in the XY plane to absorb waves travelling in the $\pm\hat{z}$ directions. The CFS-PML parameters κ, σ, and α can be adjusted for the performance of absorption [148]. For waveguide ports not placed in the XY

plane, a transformation of the constitutive tensors is required [172]

$$\overline{\mathbf{L}}_1' = \mathbf{R}^{\mathrm{T}}\overline{\mathbf{L}}_1\mathbf{R}, \quad \overline{\mathbf{L}}_2' = \mathbf{R}\overline{\mathbf{L}}_2\mathbf{R}^{\mathrm{T}} \tag{9.21}$$

to absorb waves travelling in the desired directions, where $\mathbf{R}$ is a unitary rotation matrix.

To further improve the absorption of waveguide modes and increase the time marching stability, the ABC

$$\hat{n} \times \left(\frac{1}{\mu}\nabla \times \mathbf{E}\right) + \sqrt{\frac{\epsilon}{\mu}}\frac{\partial}{\partial t}(\hat{n} \times \hat{n} \times \mathbf{E}) = 0 \tag{9.22}$$

is applied to truncate the CFS-PML. Using the standard Galerkin method for spatial discretization, a matrix equation is yielded

$$[T]\left\{\frac{\mathrm{d}^2 E}{\mathrm{d}t^2}\right\} + [R]\left\{\frac{\mathrm{d}E}{\mathrm{d}t}\right\} + [S]\{E\} - \{h\} + \{g\} = \{b\}, \tag{9.23}$$

where

$$\begin{aligned}
T_{ij} &= \int_V \epsilon \mathbf{N}_i \cdot \overline{\boldsymbol{\kappa}} \cdot \mathbf{N}_j \mathrm{d}\mathbf{r}, && (9.24)\\
R_{ij} &= \int_V \sigma_{\mathrm{e}} \mathbf{N}_i \cdot \mathbf{N}_j \mathrm{d}\mathbf{r} + \int_V \epsilon_{\mathrm{r}} \mathbf{N}_i \cdot \overline{\boldsymbol{\kappa}} \cdot \overline{\mathbf{J}} \cdot \mathbf{N}_j \mathrm{d}\mathbf{r}\\
&\quad + \int_{S_{\mathrm{ABC}}} \mu_0 \sqrt{\frac{\epsilon}{\mu}} (\hat{n} \times \mathbf{N}_i) \cdot (\hat{n} \times \mathbf{N}_j) \mathrm{d}\mathbf{r}, && (9.25)\\
S_{ij} &= \int_V \frac{1}{\mu} (\nabla \times \mathbf{N}_i) \cdot \overline{\boldsymbol{\kappa}}^{-1} \cdot (\nabla \times \mathbf{N}_j) \mathrm{d}\mathbf{r}\\
&\quad + \int_V \frac{\epsilon}{\epsilon_0^2} \mathbf{N}_i \cdot \overline{\boldsymbol{\kappa}} \cdot \overline{\mathbf{K}}_1 \cdot \mathbf{N}_j \mathrm{d}\mathbf{r}, && (9.26)\\
h_i &= \int_V \frac{\epsilon}{\epsilon_0^3} \mathbf{N}_i \cdot \overline{\boldsymbol{\kappa}} \cdot \sum_{j=1}^{N} \overline{\mathbf{K}}_2 \cdot \mathrm{e}^{-\frac{\overline{\boldsymbol{\sigma}}}{\epsilon_0}t} \cdot \mathbf{N}_j \mathrm{u}(t) * E_j(t) \mathrm{d}\mathbf{r}, && (9.27)\\
g_i &= \int_V \frac{1}{\mu \epsilon_0} (\nabla \times \mathbf{N}_i) \cdot \overline{\boldsymbol{\kappa}}^{-1}\\
&\quad \cdot \sum_{j=1}^{N} \overline{\mathbf{J}} \cdot \mathrm{e}^{-\frac{\overline{\boldsymbol{\tau}}}{\epsilon_0}t} \cdot (\nabla \times \mathbf{N}_j) \mathrm{u}(t) * E_j(t) \mathrm{d}\mathbf{r}, && (9.28)\\
b_i &= -\int_V \mathbf{N}_i \cdot \frac{\partial \mathbf{J}_{\mathrm{imp}}}{\partial t} \mathrm{d}\mathbf{r}. && (9.29)
\end{aligned}$$

To perform a time-domain simulation, it remains to temporally discretize

(9.23) to form a time marching scheme. The Newmark-beta method is implemented for the proposed hybrid algorithm to achieve a second-order temporal accuracy and unconditional stability [157].

It is worth mentioning that the CFS-PML is essentially a uniaxial anisotropic material [173], which has different attenuations for different field components. Hence, we use full-order curl-conforming bases to better resolve the field in the CFS-PML region so that the time marching stability of the proposed algorithm can be significantly improved [174]. Computationally, the shifted poles in the CFS-PML constitutive tensors give rise to the time-consuming convolutions in (9.27) and (9.28), even though $\{h_i\}$ and $\{g_i\}$ are non-vanishing only in the CFS-PML medium. Fortunately, the convolutions can be implemented in a recursive fashion to reduce the computational cost remarkably [174].

9.2.3 RCS Calculation and ISAR Imagery

In the proposed hybrid FETD-GSM algorithm, the incident and reflected fields are both expanded by the same set of modal bases $\{\mathbf{u}_i\}$

$$\mathbf{E}^{\mathrm{inc}} = \sum_{i=1}^{M} a_i \mathbf{u}_i, \quad \mathbf{E}^{\mathrm{ref}} = \sum_{i=1}^{M} b_i \mathbf{u}_i, \tag{9.30}$$

where the coefficients for incident modes a_i are expressed as

$$a_i = \int_S \mathbf{u}_i \cdot \mathbf{E}^{\mathrm{inc}} \mathrm{d}\mathbf{r}. \tag{9.31}$$

The coefficients for the incident and reflected modal fields are related via the GSM $[S_{ij}]$

$$\{b_i\} = [S_{ij}]\{a_j\}, \tag{9.32}$$

where

$$S_{ji} = \frac{\int_S \mathbf{u}_j \cdot (\mathbf{E}_i^{\mathrm{tot}} - \mathbf{E}_i^{\mathrm{inc}}) \mathrm{d}\mathbf{r}}{\int_S \mathbf{u}_i \cdot \mathbf{E}_i^{\mathrm{inc}} \mathrm{d}\mathbf{r}}. \tag{9.33}$$

In (9.33), $\mathbf{E}_i^{\mathrm{tot}}$ and $\mathbf{E}_i^{\mathrm{inc}}$ are the total and incident fields with the launching of the ith modal incidence. Once the broadband GSM is obtained, the reflected modal coefficients can be calculated through (9.32) and then the reflected field from the second equation in (9.30).

The RCS contributed by the interior of an open cavity is calculated as

$$\sigma = \lim_{r\to\infty} 4\pi r^2 \frac{|\mathbf{E}^{\mathrm{sca}}(\mathbf{r})|^2}{|\mathbf{E}^{\mathrm{inc}}(\mathbf{r})|^2}, \tag{9.34}$$

where the scattered far-field $\mathbf{E}^{\mathrm{sca}}(\mathbf{r})$ is given by

$$\mathbf{E}^{\mathrm{sca}}(\mathbf{r}) \approx \mathrm{j}k_0 \frac{\mathrm{e}^{-\mathrm{j}k_0 r}}{4\pi r} \int_S \hat{r} \times (\hat{r} \times \eta_0 \mathbf{J}_{\mathrm{s}} + \mathbf{M}_{\mathrm{s}}) \mathrm{e}^{\mathrm{j}k_0 \hat{r}\cdot\mathbf{r}'} \mathrm{d}\mathbf{r}'. \tag{9.35}$$

In (9.35), η_0 denotes the free-space intrinsic impendence, $\mathbf{J}_{\mathrm{s}}$ is the equivalent electric current on the cavity aperture which can be approximated by the physical optics (PO) technique and vanishes when an infinite ground plane is present, and $\mathbf{M}_{\mathrm{s}}$ is the equivalent magnetic current on the cavity aperture which is directly evaluated using the reflected field [98]. A straightforward implementation of (9.35) can be computationally expensive when the numbers of source points M and field points N are very large. The MLFMA is adopted to reduce the computational complexity from $O(MN)$ to $O(N \log M)$ [2].

The broadband wide-angle scattered fields can be further processed to produce ISAR images, which are important for target identification, recognition, and classification [166–169]. The ISAR imagery is usually formed on the two-dimensional (2D) range and cross-range plane via [169]

$$\mathrm{ISAR}(x, y) = \frac{1}{\Delta} \int_{\theta_1}^{\theta_2}\int_{k_1}^{k_2} \hat{p} \cdot \mathbf{E}^{\mathrm{sca}}(k, \theta) \mathrm{e}^{\mathrm{j}2(k_x x + k_y y)} \mathrm{d}k\mathrm{d}\theta, \tag{9.36}$$

where $\mathbf{E}^{\mathrm{sca}}(k, \theta)$ is the scattered field represented in the k-θ plane with $[\theta_1, \theta_2]$ and $[k_1, k_2]$ respectively denoting the angle and wavenumber sweeping ranges, $\hat{p}$ is the polarization of interested, $\Delta = (k_2 - k_1)(\theta_2 - \theta_1)$, $k_x = k\cos\theta$, and $k_y = k\sin\theta$. Again, the direct evaluation of (9.36) is expensive. A more efficient approach is to resample the scattered field in the k_x-k_y plane so that the FFT can be utilized to accelerate the imaging process [169].

9.2.4 Dominant Scattering Modes

Theoretically, all the modes should be considered at the waveguide port in order to form a complete set of bases. However, because of the finite element discretization, not all the modes can be resolved. In addition, modes with large attenuation constants tend to contribute less in the RCS predictions. Hence, we use the following criteria in the modal profile calculations:

$$0 \leq \frac{\Theta^2 + \gamma^2}{\Theta^2} \leq 1. \tag{9.37}$$

Since each modal basis has to be launched as an incidence, the number of modes plays an important role in the efficiency of the proposed algorithm. Fortunately, only a portion of the modes calculated with (9.37) contribute significantly to the RCS. Since $\{a_i\}$ in (9.31) is a function of frequency, incident angle, polarization, and modal index, we sweep all the parameter combinations to find the dominant modes. More specifically, the modal powers

$$P_i = 20 \log_{10} |a_i| \tag{9.38}$$

are normalized with the most dominant mode, and all the modes with normalized modal power below -60 dB are eliminated from the computation. Since higher frequencies require more modes and, more importantly, since modes calculated at lower frequencies are a subset of those calculated at higher frequencies, we can use the highest frequency of interest when performing the parameter sweep.

9.3 Numerical Results

In this section, we first present two straight open-cavity scattering examples to validate the hybrid FETD-GSM algorithm. After that, another two well-known structures with more complicated geometries are simulated to demonstrate the capabilities of the proposed algorithm for broadband monostatic RCS calculation of large and deep open cavities. Based on the far-fields, the ISAR images are processed to investigate the effects of geometrical configurations and internal lossy coatings on target signatures. For numerical simulation, the computational domain is discretized into curvilinear tetrahedra with mixed and full 2nd-order curl-conforming basis functions to expand the electric field in the FE and CFS-PML regions, respectively. The reflection from the CFS-PML is set to -45 dB to achieve a balance between artificial reflection and time marching stability. In each time step, the linear system is solved by the direct sparse solver PARDISO [105]. The calculations are carried out in double float precision on a 96-node Cisco cluster, with each computing node configured with two Intel Xeon E5-2680 CPUs and 256-GB memory.

9.3.1 Validation I–Square Duct Cavity

The first validation example is the scattering from a square duct cavity with interior dimensions of 2.75 inches × 2.75 inches × 27.0 inches. The measured broadband monostatic RCS data are plotted in Fig. 9.1 for 10–18 GHz. The simulation results, carried out using 110 modes, are displayed in Fig. 9.2, showing a good correlation with the measurements. The discrepancy is mainly due to the different color schemes used in the plotting software, the interference of the environment in the measurement, and the fact that the exterior scattering and edge diffraction are not included in the simulation.

9.3.2 Validation II–Circular Cavity

The next example simulates the scattering from a circular cavity to further validate the proposed hybrid algorithm. The cavity has a radius of 12 inches and a depth of 60 inches. Since the highest frequency of interest is 5 GHz, 509 modal bases are employed in the numerical simulations. The measured and simulated results are plotted in Figs. 9.3 and 9.4, respectively, again showing a good agreement between the two results except for the discrepancy noted earlier.

9.3.3 Channel Duct Cavity

After the two validation examples with straight geometries, we now demonstrate the capabilities of the proposed algorithm for more complicated structures and apply the obtained broadband wide-angle scattered fields to the ISAR imagery. The first example considered here is an elongated PEC cavity called Channel Duct [91]. The Channel Duct has an elliptical cross section (major and minor radii are respectively 118.03 mm and 58.77 mm) at its aperture, which gradually evolves to a circular shape (radius is 92.35 mm) at its termination, as illustrated in Fig. 9.5. The cavity has a depth of 1360 mm in the z-direction. Since the highest frequency of interest for the simulation is 16 GHz, the geometry is discretized into curvilinear tetrahedral elements with a size of 9.375 mm, which results in 6,836,838 total DoFs. In the simulation, the cavity aperture is truncated by a 25-mm thick ABC-backed CFS-PML. The time step size is set to 1.0 ps and the number of time steps is 32,000. With 360 dominant modes to expand the electric field at the cavity aperture, the entire simulation was carried out on 90 computing nodes in 112 hours.

The calculated monostatic RCS results at 16 GHz in the YZ plane are plotted in Fig. 9.6, together with the frequency-domain FEBI and measurement results [92]. Overall, the agreement between the three sets of results is very good, especially for the FEBI and hybrid FETD-GSM results. The discrepancy with the experimental data at large incident angles is caused by the imperfect measurement and the fact that the exterior scattering and edge diffraction are not included in the FEBI and FETD-GSM simulations. The broadband wide-angle monostatic RCS results in the XZ plane from 6 GHz to 16 GHz are plotted in Fig. 9.7, with the presence of an infinite ground plane around the aperture. Because of the geometrical symmetry in the XZ plane, the obtained RCS results are also symmetrical. Since one of the main strengths of this hybrid algorithm is its ability to perform fast broadband wide-angle sweep far-field computations, which makes the ISAR imagery possible, Fig. 9.8 shows the generated ISAR images together with the aperture and termination information of the physical cavity. Apparently, the aperture location and its dimension along the x-direction are correctly captured. The termination location is also predicted accurately because at the normal incidence the wave propagates approximately in a straight direction, due to the large cross section of the cavity as compared to the wavelength, and thus reaches the termination and gets reflected directly. However, its dimension cannot be accurately predicted because of the waveguide mode effect. The images in the cross range are caused by the higher-order modes excited by the incident waves from large oblique directions and their multiple bounces during propagation in the cavity. Note that since the cavity is not curved in the x-direction, all the cross-range images appear at or behind the physical location of the termination.

By changing the observation plane, other cavity dimensions can be revealed in the RCS and ISAR images. To see this, the broadband RCS results in the YZ plane for the Channel Duct cavity with an infinite ground plane are depicted in Fig. 9.9, showing nonsymmetric scattering patterns due to the nonsymmetric geometry along the y-direction. The corresponding ISAR images are shown in Fig. 9.10. Clearly, the aperture location and its dimension along the y-direction are accurately identified. As expected, the predicted termination size is enlarged due to the more pronounced waveguide mode effect because of the narrower dimension of the aperture in the y-direction, even though the termination location is still correctly predicted for the reason elaborated above. On comparing with Fig. 9.8, it is obvious that the electromagnetic waves now experience the curvature effect in the YZ plane. Consequently, at large cross ranges, the predicted cavity depth is smaller than the physical depth in the z-direction due to the "early" reflections at large incident angles (the waves reflected before reaching the termination).

For some open cavities such as jet engine inlets, there is no ground plane surrounding the cavity aperture. The effect of the ground plane can be removed by including the PO current $\mathbf{J}_{\mathrm{s}}$ in the calculation of (9.35). To study the effect of an infinite ground plane on the RCS results and ISAR images, Fig. 9.11 presents the broadband RCS results in the XZ plane of the Channel Duct cavity without a ground plane. On comparing with Fig. 9.7, it is obvious that without an infinite ground plane the RCS at and near normal incidence is significantly reduced. The corresponding ISAR images are shown in Fig. 9.12, which shows that the cavity aperture is virtually invisible in the ISAR images because the edge diffraction and scattering by the external surfaces are not included in the RCS calculation. The computed broadband RCS results in the YZ plane without an infinite ground plane are given in Fig. 9.13, and the corresponding ISAR images are given in Fig. 9.14, clearly showing the significant effect of the curvature in the y-direction.

9.3.4 COBRA Cavity

The second example simulated is a curved cavity known as COBRA cavity with a cross section of 84 mm × 110 mm and a z-direction depth of approximately 437 mm [97], as illustrated in Fig. 9.15. For numerical simulation, the cavity aperture is truncated by an ABC-backed CFS-PML with a thickness of 30 mm. The entire structure is discretized into curvilinear tetrahedral elements with a mesh size of 8.5 mm, which is about 0.5 wavelength at the highest frequency of 17.5 GHz. Although 157 modes are supported at the highest frequency, only 113 dominant modes contribute to the RCS significantly and hence are considered in the calculations. The total number of DoFs in the computational domain is 1,345,563. The time step size is set to 0.95 ps to resolve the higher-order modes and the number of time steps in the simulation is 30,000. The calculation was carried out on 57 computing nodes with 4.7 hours. The monostatic RCS results in the YZ cut, simulated with the presence of an infinite ground plane, are plotted in Fig. 9.16 from 6 GHz to 17.5 GHz, showing a slower frequency variation than the Channel Duct RCS results because the COBRA cavity is not as deep and large as the Channel Duct. The processed ISAR images in Fig. 9.17 show the correct cavity aperture location and dimension. It is also apparent in the images that the multi-bounces of the fields inside the cavity lead to an enlarged cross-range image. Because of the curved structure of the COBRA cavity, electromagnetic waves propagate beyond the physical depth in the z-direction. Hence, the predicted termination location is behind the physical location, as illustrated in Fig. 9.17.

For low observable applications, open cavities are often coated with a radar absorbing material on its internal surfaces. To study the effect of the coating on the RCS and ISAR images, we place a 3-mm thick lossy dielectric ($\epsilon_{\mathrm{r}} = 6.0$ and $\sigma_{\mathrm{e}} = 4.4506$ S/m) on the internal surfaces of the COBRA cavity. The numerical discretization of this coated COBRA cavity results in 1,423,235 total DoFs and 684 modal bases. With 57 nodes employed in the parallel computing, the total simulation time is 30.4 hours. Plotted in Fig. 9.18 are the broadband monostatic RCS results in the YZ plane, which show a significant RCS reduction compared with the results obtained for the PEC COBRA cavity. The processed ISAR images are depicted in Fig. 9.19. Although the correct aperture location and dimension are identified, the termination information is not observable in the ISAR images because of the absorption by the absorbing material, which is enhanced by the curved structure that traps the field inside the cavity where the electromagnetic energy is eventually dissipated in the internal coating.

9.4 Summary

In this chapter, we proposed a hybrid algorithm that combines the FETD method and GSM technique to efficiently compute the broadband monostatic RCS of a large and deep open cavity. For this, we presented the formulation and implementation details for the numerical modal analysis of arbitrary cross-sections and the FETD method equipped with an ABC-backed CFS-PML truncation for transient simulations. We then described the broadband monostatic RCS evaluation using GSM and discussed the selection of dominant scattering modes to further improve the efficiency of this hybrid algorithm. Finally, we presented two straight cavities to validate our algorithm and then two complicated structures to demonstrate its accuracy and efficiency for broadband monostatic RCS computation and ISAR imagery of large and deep open cavities. In passing, we note that the efficiency of this hybrid algorithm is the result not only of the hybridization of the FETD and GSM, but also of the hybridization between the time- and frequency-domain computations and the implied model-order reduction strategy.

9.5 Figures

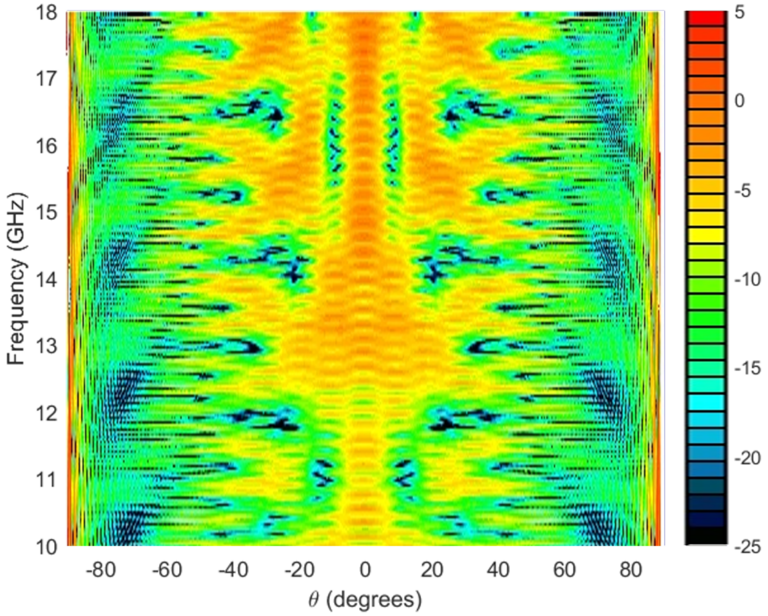

(a)

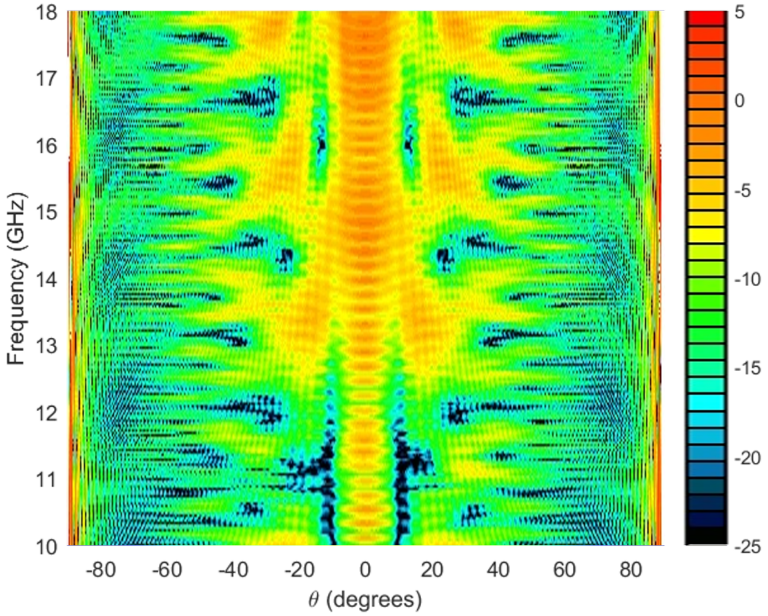

(b)

Figure 9.1: Measured broadband monostatic RCS (dBsm) for the square duct cavity. (a) $\phi\phi$ polarization. (b) $\theta\theta$ polarization.

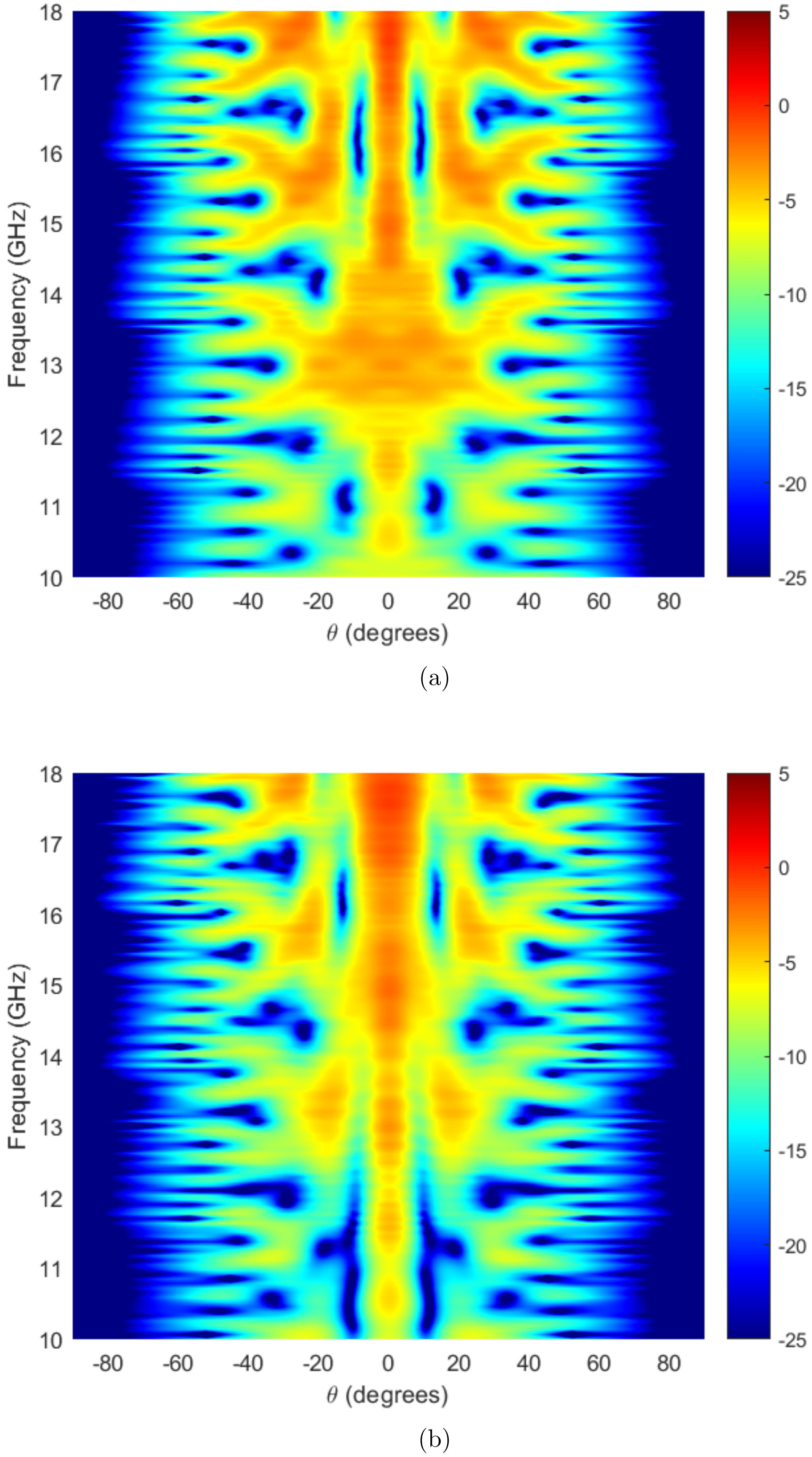

Figure 9.2: Simulated broadband monostatic RCS (dBsm) for the square duct cavity. (a) $\phi\phi$ polarization. (b) $\theta\theta$ polarization.

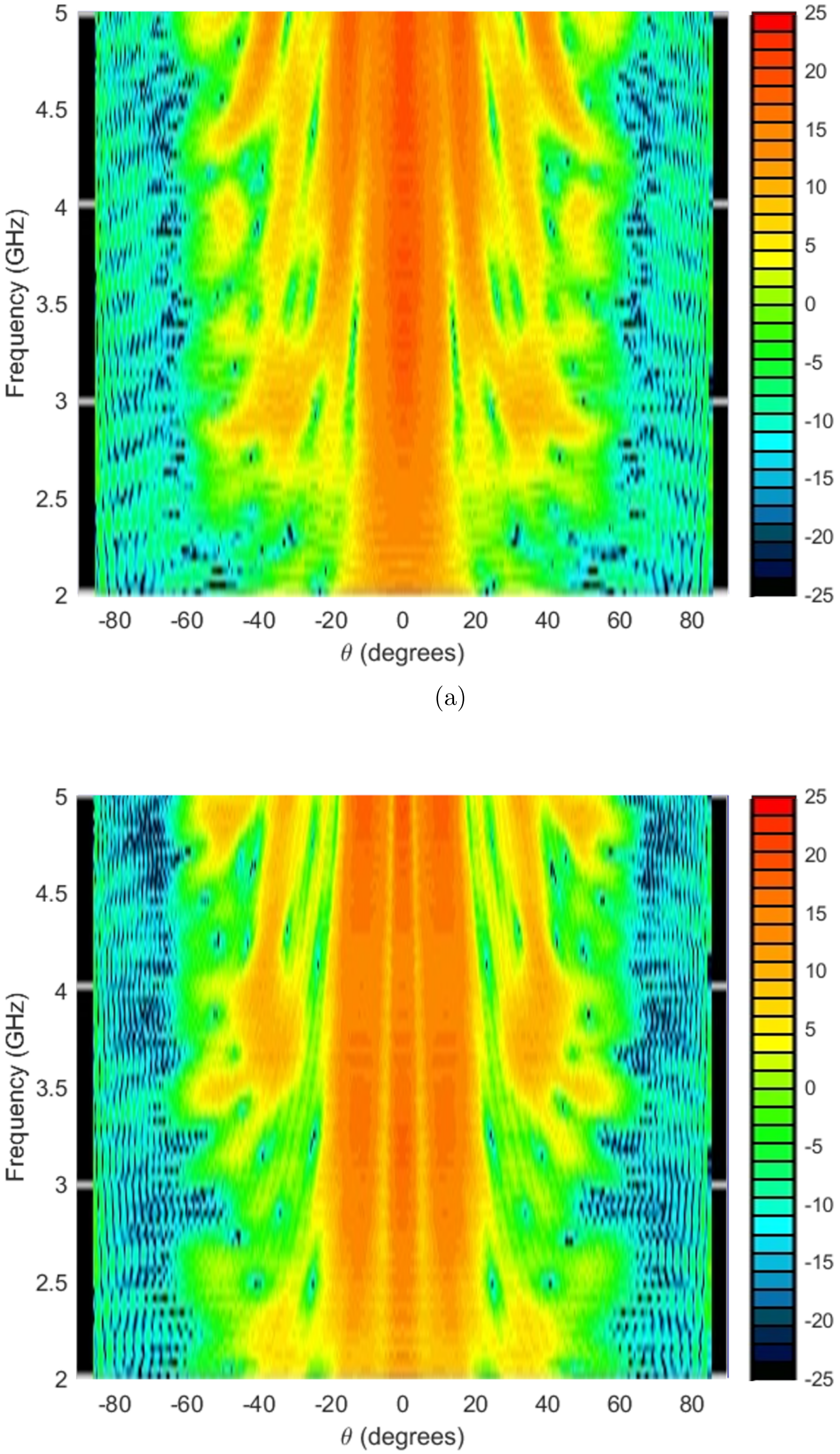

(a)

(b)

Figure 9.3: Measured broadband monostatic RCS (dBsm) for the circular cavity. (a) $\phi\phi$ polarization. (b) $\theta\theta$ polarization.

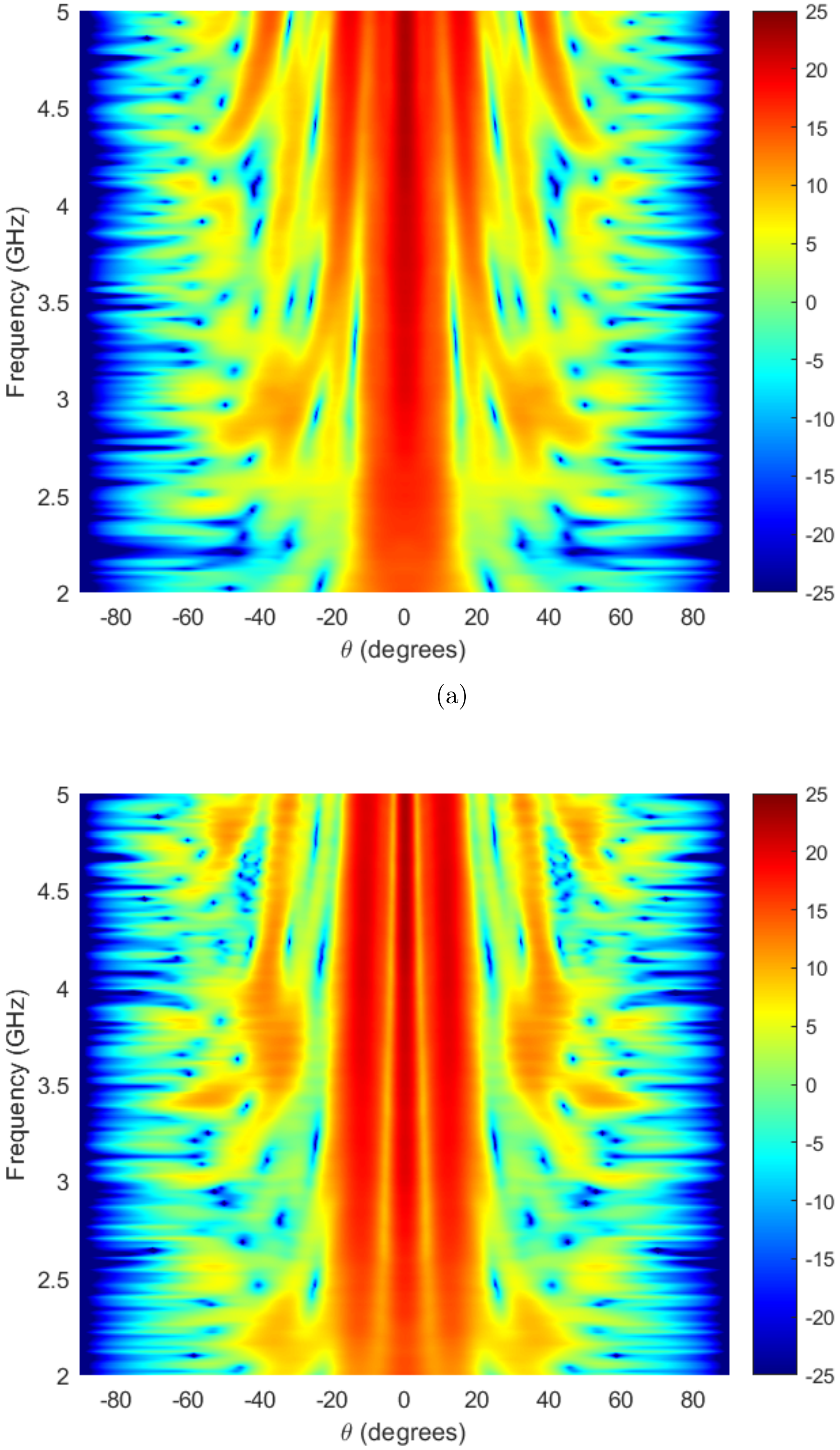

(a)

(b)

Figure 9.4: Simulated broadband monostatic RCS (dBsm) for the circular cavity. (a) $\phi\phi$ polarization. (b) $\theta\theta$ polarization.

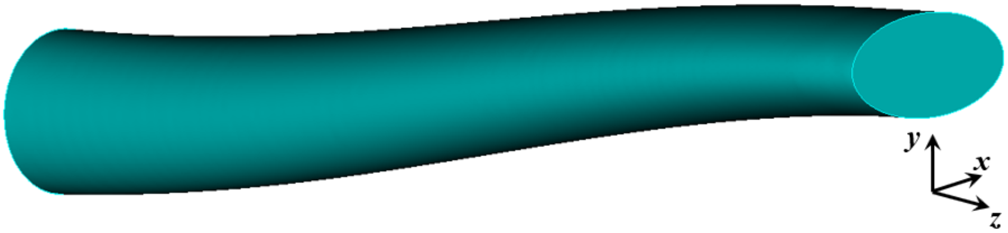

Figure 9.5: Geometry of the Channel Duct cavity.

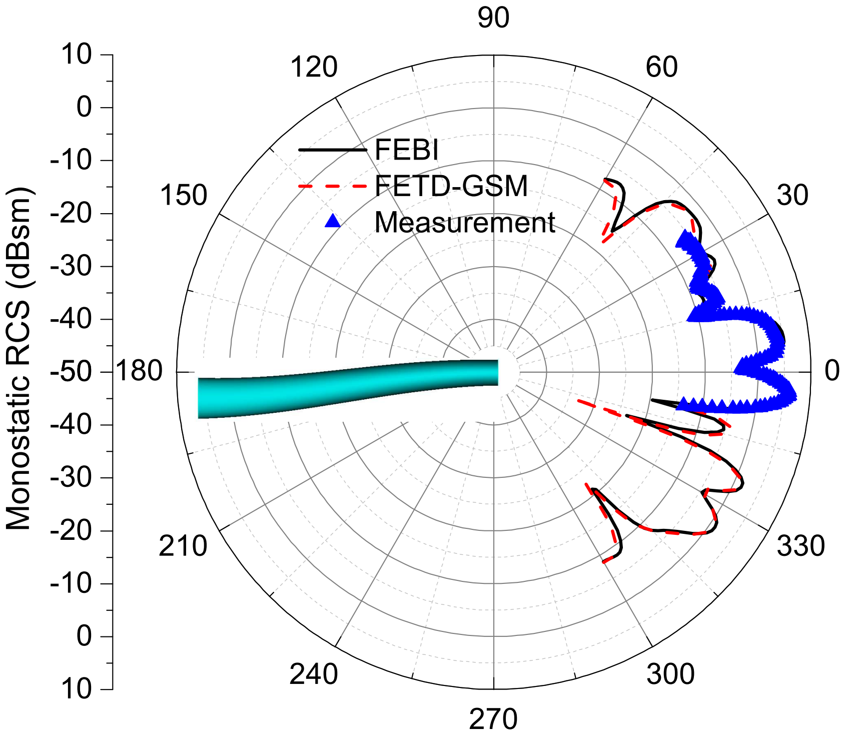

(a)

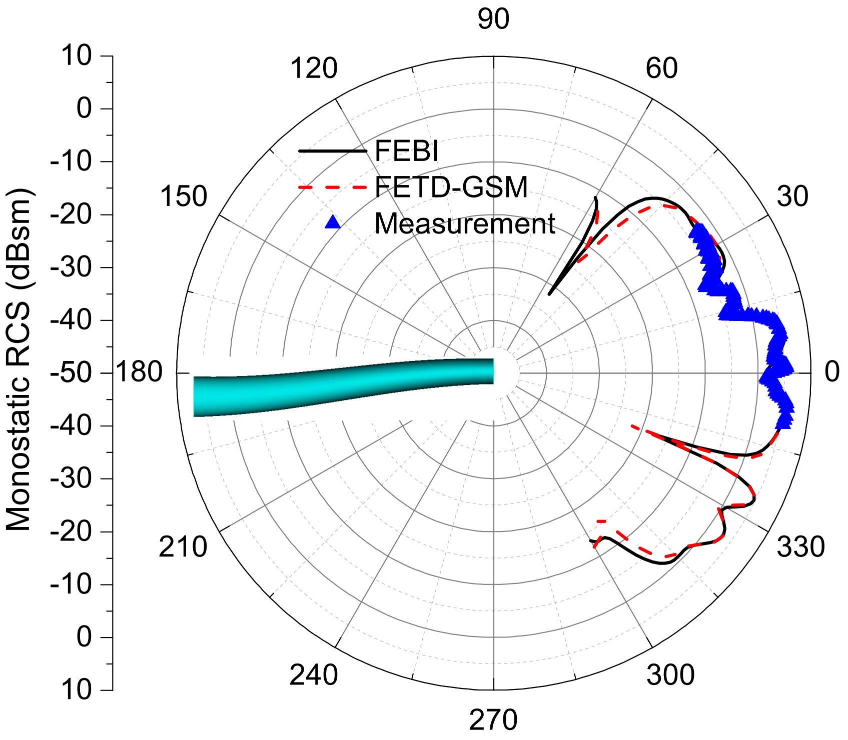

(b)

Figure 9.6: Monostatic RCS comparison of the Channel Duct cavity at 16 GHz in the YZ plane. (a) $\phi\phi$ polarization. (b) $\theta\theta$ polarization.

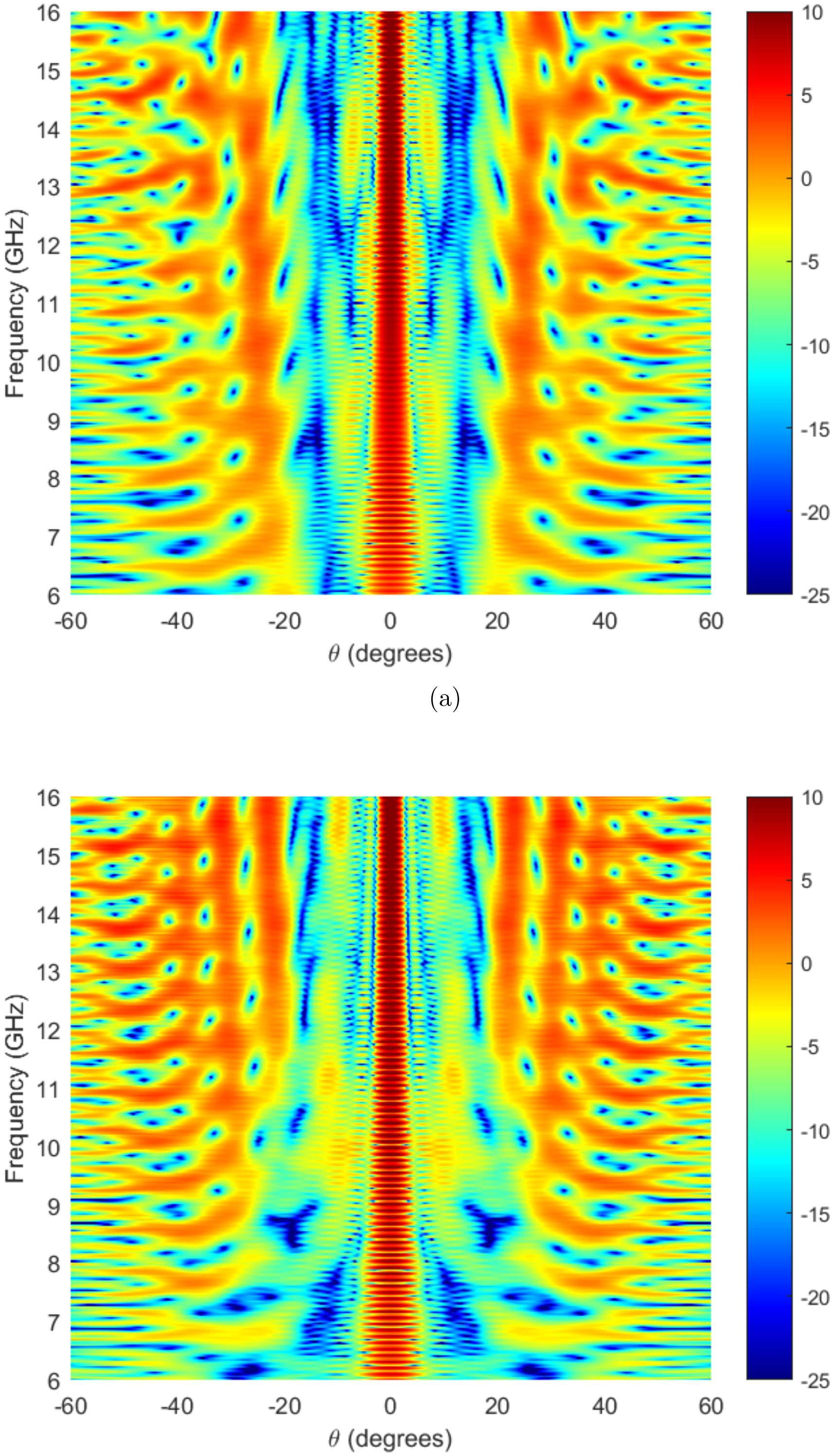

(a)

(b)

Figure 9.7: Broadband monostatic RCS (dBsm) in the XZ plane for the Channel Duct cavity with an infinite ground plane. (a) $\phi\phi$ polarization. (b) $\theta\theta$ polarization.

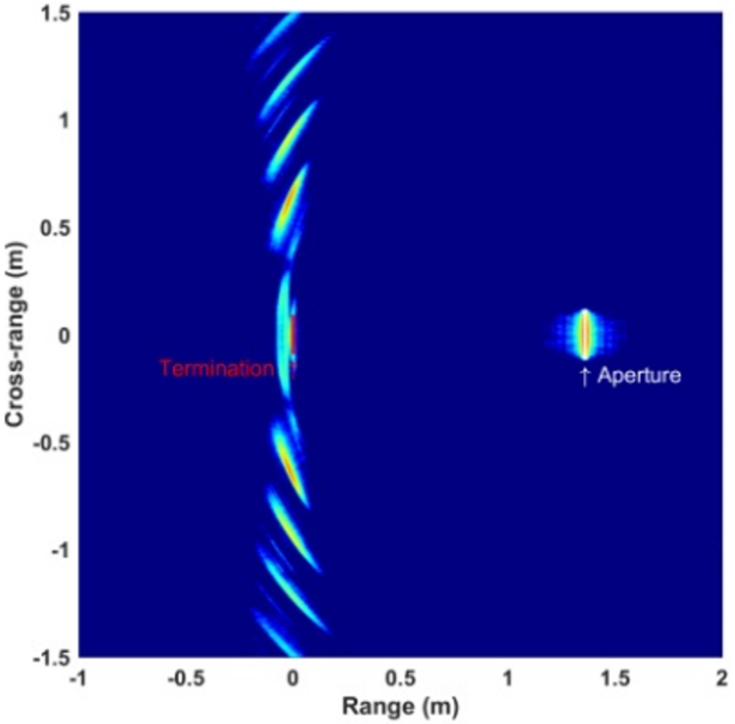

(a)

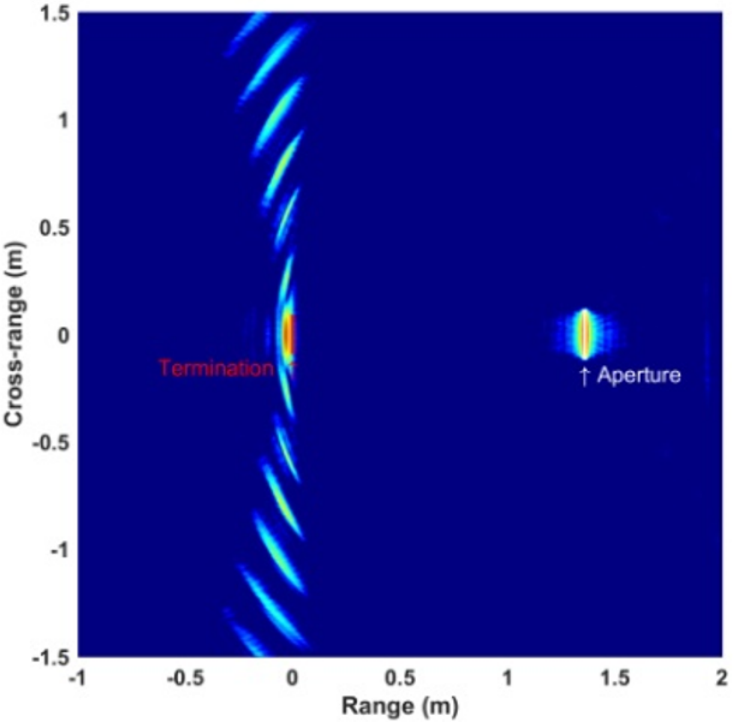

(b)

Figure 9.8: ISAR images in the XZ plane for the Channel Duct cavity with an infinite ground plane. (a) $\phi\phi$ polarization. (b) $\theta\theta$ polarization.

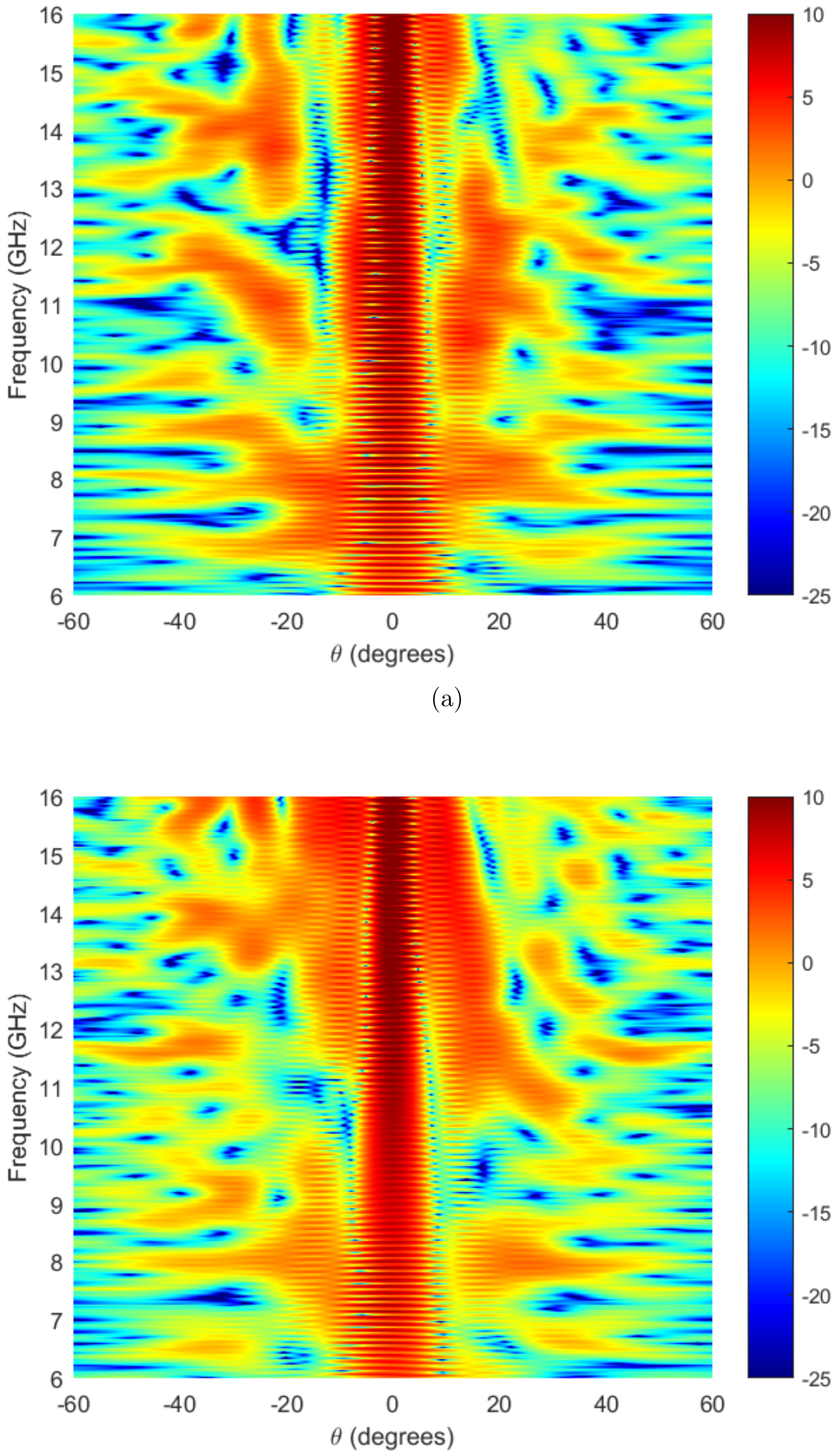

(a)

(b)

Figure 9.9: Broadband monostatic RCS (dBsm) in the YZ plane for the Channel Duct cavity with an infinite ground plane. (a) $\phi\phi$ polarization. (b) $\theta\theta$ polarization.

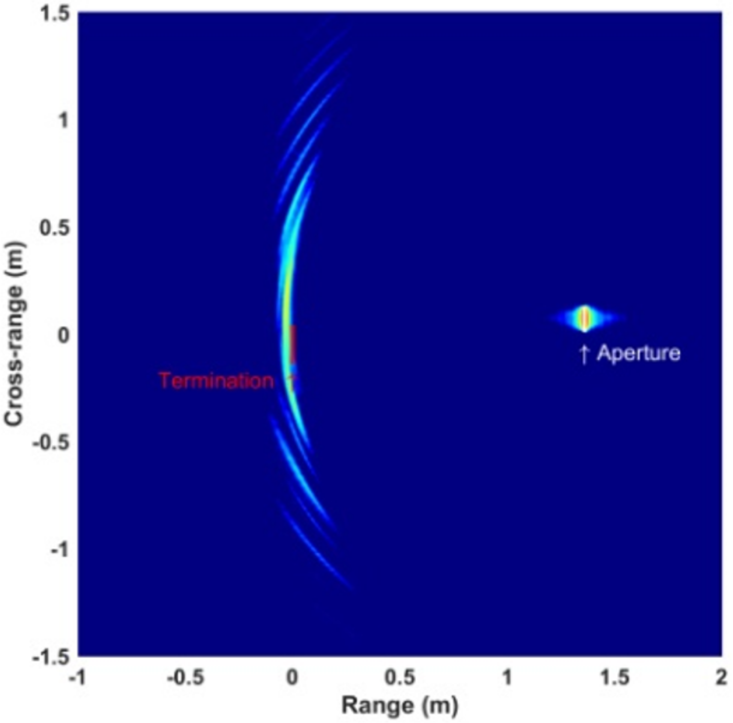

(a)

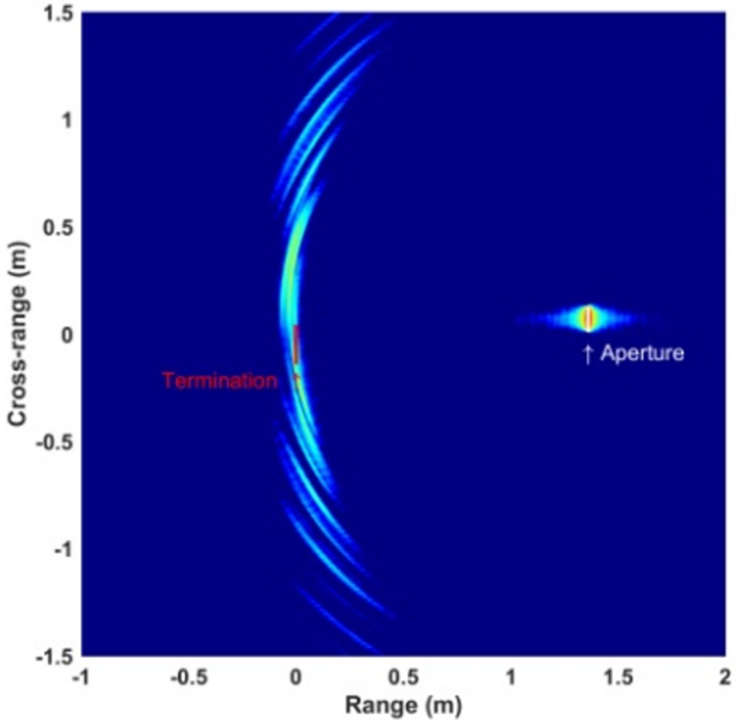

(b)

Figure 9.10: ISAR images in the YZ plane for the Channel Duct cavity with an infinite ground plane. (a) $\phi\phi$ polarization. (b) $\theta\theta$ polarization.

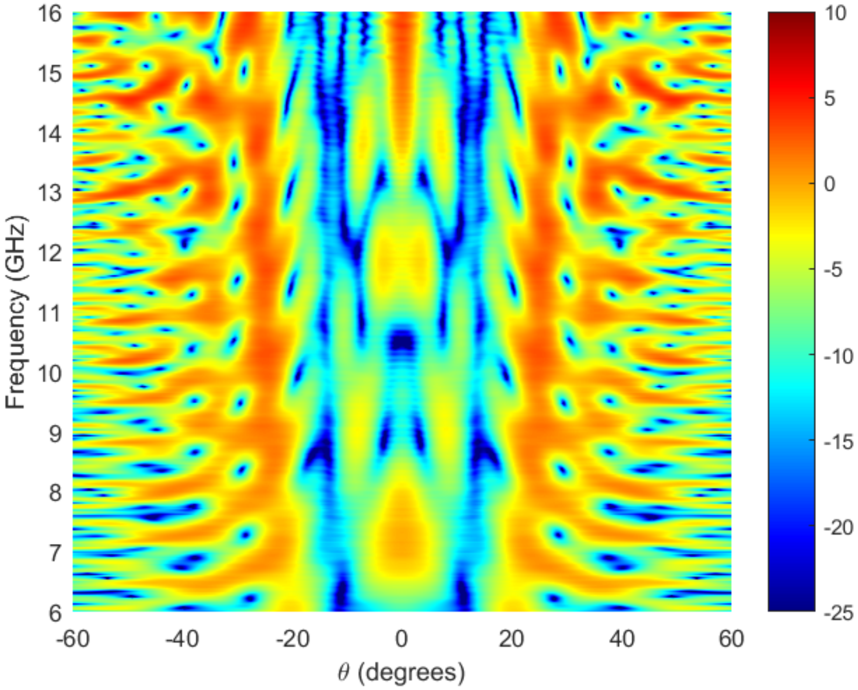

(a)

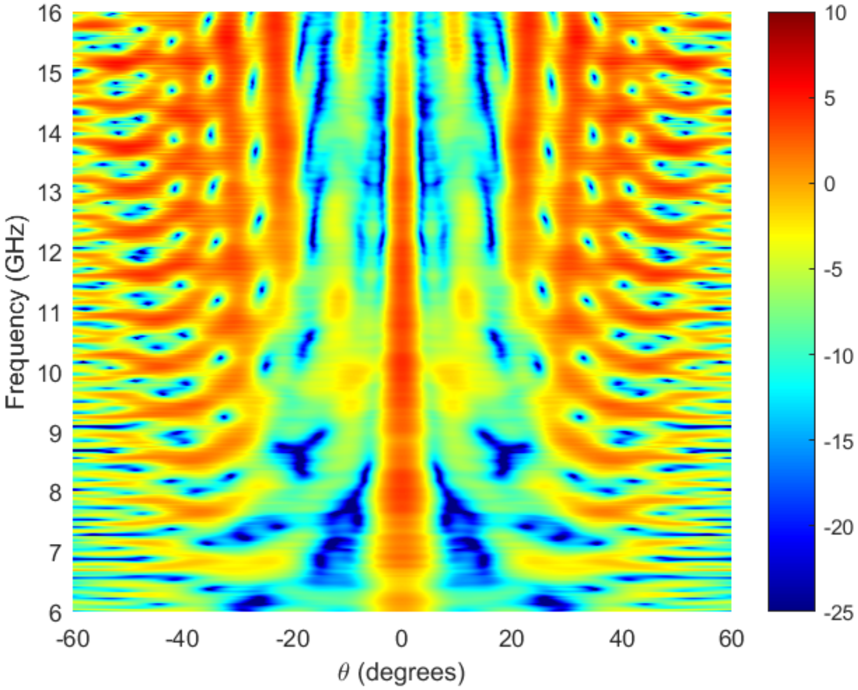

(b)

Figure 9.11: Broadband monostatic RCS (dBsm) in the XZ plane for the Channel Duct cavity without an infinite ground plane. (a) $\phi\phi$ polarization. (b) $\theta\theta$ polarization.

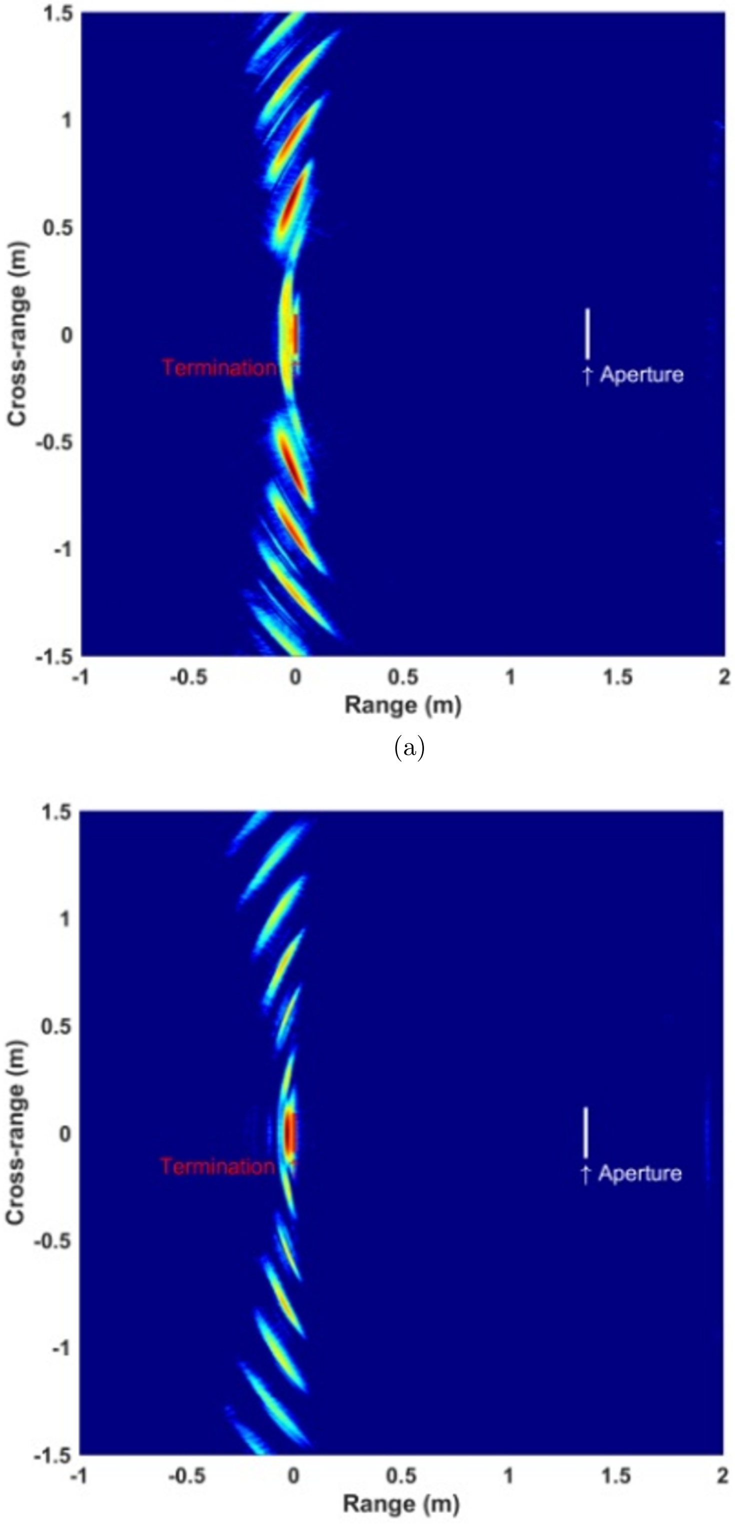

(a)

(b)

Figure 9.12: ISAR images in the XZ plane for the Channel Duct cavity without an infinite ground plane. (a) $\phi\phi$ polarization. (b) $\theta\theta$ polarization.

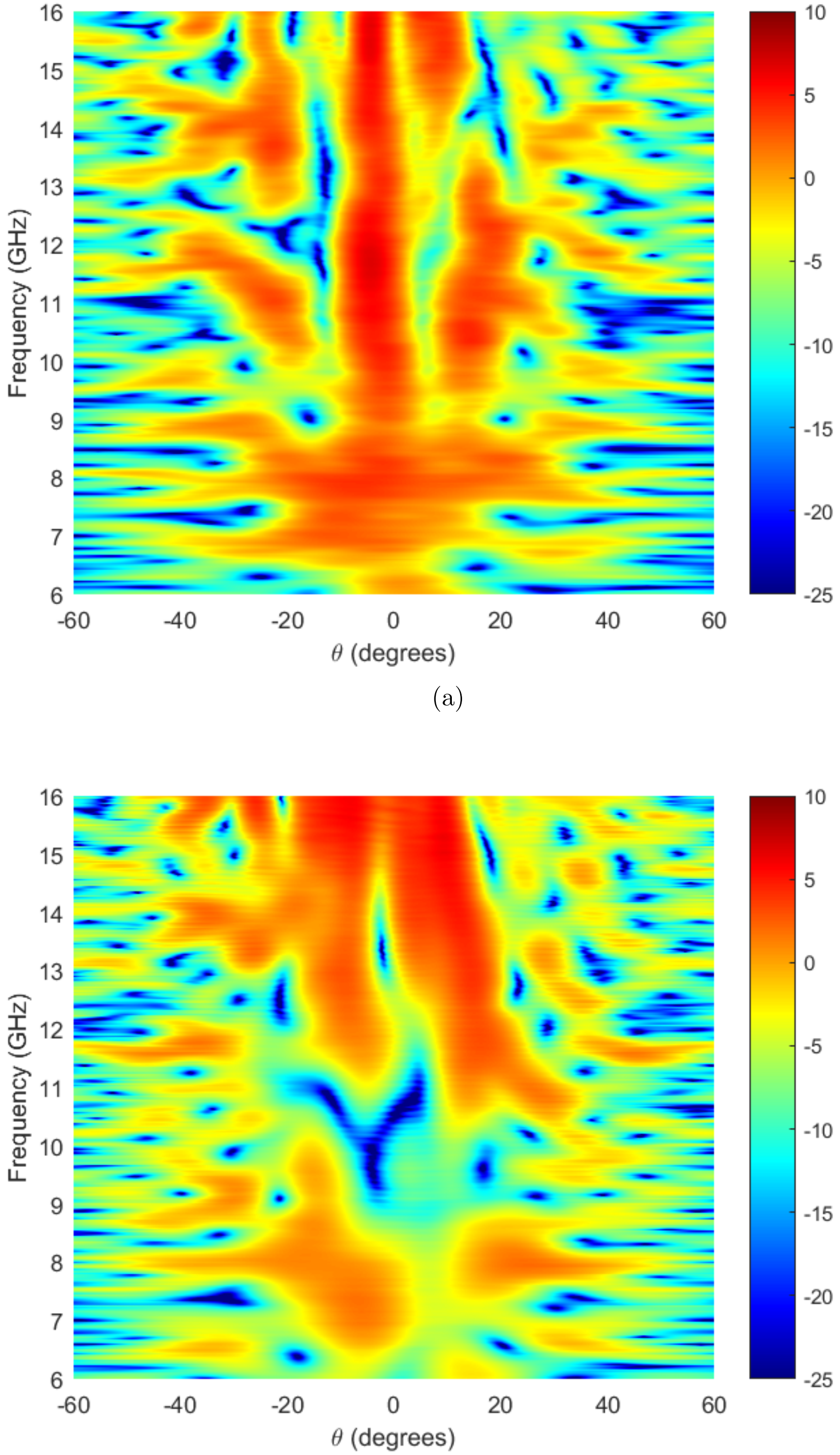

(a)

(b)

Figure 9.13: Broadband monostatic RCS (dBsm) in the YZ plane for the Channel Duct cavity without an infinite ground plane. (a) $\phi\phi$ polarization. (b) $\theta\theta$ polarization.

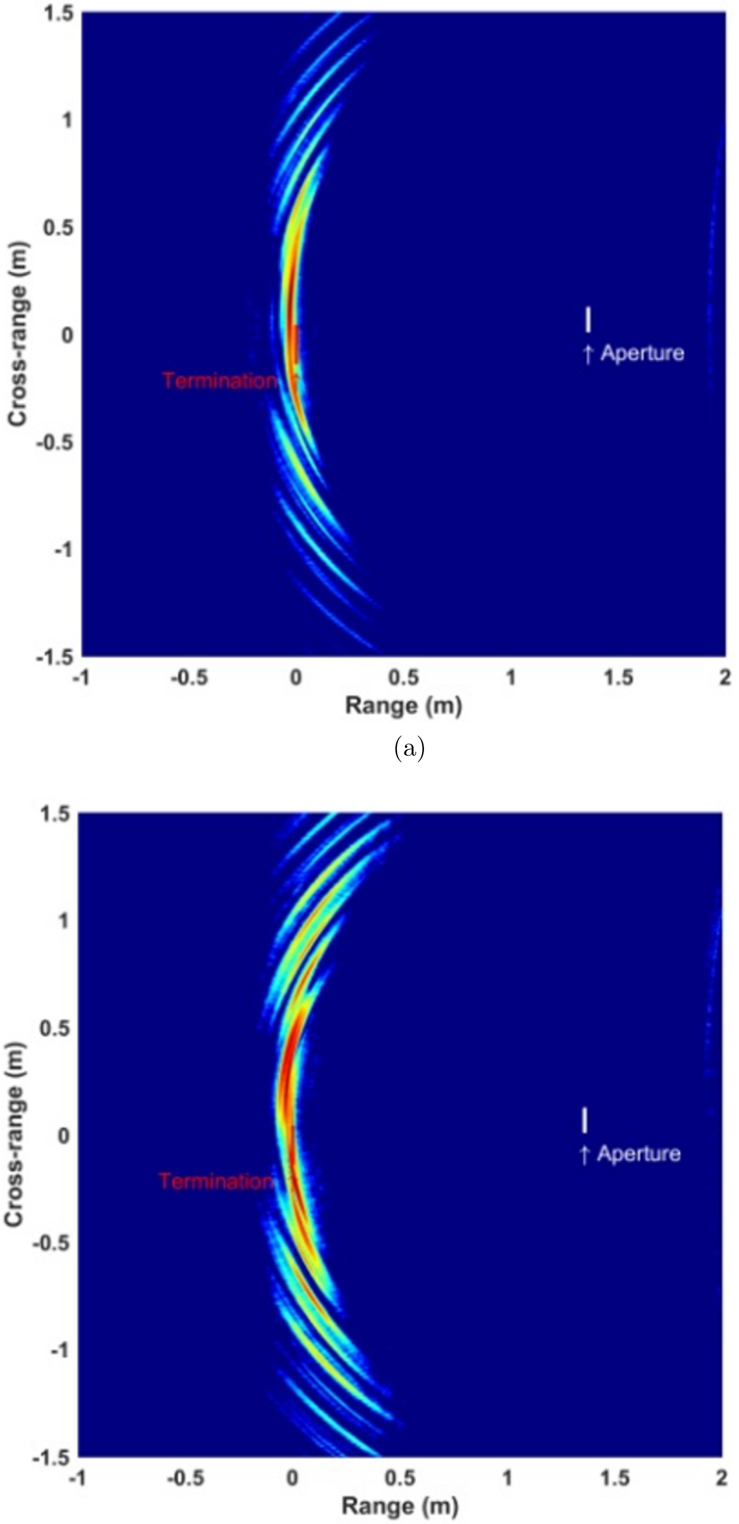

(a)

(b)

Figure 9.14: ISAR images in the YZ plane for the Channel Duct cavity without an infinite ground plane. (a) $\phi\phi$ polarization. (b) $\theta\theta$ polarization.

Figure 9.15: Geometry of the COBRA cavity.

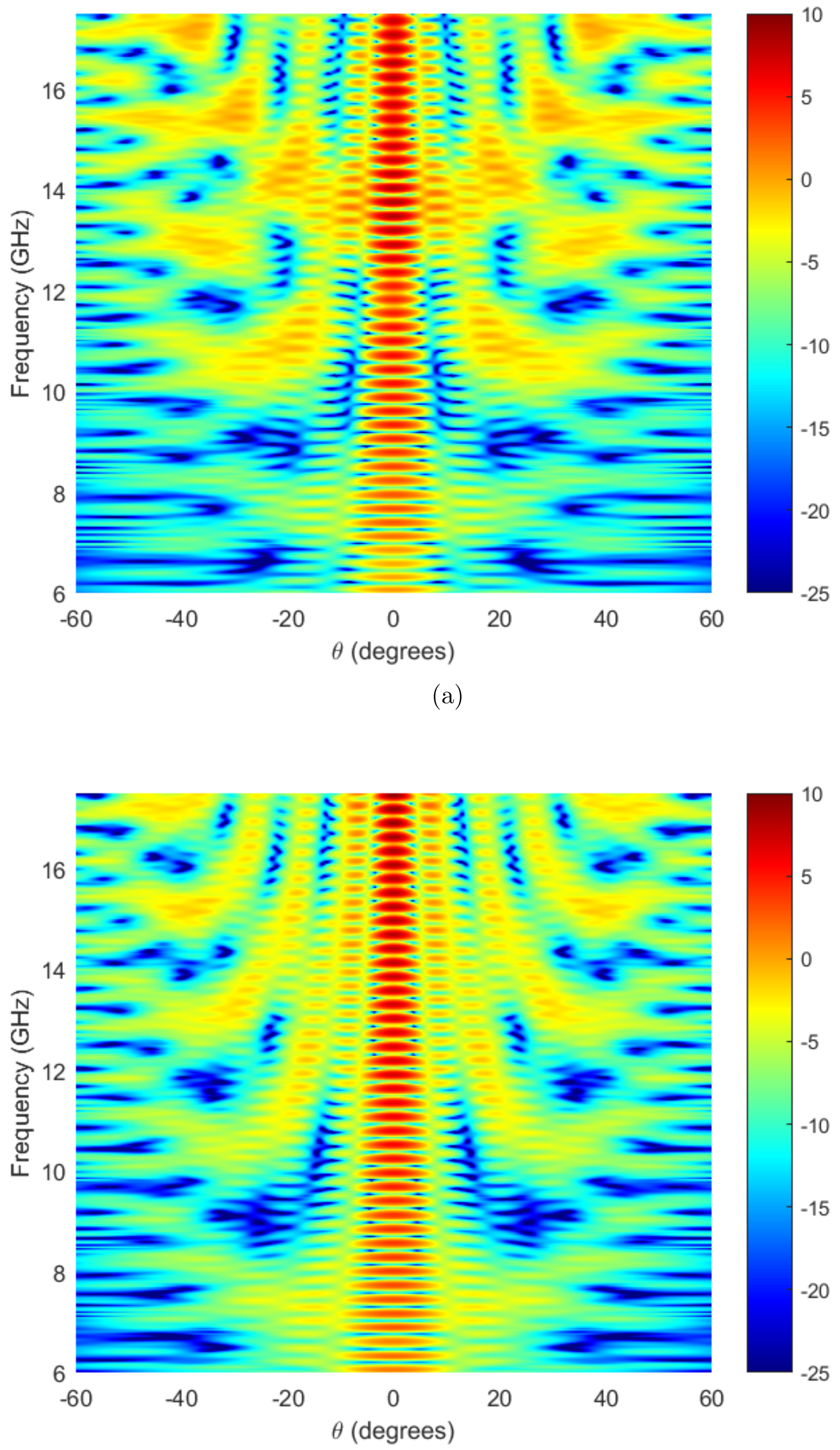

(a)

(b)

Figure 9.16: Broadband monostatic RCS (dBsm) in the YZ plane for the PEC COBRA cavity with an infinite ground plane. (a) $\phi\phi$ polarization. (b) $\theta\theta$ polarization.

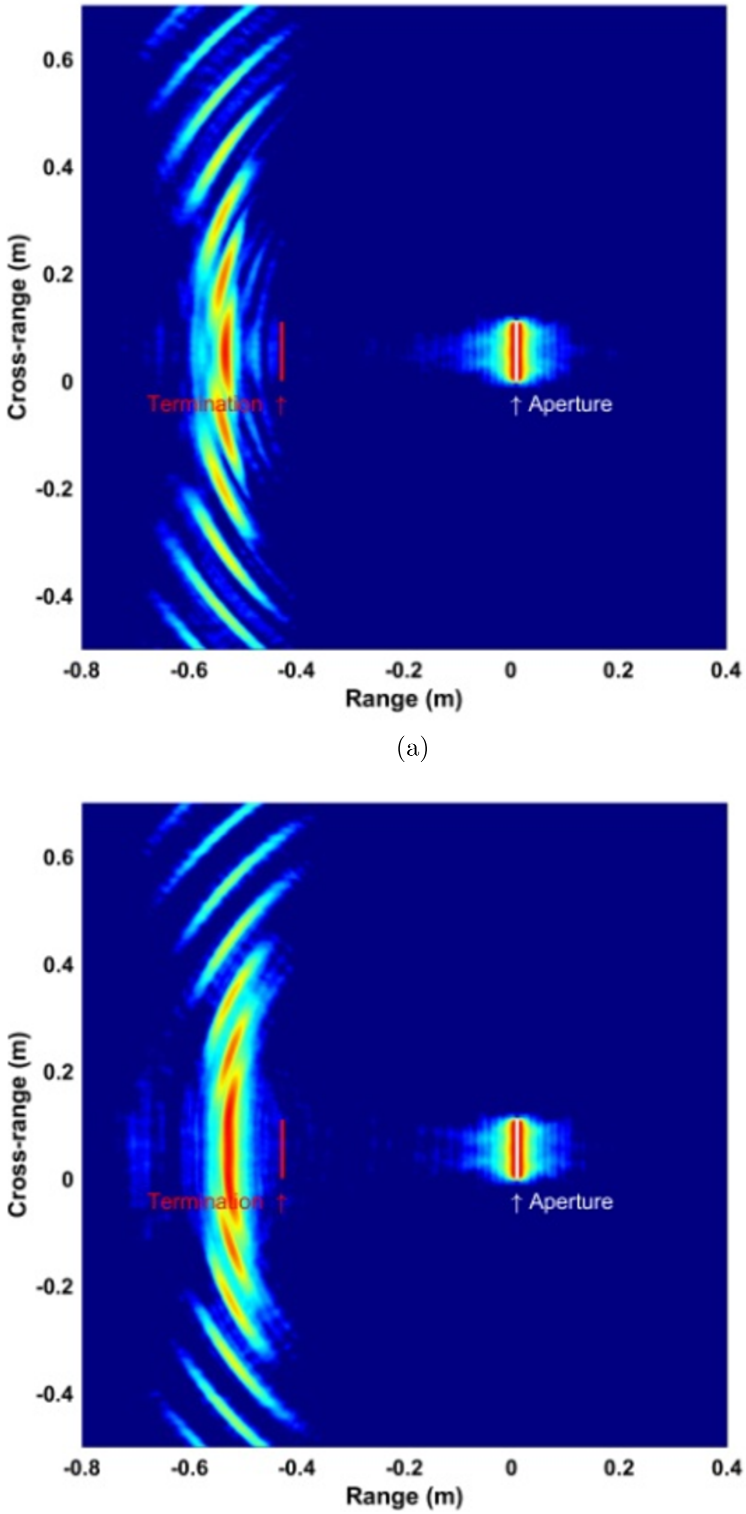

(a)

(b)

Figure 9.17: ISAR images in the YZ plane for the PEC COBRA cavity with an infinite ground plane. (a) $\phi\phi$ polarization. (b) $\theta\theta$ polarization.

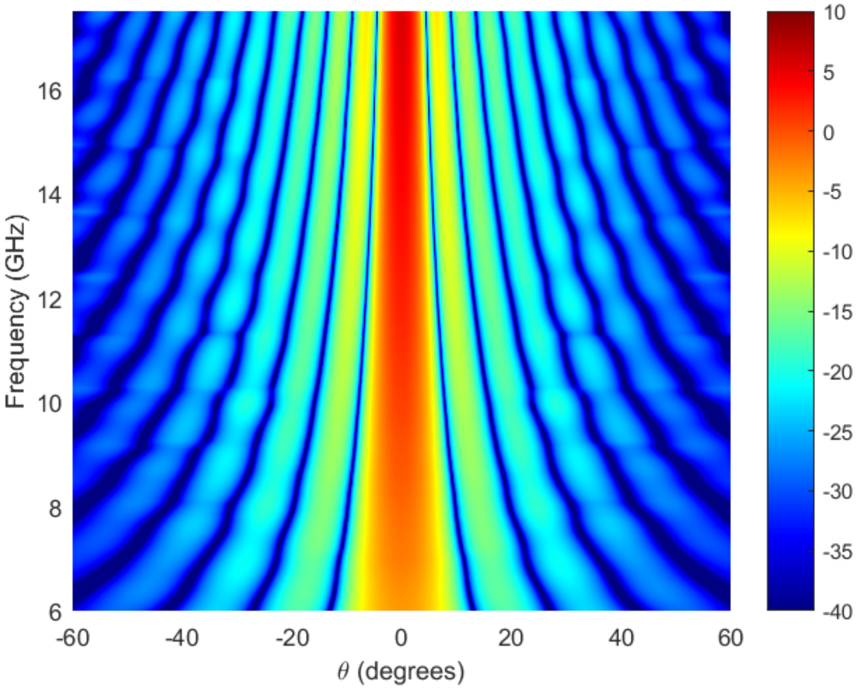

(a)

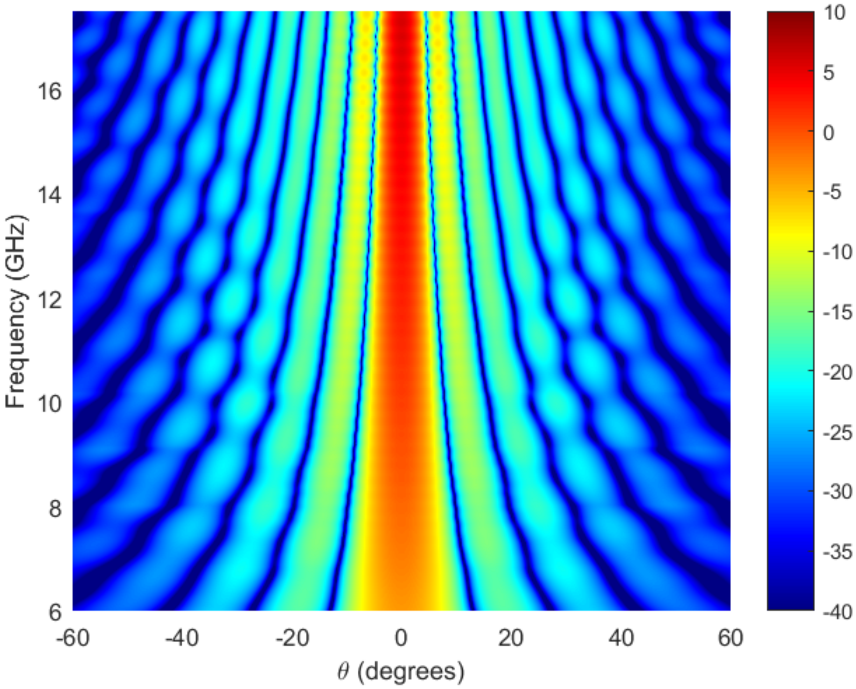

(b)

Figure 9.18: Broadband monostatic RCS (dBsm) in the YZ plane for the coated COBRA cavity with an infinite ground plane. (a) $\phi\phi$ polarization. (b) $\theta\theta$ polarization.

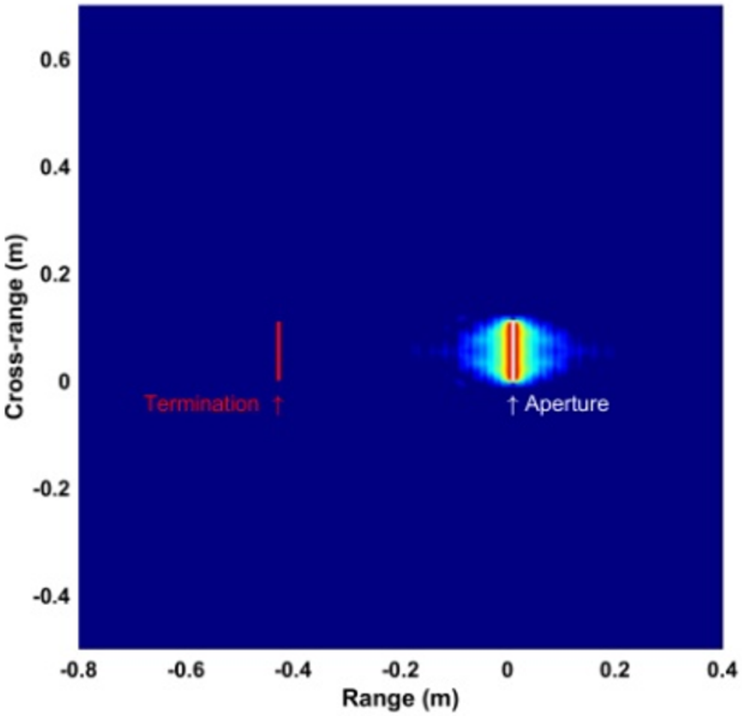

(a)

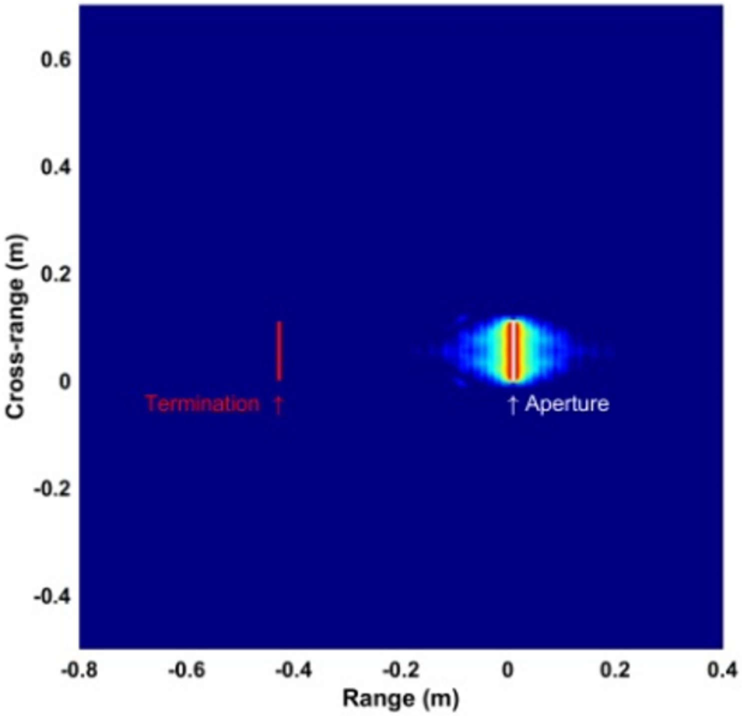

(b)

Figure 9.19: ISAR images in the YZ plane for the coated COBRA cavity with an infinite ground plane. (a) $\phi\phi$ polarization. (b) $\theta\theta$ polarization.

Chapter 10

Conclusion and Future Work

10.1 Conclusion

This dissertation is primarily focused on the development of an IGFEM for efficient simulation and optimization of electromagnetic composite materials, a parallel FETI-DP algorithm for large-scale electromagnetic scattering analysis, and a hybrid FETD-GSM technique for fast broadband analysis of resonant waveguide structures. The contribution of this research work and the conclusion for each topic in the previous chapters are summarized as follows.

10.1.1 Modeling of Composite Materials

An IGFEM is introduced for efficient 2-D and 3-D electromagnetic analyses of heterogeneous materials. To alleviate the use of meshes that conform to the material microstructures, thereby greatly reducing the burden of mesh generation, the method assigns generalized DoFs at material interfaces to capture the discontinuities of the field and its derivatives. The generalized DoFs are supported by enriched vector basis functions, which are constructed through a linear combination of the vector basis functions from the sub-elements. The IGFEM is shown not sensitive to the quality of the sub-elements and maintains the same level of solution accuracy and computational complexity as the standard FEM based on conformal meshes. The ability to work on a fixed background mesh with morphing geometries makes this method very attractive in statistical study of composite materials and in shape/topology optimization. Therefore, a gradient-based shape optimization scheme combined with the IGFEM is proposed to optimize electromagnetic problems. The sensitivity analysis of the objective functions and constraints are analytically derived instead of using a finite-difference scheme to reduce computational cost and numerical errors. Furthermore, the so-called *design velocity field* in the sensitivity analysis is evaluated only at the material interfaces, significantly speeding up the optimization process.

10.1.2 Scattering Analysis and CCD Imaging of Electrically Large Objects

An efficient parallelization of the FETI-DP algorithm is presented for large-scale electromagnetic simulations. To achieve a good load balance for parallel computation, the original computational domain is decomposed into subdomains with similar sizes and shapes. The subdomains are then distributed to processors based on their close proximity to minimize inter-processor communication. The parallel GMRES, enhanced with the ICGS orthogonalization scheme to reduce global communication, is adopted to solve the global interface problem with a fast convergence rate. The global corner-related coarse problem is solved iteratively with a parallel CA-BICGSTAB method to minimize global communication, and its convergence is accelerated by a diagonal preconditioner constructed from the coarse system matrix. To alleviate neighboring communication overhead, the non-blocking communication approach is employed in both GMRES and CA-BICGSTAB iterative solutions. To enable the scattering analysis of objects above, straddling, and/or embedded in a stratified medium, an inhomogeneous ABC is developed for the parallel FETI-DP algorithm. An MLFMA-based fast far-field calculation approach is implemented to reduce the computational complexity. With these techniques, a systematic scheme to model a 4f imaging system is proposed. The time-consuming Debye-Wolf integrals in the imaging formulation are accelerated by a linear interpolation technique so that the large-scale vectorial field imaging of an arbitrary object is possible.

10.1.3 Modeling of Resonant Waveguide Structures

A hybrid algorithm that combines the FETD method with the GSM technique is proposed to efficiently characterize the properties of wave propagation in highly resonant waveguide devices and compute the broadband monostatic RCS of large and deep open cavities. To alleviate the problem of an extremely large number of time steps required for a highly resonant device, the algorithm first divides the device into several less resonant subdomains to reduce the number of time steps. The subdomain interfaces are modeled with the WPBC to absorb any impinging waveguide modes. Each subdomain is then represented by a broadband GSM, which is computed by the FFT of the FETD solutions. The global GSM of the original resonant device is obtained by cascading the subdomain GSMs. For an open cavity scattering analysis, the time-domain CFS-PML is implemented to truncate an arbitrary waveguide port. The broadband monostatic RCS is evaluated using a broadband GSM obtained by the FETD solutions.

10.2 Future Work

The developed methods have been shown to be powerful and efficient, and their potential applications are far beyond the examples demonstrated in this dissertation. Several aspects of this research work can be extended in the future to further improve the efficiency and capability of these methods.

10.2.1 More Efficient Modeling and Optimization of Composite Materials

As shown in Chapters 2–4, the IGFEM significantly alleviates the expensive process of creating meshes conformal to the complex internal structures. However, for applications that have tiny geometrical features, sharp corners, and/or high contrast materials, which are typically encountered in the design of advanced multifunctional composite materials and compact waveguide filters, a sufficiently fine mesh is required to reduce the geometry discretization error and resolve the field variation around those structures. Since the locations of the internal structures are constantly changing during a statistical analysis and an optimization process, the current IGFEM uses a uniform background mesh with a global minimal mesh size to ensure the accuracy of the numerical simulations. Unfortunately, the global fine mesh significantly increases the total number of DoFs and inevitably undermines the efficiency of the IGFEM. A more natural way is to use a coarse background mesh and automatically refine the mesh in the regions needed to achieve a desired solution accuracy with far fewer DoFs than the IGFEM with a global small mesh size. The envisioned challenges associated with this adaptive meshing technique are creating the refined elements with appropriate aspect ratios and determining the level of refinements around the tiny features and sharp corners. These challenges can be investigated in future work.

Because of the fixed mesh nature, it is computationally economical to perform an analytical sensitivity analysis using IGFEM on the finite elements intersected with internal structures. This salient property has been exploited by a gradient-based shape optimization scheme proposed in Chapter 4. As a proof-of-concept, the proposed scheme was applied to various 2-D electromagnetic optimization problems using nodal basis functions and has demonstrated its efficiency in terms of computational complexity and convergence rate. The extension of the current optimization scheme to the design of real-life 3-D applications is more important and rewarding. Since H(curl)-conforming basis functions are normally adopted in the 3-D electromagnetic analyses to avoid spurious solutions, the difficulty is to perform the sensitivity analysis analytically, which requires the derivation of the derivatives of the bases and their curls with respect to the design parameters for various finite elements (tetrahedra, prisms, and pyramids). The challenges and potentially broad impacts of this work make it another future research topic.

10.2.2 More Efficient Modeling of Coherent Optical Microscopes

In Chapter 7, a systematic numerical modeling of coherent optical microscopes was proposed, which consists of a near-field simulation with the parallel FETI-DP algorithm to enable large-scale scattering analyses, a near-field to far-field transformation with the MLFMA to reduce the computational complexity, and a far-field to image process with a linear interpolation to speed up the Debye-Wolf integrals. The proposed approach has demonstrated its efficiency and capability by successfully imaging a general object with a cross-section of 10,000 square wavelengths. However, the bottleneck of the current method is that the number of far-field points is on the order of D^4, where D is the dimension of the scatterer. Fortunately, for periodic structures, such as a large-scale nanopatterned semiconductor wafer, the computational cost can be significantly reduced by exploiting the periodicity of the structure. To this end, a diffraction grating-based method [175] is proposed as a future research direction for the fast vectorial imaging of periodic structures, where only $O(D^2)$ far-field points need to be evaluated.

In the proposed new method, the entire semiconductor wafer, which contains many nanopatterned unit cells that may have defective patterns, is treated as a super cell. The super cell will be simulated using the parallel FETI-DP algorithm with the PBC applied to the four sidewalls. Because of the higher-order Bloch modes excited by the periodic structure, the traditional ABC is not effective for the truncation of the top and bottom surfaces. The BI-based PRC implemented in Chapter 3 can absorb all the higher-order modes. However, the BI-resultant full matrix is not preferred in the DDM-based parallel FETI-DP algorithm. Therefore, the CFS-PML, which can also absorb all the modes yet still produce a sparse system matrix, can be adopted to truncate the non-periodic surfaces. The periodicity in the super cell can be exploited by the FETI-DP algorithm to significantly reduce the memory consumption and computational time. The Bloch modes can be adopted as basis functions to expand the far fields. By using each Bloch mode as an incidence, a GSM that characterizes the scattering property of the super cell can be obtained. Since the image of each Bloch mode can be efficiently calculated via a 2-D FFT, the real image of a scatterer can be easily obtained by coherently summing up the contributions from all the Bloch modes.

10.2.3 More Accurate Modeling of Open Cavities

In Chapter 9, an efficient hybrid FETD-GSM algorithm was proposed for the fast broadband monostatic RCS calculation and ISAR imagery of large and deep open cavities. The proposed algorithm yields RCS results comparable to those of the full-wave rigorous FEBI method, when the incident angles are less than 60 degrees. At large incident angles, the discrepancy between the two sets of results becomes obvious. The reason is that the edge diffraction effect at the cavity aperture is not considered in the current hybrid FETD-GSM algorithm and its contribution to the overall RCS can be dominant compared to the internal cavity scattering at large incident angles. To include the edge diffraction effect and maintain the efficiency of the current algorithm in the meanwhile, a BI-based method can be adopted in the hybrid FETD-GSM algorithm for more accurate RCS computation. To be more specific, instead of projecting the incident plane wave onto the modal bases at the cavity aperture and then calculating the reflected field based on the extracted GSM, a new algorithm can be proposed to adopt the GSM and BI as the inner and outer boundary conditions for the cavity aperture, respectively. With the broadband GSM, the system matrix only needs to be filled and factorized once at each frequency point. What is more, because of a 2-D structure of the cavity aperture, the dimensions of the aperture system matrix are very small, and hence the broadband monostatic RCS results can be obtained with little cost. With the aforementioned accuracy and efficiency, the proposed new algorithm serves as a promising future research direction.

References

[1] P. P. Silvester and R. L. Ferrari, *Finite Elements for Electrical Engineers*, 3rd ed. Cambridge: Cambridge University Press, 1996.

[2] W. C. Chew, J.-M. Jin, E. Michielssen, and J. M. Song, Eds., *Fast and Efficient Algorithm in Computational Electromagnetics.* Boston, MA: Artech House, 2001.

[3] J.-M. Jin, *The Finite Element Method in Electromagnetics*, 3rd ed. Hoboken, NJ: Wiley, 2014.

[4] J. P. Webb, "Hierarchal vector basis functions of arbitrary order for triangular and tetrahedral finite elements," *IEEE Trans. Antennas Propag.*, vol. 47, no. 8, pp. 1244–1253, Aug. 1999.

[5] R. D. Graglia, D. R. Wilton, and A. F. Peterson, "Higher order interpolatory vector bases for computational electromagnetics," *IEEE Trans. Antennas Propag.*, vol. 45, no. 3, pp. 329–341, Mar. 1997.

[6] R. D. Graglia and A. F. Peterson, *Higher-Order Techniques in Computational Electromagnetics.* Edison NJ: SciTech Publishing, 2015.

[7] B. Engquist and A. Majda, "Absorbing boundary conditions for the numerical simulation of waves," *Math. Comp.*, vol. 31, no. 139, pp. 629–651, Jul. 1977.

[8] J. P. Berenger, "A perfectly matched layer for the absorption of electromagnetic waves," *J. Comput. Phys.*, vol. 114, no. 2, pp. 185–200, Oct. 1994.

[9] S.-H. Lee and J.-M. Jin, "Adaptive solution space projection for fast and robust wideband finite-element simulation of microwave components," *IEEE Microwave Wireless Comp. Lett.*, vol. 17, no. 7, pp. 474–476, Jul. 2007.

[10] Z. Lou and J.-M. Jin, "An accurate waveguide port boundary condition for the time-domain finite-element method," *IEEE Trans. Microwave Theory Tech.*, vol. 53, no. 9, pp. 3014–3023, Sep. 2005.

[11] Z. Gong and A. W. Glisson, “A hybrid equation approach for the solution of electromagnetic scattering problems involving two-dimensional inhomogeneous dielectric cylinders,” *IEEE Trans. Antennas Propag.*, vol. 38, no. 1, pp. 60–68, Jan. 1990.

[12] X. Yuan, “Three-dimensional electromagnetic scattering from inhomogeneous objects by the hybrid moment and finite element method,” *IEEE Trans. Microwave Theory Tech.*, vol. 38, no. 8, pp. 1053–1058, Aug. 1990.

[13] J.-M. Jin, S. S. Ni, and S.-W. Lee, “Hybridization of SBR and FEM for scattering by large bodies with cracks and cavities,” *IEEE Trans. Antennas Propag.*, vol. 43, no. 10, pp. 1130–1139, Oct. 1995.

[14] T. Rylander and A. Bondeson, “Stable FEM-FDTD hybrid method for Maxwell’s equations,” *Comput. Phys. Commun.*, vol. 125, no. 1-3, pp. 75–82, Mar. 2000.

[15] J.-F. Lee, R. Lee, and A. Cangellaris, “Time-domain finite-element methods,” *IEEE Trans. Antennas Propag.*, vol. 45, no. 3, pp. 430–442, Mar. 1997.

[16] D. Jiao and J.-M. Jin, “An effective algorithm for implementing perfectly matched layers in time-domain finite-element simulation of open-region EM problems,” *IEEE Trans. Antennas Propag.*, vol. 50, no. 11, pp. 1615–1623, Nov. 2002.

[17] D. J. Riley and J.-M. Jin, “Finite-element time-domain analysis of electrically and magnetically dispersive periodic structures,” *IEEE Trans. Antennas Propag.*, vol. 56, no. 11, pp. 3501–3509, Nov. 2008.

[18] K. Zhang, A. R. Najafi, J.-M. Jin, and P. H. Geubelle, “An interface-enriched generalized finite-element analysis for electromagnetic problems with non-conformal discretizations,” *Int. J. Numer. Model.*, vol. 29, no. 2, pp. 265–279, Mar./Apr. 2016.

[19] K. Zhang, J.-M. Jin, and P. H. Geubelle, “A 3-D interface-enriched generalized FEM for electromagnetic problems with nonconformal discretizations,” *IEEE Trans. Antennas Propag.*, vol. 63, no. 12, pp. 5637–5649, Dec. 2015.

[20] J. Kataja, S. Järvenpää, J. I. Toivanen, R. A. E. Mäkinen, and P. Ylä-Oijala, “Shape sensitivity analysis and gradient-based optimization of large structure using MLFMA,” *IEEE Trans. Antennas Propag.*, vol. 62, no. 11, pp. 5610–5618, Nov. 2014.

[21] A. R. Najafi, M. Safdari, D. A. Tortorelli, and P. H. Geubelle, “A gradient-based shape optimization scheme using an interface-enriched generalized FEM,” *Comput. Methods Appl. Mech. Engrg.*, vol. 296, pp. 1–17, Nov. 2015.

[22] Y. J. Li and J.-M. Jin, “A new dual-primal domain decomposition approach for finite element simulation of 3-D large-scale electromagnetic problems,” *IEEE Trans. Antennas Propag.*, vol. 55, no. 10, pp. 2803–2810, Oct. 2007.

[23] Y. J. Li and J.-M. Jin, “Parallel implementation of the FETI-DPEM algorithm for general 3D EM simulations,” *J. Comput. Phys.*, vol. 228, no. 9, pp. 3255–3267, May 2009.

[24] K. Zhao, V. Rawat, and J. F. Lee, “A domain decomposition method for electromagnetic radiation and scattering analysis of multi-target problems,” *IEEE Trans. Antennas Propag.*, vol. 56, no. 8, pp. 2211–2221, Aug. 2008.

[25] Z. Peng, V. Rawat, and J. F. Lee, “One way domain decomposition method with second order transmission conditions for solving electromagnetic wave problems,” *J. Comput. Phys.*, vol. 229, no. 4, pp. 1181–1197, Feb. 2010.

[26] Z. Peng and J. F. Lee, “Non-conformal domain decomposition method with second-order transmission conditions for time-harmonic electromagnetics,” *J. Comput. Phys.*, vol. 229, no. 16, pp. 5615–5629, Aug. 2010.

[27] M.-F. Xue and J.-M. Jin, “Nonconformal FETI-DP methods for large-scale electromagnetic simulation,” *IEEE Trans. Antennas Propag.*, vol. 60, no. 9, pp. 4291–4305, Sep. 2012.

[28] M.-F. Xue and J.-M. Jin, “A hybrid conformal/nonconformal domain decomposition method for multi-region electromagnetic modeling,” *IEEE Trans. Antennas Propag.*, vol. 62, no. 4, pp. 2009–2021, Apr. 2014.

[29] M.-F. Xue and J.-M. Jin, “A preconditioned dual-primal finite element tearing and interconnecting method for solving three-dimensional time-harmonic Maxwell’s equations,” *J. Comput. Phys.*, vol. 274, pp. 920–935, Oct. 2014.

[30] K. Zhang and J.-M. Jin, “Parallel FETI-DP algorithm for efficient simulation of large-scale EM problems,” *Int. J. Numer. Model.*, vol. 29, no. 5, pp. 897–914, Sep./Oct. 2016.

[31] K. Fujisaki and S. Satoh, “Numerical calculations of electromagnetic fields in silicon steel under mechanical stress,” *IEEE Trans. Magn.*, vol. 40, no. 4, pp. 1820–1825, Jul. 2004.

[32] F.-Z. Kong, W.-Y. Yin, J.-F. Mao, and Q. H. Liu, “Electro-thermo-mechanical characterizations of various wire bonding interconnects illuminated by an electromagnetic pulse,” *IEEE Trans. Adv. Packag.*, vol. 33, no. 3, pp. 729–737, Aug. 2010.

[33] X. Sun, M. Cheng, S. Zhu, and J. Zhang, “Coupled electromagnetic-thermal-mechanical analysis for accurate prediction of dual-mechanical-port machine performance,” *IEEE Trans. Ind. Appl.*, vol. 48, no. 6, pp. 2240–2247, Nov./Dec. 2012.

[34] S. Yan, A. D. Greenwood, and J.-M. Jin, “Modeling of plasma formation during high-power microwave breakdown in air using the discontinuous Galerkin time-domain method,” *IEEE J. Multiscale and Multiphys. Comput. Techn.*, vol. 1, pp. 2–13, Apr. 2016.

[35] T. Lu and J.-M. Jin, “Coupled electricalthermalmechanical simulation for the reliability analysis of large-scale 3-D interconnects,” *IEEE Trans. Compon. Packag. Technol.*, vol. 7, no. 2, pp. 229–237, Feb. 2017.

[36] A. P. Golden and J. Tien, “Fabrication of microfluidic hydrogels using molded gelatin as a sacrificial element,” *Lab Chip*, vol. 4, no. 6, pp. 720–725, 2007.

[37] K. S. Toohey et al., “Self-healing materials with microvascular networks,” *Nature Mater.*, vol. 6, pp. 581–585, Jun. 2007.

[38] A. P. Esser-Kahn et al., “Three-dimensional microvascular fiber-reinforced composites,” *Adv. Mater.*, vol. 23, no. 32, pp. 3654–3658, Jul. 2011.

[39] J.-M. Jin, *Theory and Computation of Electromagnetic Fields.* Hoboken, NJ: Wiley, 2010.

[40] S. Soghrati, A. M. Aragón, C. A. Duarte, and P. H. Geubelle, “An interface-enriched generalized FEM for problems with discontinuous gradient fields,” *Int. J. Numer. Meth. Eng.*, vol. 89, no. 8, pp. 991–1008, Feb. 2012.

[41] C. A. Duarte, I. Babuška, and J. T. Oden, “Generalized finite element methods for three-dimensional structural mechanics,” *Comput. Struct.*, vol. 77, no. 2, pp. 215–232, Jun. 2000.

[42] C. Lu and B. Shanker, “Generalized finite element method for vector electromagnetic problems,” *IEEE Trans. Antennas Propag.*, vol. 55, no. 5, pp. 1369–1381, May 2007.

[43] A. M. Aragón, S. Soghrati, and P. H. Geubelle, "Effect of in-plane deformation on the cohesive failure of heterogeneous adhesives," *J. Mech. Phys. Solids*, vol. 61, no. 7, pp. 1600–1611, Jul. 2013.

[44] N. Moës, J. Dolbow, and T. Belytschko, "A finite element method for crack growth without remeshing," *Int. J. Numer. Meth. Eng.*, vol. 46, no. 1, pp. 131–150, Sep. 1999.

[45] J. Canales, J. A. Tárrago, and A. Hernández, "An adaptive mesh refinement procedure for shape optimal design," *Adv. Eng. Soft.*, vol. 18, no. 2, pp. 131–145, 1993.

[46] P. Tao, K. Sertel, and J. L. Volakis, "Fully overlapping domain decomposition for fast optimization of small antennas in large-scale composite media," *Comput. Electromag. Int. Workshop*, pp. 77–81, 2009.

[47] Z. Yue and D. H. R. Jr, "Adaptive superposition of finite element meshes in non-linear transient solid mechanics problems," *Int. J. Numer. Meth. Eng.*, vol. 72, no. 9, pp. 1063–1094, Nov. 2007.

[48] M. Griebel and M. A. Schweitzer, Eds., *Meshfree Methods for Partial Differential Equations.* New York: Springer Verlag, 2003.

[49] I. Babuška and J. M. Melenek, "The partition of unity method," *Int. J. Numer. Meth. Eng.*, vol. 40, no. 4, pp. 727–858, Feb. 1997.

[50] P. J. Frey and P. L. George, *Mesh Generation: Application to Finite Elements*, 2nd ed. Hoboken, NJ: Wiley, 2008.

[51] A. Combescure, A. Gravouil, D. Grégoire, and J. Réthoré, "X-FEM a good candidate for energy conservation in simulation of brittle dynamic crack propagation," *Comput. Methods Appl. Mech. Eng.*, vol. 197, no. 5, pp. 309–318, Jan. 2008.

[52] J. Lee, E. M. Dede, and T. Nomura, "Simultaneous design optimization of permanent magnet, coils, and ferromagnetic material in actuators," *IEEE Trans. Magn.*, vol. 47, no. 12, pp. 4712–4716, Dec. 2011.

[53] M. M. Gavrilovic and J. P. Webb, "Accuracy control in the optimization of microwave devices by finite-element methods," *IEEE Trans. Microwave Theory Tech.*, vol. 50, no. 8, pp. 1901–1911, Aug. 2002.

[54] K. Tani, T. Nishio, and T. Yamada, "Transient finite element method using edge elements for moving conductor," *IEEE Trans. Magn.*, vol. 35, no. 3, pp. 1384–1386, May 1999.

[55] O. Tuncer, B. Shanker, and L. C. Kempel, "Tetrahedral-based vector generalized finite element method and its applications," *IEEE Antennas Wireless Propag. Lett.*, vol. 11, pp. 945–948, Aug. 2012.

[56] S. Soghrati and P. H. Geubelle, “A 3D interface-enriched generalized finite element method for weakly discontinuous problems with complex internal geometries,” *Comput. Methods Appl. Mech. Eng.*, vol. 217-220, pp. 46–57, Apr. 2012.

[57] C. T. Wolfe, U. Navsariwala, and S. D. Gedney, “A parallel finite-element tearing and interconnecting algorithm for solution of the vector wave equation with PML absorbing medium,” *IEEE Trans. Antennas Propag.*, vol. 48, no. 2, pp. 278–284, Feb. 2000.

[58] M. N. Vouvakis, Z. Cendes, and J. F. Lee, “A FEM domain decomposition method for photonic and electromagnetic band gap structures,” *IEEE Trans. Antennas Propag.*, vol. 54, no. 2, pp. 721–733, Feb. 2006.

[59] C. Farhat, A. Macedo, and M. Lesoinne, “A two-level domain decomposition method for the iterative solution of high frequency exterior Helmholtz problems,” *Numer. Math.*, vol. 85, no. 2, pp. 283–308, Apr. 2000.

[60] M. Bhardwaj et al., “Application of the FETI method to ASCI problems–scalability results on 1000 processors and discussion of highly heterogeneous problems,” *Int. J. Numer. Meth. Eng.*, vol. 47, no. 1-3, pp. 513–535, Jan. 2000.

[61] E. H. Newman and D. Forrai, “Scattering from a microstrip patch,” *IEEE Trans. Antennas Propag.*, vol. AP-35, no. 3, pp. 245–251, Mar. 1987.

[62] M. Meng, Y. Chen, W. Luo, Z. Nie, and J. Hu, “Fast analysis of electromagnetic scattering from conducting objects buried under a lossy ground,” *IEEE Trans. Antennas Propag.*, vol. 13, no. 4, pp. 555–559, Apr. 2016.

[63] Y. Ren, Q. H. Liu, and Y. P. Chen, “A hybrid FEM/MoM method for 3-D electromagnetic scattering in layered medium,” *IEEE Trans. Antennas Propag.*, vol. 64, no. 8, pp. 3487–3495, Aug. 2016.

[64] Y. P. Chen, L. Jiang, S. Sun, W. C. Chew, and J. Hu, “Calderón preconditioned PMCHWT equations for analyzing penetrable objects in layered medium,” *IEEE Trans. Antennas Propag.*, vol. 62, no. 11, pp. 5619–5627, Nov. 2014.

[65] C. W. Freudiger et al., “Label-free biomedical imaging with high sensitivity by stimulated Raman scattering microscopy,” *Science*, vol. 322, no. 5909, pp. 1857–1861, Dec. 2008.

[66] P. J. Campagnola, M. Wei, A. Lewis, and L. M. Loew, “High-resolution nonlinear optical imaging of live cells by second harmonic generation,” *Biophys. J.*, vol. 77, no. 6, pp. 3341–3349, Dec. 1999.

[67] A. K.-K. Wong, *Resolution Enhancement Techniques in Optical Lithography.* WA: SPIE Press, 2001.

[68] R. Zhou et al., “Detecting 20 nm wide defects in large area nanopatterns using optical interferometric microscopy,” *Nano Lett.*, vol. 13, no. 8, pp. 3716–3721, Jul. 2013.

[69] R. M. Silver et al., “Scatterfield microscopy for extending the limits of image-based optical metrology,” *Appl. Opt.*, vol. 46, no. 20, pp. 4248–4257, 2007.

[70] P. Török, P. R. T. Munro, and E. E. Kriezis, “Rigorous near- to far-field transform for vectorial diffraction calculations and its numerical implementation,” *J. Opt. Soc. Am. A*, vol. 23, no. 3, pp. 713–722, Mar. 2006.

[71] D. M. Pozar, *Microwave Engineering*, 4th ed. NY: Wiley, 2012.

[72] N. Marcuvitz, *Waveguide Handbook.* NY: McGraw-Hill, 1951.

[73] R. Levy and S. Cohn, “A history of microwave filter research, design, and development,” *IEEE Trans. Microwave Theory Tech.*, vol. 32, no. 9, pp. 1055–1067, Sep. 1984.

[74] T. Itoh, Ed., *Numerical Techniques for Microwave and Millimeter-Wave Passive Structures.* NY: Wiley, 1989.

[75] T. Sieverding and F. Arndt, “Field theoretic CAD of open or aperture matched T-junction coupled rectangular waveguide structures,” *IEEE Trans. Microwave Theory Tech.*, vol. 40, no. 2, pp. 353–362, Feb. 1992.

[76] U. Papziner and F. Arndt, “Field theoretical compute-aided design of rectangular and circular iris coupled rectangular or circular waveguide cavity filters,” *IEEE Trans. Microwave Theory Tech.*, vol. 41, no. 3, pp. 462–471, Feb. 1993.

[77] A. P. Orfanidis, G. A. Kyriacou, and J. N. Sahalos, “A mode-matching technique for the study of circular and coaxial waveguide discontinuities based on closed-form coupling integrals,” *IEEE Trans. Microwave Theory Tech.*, vol. 48, no. 5, pp. 880–883, May 2000.

[78] P. Matras, R. Bunger, and F. Arndt, “Modal scattering matrix of the general step discontinuity in elliptical waveguides,” *IEEE Trans. Microwave Theory Tech.*, vol. 45, no. 3, pp. 453–458, Mar. 1997.

[79] F. Arndt et al., "Automated design of waveguide components using hybrid mode-matching/numerical EM building-blocks in optimization-oriented CAD frameworks–state-of-the-art and recent advances," *IEEE Trans. Microwave Theory Tech.*, vol. 45, no. 5, pp. 747–760, May 1997.

[80] F. Arndt et al., "Fast CAD and optimization of waveguide components and aperture antennas by hybrid MM/FE/MOM/FD methods–state-of-the-art and recent advances," *IEEE Trans. Microwave Theory Tech.*, vol. 52, no. 1, pp. 292–305, Jan. 2004.

[81] J.-M. Jin and D. J. Riley, *Finite Element Analysis of Antennas and Arrays.* Hoboken NJ: Wiley, 2009.

[82] H. Ling, R. C. Chou, and S.-W. Lee, "Shooting and bouncing rays: Calculating RCS of an arbitrarily shaped cavity," *IEEE Trans. Antennas Propag.*, vol. 37, no. 2, pp. 194–205, Feb. 1989.

[83] P. H. Pathak and R. J. Burkholder, "Modal, ray and beam techniques for analyzing the EM scattering by open-ended waveguide cavities," *IEEE Trans. Antennas Propag.*, vol. 37, no. 5, pp. 635–647, May 1989.

[84] A. G. Pino, F. Obelleiro, and J. L. Rodriguez, "Scattering from conducting open cavities by generalized ray expansion (GRE)," *IEEE Trans. Antennas Propag.*, vol. 41, no. 7, pp. 989–992, Jul. 1993.

[85] F. Obelleriro, J. L. Rodirguez, and R. J. Burkholder, "An iterative physical optics approach for analyzing the electromagnetic scattering by large open-ended cavities," *IEEE Trans. Antennas Propag.*, vol. 43, no. 4, pp. 356–361, Apr. 1995.

[86] H. Ling, "RCS of waveguide cavities: a hybrid boundary-integral/modal approach," *IEEE Trans. Antennas Propag.*, vol. 38, no. 9, pp. 1413–1420, Sep. 1990.

[87] R. Lee and T. T. Chia, "Analysis of electromagnetic scattering from a cavity with a complex termination by means of a hybrid ray-FDTD method," *IEEE Trans. Antennas Propag.*, vol. 41, no. 11, pp. 1560–1569, Nov. 1993.

[88] D. C. Ross, J. L. Volakis, and H. T. Anastassiu, "Hybrid finite element-modal analysis of jet engine inlet scattering," *IEEE Trans. Antennas Propag.*, vol. 43, no. 3, pp. 277–285, Mar. 1995.

[89] T. T. Chia, R. J. Burkholder, and R. Lee, "The application of FDTD in hybrid methods for cavity scattering analysis," *IEEE Trans. Antennas Propag.*, vol. 43, no. 10, pp. 1082–1090, Oct. 1995.

[90] T.-M. Wang and H. Ling, "Electromagnetic scattering from three-dimensional cavities via a connection scheme," *IEEE Trans. Antennas Propag.*, vol. 39, no. 10, pp. 1505–1513, Oct. 1991.

[91] A. Barka, P. Soudais, and D. Volpert, "Scattering from 3-D cavities with a plug and play numerical scheme combining IE, PDE, and modal techniques," *IEEE Trans. Antennas Propag.*, vol. 48, no. 5, pp. 704–712, May 2000.

[92] C.-F. Wang and P. Liu, "Benchmarks for electromagnetic scattering from large cavities," in *IEEE Antennas Propag. Society Int. Symp. Dig.*, Orlando, FL, USA, July 7–13, 2013, pp. 1996–1997.

[93] Z. Peng and X.-Q. Sheng, "A flexible and efficient higher order FE-BI-MLFMA for scattering by a large body with deep cavities," *IEEE Trans. Antennas Propag.*, vol. 56, no. 7, pp. 2031–2042, Jul. 2008.

[94] Z. Peng, K.-H. Lim, and J.-F. Lee, "A boundary integral equation domain decomposition method for electromagnetic scattering from large and deep cavities," *J. Comput. Phys.*, vol. 280, pp. 626–642, Jan. 2015.

[95] J. Liu and J. M. Jin, "A special higher order finite-element method for scattering by deep cavities," *IEEE Trans. Antennas Propag.*, vol. 48, no. 5, pp. 694–703, May 2000.

[96] J. Liu and J. M. Jin, "Scattering analysis of a large body with deep cavities," *IEEE Trans. Antennas Propag.*, vol. 51, no. 6, pp. 1157–1167, Jun. 2002.

[97] J. M. Jin, J. Liu, Z. Lou, and C. S. T. Liang, "A fully high-order finite-element simulation of scattering by deep cavities," *IEEE Trans. Antennas Propag.*, vol. 51, no. 9, pp. 2420–2429, Sep. 2003.

[98] J. M. Jin, "Electromagnetic scattering from large, deep, and arbitrarily-shaped open cavities," *Electromagn.*, vol. 18, no. 1, pp. 3–34, Jan. 1998.

[99] H. T. Anastassiu, "A review of electromagnetic scattering analysis for inlets, cavities, and open ducts," *IEEE Antennas Propag. Mag.*, vol. 45, no. 6, pp. 27–40, Dec. 2003.

[100] X.-Q. Sheng and E. K. N. Yung, "Implementation and experiments of a hybrid algorithm of the finite-element boundary-integral method for open-region inhomogeneous electromagnetic problems," *IEEE Antennas Propag. Mag.*, vol. 50, no. 2, pp. 163–167, Feb. 2002.

[101] R. M. Jones, *Mechanics of Composite Materials*, 2nd ed. FL: CRC Press, 1999.

[102] S. M. Sapuan and I. M. Mujtaba, *Composite Materials Technology: Neural Network Applications.* FL: CRC Press, 2010.

[103] Y. Saad and M. H. Schultz, "GMRES: A generalized minimal residual algorithm for solving nonsymmetric linear systems," *SIAM J. Sci. Stat. Comput.*, vol. 7, no. 3, pp. 856–869, 1986.

[104] P. R. Amestoy, I. S. Duff, and J. Y. L'Excellent, "Multifrontal parallel distributed symmetric and unsymmetric solvers," *Comput. Methods Appl. Mech. Eng.*, vol. 184, no. 2-4, pp. 501–520, Apr. 2000.

[105] C. G. Petra, O. Schenk, M. Lubin, and K. Gaertner, "An augmented incomplete factorization approach for computing the schur complement in stochastic optimization," *SIAM J. Sci. Comput.*, vol. 36, no. 2, pp. C139–C162, 2014.

[106] R. Dyczij-Edlinger and O. Biro, "A joint vector and scalar potential formulation for driven high frequency problems using hybrid edge and nodal finite elements," *IEEE Trans. Microwave Theory Tech.*, vol. 44, no. 1, pp. 15–23, Jan. 1996.

[107] N. Tessier-Doyen et al., "Thermal conductivity of alumina inclusion/glass matrix composite materials: local and macroscopic scales," *J. Eur. Ceramic Soc.*, vol. 27, no. 7, pp. 2635–2640, 2007.

[108] W. Magnus and S. Winkler, Eds., *Hill's Equation.* New York: Dover, 1979.

[109] D. T. McGrath and V. P. Pyati, "Phased array antenna analysis with the hybrid finite element method," *IEEE Trans. Antennas Propag.*, vol. 42, no. 12, pp. 1625–1630, Dec. 1994.

[110] J.-L. Coulomb, F.-X. Zgainski, and Y. Maréchal, "A pyramidal element to link hexahedral, prismatic and tetrahedral edge finite elements," *IEEE Trans. Magn.*, vol. 33, no. 2, pp. 1362–1365, Mar. 1997.

[111] R. D. Graglia and A. F. Peterson, "Hierarchical curl-conforming Nédélec elements for triangular-prism cells," *IEEE Trans. Antennas Propag.*, vol. 60, no. 7, pp. 3314–3324, Jul. 2012.

[112] G. Bedrosian, "Shape functions and integration formulas for three-dimensional finite element analysis," *Int. J. Numer. Methods Eng.*, vol. 35, no. 1, pp. 95–108, Jul. 1992.

[113] W. W. Hager, "Condition estimates," *SIAM J. Sci. Stat. Comput.*, vol. 5, no. 2, pp. 311–316, Jun. 1984.

[114] M. Inoue, “Enhancement of local field by a two-dimensional array of dielectric spheres placed on a substrate,” *Phys. Rev. B*, vol. 36, no. 5, pp. 2852–2862, Aug. 1987.

[115] “Cubit 13.0 user documentation,” 2011. [Online]. Available: cubit.sandia.gov

[116] S. L. Ho, Y. Zhao, and W. N. Fu, “An efficient parameterized mesh method for large shape variation in optimal designs of electromagnetic devices,” *IEEE Trans. Magn.*, vol. 48, no. 11, pp. 4507–4510, Nov. 2012.

[117] K. Zhang, C.-F. Wang, and J.-M. Jin, “A hybrid FETD-GSM algorithm for broadband full-wave modeling of resonant waveguide devices,” *IEEE Trans. Microw. Theory Techn.*, vol. 65, no. 9, pp. 3147–3158, Sep. 2017.

[118] C.-I. G. Hsu and H. A. Auda, “Multiple dielectric posts in a rectangular waveguide,” *IEEE Trans. Microwave Theory Tech.*, vol. MTT-34, no. 8, pp. 883–891, Aug. 1986.

[119] S. J. Fiedziuszko, I. C. Hunter, T. Itoh, Y. Kobayashi, T. Nishikawa, S. N. Stitzer, and K. Wakino, “Dielectric materials, devices, and circuits,” *IEEE Trans. Microwave Theory Tech.*, vol. 50, no. 3, pp. 706–720, Mar. 2002.

[120] C. Bachiller, H. Esteban, H. Mata, M. A. Valdés, V. E. Boria, A. Belenguer, and J. V. Morro, “Hybrid mode matching method for the efficient analysis of metal and dielectric rods in H plane rectangular waveguide devices,” *IEEE Trans. Microwave Theory Tech.*, vol. 58, no. 12, pp. 3634–3644, Dec. 2010.

[121] C. Bachiller, H. Esteban, V. E. Boria, J. V. Morro, M. Taroncher, and B. Gimeno, “Cad of evanescent mode waveguide filters with circular dielectric resonators,” in *IEEE Antennas Propag. Society Int. Symp. Dig.*, Orlando, FL, USA, July 9–14, 2006.

[122] W. Hoffmann, “Iterative algorithms for Gram-Schmidt orthogonalization,” *Computing*, vol. 41, no. 4, pp. 335–348, Dec. 1989.

[123] E. Carson, N. Knight, and J. Demmel, “Avoiding communication in nonsymmetric Lonczon-based Krylov subspace methods,” *SIAM J. Sci. Comput.*, vol. 35, no. 5, pp. S42–S61, 2013.

[124] L. Hamandi and R. L. F. Özgüner, “Review of domain-decomposition methods for the implementation of FEM on massively parallel computers,” *IEEE Trans. Antennas Propag.*, vol. 37, no. 1, pp. 93–98, Feb. 1995.

[125] G. Karypis and V. Kumar, "A fast and high quality multilevel shceme for partitioning irregular graphs," *SIAM J. Sci. Comput.*, vol. 20, no. 1, pp. 359–392, Aug. 1998.

[126] H. A. van der Vorst, "Bi-CGSTAB: A fast and smoothly converging variant of Bi-CG for the solution of nonsymmetric linear systems," *SIAM J. Sci. Comput.*, vol. 13, no. 2, pp. 631–644, Mar. 1992.

[127] C. Farhat, K. Pierson, and M. Lesoinne, "The second generation FETI methods and their application to the parallel solution of large-scale linear and geometrically non-linear structureal analysis problems," *Comput. Methods Appl. Mech. Eng.*, vol. 184, no. 2-4, pp. 333–374, Apr. 2000.

[128] C. Farhat, P. Avery, R. Tezaur, and J. Li, "FETI-DPH: A dual-primal domain decomposition method for acoustic scattering," *J. Comput. Acoust.*, vol. 13, no. 3, pp. 499–524, Sep. 2005.

[129] Z. Peng and J. F. Lee, "A scalable nonoverlapping and nonconformal domain decomposition method for solving time-harmonic Maxwell equations in R3," *SIAM J. Sci. Comput.*, vol. 34, no. 3, pp. A1266–A1295, 2012.

[130] B. Alberts et al., *Essential Cell Biology*, 4th ed. NY: Garland Science, 2014.

[131] J. Genzer and J. Groenewold, "Soft matter with hard skin: From skin wrinkles to templating and material characterization," *Soft Matter*, vol. 2, pp. 310–323, 2006.

[132] D. G. Flagello, T. Milster, and A. E. Rosenbluth, "Theory of high-NA imaging in homogeneous thin films," *J. Opt. Soc. Am. A*, vol. 13, no. 1, pp. 53–64, Jan. 1996.

[133] Y. M. Engelberg and S. Ruschin, "Fast method for physical optics propagation of high-numerical-aperture beams," *J. Opt. Soc. Am. A*, vol. 21, no. 11, pp. 2135–2145, Nov. 2004.

[134] J. Judkins and R. Ziolkowski, "Finite-difference time-domain modeling of nonperfectly conducting metallic thin-film gratings," *J. Opt. Soc. Am. A*, vol. 12, no. 9, pp. 1974–1983, Sep. 1995.

[135] L. Liu, Z. Shi, and S. He, "Analysis of the polarization-dependent diffraction from a metallic grating by use of a three-dimensional combined vectorial method," *J. Opt. Soc. Am. A*, vol. 21, no. 8, pp. 1545–1552, Aug. 2004.

[136] B. Karczewski and E. Wolf, "Comparison of three theories of electromagnetic diffraction at an aperture Part I: coherence matrices, Part II: The far field," *J. Opt. Soc. Am.*, vol. 56, no. 9, pp. 1207–1219, Sep. 1966.

[137] P. R. T. Munro and P. Török, "Calculation of the image of an arbitrary vectorial electromagnetic field," *Opt. Express*, vol. 15, no. 15, pp. 9293–9307, Jul. 2007.

[138] E. Y. Lam and A. K. K. Wong, "Computational lithography: virtual reality and virtual virtuality," *Opt. Express*, vol. 17, no. 15, pp. 12 259–12 268, Jul. 2009.

[139] S. H. Chan, A. K. Wong, and E. Y. Lam, "Initialization for robust inverse synthesis of phase-shifting masks in optical projection lithography," *Opt. Express*, vol. 16, no. 19, pp. 14 746–14 760, Sep. 2008.

[140] B. M. Barnes et al., "Three-dimensional deep sub-wavelength defect detection using $\lambda = 193$ nm optical microscopy," *Opt. Express*, vol. 21, no. 22, pp. 26 219–26 226, Nov. 2013.

[141] J. Zhu et al., "Electromagnetic field modeling for defect detection in 7 nm node patterned wafers," *Proc. SPIE*, vol. 9778, p. 97780P, Feb. 2016.

[142] J. Zhu et al., "Improved deep-etched multilayer grating reconstruction by considering etching anisotropy and abnormal errors in optical scatterometry," *Opt. Lett.*, vol. 40, no. 4, pp. 471–474, Feb. 2015.

[143] J. Zhu et al., "Robust solution to the inverse problem in optical scatterometry," *Opt. Express*, vol. 22, no. 18, pp. 22 031–22 042, Sep. 2014.

[144] J. Zhu, Y. Shi, L. L. Goddard, and S. Liu, "Application of measurement configuration optimization for accurate metrology of sub-wavelength dimensions in multilayer gratings using optical scatterometry," *Appl. Opt.*, vol. 55, no. 25, pp. 6844–6849, Sep. 2016.

[145] L. T. Pillage and R. A. Rohrer, "Asymptotic waveform evaluation for timing analysis," *IEEE Trans. Comput.-Aided Design Integr. Circuits Syst.*, vol. 9, no. 4, pp. 352–366, Apr. 1990.

[146] J. E. Bracken, V. Raghavan, and R. A. Rohrer, "Extension of the asymptotic waveform evaluation technique with the method of characteristics," *IEEE/ACM Int. Conf. Comput.-Aided Design*, pp. 71–75, 1992.

[147] R. D. Slone, J.-F. Lee, and R. Lee, "A comparison of some model order reduction techniques," *Electromagnetics*, vol. 22, no. 4, pp. 275–289, Nov. 2002.

[148] A. Taflove and S. C. Hagness, *Computational Electrodynamics: The Finite-Difference Time-Domain Method*, 3rd ed. MA: Artech House, 2005.

[149] S. M. Rao, *Time Domain Electromagnetics.* San Diego: Academic, 1999.

[150] Y. Shi and J.-M. Jin, "A time-domain volume integral equation and its marching-on-in-degree solution for analysis of dispersive dielectric objects," *IEEE Trans. Antennas Propag.*, vol. 59, no. 3, pp. 969–978, Mar. 2011.

[151] F. B. Hildebrand, *Introduction to Numerical Analysis.* NY: Dover, 1974.

[152] W. L. Ko and R. Mittra, "A combination of FD-TD and Prony's methods for analyzing microwave integrated circuits," *IEEE Trans. Microwave Theory Tech.*, vol. 39, no. 12, pp. 2176–2181, Dec. 1991.

[153] S. M. Kay and S. L. Marple, "Spectrum analysis–a modern perspective," *Proc. IEEE*, vol. 69, no. 11, pp. 1380–1419, Nov. 1981.

[154] S. Dey and R. Mittra, "Efficient computation of resonant frequencies and quality factors of cavities via a combination of the finite-difference time-domain technique and the Padé approximation," *IEEE Mircow. Guided Wave Lett.*, vol. 8, no. 12, pp. 415–417, Dec. 1998.

[155] F. Zheng, Z. Chen, and J. Zhang, "Toward the development of a three-dimensional unconditionally stable finite-difference time-domain method," *IEEE Trans. Microwave Theory Tech.*, vol. 48, no. 9, pp. 1550–1558, Sep. 2000.

[156] S. G. García, T.-W. Lee, and S. C. Hagness, "On the accuracy of the ADI-FDTD method," *IEEE Antennas Wireless Propag. Lett.*, vol. 1, no. 1, pp. 31–34, May 2002.

[157] N. M. Newmark, "A method of computation for structural dynamics," *J. Eng. Mech. Div., Proc. Am. Soc. Civil Eng.*, vol. 85, no. 3, pp. 67–94, Jul. 1959.

[158] A. Yilmaz et al., "Fast analysis of transient scattering in lossy media," *IEEE Antennas Wireless Propag. Lett.*, vol. 1, no. 1, pp. 14–17, Dec. 2002.

[159] I.-T. Chiang and W. C. Chew, "Fast real-time convolution algorithm for transients of nonlinearly-terminated microwave multiport circuits," *Microw. Opt. Techn. Lett.*, vol. 39, no. 4, pp. 280–281, Nov. 2003.

[160] X. Li and J.-M. Jin, "Time-domain finite-element modeling of electrically and magnetically dispersive medium via recursive FFT," *Microw. Opt. Techn. Lett.*, vol. 50, no. 7, pp. 1837–1841, Jul. 2008.

[161] P. Silvester, "A general high-order finite-element waveguide analysis program," *IEEE Trans. Microwave Theory Tech.*, vol. 17, no. 4, pp. 204–210, Apr. 1969.

[162] E. Polizzi, "Density-matrix-based algorithms for solving eigenvalue problems," *Phys. Rev. B.*, vol. 79, p. 115112, 2009.

[163] J. R. Montejo-Garai and J. Zapata, "Full-wave design and realization of multicoupled dual-mode circular waveguide filters," *IEEE Trans. Microwave Theory Tech.*, vol. 43, no. 6, pp. 1290–1297, Jun. 1995.

[164] C. Carceller, P. Soto, V. E. Boria, and M. Guglielmi, "Design of hybrid folded rectangular waveguide filters with transmission zeros below the passband," *IEEE Trans. Microwave Theory Tech.*, vol. 64, no. 2, pp. 475–485, Feb. 2016.

[165] J. R. Montejo-Garai, J. A. Ruiz-Cruz, J. M. Rebollar, and T. Estrada, "In-line pure E-plane waveguide band-stop filter with wide spurious-free response," *IEEE Trans. Microwave Theory Tech.*, vol. 21, no. 4, pp. 209–211, Apr. 2011.

[166] L. C. Trintinalia and H. Ling, "Extraction of waveguide scattering features using joint time-frequency ISAR," *IEEE Microw. Guided Wave Lett.*, vol. 6, no. 1, pp. 10–12, Jan. 1996.

[167] S. Wagner and J. Ender, "Recognition of jet engines via sparse decomposition of ISAR images using a waveguide scattering model," *Int. J. Microw. Wireless Techn.*, vol. 9, no. 6, pp. 1339–1343, Jul. 2017.

[168] V. C. Chen and M. Martorella, *Inverse Synthetic Aperture Radar Imaging: Principles, Algorithms and Applications.* Edison, NJ: SciTech Publishing, 2014.

[169] C. Özdemir, *Inverse Synthetic Aperture Radar Imaging with MATLAB Algorithms.* Hoboken, NJ: Wiley, 2012.

[170] J. P. Bérenger, "Application of the CFS PML to the absorption of evanescent waves in waveguides," *IEEE Microw. Wireless Compon. Lett.*, vol. 12, pp. 218–220, 2002.

[171] J.-F. Lee, "Finite element analysis of lossy dielectric waveguides," *IEEE Trans. Microw. Theory Techn.*, vol. 42, no. 6, pp. 1025–1031, Jun. 1994.

[172] M. Kuzuoglu and R. Mittra, “Investigation of nonplanar perfectly matched absorbers for finite-element mesh truncation,” *IEEE Trans. Antennas Propag.*, vol. 45, no. 3, pp. 473–486, Mar. 1997.

[173] Z. S. Sacks, D. M. Kingsland, R. Lee, and J.-F. Lee, “A perfectly matched anisotropic absorber for use as an absorbing boundary condition,” *IEEE Trans. Antennas Propag.*, vol. 43, no. 12, pp. 1460–1463, Dec. 1995.

[174] T. Rylander and J.-M. Jin, “Perfectly matched layer for the time domain finite element method,” *J. Comput. Phys.*, vol. 200, no. 1, pp. 238–250, Oct. 2004.

[175] O. Golani, I. Dolev, J. Pond, and J. Niegemann, “Simulating semiconductor structures for next-generation optical inspection technologies,” *Opt. Engrg.*, vol. 55, no. 2, p. 025102, Feb. 2016.